Multiscale quantification of damage in composite structures

Thesis submitted to The University of Manchester for the degree of Doctor of Philosophy in the Faculty of Science and Engineering

2023

Anuj Prajapati

Department of Materials, School of Natural Sciences, The University of Manchester.

Table of Contents

Final word count: 67890

List of Figures

List of Tables

List of Abbreviations

XCT	X-ray computed tomography
SEM	Scanning electron microscopy
CT	Computed tomography
DE	Destructive evaluation
NDE	Non-destructive evaluation
CCD	Charged couple device
FIB	Focussed ion beam
DIC	Digital image correlation
DVC	Digital volume correlation
UD	Unidirectional
HMXIF	Henry Moseley X-ray Imaging Facility
FRCs	Fibre-reinforced composites
FBP	Filtered back-projection

List of Symbols

μ	linear attenuation coefficient/micro
ρ	density
K	x-ray attenuation constant
Z	atomic number
E	photon energy
I	x-ray intensity
(r, Θ)	polar coordinates
ν	wave frequency

Abstract

Fatigue damage in wind turbine blades, made of unidirectional non-crimp glass fibre reinforced polymers (UD-NCF GFRP), has been researched for decades, but the understanding of the damage initiation and progression is not entirely clear. Demand for higher energy output and efficiency drives the need for larger and heavier blades, for which the complex damage interaction needs to be better understood. This study focuses on the tensile fatigue damage mechanisms in a UD-NCF GFRP, their relation to the material architecture, the evolution of strain, and stiffness reduction.

A correlative time-lapse workflow was developed using 3D imaging modalities of x-ray computed tomography (XCT) & scanning electron microscopy (SEM), strain characterization from digital image and volume correlation (DIC-DVC), with tension-tension fatigue testing. The stiffness reduction was attributed to damage found from DIC-DVC strain maps, and damage observed in XCT. These damaged regions of interest were excavated in SEM to enable high-resolution studies.

The results show that damage initiates independently on the surface and the bulk. Surface imperfections including voids and micro-scale notches lead to damage. The voids give rise to matrix cracking, progressing into off-axis cracks in the supporting backing bundles (BB). Off-axis cracks then propagate into the neighbouring load-carrying UD bundles, bridged by matrix cracking, at which point the deformation is severe and the strain localisation is observed in DIC-DVC strain maps. Due to stronger UD fibres failing, the local region becomes more compliant, leading to UD and BB fibre failures in nearby regions and a significant loss in stiffness.

In the bulk, UD fibre breaks originate close to BB and proceed more in width than thickness due to the reduction of BB-induced waviness in width. These clustered UD fibre breaks lead to matrix cracks in resin-rich regions, leading to near-off-axis cracks and UD fibre breaks. UD fibres away from the backing bundle exhibit late-stage failure due to absence of waviness and misalignment. Through DVC, ‘bands’ of strain concentrations are observed, in higher compliance regions that are resin-rich and have backing bundles. This is also corroborated by the damaged regions observed predominantly in these bands, and with a tensile model that shows higher stresses in these bands. At some point, this surface and bulk damage can possibly join up with larger splits to progress further and can lead to complete failure.

This PhD thesis is a two-pronged approach. In addition to the experimental workflow, image analysis methods were developed to quantify fibres and damage. A novel workflow to trace individual fibres and segment phases to study their morphology was developed and compared against existing workflows. Another novel method to automatically detect damage and its evolution in a series of 3D images using fibre tracing and machine learning was developed. A combination of these parts is crucial in understanding complex fatigue behaviour.

A better understanding of the fatigue damage mechanisms allows us to design better fibre architecture by optimising the weak links including backing bundles, resin-rich regions, surface defects, and densely packed fibres. The improved composite can withstand higher stresses and longer service life. This also enables accurate modelling of fatigue behaviour, ultimately pushing the design limits and reducing the cost of energy. The correlative workflow and the image analysis methods can be applied to other types of FRPs to study a variety of time-dependent phenomena.

Declaration

No portion of the work referred to in this thesis has been submitted in support of an application for another degree or qualification of this or any other university or other institute of learning.

Scientific contributions

The main findings from this project have been prepared into manuscripts for publication in peer-review journals. To date, Chapter 6 has been published in IOP Conference Series: Materials Science and Engineering, for the 41st Risø International Symposium on Materials Science: "Materials and Design for Next Generation Wind Turbine Blades", Denmark. Chapter 5, 7, and 8 are ready for submission. In addition, outputs from collaborations and attended conferences during this PhD study are also listed.

1) Time-lapse correlative study of the fatigue damage evolution and strain fields in quasi-unidirectional glass fibre composites using three-dimensional imaging.
   (Planned submission in Composites Part B)
   Anuj Prajapati, Robert M. Auenhammer, Stuart Morse, Ali Chirazi, Daniel Lichau, Lars P. Mikkelsen, Timothy Burnett and Philip J. Withers (2023).

2) A comparative study of a novel and existing segmentation and quantification methods for 3D imaging data of fibre composites.
   (Planned submission in Composites Part B)
   Anuj Prajapati, Robert M. Auenhammer, Amin Garbout, Lars P. Mikkelsen, Timothy L. Burnett, and Philip J. Withers (2023).

3) A novel automated workflow involving machine learning to study damage progression of fibre-reinforced composites by time-lapse 3D x-ray tomography.
   (Planned submission in Composites Part B)
   Anuj Prajapati, Daniel Lichau, Ali Chirazi, Lars P. Mikkelsen, Timothy L. Burnett, and Philip J. Withers (2023).

4) Observing the evolution of fatigue damage and associated strain fields in a correlative, multiscale 3D time-lapse study of quasi-unidirectional glass fibre composites.
   Anuj Prajapati, Ali Chirazi, Lars P Mikkelsen, Timothy Burnett, Philip J Withers 2020 IOP Conf. Ser.: Mater. Sci. Eng. 942 012039

5) Low resolution X-ray computed tomography scans of short fibre injection molded composites for automotive crash modelling.
   (Planned submission in Composites Part B)
   Robert M. Auenhammer, Anuj Prajapati, Lars P. Mikkelsen, Philip J. Withers, Leif E. Asp, Renaud Gutkin (2023).

6) Comparison and validation of tensile fatigue damage in quasi-unidirectional glass-fiber composites with X-ray computed tomography-based modelling, Tomography for Scientific Advancement (ToScA), 2022.
   Anuj Prajapati, Robert Auenhammer, Ali Chirazi, Daniel Lichau, Lars P. Mikkelsen, Timothy L. Burnett, Philip J. Withers.

7) Multiscale quantification of damage in composite structures, Composites@Manchester, 2019.
   Anuj Prajapati, Ali Chirazi, Lars P. Mikkelsen, Timothy L. Burnett, Philip J. Withers.

Acknowledgements

It is nearly the end of my PhD after countless hours of experiments, writing up and delays (thanks COVID!). I would like to express my heartfelt gratitude to the people that contributed immensely to this project and my experience.

I fall short of words trying to describe how grateful I am to my supervisor Prof Philip Withers. You are a great role model and an inspiration to work with. Thank you for nurturing and guiding me to be a qualified researcher, I genuinely appreciate your patience and knowledge which helped me a lot during this project.

I would also like to thank my co-supervisor Prof Timothy Burnett for your kind help and supervision throughout my project. I appreciate your professional knowledge which constructively steered the direction of this thesis. I also thank Stuart Morse for greatly assisting me throughout the project.

I would also like to express heartfelt gratitude to my industrial collaborators from Thermo Fisher, Dr Ali Chirazi and Daniel Lichau. Thanks a lot for hosting me so well in Bordeaux during my secondment and for your continued support, your selfless help and support have greatly improved this thesis.

Many thanks to my friends and colleagues here at the Henry Moseley X-ray Imaging Facility – Chakri, Ying, Yuan, Sam, Julia, Amin, Berzah, Evangelos, Suleyman, Dongze, Jiaqi, Zihan, Leping, and all my well-wishers. I am fortunate for all your help and support. You made my time here great.

I would also like to thank my EU Horizon MUMMERING advisors Prof Lars Mikkelsen, Professor Anders Bjorholm Dahl, and Vedrana Andersen Dahl, for their selfless support and guidance. Thanks to Robert Auenhammer, Jakeoung Koo, and Elise Brenne for guiding and collaborating throughout this project, you have helped me improve this thesis greatly.

Finally, I would like to say thanks to my partner Amy, my parents Ajai Pal and Sangeeta, and friends and family for their continued support, I could not have done this without you.

1. Introduction

This thesis examines the fatigue behaviour of quasi-unidirectional non-crimp glass-fibre composites, commonly used in wind turbine blades. It derives from over 4 years of research work carried out at The University of Manchester's Henry Moseley X-ray Imaging Facility and the Northwest Composites Centre, written as a compilation of four research papers. In addition to the papers, the thesis has chapters introducing the motivation for this research, existing knowledge and the methodology undertaken for this work.

This chapter introduces the problem statement and motivation behind this work, highlights the aims and achievements, and finally gives an overview of the thesis layout.

1.1. Motivation

With the ever-increasing awareness of the disastrous impact of climate change on communities worldwide, climate change actions have never been more important. United Nations' net zero carbon emissions target of reducing emissions by 45% by 2030 and reaching net zero by 2050 will help limit the global warming temperatures increase to 1.5°C above pre-industrial levels [1]. This climate crisis combined with the recent realisation of the need for energy sovereignty due to geopolitical tensions makes it critical to move away from conventional fossil fuel-based energy sources to renewable and sustainable sources.

Wind power has proven to be a great alternative to bring about this shift, as the installations of wind energy are on the rise worldwide [2], as evidenced in Figure 1.1. Projections show that at the current rates of adoption, onshore wind will have the lowest levelized cost of energy (LCOE) by 2025. International Energy Agency's (IEA) Net Zero by 2050 roadmap recommends a global electricity combination of wind (35%), solar (33%), hydropower (12%), nuclear (8%), bioenergy (5%), hydrogen-based (2%), and fossil-fuel based sources (2%) [3], [4]. But to properly realise the goals of net zero emissions by 2050, wind energy needs to be more competitive as the installations lag – it is projected that at the current compound annual growth rates (CAGR), by 2030 there will be less than two-thirds of the wind energy capacity required for a net zero pathway to 2050 [2], as shown in Figure 1.2.

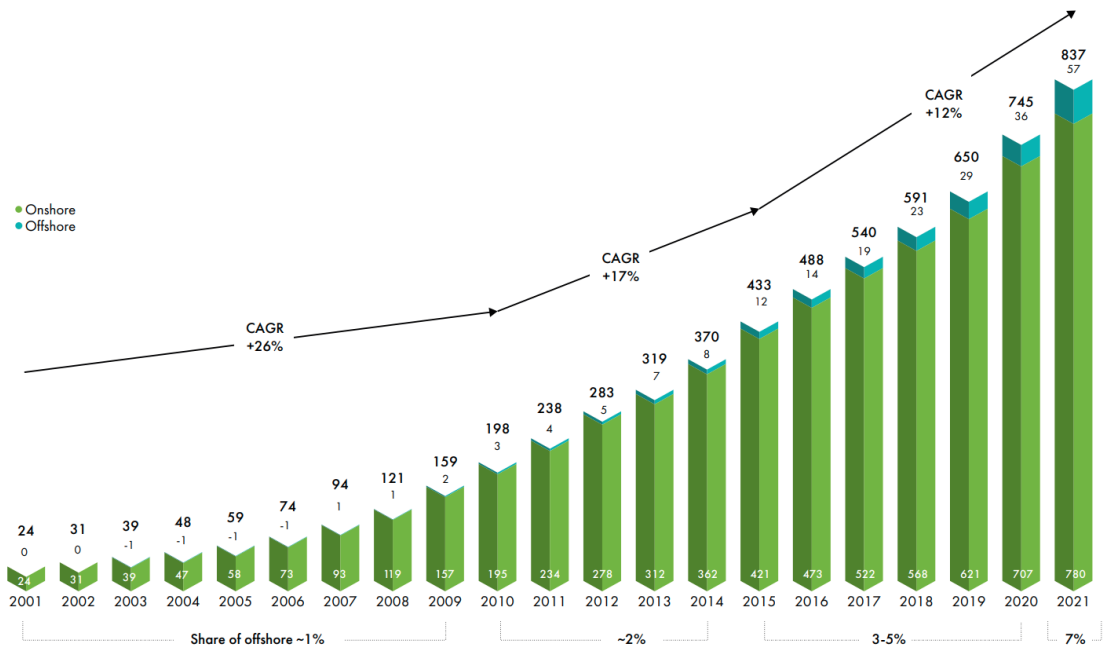

Figure 1.1 Total installed wind capacity (GW) per year. The growth has been dominated by onshore installations [2].

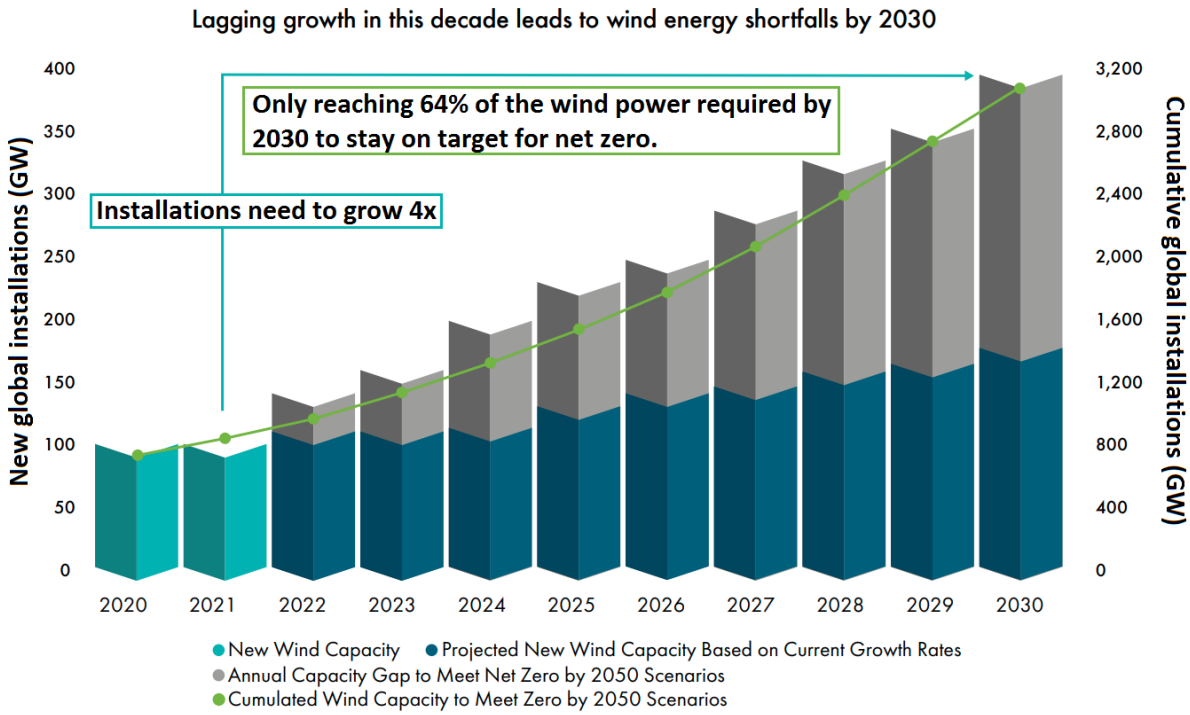

Figure 1.2 Projected demand to meet net zero emissions vs current and estimated growth rates. The growth lags about ~36% behind targets [2].

As with any power source, the cost of energy is defined the cumulative cost of equipment, installation, and maintenance, per unit of energy produced. It can be formulated in Eq 1.1 as:

$$\boldsymbol{Cost\ of\ energy\ (CoE)} = \frac{\boldsymbol{Equipment\ cost + Installation\ cost + Maintenance\ cost}}{\boldsymbol{Power\ produced}} \qquad \mathbf{1.1}$$

Each of the variables can be optimised to decrease the CoE, especially the power produced. One way to increase the power produced is to build longer blades, as the power produced by the wind turbine is proportional to the captured wind area [5]; swept area of the rotor blades is proportional to the squared blade length. Therefore, increasing blade length leads to a pronounced increase in the power produced. This has been demonstrated in the larger blades used in wind farms worldwide, General Electrics' Haliade-X pushing above 100m [6]. Bigger blades tend to be heavier, which

implies that the materials used to construct the blades must be stronger, which can be done by improving and redesigning materials.

Due to the repeated loading of the blades from wind and gravitational loads, fatigue becomes the primary driver of wind blade design, as the wind blade goes through an estimated 10^8-10^9 load cycles during its 20-30 years of service life [7], during which its mechanical properties including stiffness progressively deteriorate, leading to poor performance. The blade also experiences significant centrifugal loads, and these are more pronounced at the blade roots [8]. As shown in Figure The primary fatigue loads are borne by spar caps, which are mainly comprised of quasi-unidirectional (UD) non-crimp-fabric (NCF) glass-fibre reinforced polymers (GFRP), with bundles of fibres mostly aligned in one direction towards the load.

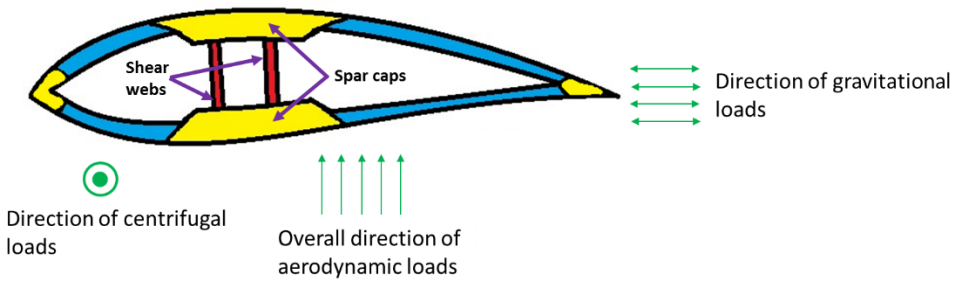

Figure 1.3 Spar caps are shown in the cross-section of a wind blade. These are the main load-carrying components in a wind-blade, made of unidirectional fibre-reinforced composites. Adapted from [9].

As shown in Figure 1.4, the composite materials demonstrate an exceptional set of mechanical properties including high stiffness-to-weight ratios and excellent fatigue resistance, among others. Apart from the higher specific stiffness and strength that CFRPSs exhibit, they also have better fatigue resistance, leading to a potentially longer wind blade service life compared to GFRPs [10]. Leading manufactures including

Gamesa Technology Corp and Vestas Wind Systems have already replaced select structural parts of the wind blades with CFRPs [11]. The higher cost of carbon fibre has deterred some manufacturers from switching, but some novel lower-cost textile-derived CFRPs are being trialled to be used in wind blades [12].

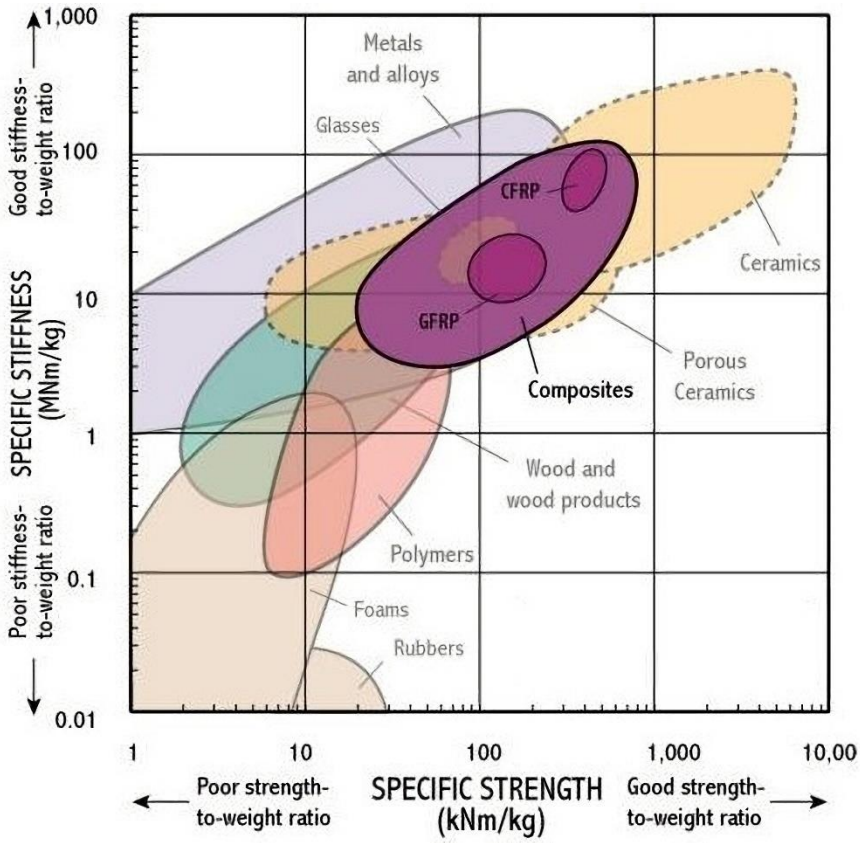

Figure 1.4 Different classes of materials exhibiting a varied set of specific stiffness and specific strengths. Both GFRPs and CFRPs are exceptional at high specific stiffness and strength. Adapted from [13].

But the fatigue damage mechanisms of UD-NCF materials are not completely understood, despite active research in recent decades [14], due to incredibly complex damage mechanisms interplaying between different damage modes. Also, conventional studies focused on two-dimensional imaging, which does not accurately resolve the 3D structures. This lack of understanding imposes several additional safety

factors. Improving our understanding of the damage mechanisms using 3D characterisation will help us predict the lifetime and the damage progress better, allow for an informed maintenance and inspection routine, and allow us to design closer to the limit, so they can sustain heavier load cycles for longer. This will bring down the capital costs as well, improving the cost of energy.

This is also important to consider as loss in stiffness leads to a reduction in energy efficiency, can trigger premature or sudden failures of blades and possibly lead to a catastrophic collision with the towers, as shown in Figure 1.5. All these factors can deter their rates of adoption, falling behind in the net-zero targets. Once we improve our understanding of these damage mechanisms, we can use this knowledge to optimize the material architecture e.g. modifying the fibre layup and/or changing the constituent reinforcements or the matrix.

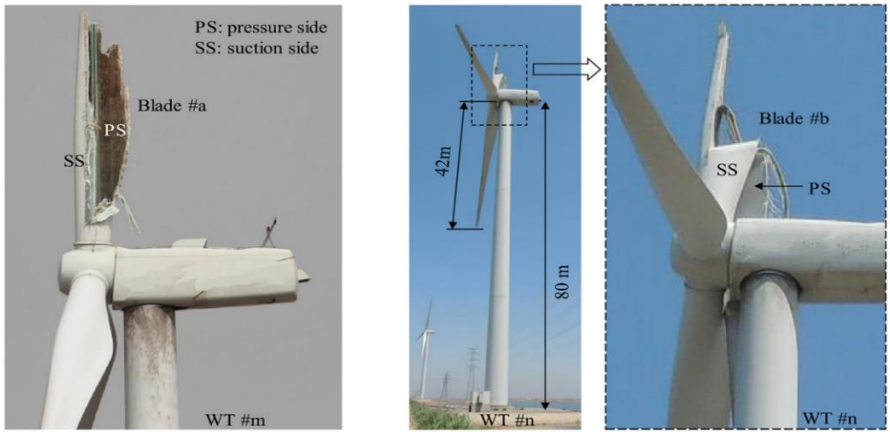

Figure 1.5 Images showing premature fatigue failure of two separate wind blades #a and #b in two separate wind turbines #m and #n [15].

The motivation behind this PhD study – improving our understanding of fatigue in composites for the uptake of wind energy and mitigation of climate change, has been discussed. Therefore, this topic of understanding fatigue damage and its progression in UD-NCF GFRPs was selected. This target was realised via developing a novel time-lapse correlative workflow which includes mechanical testing and a suite of

interspersed imaging and characterization routines. Additional work was undertaken to develop image analysis methods for the broader field of fibre composites.

1.2. Aims and objectives

This project aimed to understand the fatigue damage mechanisms of UD-NCF GFRPs, particularly from the initiation-progression point of view. This progression in damage was to be linked to the microstructural features and eventually related to observed deterioration in stiffness. This was extended via a two-pronged approach of developing time-lapse experimental methods to facilitate 4D observations (time is the 4th dimension), and develop post-acquisition image analysis methods, both being critical in understanding complex time-dependent 3D behaviour.

The objectives were:

1) To develop an experimental ex-situ time-lapse, multiscale, and correlative workflow involving x-ray tomography (XCT), along with complementary digital image correlation (DIC) and post-mortem 3D-serial sectioning scanning electron microscopy (SEM) to study the initiation and progression of the fatigue damage mechanisms and its relation to stiffness reduction.
2) To develop novel and benchmark existing image analysis methods for fibre composites which can be used to generate statistically relevant information on population and location of damage features, and fibre/bundle orientation-morphology, eventually enabling image-based modelling for composites.
3) To locate the microstructural features and regions of interest which initiate damage modes of fibre breaks, matrix cracking and splits, and identify the ones that progress and give rise to other modes of damage.

4) To develop image analysis methods for automated damage detection to help study damage progression in time-lapse x-ray tomography data.
5) To evaluate the stresses and strains in those regions to find out weaker links in the material architecture.
6) To generate this knowledge for manufacturers to modify microstructure, and to inform and verify modelling and simulations.

1.3. Thesis outline

This thesis is a compilation of four papers written during this PhD, in addition to the chapters that lay the necessary groundwork and document the methodology.

Chapter 2 contains the literature review on wind turbine blades and composites, including – the fibre architecture and design of UD-NCF FRPs, our existing understanding of fatigue behaviour in terms of damage mechanisms, their progression and the complicated interplay, and their use in wind turbine blades.

Chapter 3 contains the literature review on the imaging and characterisation of FRPs, with a focus on x-ray computed tomography, electron microscopy and digital image correlation. Additionally, post-acquisition image analysis and quantification methods have been discussed.

Chapter 4 documents the materials and methods used in this thesis, namely, the time-lapse experiments and the image analysis methodology undertaken for this PhD, discussing the correlative aspect of employing multiple imaging modalities.

Chapter 5 is the published paper precursing the following keystone paper, looking at the evolution of tension-tension fatigue damage via x-ray tomography in a region of interest identified from digital image correlation, to find damage that could be responsible for stiffness loss.

Chapter 6 is the manuscript of the keystone paper of this study, which brings mechanical testing, x-ray tomography, electron microscopy, and digital image correlation in a novel multiscale correlative workflow to observe the evolution of full-field tension-tension fatigue damage and the associated strain fields in UD-NCF GFRPs, eventually observing the relation between damage and stiffness.

Chapter 7 is a manuscript which introduces a novel image analysis workflow for studying imaging data of fibre composites and benchmarks them against three established workflows, ranking on various parameters from accuracy to versatility to financial costs. This paper quantitatively ranks the merits and demerits of the workflows against each other and gives a guided introduction to image analysis methods for FRCs to the composites community.

Chapter 8 is a manuscript introducing a novel image analysis workflow to study damage progression in fibre-reinforced composites via an automatic fibre break detection method using machine learning, developed in collaboration with Thermo Fisher Scientific during an industrial secondment.

Chapter 9 and 10 summarise the main conclusions of this project and potential opportunities for future work.

2. Literature review on wind turbine blades and composites

This chapter summarises the state of the art in wind turbine design and the characterisation on which the research in this dissertation builds.

The next section expands on the loading conditions on a wind blade which drives the material design of the load-bearing components.

2.1. Wind blade loading conditions

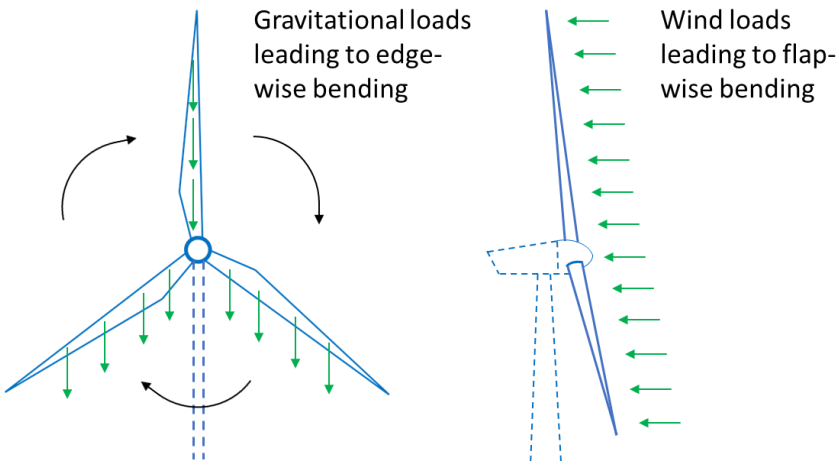

Figure 2.1 Gravitational and wind-induced loads leading to edge-wise and flap-wise loading on the wind blades respectively. Adapted from [9].

A wind turbine generates energy by extracting some of the kinetic energy of the wind flowing through it. The wind direction is measured, and the rotor is turned to face against the wind. The wind loads cause the blades to bend normal to the plane of revolution, causing flap-wise loads which are quite variable and unstable [16]. As the blades rotate and the wind speed changes, it causes a change in the magnitude and direction of both these types of loads, leading to fatigue. Particularly, the backside of the blade is under a

compression-compression fatigue loading regime, and the front side is under tension-tension fatigue loading. The blades experience many kinds of loads, but the most significant of them are the loads resulting due to wind pressure and the blades' own weight, as shown in Figure 2.1. The loads resulting from the wind dynamics are quite variable as the wind speeds are stochastic.

The gravity loads act downwards to the ground, which changes direction twice during a revolution, causing edgewise bending. Although they are designed to be light-weight, each blade can easily weigh ~12 tonnes [17]. These loads lead to the leading edge and the trailing edge to be in an alternating tension-compression loading regime. Edgewise bending is also caused by the torques driving the turbines. These loads are regular compared to the flap-wise bending loads, but still variable as the wind loads interplay [18]. The combination of these dominant gravitational, centrifugal, and wind-induced loads leads to a complicated loading regime for the wind blade materials.

The blades also undergo other significant loading conditions including centrifugal forces, which increase squared with the rotation speed, but these are in a static tensile regime and damage mechanisms are very different for cyclic and static loading and will therefore not be a part of this study.

A typical turbine is designed for a service life of more than 20 years, during that it experiences a high-cycle fatigue regime for up to 10^8-10^9 stress cycles [7]. For wind blades, the loads are higher and the number of fatigue cycles is comparable to the fatigue experienced by aerospace and automobile structures [7]. As the wind turbines get bigger to increase the power output, these loads increase in magnitude and variability, thus requiring aggressive measures to mitigate the degradation of strength and stiffness arising from such an extreme number of stress cycles. This requires a careful selection of

materials for each part of the blade as they experience different loading conditions and are designed accordingly.

The loads on each part of the blade drive the choice of materials as shown in Figure 2.2; the spar caps shown in yellow bear the dominant axial loads induced by the wind leading to flap-wise bending fatigue in tension-tension and compression-compression regimes. The spar caps are made with unidirectional (UD) composites, while the shear webs and the outer shells are borne by foams and multidirectional laminates [9], [19].

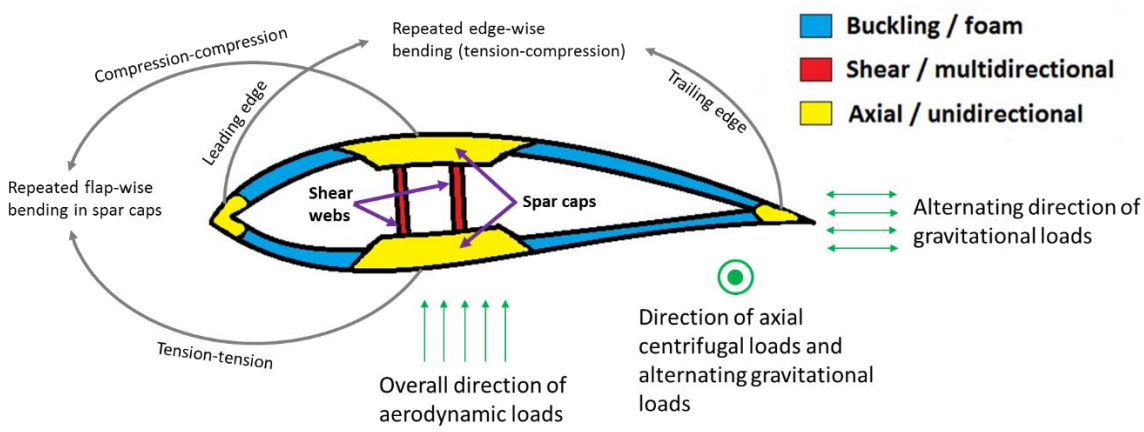

Figure 2.2 The loading regimes for each part of the blade as a choice based on materials; the spar caps being the main load-carrying components. Figure adapted from [7], [9].

The fatigue damage mechanisms from tension and compression are fundamentally different, the latter being affected by kink bands [20]. The damage mechanisms in UD composites due to tension-tension fatigue, which is a major load regime in spar caps, are not fully understood and require additional safety factors in design, also restricting the design of bigger and more energy-efficient blades. For these reasons, tension-tension fatigue in UD composites was chosen as a focus of this PhD study.

Of course, the versatile methodology used in this study can be comfortably extended to study other damage mechanisms of wind blade materials.

In the next section, we introduce different materials used in wind turbine blades.

2.2. Choices of materials in wind turbine blades

Due to the varied types of loads a wind blade is subjected to, each part is designed and considered separately. Fibre-reinforced polymers are materials made of stiff, strong fibres, embedded in a softer, ductile matrix of polymers. Since both the constituents are lighter than conventional metals, they can enable us to design lighter materials which are also damage tolerant. The resulting composite made of stiff fibres and a softer matrix possesses superior mechanical properties including high stiffness, good strength-to-weight ratio, and good fracture toughness, hence they are considered for most parts of the wind blades [21]. Other advantages include orienting the fibres in the direction of the load, so it is possible to prioritise directional mechanical property requirements. Also, they can be designed and conformed to the manufacture of complex shapes with tailored properties. The epoxy provides mitigation of compression loads but also serves as a medium to keep the fibres embedded in place.

Various types of fibre composites exist, which can be classified depending on the types of the matrices; metal matrix composites (MMCs), ceramic matrix composites (CMCs), carbon/carbon composites (C/C), and polymer matrix composites (PMCs), the last one being the preferred choice in wind turbine blades due to its attractive suite of superior mechanical and anti-corrosive properties, including high stiffness-to-weight ratio and fatigue resistance. Quasi-unidirectional glass fibre composites, also known as non-crimp fabric based composites, are hence chosen as the focus of this study. This type of material has most fibres aligned in the load direction, while a smaller amount of ‘backing fibres’ running across the main fibre direction.

The PMCs can be of various types, mostly depending on the manufacturing process; pultruded, filament wound, pre-impregnated (prepreg), resin-transfer etc. They can also

be classified based on the types of reinforcement used; glass, carbon, aramid, basalt etc. As the popular choice of material in wind-turbine blades, we choose glass fibre-reinforced polymers manufactured via vacuum-assisted resin transfer moulding for this study. Common fibre architectures include woven crimp fabrics, non-crimp fabrics and UD prepregs, which are described below.

Woven fabrics

These are the type of fibre architecture in which the fibre bundles are woven and intertwined with each other in a clothing fabric manner, as shown in Figure 2.3. These fibre bundles are woven in a textile zoom, where the 'warp' is the stationary longitudinal fibre bundle held in tension, over which the 'weft' bundle is drawn over and under to weave the fabric. This fabric can be impregnated by resin and cured to form the composites, although pre-impregnated 'prepregs' with woven fabrics are also available. These have significant advantages over 2D laminates like better delamination resistance and impact damage [22], [23]. Apart from the plain weave shown here, different weaving patterns can be used to tailor the mechanical properties. As the fibre bundles are intricately linked, the structural integrity is improved [24].

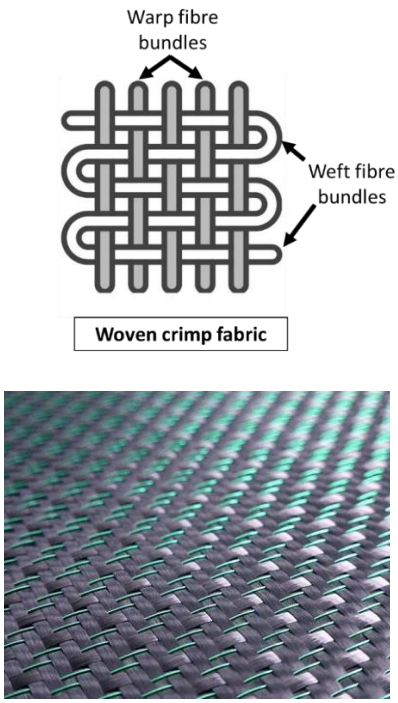

Figure 2.3 Woven fabric-based composites architecture, the fibre bundles are woven at right angles to each other where the weft goes over and under the warp. As evident, this induces waviness in the structure which can lead to damage initiation. Adapted from [25]–[27].

UD prepeg-based laminates

These materials come with the matrix already impregnated into the fibres forming partially cured laminates. This helps eliminate the handling of dry fibres as the fibres are held in place by the semi-cured polymers, also allowing the use of precisely placed unidirectional layers as shown in Figure 2.4. These can be cured by high-temperature applications such as autoclaves, while some cure even at room temperature, decreasing their shelf life. The manufacturing although expensive, yield good quality materials with high fibre content. Such materials find their applications in the automotive and aerospace sectors [28].

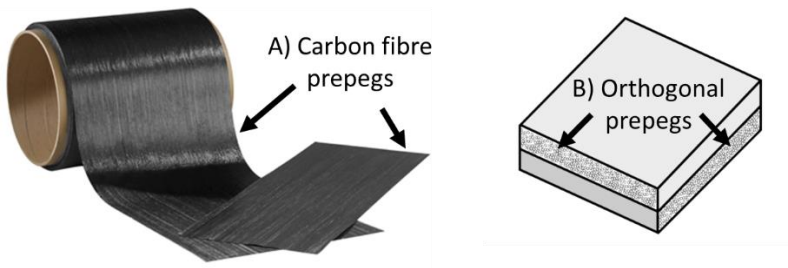

Figure 2.4 A) Carbon-fibre unidirectional prepregs that can be used in a variety of layups. B) A composite with prepregs placed orthogonally. Adapted from [9], [29].

Non-crimp fabrics

The non-crimp fabrics are the class of fabrics which are laid out in a straight fashion without having an intertwined or woven fibre architecture. They are held in position through stitching threads to facilitate easy handling during manufacturing. The basic architecture is comprised of the primary fibre bundles which are tied to the other bundles using stitching threads as shown in Figure 2.5. As they are not woven, these are more homogenous in terms of orientation which ensures there is minimal waviness and sporadicity, meaning there are fewer incoherent sites for damage initiation. Nevertheless, as mentioned in the text later, inhomogeneities like matrix-rich regions are postulated sites for damage initiation in such materials.

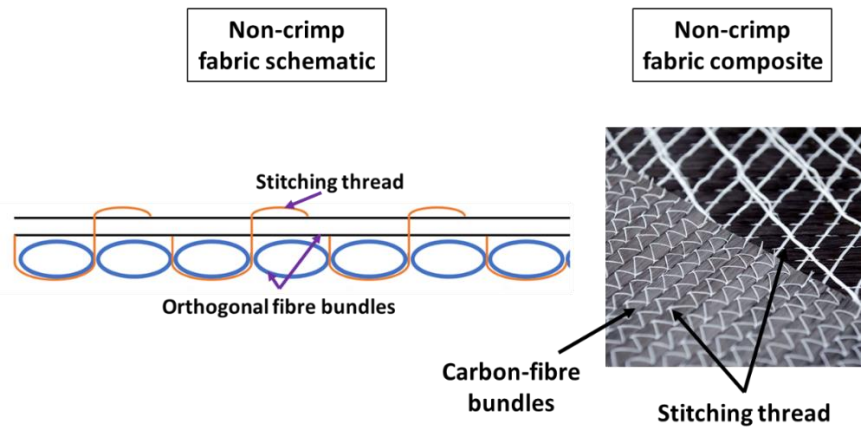

Figure 2.5 The non-crimp fabric architecture. The fibre bundles are laid out in a straight fashion without inducing crimp in the material, unlike the case of woven fabric. Adapted from [30].

Unidirectional non-crimp fabrics (UD-NCF)

The unidirectional NCF composites are a subclass of non-crimp fabric composites that have the most fibres aligned in a particular direction, usually in the direction of the main loads that the material carries as shown in Figure 2.6. These UD fibre bundles are tied to each other using stitching threads, or they can have backing bundles to which they can be stitched to facilitate handling and manufacturing. One of the most popular manufacturing techniques of these non-crimp fabric-based composites is vacuum-assisted resin transfer moulding (VARTM), particularly for wind blades [31]. This method requires dry non-crimped fabrics to be placed on top of each other requiring the desired layup, and then the setup is sealed in a vacuum using a plastic seal. The bundles are laid together on top of one another to achieve a particular design and shape, which in the case of a wind turbine is thicker at the root and thinner at the ends. As mentioned, unidirectional fibre bundles can also be stitched to a much thinner backing fibre bundle (<10% of total fibres) using stitching threads to keep them in place. The epoxy is induced in the setup in a vacuum, so it gets sucked and makes its way into the deep, remote regions. This is a novel technique which can generate a fibre volume fraction of up to 50%-55% [31].

This UD-NCF glass-fibre composite with backing bundles, manufactured by VARTM, used in wind turbine blades is the primary material studied in this thesis. The backing fibre bundles in this material are thinner compared to the unidirectional fibre bundles and are aligned at an angle to them. These are available in a variety of layups, where the backing bundles can be aligned at ± 45°-90° with the UD bundles. This can lead to non-homogeneity resulting in the matrix and fibre-rich regions.

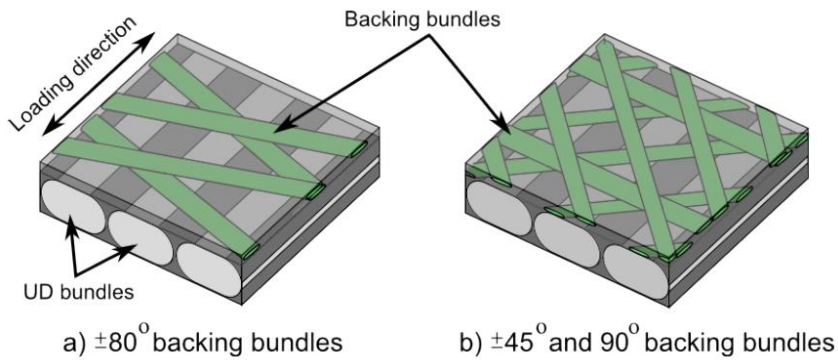

Figure 2.6 The layup of the unidirectional NCF composite, similar to the one used in this study. The UD bundles are tied to the much thinner backing bundles using stitching threads. The backing bundles are at an angle to the UD bundles. Image from [9].

The next section compares the properties of glass and carbon fibres.

Glass vs carbon fibre composites

Glass and carbon fibres both offer suitable properties in terms of mechanical properties such as tensile strength, with each having definite advantages and disadvantages. For glass fibres, E-glass alumino-borosilicate fibres, originally developed for electrical insulation (hence the name 'E-glass') are the most widely used [32]. The volume fraction of these fibres can be maximized in a composite for better stiffness and tensile strength, but it can lead to matrix-rich regions above a fibre volume fraction of 65%, which can lead to higher strength and stiffness but lower fatigue resistance, due to fibres touching each other [33], [34]. Other types of fibres including S-glass (higher silica content) are also used which are mechanically superior but quite expensive [35]. Carbon fibres are an encouraging alternative with low density and higher stiffness, as summarised in Table 2.1, compared to glass fibres but are more expensive and are susceptible to damage owing to their lower damage tolerance, compressive strength, and ultimate strain [34]. Layup manufacturing also requires more precise manual work since the resulting composites are highly sensitive to misalignment and waviness.

Mechanical properties	Glass fibres (E-glass)	Glass fibres (S-glass)	Carbon fibres
Tensile Strength	3.4 Gpa	4.6 Gpa	7 Gpa
Tensile Modulus	72 Gpa	89 Gpa	125-181 Gpa
Density	2.54 g/cm^3	2.53 g/cm^3	1.58 g/cm^3

Table 2.1 Table comparing reported mechanical properties of E-glass, S-glass, and carbon fibres [35]–[40].

As we move towards larger and heavier blades, we need more stiffness and fatigue-resistant blade materials to bear such heavy loads, for which it has been proven that the carbon-fibre reinforced blades have superior fatigue resistance and stiffness for most of the loading conditions. But of course, given the high cost of manufacturing and laying up carbon fibres, there must be a trade-off between cost and efficiency, which is why increasingly, hybrid composites are being considered, which contain both glass and carbon fibre reinforcements. The tensile strength of hybrid composites can be lower than that of pure glass or carbon fibre composites [41].

Hybrid composites involving using reinforcements by both glass and carbon fibre offer a compelling alternative where the high cost of carbon fibres is offset by the low cost of glass fibres. This has been demonstrated in the LM Wind Power's 88.4 P, an 88.4m long blade that uses a hybrid carbon-glass fabric for the spar cap, in addition to the glass fabric for the base shell laminate, both consisting of a mixture of ±45° biaxial fabric, 0°, ±45° combination fabrics, and 0° unidirectional (UD) fabrics in differing

areal weights, leading to a stronger but lighter blade [42]–[45]. This offers an optimum trade-off between cost and mechanical performance. The complete replacement of glass fibres with carbon fibres will increase the cost by 150% but will reduce the weight of the part by 80%. A partial replacement of 30% will lead to a weight decrease of 50% but will increase the cost by 90%, which is a trade-off between cost and weight, used for an 8m turbine blade [46].

The regular single-phase reinforcement has been switched to hybrid architecture for the 88.4 m blade from LM Wind Power, although for all sizes it is beneficial to be replaced by hybrids [46], [47].

2.3. Fatigue behaviour of fibre-reinforced composites

Early studies of fatigue in composites were inspired by earlier metal fatigue studies in structural and energy applications. Significant research in metal fatigue for more than a century [48] has led to a better understanding, but for composites is not understood well. This is because metal fatigue usually pertains to the initiation and propagation of single fatigue cracks, for which damage-tolerant designs can be adopted; in contrast, fatigue in fibre-reinforced composites originate and progress multiple types and numbers of damage features in a complex interrelated manner, leading to different fracture mechanics. Boller et.al [49] outline the complexities in the analysis of composite fatigue owing to multiple mechanisms of damage initiation and progressions, as is emphasised by Talreja [14] that initial analysis for composites was inspired by metal fatigue including the commonly used Paris-Erdogan law [50]–[52] for metals, shown in Equation 2.1; ‘a’ is the crack length, ‘N’ is the number of fatigue

cycles, ‘C’ and ‘m’ are constants, da/dN is the rate of crack growth, and ΔK is the range of stress intensity in a stress cycle [50], [51].

$$\frac{da}{dN} = C\Delta K^m \quad \ldots 2.1$$

A common approach to estimating the service life of a cyclically loaded is the S-N curve, also known as the Wöhler curve. The S-N curve is obtained by testing samples to failure under different maximum stress ‘S’ (or strain) levels, plotted against the number of cycles to failure, as shown in Figure 2.7.

It can be plotted for multiple stress ratios and frequencies, where stress ratio R = $\sigma_{max}/\sigma_{min}$ and frequency is defined for one stress cycle, as shown in Figure 2.7.

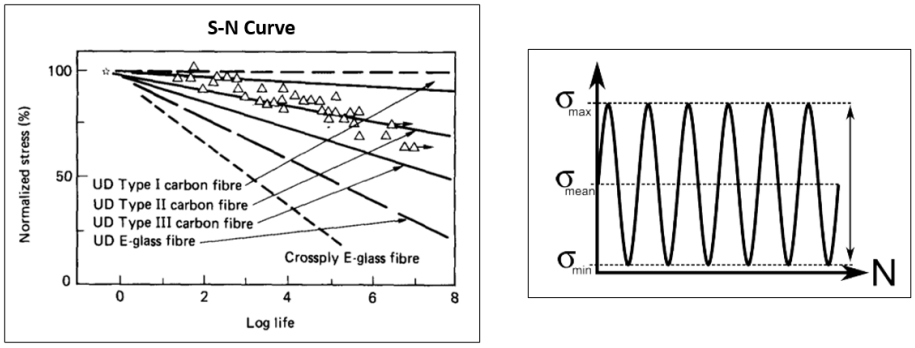

Figure 2.7 On the left is a typical S-N curve, plotted for multiple types of CFRP and GFRPs using normalised maximum stress values and the log of elapsed cycles [53]. On the right is a fatigue load cycle within maximum, minimum, and average stress values [9].

There can be multiple types of fatigue loading regimes depending on the types of tensile/compressive loads that are present. Figure 2.8 highlights a few of those types; tension-tension, tension-compression, and spectrum loading, which can also be consequently extended to compression-compression loading.

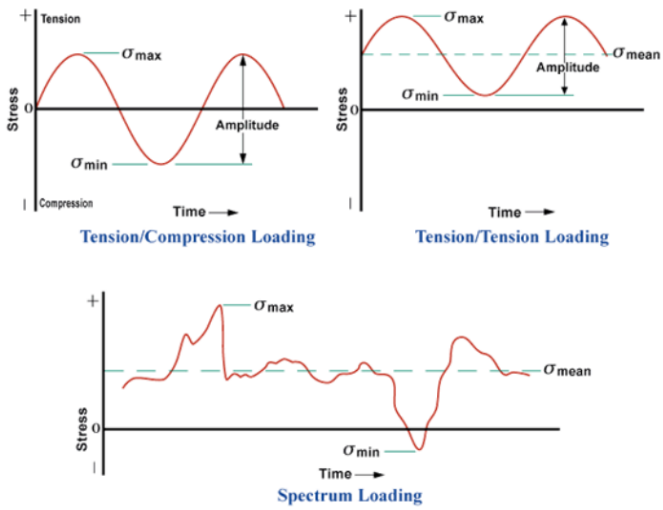

Figure 2.8 Various types of fatigue loading regimes based on constituent tensile and compressive loads [54].

Fatigue in glass-fibre composites is categorically different from metal fatigue where the latter starts from inhomogeneities of voids and grain boundaries[48], [55]. This composite fatigue relies on fundamentally different damage mechanisms of matrix cracking, fibre debonding, fibre breaks, and delamination [56]–[58] as shown in Figure 2.9, all leading to macro-cracks in a complicated interrelated manner.

Matrix cracks can appear in regions of pure matrix or close to fibres, while fibre detaching from the matrix is called debonding. Fibres also break, which often is followed by local interfacial debonding. All of the above damage features can interplay, progress and accumulate together in a complicated stochastic manner, eventually reaching a critical size where multiple damage zones can join up and cause failure [58]–[60]. This progress of fatigue damage and eventual failure is exacerbated by the presence of defects, stress concentrations and improperly placed fibres [34], [61].

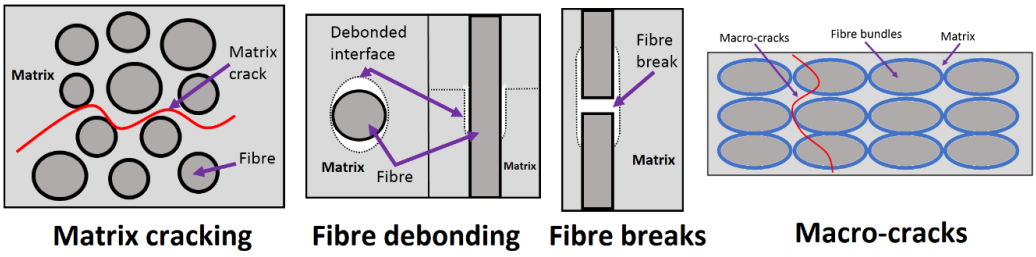

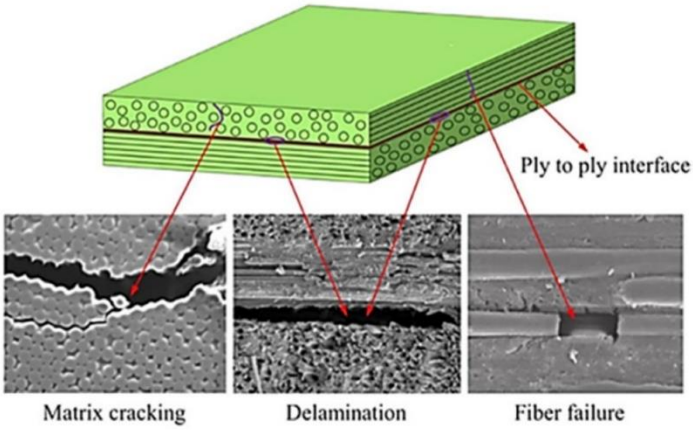

Figure 2.9 Damage mechanisms of matrix cracking, fibre debonding, delamination, and fibre breaks in fibre-reinforced composites, observed with SEM. These often lead to interlaminar macro-cracks eventually [62].

Fatigue behaviour in FRPs is also dependent on a multitude of factors – the type of fibres, volume fraction, orientation, and the type of matrix. Also, service environmental conditions including temperature, hydrothermal ingress and ageing, and corrosion can affect the behaviour [61]. Tensile fatigue damage in GFRPs is also influenced by the applied stress levels. Higher stress levels lead to a pure tension failure and fibre breaks, while at lower stress levels is dominated by stress concentrations [63], [64]. Fibre volume fraction (FVF) is also reported to have an influence on the fatigue behaviour, where higher FVF also exhibit higher porosities. FVF has a greater effect on tension-tension fatigue behaviour, where damage initiates and progresses faster for higher FVF than the lower FVF [65], [66]. This is attributed to the denser fibre packing leading to more interactions between primary and secondary oriented fibres, which is a known site of damage initiation [58], [60]. Stiffness degradation from fatigue damage has been linked to crack density observed by white light optical imaging, where the crack density increases exponentially and then saturates as number of the cycles increase, with matrix cracking and induced delamination as common damage modes [67], [68].

Several models have also been developed to predict the fatigue failure of unidirectional composites. Growth rate of the fatigue damage zones have predicted using micromechanical models, where progressive fibre breaks are caused by stress fields around previously broken fibres [69]. The damage front of fibre breaks decreases with the increase in the frictional sliding stress between debonded fibres and the matrix. Higher R-ratios and lower fibre volume fraction were also found to decrease the damage growth rate.

Another study developed a damage-entropy model to predict the fatigue life of off-axis unidirectional composites under tension-tension cyclic loading. The model was used to analyze the energy damage and temperature evolution during the damage process [70]. The results were compared with experimental data and found to be accurate. The study also examined the temperature evolution of E-glass/epoxy and T800H/2500 composites, noting that temperature increases until final failure, with more increase observed at higher load levels.

Another study presented a layer-based progressive Fatigue Damage Model (FDM) for numerical life prediction of multilayered unidirectional carbon fiber reinforced composites under different block loading conditions [71]. The FDM was further developed to predict the fatigue damage evolution under arbitrary block loading patterns, and suitable load spectra were taken from the literature. Finite Element (FE) calculations were carried out using the FDM for prediction of damage evolution under different load spectra, and the numerical results were compared with those from experiments. For block loading patterns with tensile-dominant cyclic loading, the FDM predicted higher damage in load sequences with decreasing than to increasing load amplitude. The failure points calculated by the FDM showed a good agreement when compared with experimental findings. The influence of load sequence as well as passive damage effects should be considered when designing practice-relevant composite structures by means of FE-based prediction tools.

A study on pure unidirectional flax-epoxy composites found that they have good stability of their stiffness under cyclic loading [72]. They also found that the increase in the loading frequency from 5 to 30 Hz influences the creep-fatigue damage kinetics, self-heating, and the dynamic stiffening phenomenon. However, the increase in the loading frequency does not significantly impact the fatigue endurance outside the

middle low cycle fatigue range (between 2 10^3 and 2 10^4 cycles). It was also found that the composites do not reach a fatigue limit and that a decreasing maximum stress as a function of the number of cycles has to be considered when designing flax epoxy structures. However, the composites have an excellent and outstanding behavior on the HCF range, with a maximum loss in rigidity of 5% when compared to their initial rigidity, during their own life.

Fatigue damage mechanisms in UD-NCF composites

In UD-NCF GFRPs, fatigue mechanisms differ from other fibre architectures. Jespersen et. al. [9] and Zangenberg [73], via x-ray tomography (XCT) and scanning electron microscopy (SEM) respectively, have studied this type of material and its fatigue behaviour. The fatigue behaviour related to stiffness degradation has been correlated to the microscale damage events corresponding to a combination of fibre breaks and matrix cracks starting from off-axis cracks in the backing bundles.

Zangenberg [73] et al. proposed the tension-tension fatigue damage progression in Figure 2.11, adapted by Jespersen [9] et al. The initial stiffness reduction of stage I comes from the off-axis cracks in the backing fibre bundles, similar evidence is found by Reifsnider [74]. These off-axis cracks give rise to UD fibre fractures in close proximities, and the initiation and growth of both of these are responsible for the slow stiffness reduction in stage II. Stress localisation occurs from the remaining fibres which are unable to bear the load and the material fails.

As the studies were predominantly done by destructive 2D SEM micrographs as shown in Figure 2.10, the full 3D morphology and the progression of the material could not be captured, calling for a change in imaging techniques to further our understanding.

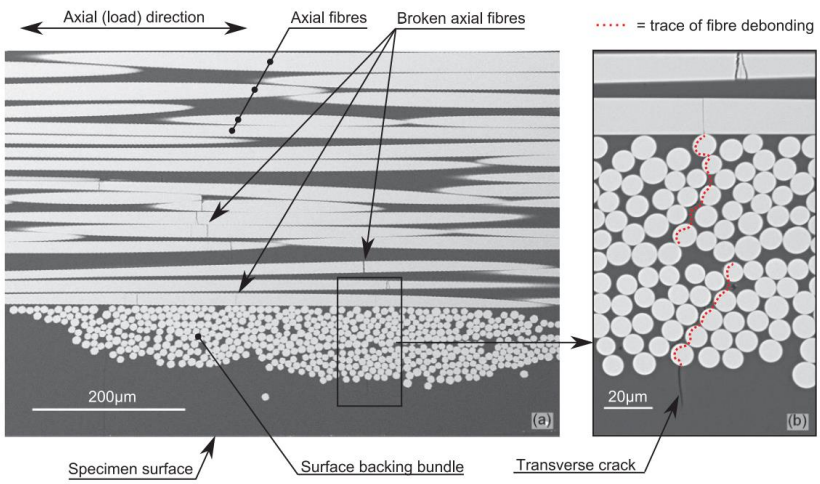

Figure 2.10 Transverse crack in the matrix close to the backing bundle, in tandem with broken UD fibres due to fatigue loading, observed with SEM [73].

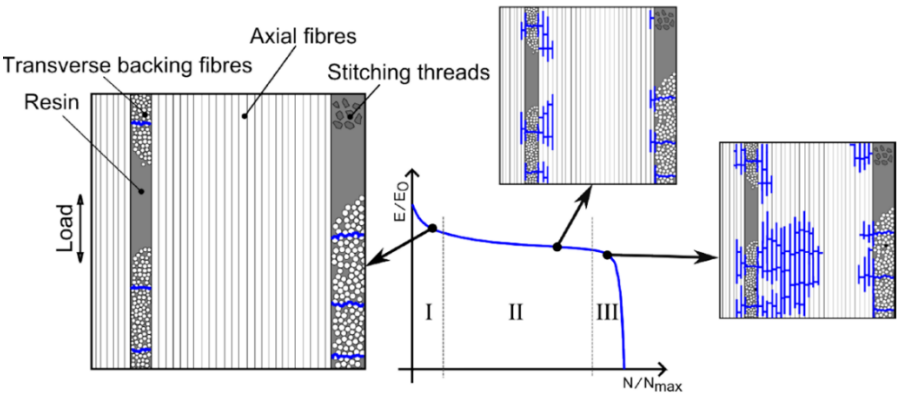

Figure 2.11 Tension-tension fatigue damage progression as the stiffness decreases, proposed by Zangenberg et al. [73]. 'N' and 'N_{max}' refer to the elapsed cycles and the total number of cycles before failure, respectively; 'E' and 'E_0' refer to the dynamic stiffness and the initial stiffness, respectively. Initial off-axis cracks are responsible for Stage I, while Stage II includes progressive UD fibre failures close to backing bundles. Stage III is the failure when the remaining fibres cannot bear the load. Figure from Zangenberg [73].

Jespersen [9] et al. improved upon this understanding by employing non-destructive x-ray computed tomography to resolve the 3D nature of the damage, and also to study the progression in a time-lapse fashion, outlined in Figure 2.12. They found off-axis cracks originating in the off-axis backing bundles in Stage I. These operate in tandem with some UD fibre breaks, particularly for UD bundles which are in close contact

with the backing fibre bundles. The number of off-axis cracks increases and they grow along their length with further loading while more UD fibre breaks keep originating. The off-axis cracks tend to saturate in the initial part of Stage II and the UD cracks begin to propagate in the thickness direction. As the UD fibres progress away from the backing bundles, they tend to spread out in the thickness direction. Later on, these damage features combine to advance together, possibly connected by bridging mechanisms like interlaminar splitting. These lead to enough fibre breaks, which results in fewer fibres not being able to bear the load, leading to failure. The material considered in Jespersen's study was a unidirectional glass fibre composite with layers of backing fibres following the layup of [b/0,b/0]s representing a layer of UD fabric tied to backing fibre bundles at an angle of ±80° using stitching threads.

The progress of damage close to backing bundles in the thickness direction has been shown by Jespersen et al. [9] in Figure 2.13, the UD fibre fractures can be seen to progress in 'cross-over' regions where multiple backing bundles with different orientation cross over each other.

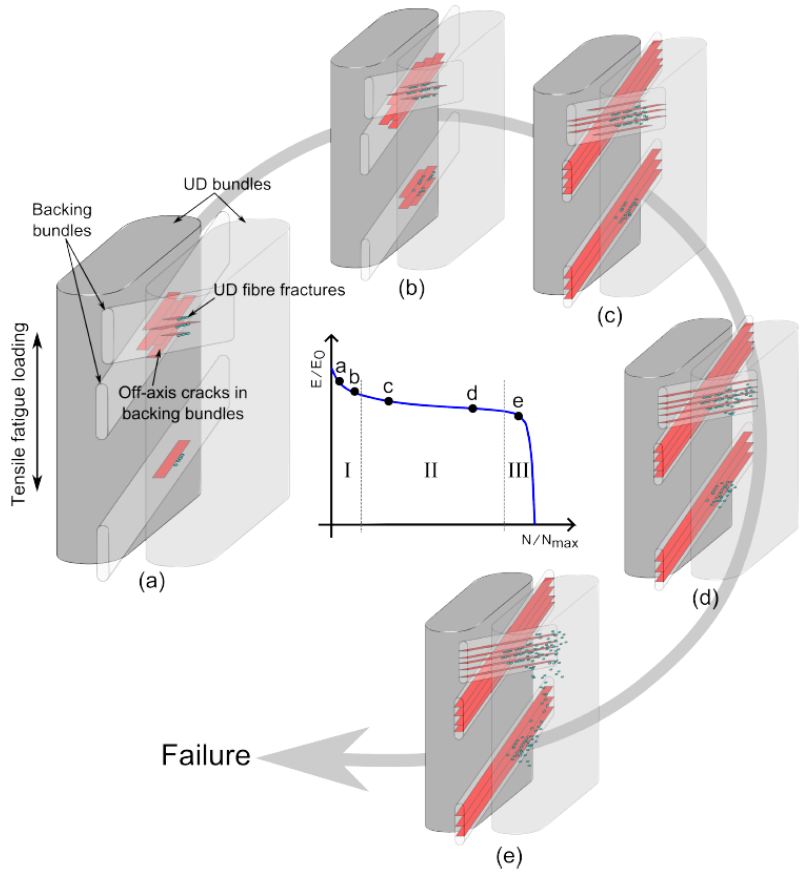

Figure 2.12 Tension-tension fatigue damage progression proposed by Jespersen [9] et al. Off-axis cracks in backing bundles initiate damage and give rise to surrounding UD fibre breaks. Off-axis cracks saturate, and UD fibre breaks continue to progress in thickness and lead to final failure aided by interlaminar splitting. Figure from Jespersen [9].

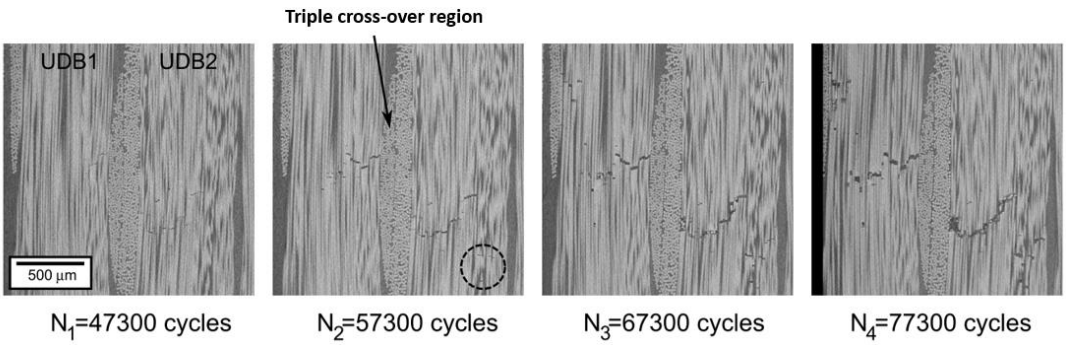

Figure 2.13 Time-lapse of a UD fibre break progression close to backing bundle cross-over region in a GFRP, observed with XCT [9].

Wang et al. [60] observed off-axis matrix cracks originating from specimen edges, some of which were deflected by stitching threads via debonding, as shown in Figure 2.14. The UD fibre breaks were found to be nucleating and propagating close to cross-over regions. The UD fibre breaks were also initiated close to regions with debonding

and longitudinal splitting, which in turn originated from debonding of stitching threads, as shown in Figure 2.15.

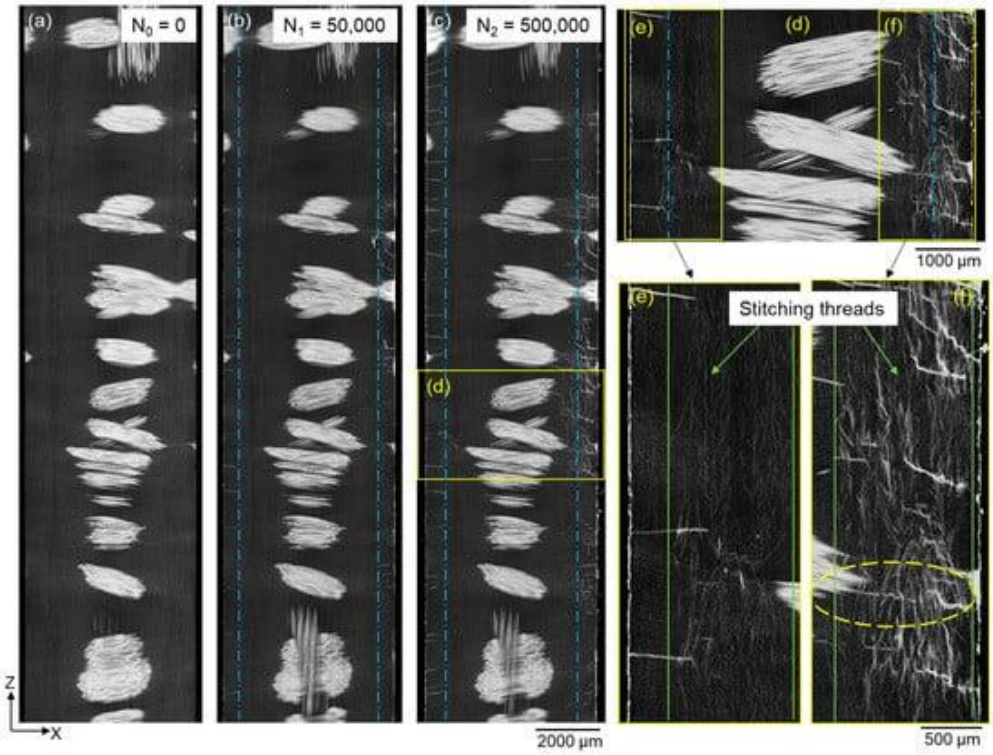

Figure 2.14 Time-lapse of matrix cracks originating from the specimen edges and getting deflected by specimen edges, observed with XCT [60].

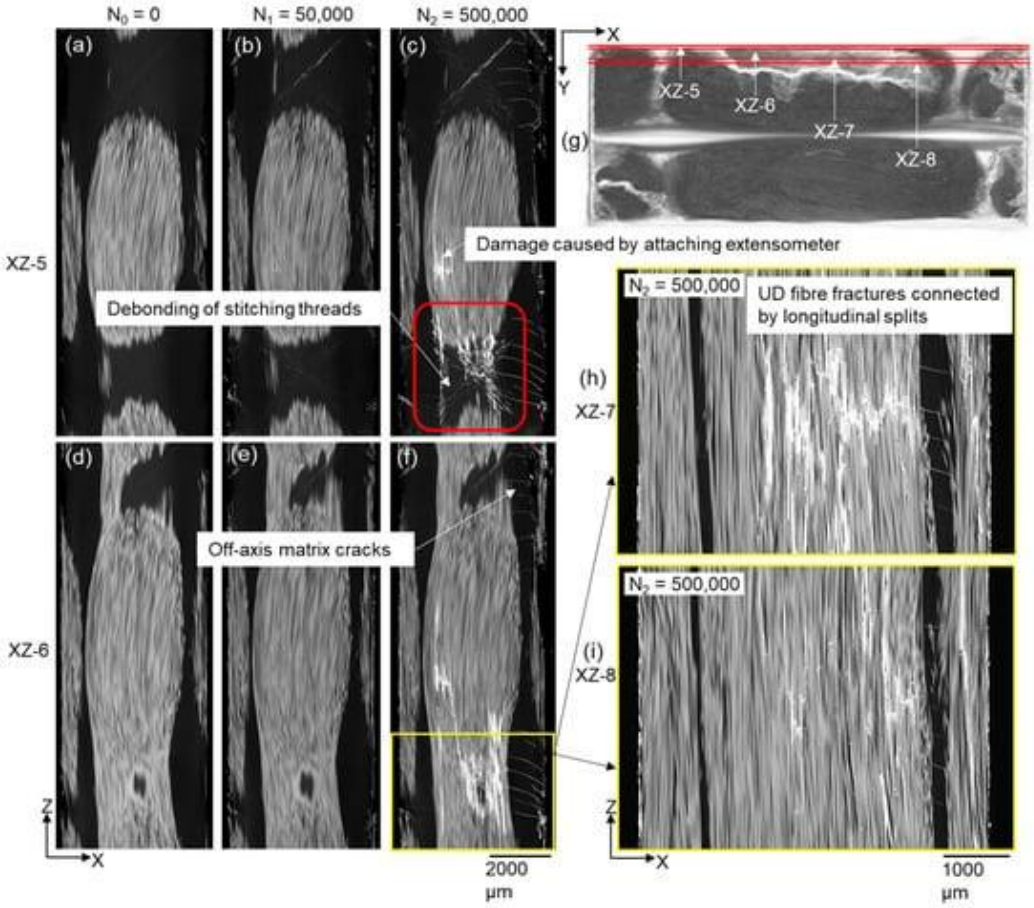

Figure 2.15 Time-lapse of UD fibre fractures present close to longitudinal splits and debonding of stitching threads [60].

2.4. Chapter Summary

In this subchapter, the wind blades, and their loading conditions, which dictate the material selection and design have been discussed. The manufacturing, characteristics, performance and applications of fibre-reinforced composites, especially unidirectional fibre composites have been reviewed. The advantages, disadvantages and trade-offs involved, have been discussed, regarding why these materials are ideal candidates and are commonly used for wind blade applications.

The mechanical behaviour in addition to the exceptional fatigue behaviour of FRPs has been discussed, with a focus on UD-NCF GFRPs. Typical damage

mechanisms/modes have been discussed, including fibre breaks, matrix cracks, debonding, and delamination. The complex interplay between different damage modes, from initiation and progression to the final failure has been discussed, and the lack of thorough knowledge leading to additional safety factors and imprecise lifetime prediction has been highlighted. This study aims to solve part of that problem by studying the fatigue and cumulative damage accumulation in these wind blade materials in a time-lapse fashion, using a correlative suite of imaging and characterisation techniques. This complementary, correlative approach will not only uncover different damage mechanisms and features but will also allow us to generate localised strain information to find strong and weak links in the microstructure. This will allow us to design stronger blades which can handle larger loads and last longer.

The next chapter introduces the common imaging and characterisation techniques used to observe the damage mechanisms and their evolution in FRPs and expands on the methods used in this PhD study. It also highlights the reasoning behind the selection of techniques based on the features of interest, and how effective they are.

3. Literature review on imaging and characterization of damage in fibre-reinforced composites

To improve the material's performance in service conditions, we continually exploit the structure-property relationship to study materials' microstructure and relate it to the macro- behaviour. Advancement of research in this field has led to a variety of imaging and characterization techniques being available to study different types of materials at varying scales, both at the surface and in bulk.

The techniques can be broadly divided into multiple levels of classification, namely destructive vs non-destructive, 2D vs 3D information and post-mortem vs ex-situ/in-situ, as illustrated in Table 3.1.

Type	2D	3D
Destructive Evaluation (DE)	Optical microscopy (OM), Scanning electron microscopy (SEM)	SEM tomography with surface milling
Non-destructive Evaluation (NDE)	X-ray radiography, Trans-illuminated white light imaging (TWLI), Digital image correlation (DIC), Infrared thermography, Acoustic emission, Raman spectroscopy, Eddy current testing, 2D ultrasound	X-ray computed tomography, neutron tomography, positron emission tomography digital volume correlation (DVC), 3D ultrasound

Table 3.1 Characterisation techniques are broadly divided into categories of destructive vs non-destructive evaluation, and information about 2D vs 3D morphology of microstructure.

Common 2D imaging techniques include optical microscopy and scanning electron microscopy, both of which offer a sufficient resolution to image individual fibres. For 3D imaging, x-ray computed tomography makes it possible to study the damage features in 3D [75].

It is worth noting that some of the 2D NDE techniques have the potential to capture subsurface or even bulk information. A common method to expand 2D techniques to capture 3D information is by milling away and imaging layers of materials simultaneously; with optical microscopes, cameras, SEM or Raman spectroscopy. Some of the common methods used to observe damage are introduced below.

3.1. Optical microscopy

Preliminary analysis involving simple sample preparation can start using an optical microscope to observe macro features on the surface including severed faces of specimens, fibre bundle placement, layups etc. With higher magnifications of 500x-100x available, individual fibres can be easily observed [76], [77]. While grinding and milling can give access to sub-surface or bulk information, polishing can clean up the surface to provide better detail. Evidently, this is destructive and prevents further time-dependent investigations. Advantages include basic sample preparation, which can include resin moulding followed by grinding and polishing for observation under the microscope [78]. It also doesn't use advanced use of computation and requires relatively unskilled analysis as opposed to SEM imaging.

Polishing can also lead to unintentional damage which can lead to false results, as shown in Figure 3.1 [73], [79]. For this reason, information from optical microscopy is often considered preliminary and qualitative.

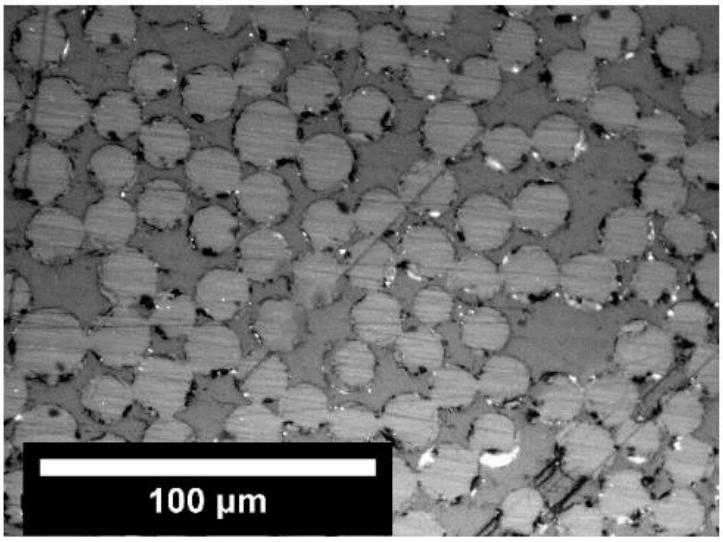

Figure 3.1 Optical microscopy image of glass-fibre reinforced epoxy [79]. The scratches are from the sample grinding and polishing.

3.2. Infrared thermography

Infrared (IR) thermography is a widely used technique for contactless surface temperature measurements. Changes in the surface temperature distribution, either by external stimulation such as a lamp, or heat generated from the damage itself, can be attributed to the presence of damage and can be located [80]. The damage and the resultant temperature distribution must be big enough to be sensed by the thermal camera, while the heat from damage can dissipate and worsen the location resolution. As this technique is limited to surface measurements only, it can take a while before the damage in the bulk propagates to the surface to be detected [81]. Figure 3.2 shows a setup involving mechanical testing and IR thermal imaging.

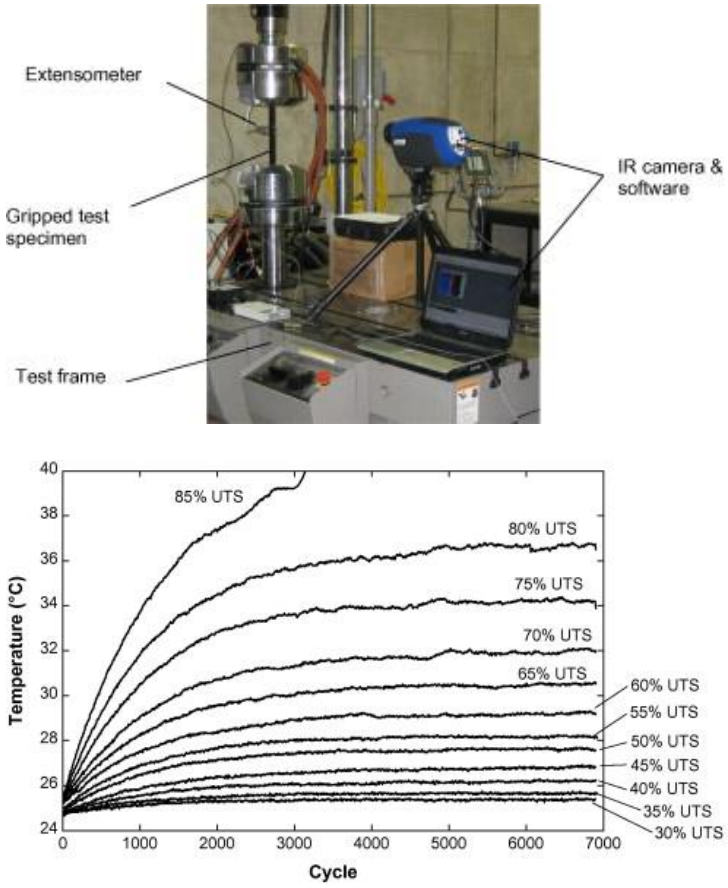

Figure 3.2 On the top is an infrared thermal imaging setup, observing temperature hotspots in a fatigue test of CFRP [82]. On the bottom are the results of temperature increase as the number of fatigue cycles increase, for different maximum stress levels (as a percentage of ultimate tensile strengths.

3.3. Acoustic emission

Acoustic emission (AE) is an NDT method which detects damage via soundwave signals that are generated as a sudden release of elastic energy when damage occurs. An array of piezoelectric sensors, which convert detected elastic waves into electrical signals, are placed on the component under testing, where the test stimuli can include mechanical loads, high temperatures, and pressure. Most piezoelectric sensors can detect elastic waves within a broad band of frequencies, but these can be very sensitive to external vibrations and noise [83]. There are two common types of AE tests, transient and continuous; the transient type records elastic wave events which exceed a certain loudness threshold, while the continuous type captures information for a

specified time and is used for poor-quality, low-intensity signals. The transient method can be used to extract features such as peak amplitude, signal energy and duration, the continuous type can provide the average signal level and root-mean-squared values for weak signals, which can be amplified [84]. Originally used to investigate damage in metals, AE was expanded to FRPs' analysis later [85].

Continuous improvement in AE has made it possible to differentiate between damage mechanisms of matrix cracking, fibre breaks, and fibre-matrix debonding, based on the variant features of the detected elastic waveforms, which can include peak amplitude, counts above threshold etc. [86]–[90], as shown in Figure 3.3. These waveforms are statistically identified by classification algorithms as belonging to a particular damage mechanism, based on empirical data [91]. It has even been expanded to study fibre breaks from dynamic fatigue damage in FRPs with success [92]. As the acquisition from AE can be quite noisy, later success has been attributed to improved post-acquisition signals processing [85], a move from older methods including k-means clustering [93] to machine learning-based methods [91] as the noise captured can interfere with the damage detection.

While this method has the advantages of being non-invasive, allowing for in-situ structural health monitoring, and being able to differentiate between damage mechanisms; it is limited to detecting larger damage features, is slower, and usually requires further inspection with a different technique for a complete diagnosis [84].

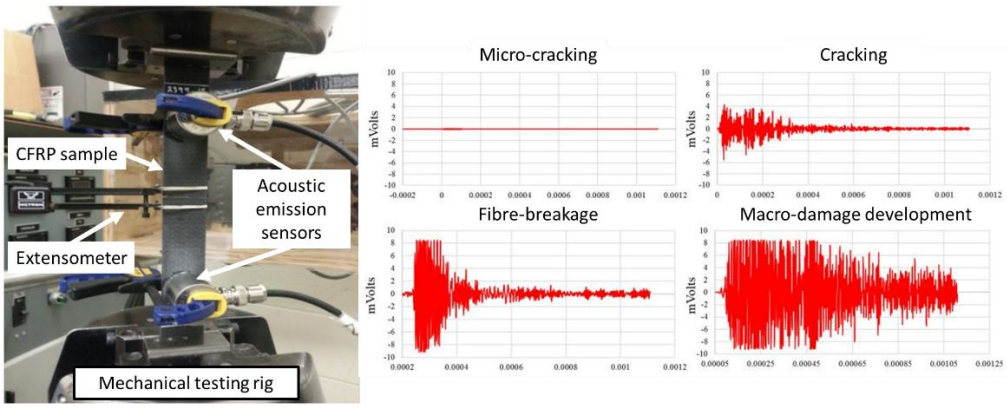

Figure 3.3 On the left is an acoustic emission setup in a mechanical testing rig to detect damage in a wind blade CFRP [94]. On the right are the resulting signals from a different test, showing four different damage modes of micro-cracking, cracking, fibre-breaks and macro-damage [87].

3.4. Ultrasonic testing

Ultrasonic testing refers to using pulses of high-frequency sound waves that are emitted using a transmitter throughout the sample, to detect defects and damage. Upon encountering damage, the waves can be reflected or deflected, which are then sensed by the receiver. To transmit the signals efficiently, water or gels are commonly used as coupling agents with the receivers as air attenuates most of the signals [95]. The time it takes to receive the signals can give information on the depth location of the damage. Handheld probes for off-site investigations usually have the transmitters and the receiver in the same unit, while more advanced on-site setups can have both at opposite phases. While time-resolved one-dimensional scans where information comes from a region directly under the probe are called A-scans, multiple A-scans can be reconstructed over two dimensions or even three dimensions and are referred to as B-scans and C-scan, as shown in Figure 3.4.

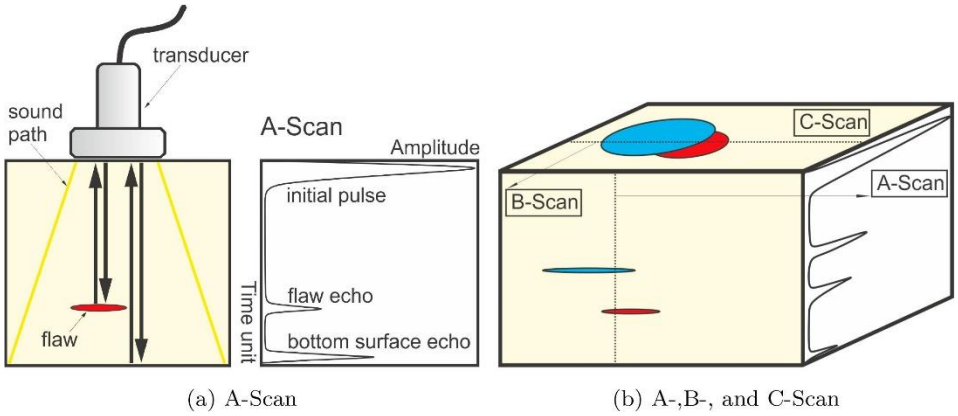

Figure 3.4 a) The schematic of acquiring an A-scan of a material flaw; there are three distinct signal peaks recorded – the initial pulse, flaw echo, and bottom surface echo. b) Extending the A-scan in two and three dimensions result in the B-scan and the C-scan respectively [95].

Although conventional ultrasonic scans for anisotropic composites have lower fidelity owing to random scattering and high attenuation, recent developments in Phased array ultrasonic testing (PAUT) have partly these limitations by providing the capability of focusing and steering signals at desired angles and locations [96]. These are customizable equipment where multiple transducer elements can be programmed to fire with set delays, essentially sending out a guided wave appropriate for the test components [96]. While the technique allows for non-destructive detection of damage locations and their size, it is limited by its requirement of highly skilled operators and susceptibility to false detections, which require other techniques for validation [97].

3.5. Camera-based imaging

Cameras have been used to capture images for centuries and their uses have been expanded to materials science for decades. A camera can non-destructively observe surface damage in the test component and its progression. Macrostructural damage features can be resolved, such as delamination and interlaminar splitting. High-resolution cameras with magnified lens setups can be used to investigate close-to micro-scale regimes and record movies to capture the whole damage sequence.

Additionally, if the sample is thinner and translucent, damage from the bulk can also be resolved if the light source and camera are on opposite sides of the sample. This is referred to as transilluminated white light imaging (TWLI) as shown in Figure 3.5 and has been used successfully to locate and monitor damage [9]. The technique consequently fails for thick and/or opaque samples.

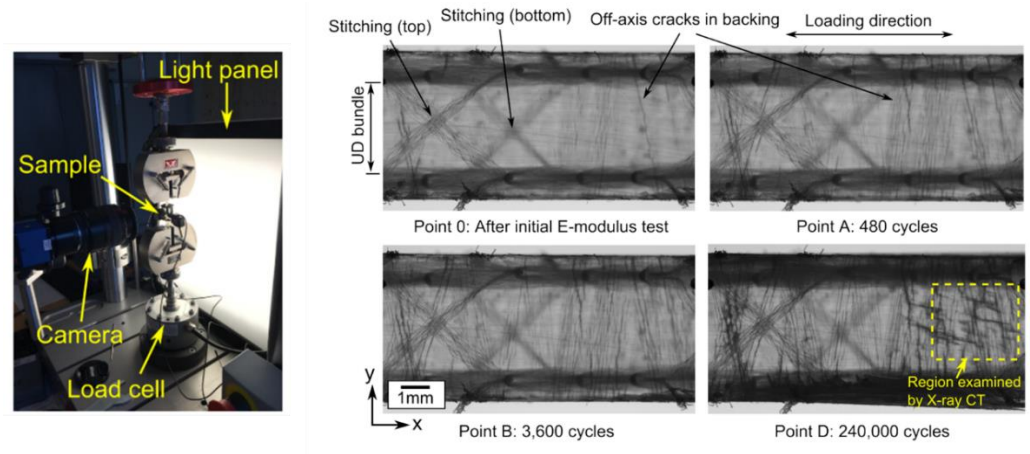

Figure 3.5 On the left is a TWLI setup on a fatigue test, monitoring damage intermittently. On the right is the damage progression observed by TWLI, where the off-axis cracks can be seen progressing into a severely damaged region [9]. This method is limited to translucent/transparent samples for light to be transmitted through, and 2D images, which have been augmented by using 3D x-ray computed tomography in the cited research.

An advanced quantitative case of a cameras-based imaging method is digital image correlation (see section 3.7), which uses a sequence of images to track movement and compute displacement. The method can be a cheaper alternative to more expensive imaging methods including acoustic emission, ultrasonic testing and x-ray tomography but is limited to 2D translucent/transparent sample observations. However, this method has great potential to be exploited as part of this recently developed tomography workflow [98], which uses visible light image projections to generate 3D images, similar to x-ray computed tomography.

3.6. Digital image correlation

Digital image correlation (DIC) is a technique used to infer displacements and strain maps over a surface via tracking the movement of individually correlated regions [99], [100]. It's a non-contact, full-field technique which uses surface patterns to correlate individual regions and track and generate their deformation maps. It takes inspiration from particle image velocimetric methods, which use markers to track the movements of individual regions to track the flow of fluids.

The method is based on acquiring a series of images of samples undergoing deformation from external stimuli. These regions through their patterns are correlated, and these regions are located in successive images. A displacement vector can be computed from the original location of these regions to the final location, and this vector field can be differentiated to generate strain maps [101].

Sometimes the natural texture of these sample surfaces might be enough as a contrast pattern, but if not, they can be made artificially by 'speckling' using spray paints. The speckle size has been reported to be ideally th\e size of 3-5 pixels [102]. The sequential images during the loading are compared together and correlated using appropriate algorithms. As shown in Figure 3.8, images are divided into smaller subregions containing markers, and the movement of the markers is used to compute displacement maps and strain maps. Each subregion moves after deformation, the algorithm searches both images for matching subregions and features and gives the region with the highest probability of matching i.e. correlation index. This is used to calculate the displacement of the local regions. Commonly used algorithms used are subset-based cross-correlation/sum-squared difference, normalized cross-correlation etc. the latter of which works better at compensating for irregular speckle marker patterns [103]. This results in the generation of a surface vector in locally correlated regions, which results in a full-field strain map [104].

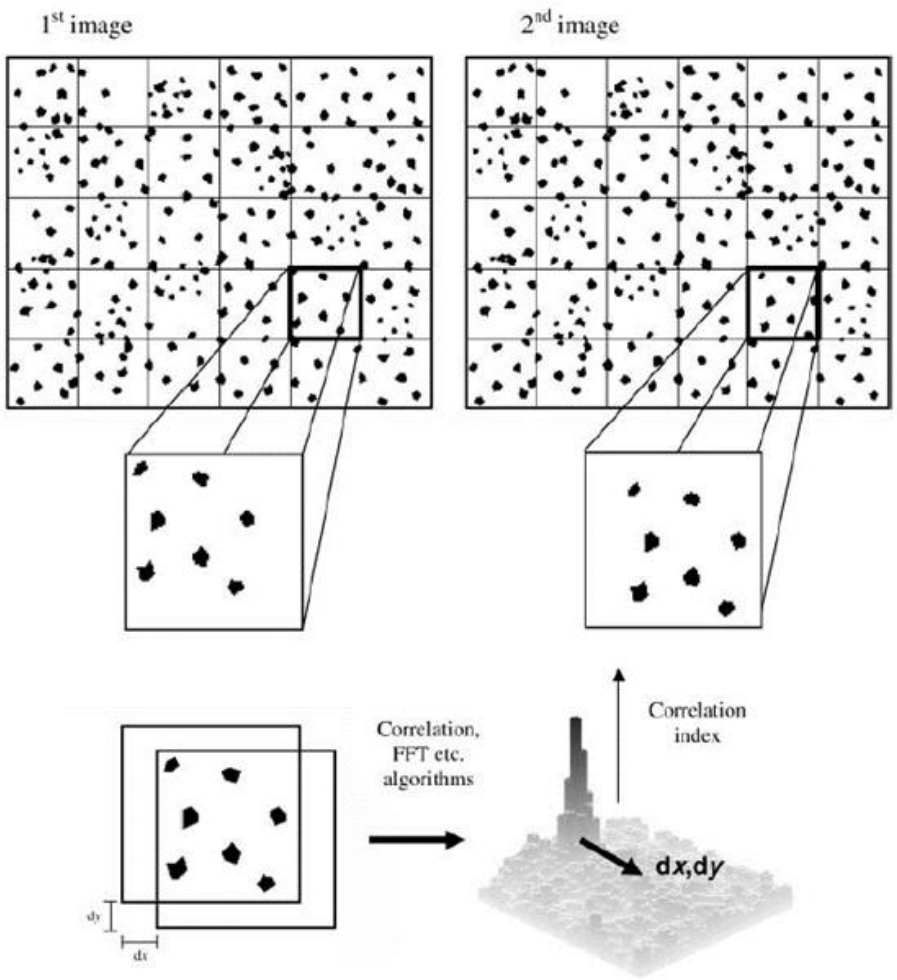

Figure 3.6 DIC schematic for computation of local maps, where the individual speckles used as markers are tracked during displacements so that local displacement maps and hence strain maps can be eventually computed [101].

This method does not require complex sample preparation techniques as other surface study techniques and can be employed using cheaper equipment than SEMs and x-ray microscopes. Another requirement is that the movements needed parallel to the plane of camera observation can be recorded accurately, however using a stereoscopic set of cameras can reveal deformations in three directions, often being called ‘3D DIC’, as shown in Figure 3.9.

For anisotropic materials like fibre composites, this technique is especially important as the resulting strain distribution is to be also heterogeneous, much pronounced at discontinuities or interfaces.

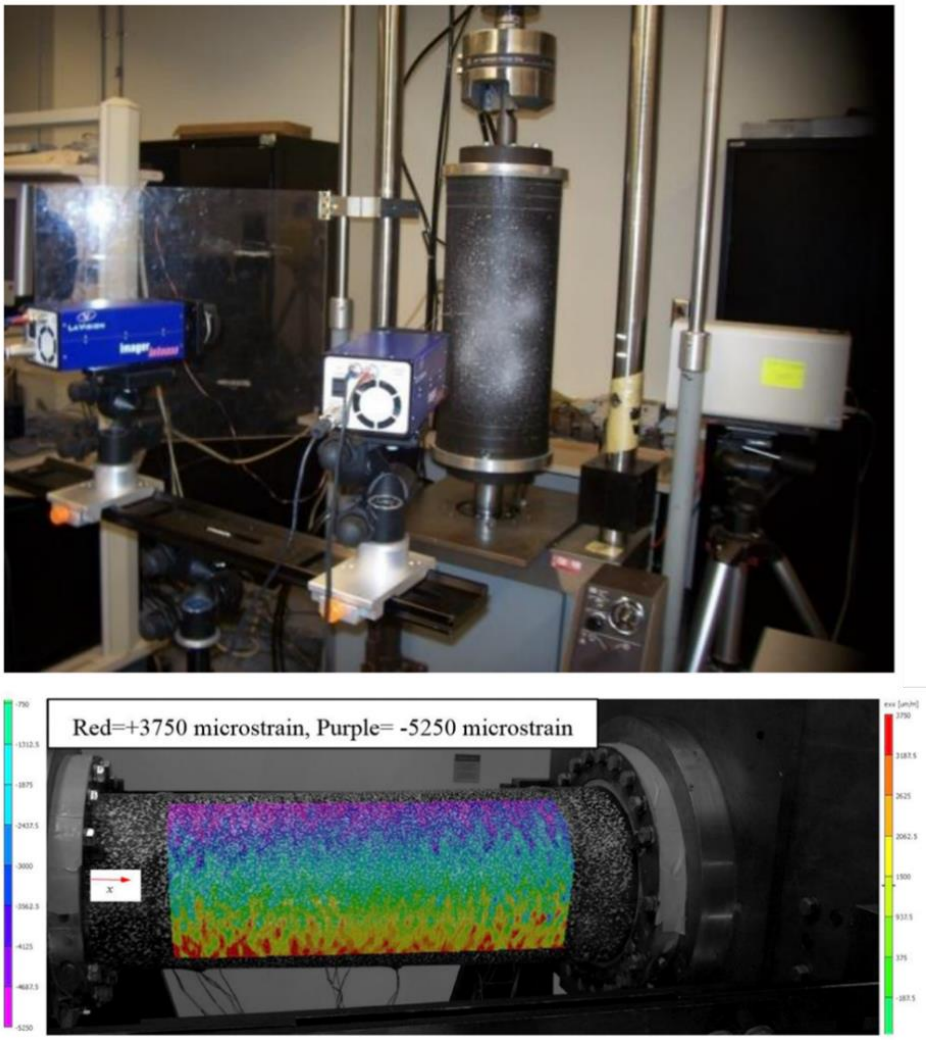

Figure 3.7 On the top is a DIC setup for an axial buckling test on a tubular CFRP with speckled paint, using two cameras placed in a stereoscopic manner to interpret out-of-plane deformation. On the bottom is the result showing ε_{xx} strain with the colourmap [105].

Strain measurement using extensometers or bonded strain gauges will only provide gross average strain over the sample gauge, which is not useful in studying local events which lead to the onset of degradation and failure.

Strain mapping by DIC can be overlayed on the microstructural images to pinpoint the region of interest which have high local strains and might be the regions where the damage starts. This is of particular interest to us as this project focused on studying

the damage initiation, DIC techniques will be one of the central themes of this project. DIC results can serve as a validation tool when compared its results with FEM models.

While the DIC technique has the advantages of being cheaper (in principle the only hardware requirement is a stable camera), generating full-field deformation maps instead of gross deformation, allowing for a wide range of sample sizes, and its use as validation for FEM models; it is limited to use only in good lighting conditions with a camera that can record at higher frame rates for fast evolving samples, and the setup needs to be very stable to avoid introducing false movements and erroneous results [106].

3.7. X-ray computed tomography

X-ray computed tomography (XCT) has emerged as a promising technique to study and investigate composite materials, due to its capability of non-destructive analysis in 3D giving information about the bulk material, in contrast to the destructive approach and 2D information available in other imaging high-resolution imaging methods including optical and electron microscopy. This reveals a great deal of information on its microstructure, microstructural features often have a 3D morphology, and 2D imaging just captures a part of that morphology. In principle, x-ray tomography reconstructs a 3D image stack of a sample from a set of 2D projections acquired rotationally over a range of angles, as shown in Figure 3.10.

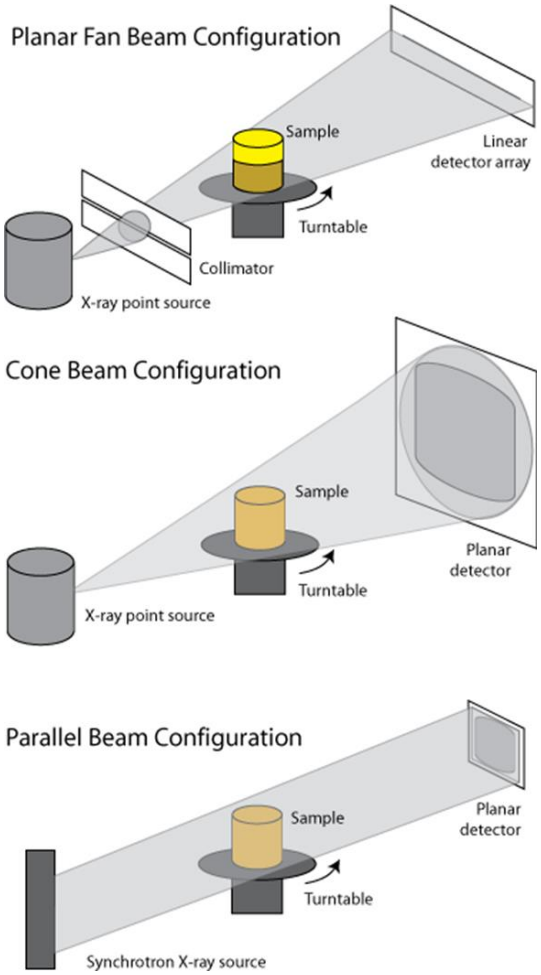

Figure 3.8 Schematic showing three types of XCT acquisition setups based on the x-ray beam: planar fan, cone beam, and parallel beam. While fan beams are popular in medical XCT, cone beams are common in lab-based XCT, and parallel beams are available at synchrotrons [107]. The sample is rotated on a calibrated turntable, while the detector records images at multiple angular positions. The x-ray beam is projected onto a sample, where the detector pixels record the attenuation of the x-rays passing through the sample and converts this information into visible light.

XCT is adept at imaging composites and their complex microstructural features including damage, for which 3D imaging is beneficial. It has been successfully used to study composites and damage features including matrix cracking, fibre breaks, and delamination [59], [75], [108]–[112], as shown in Figure 3.11.

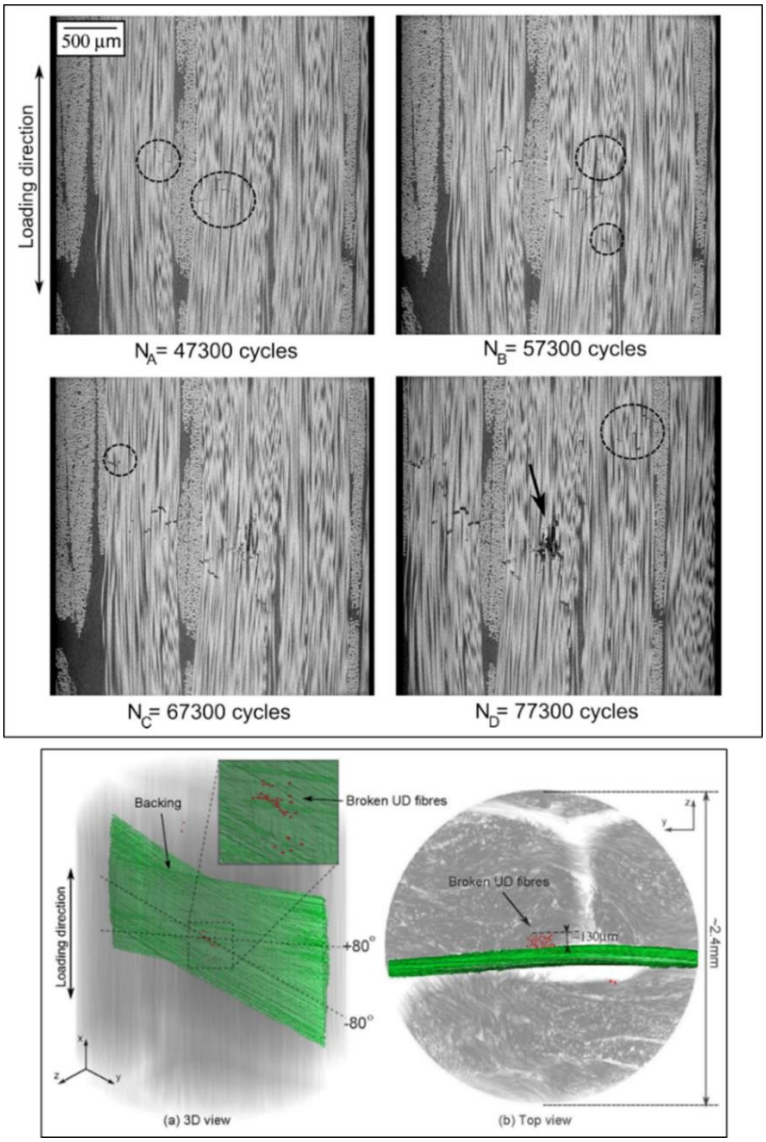

Figure 3.9 On the top is the damage progression of fatigue in GFRP observed via XCT, highlighting fibre breaks in unidirectional bundles. The bottom image shows the 3D distribution of UD fibre breaks in proximity to the backing bundle highlighted in green [9].

3.7.1. XCT Data Acquisition

As shown in Figure 3.12, the sample specimen to be analysed is placed on a sample holder, which is located between an x-ray source and a detector. X-rays are irradiated upon the sample towards the detector. The penetrating property of x-rays allows them to traverse through the whole sample. The physics of x-rays interaction with the material phases is governed by Beer-Lambert's law[113], manifested in Equation 3.1.

$$\mathbf{I = I_0.e^{-\mu x}} \qquad \text{....3.1}$$

where ‘I_0’ represents the incident x-ray intensity, ‘I’ represents the recorded x-ray intensity, ‘x’ represents the path of x-rays traversed inside the sample and ‘μ’ represents the linear x-ray attenuation of the material phase, both x and μ provide information about the phase and its morphology. X-ray interaction with materials leads to attenuation, the extent of which depends on the material phase it’s interacting with and is a function of the density of the material, the atomic number and the energy of the X-rays as proven in Equation 3.2 by Attix et. al [114]. μ is the linear attenuation coefficient, ρ is the density of the material phase, Z is the atomic number, E is the energy of the incident x-ray photon and K is a constant.

$$\mu/\rho = K.\ (Z^4/E^3) \qquad \text{....3.2}$$

This difference gives contrast to each phase which can be recorded as a signal on a detector to generate information. The sample is placed on a turntable sample holder which rotates as the samples are irradiated with x-rays. Projections are acquired over a range of angles usually for 180°/360°, which are then fed into a reconstruction algorithm for the generation of the 3D image volume. The incoming radiation is firstly converted to visible light using a scintillator, and this visible light is read typically on a charged coupled device (CCD), which is divided into a discrete number of pixels. These pixels record the transmitted signal and form the final 2D projection.

Two broad cases of x-ray analysis stem from the sources used for x-ray generation: lab-based sources or synchrotron sources. They have differences in terms of x-ray energies, brightness (photon flux), and magnification (therefore resolution), among others.

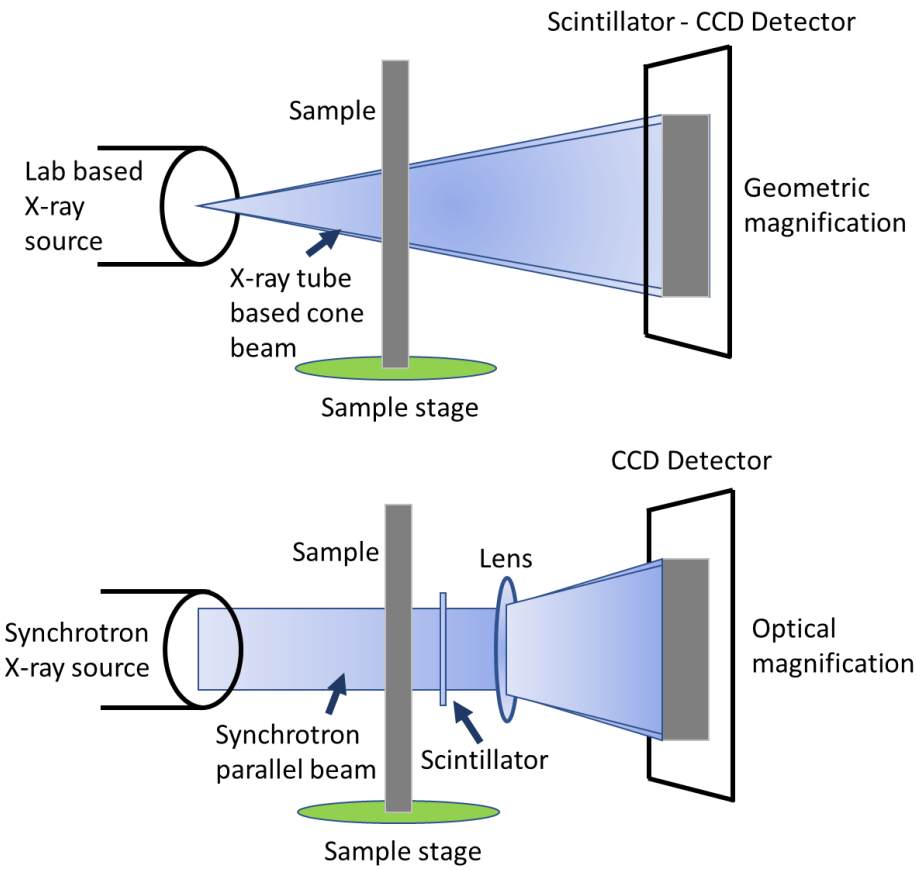

Figure 3.10 Differences between a lab x-ray tube-based XCT setup v/s a synchrotron-based x-ray source. Geometric magnification is inherently produced due to the conical beam, but synchrotron parallel beams need optical magnification systems to enlarge the image.

- <u>Synchrotron vs Lab CT source</u>

As shown in Figure 3.12, synchrotron radiation can provide parallel, higher flux, and monochromatic x-rays, as opposed to laboratory x-ray sources which provide point-sourced, polychromatic divergent x-rays, either a fan beam or a cone beam setup. Fan beam refers to planar irradiation commonly available in medical CT as opposed to a 3D cone beam. Point sources are an assumption, in practice, the source has a definite size which can lead to blurring in projections [115]. Synchrotron uses electrons which are accelerated and bent using powerful magnets, leading to a change in momentum, which gives off x-ray photons. For a relatively monochromatic beam, additional crystals can be used to select a particular range of energies. For lab sources, filters can

be used to ‘harden’ x-rays, to reduce the spread but this comes at the cost of further reducing the flux of the lab source. As per Beer Lamberts’ Law [113], the x-ray beam is assumed monochromatic for reconstruction, if not the polychromatic beam will lead to non-true attenuation leading to beam hardening artefacts and other issues. Also, as the flux is higher for synchrotron sources, these are more suited for in-situ studies compared to the lab sources, because they can generate the same signal intensity for less exposure time, this results in lower acquisition time which can capture events at higher frame rate, suited well for temporal capture of data.

Another advantage of using a synchrotron is phase contrast imaging. This imaging technique uses the change in wave nature of x-rays to generate contrast, for which the beam needs to be phase-coherent. As the beam is coherently generated from large source to sample distances, this can be beneficial for studying materials which have phases with low contrast, which appear similar in absorption contrast. Techniques like phase contrast, which rely on the phase changes of x-rays rather than attenuation in energy, are much better at generating contrast for weakly attenuating or similar materials, especially enhancing contrast at the phase edges, rather than bulk [116].

A major downside of using synchrotron sources is the limited access to beamtimes in the synchrotrons the world over. Most of them are not charged to the user for academic access, but every proposal is subjected to a thorough review to be deemed worthy of beamtime, which is expensive. As opposed to this lab CT systems have more availability, usually housed at a research lab dedicated to a single facility. Another demerit is the limitation to only smaller samples, as the synchrotron source delivers a parallel beam and not a cone beam as in lab-based sources and therefore cannot cover a bigger field of view or provide magnification, latter of which is mitigated by using lenses[113].

The magnification can be achieved using geometric or optical modifications [113]. Geometric magnification can be modified by changing source-to-object and detector-to-object distance. It can be maximised by decreasing source-to-sample distance and increasing sample-to-detector distance. The former also maximises the flux passing through the sample, yielding a better signal-to-noise ratio. Conversely, higher magnification means a lower field of view and vice versa.

Once the XCT data has been acquired, it goes through a pipeline of processing, the steps of which have been explained below.

3.7.2. XCT Image Reconstruction

Data acquisition of radiographs is usually followed by data reconstruction, which means converting the 2D radiographic projections taken at multiple angles to generate a 3D image volume which can be viewed using appropriate visualization software.

Various reconstruction algorithms are available. The most common analytical method is the “filtered back projection” algorithm, which essentially smears the pixel value across the whole ray path and the solution gets closer as a higher number of projections are used for the computation of the result, as shown in Figure 3.13. The signal is filtered before it’s back-projected to remove blurs, due to non-uniform sampling along the ray paths. The reconstruction will be near-perfect if the input approaches an infinite number of projections [113].

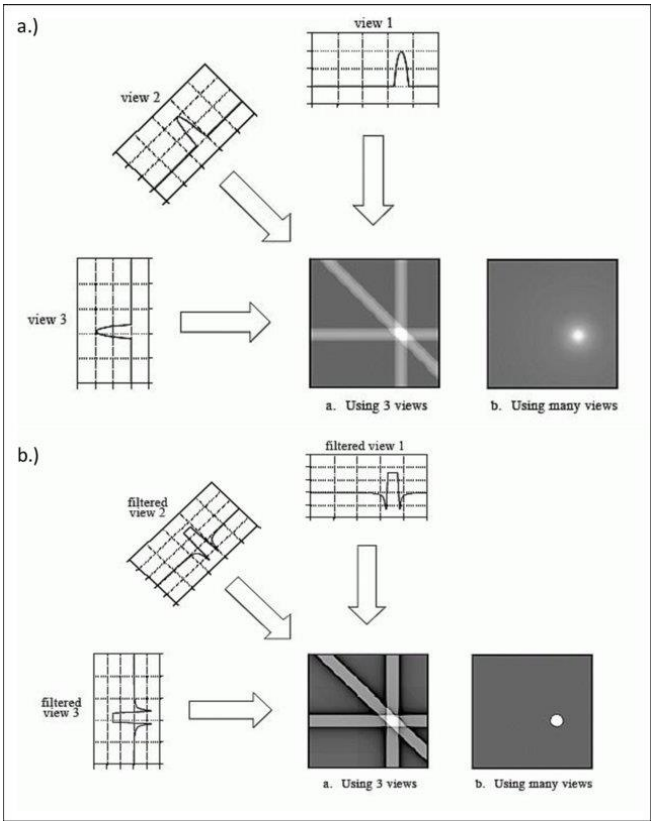

Figure 3.11 Reconstruction from a filtered back projection algorithm a) shows simple back projection which leads to blurry edges while b) shows filtered back projection showing clear edges. Pixels registered on the detector are smeared back in virtual 2D space, for all angles till the position of the pixel is found in the x-y plane, this is done for all the slices so the location of that pixel is identified in all x, y and z coordinates [117].

As acquiring each projection takes a finite amount of time, a lot of current research in this area focuses on reconstructing image volumes with a minimum number of projections available, so faster evolving events can be imaged with good temporal resolution [118].

As the conditions during long scanning times tend to change within the duration of the scan e.g., dead pixels, wobbling of the sample, destabilizing of the source etc., additional correction projections are used to improve the quality of reconstruction achieved. Some of them are dark fields, bright fields and keyframes, where a dark-field means acquisition with the x-ray source switched off, a bright-field with x-rays switched on and the sample out of the field of view [119].

3.7.3. XCT Image Segmentation

The reconstruction step outputs a digital 3D volume of the sample which is stored as a stack of image slices. Although certain measurements can be taken on the reconstructed grayscale 3D data, it's usually preferable to segment the data for quantification. Segmenting the data means assigning a particular label to each voxel belonging to a particular phase and using it to perform measurements and extraction of meaningful quantitative insights.

Various algorithms are available to segment data, starting from the basic ones being just segmenting by using a threshold to separate grayscale value. A phase with its pixels having a certain grayscale value below/above/equal can be labelled uniquely. For datasets with poor contrast, high noise, or pixels with a wide distribution of grayscale values, such simple segmentation methods yield poor results.

This method leads to errors in segmenting the boundary regions and interfaces where the distribution of grayscale is large and gradual and/or not clearly defined. Images can be pre-processed to reduce noise and enhance contrast to facilitate the segmentation process. Most of these pre-processing techniques eliminate or suppress unwanted features including artefacts, and noise, while some enhance features of interest such as boundaries and interfaces, features like cracks and similar regions of interest.

For very complicated datasets with poor contrast, high noise, and multiple phases such as in biological samples, some level of human input like manually annotating pixels is required and is therefore subjective to each user. This leads to irregularity in output results for the same datasets and introduces errors in analysis. The presence of artefacts

in images during data acquisition also leads to the process of segmentation becoming more cumbersome [119].

To solve problems, the advanced segmentation algorithms used today are heavily derived from computer and machine vision techniques and involve concepts like deep learning and neural networks. They are more aptly called probabilistic image segmentation as they do not label the image into binary classes explicitly, rather they generate a probability map for each class instead [120], [121]. The effectiveness of such methods can be illustrated in Figure 3.14 below, which clearly validates the superiority of advanced segmentation algorithms compared to regular thresholding methods.

These computer vision-based techniques require less human intervention, using feedback from continual training and iteration of the models, so the models get better as they are exposed to more input data. As imaging data of FRPs can be noisy, these techniques will become a major part of this study. Nevertheless, the most widely used techniques, both simple and advanced will be compared below in an introductory manner without going into detail.

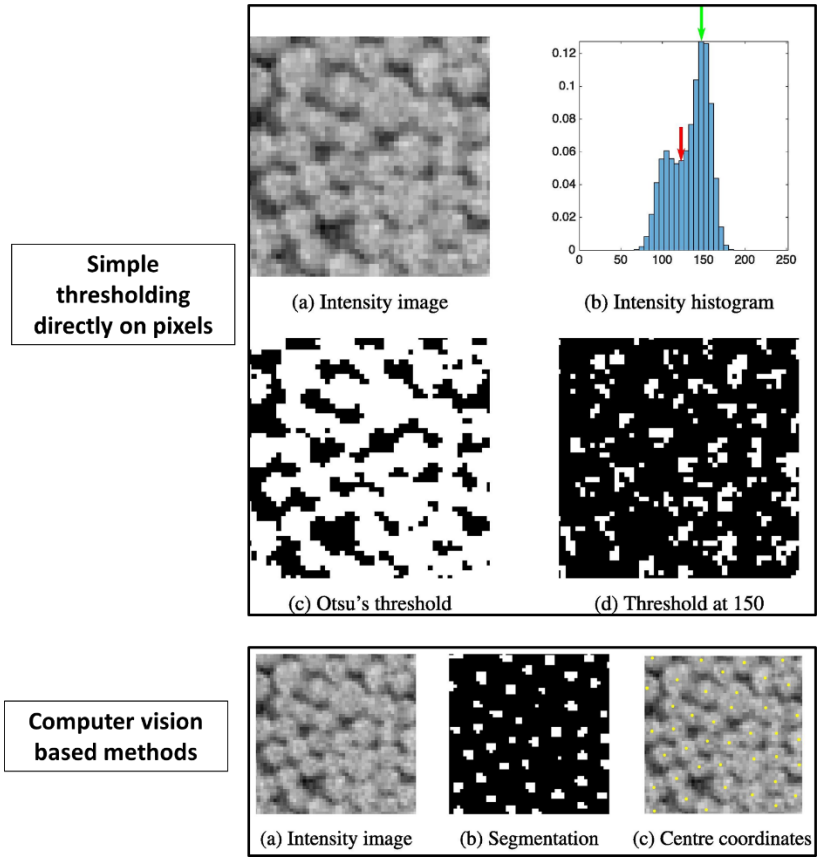

Figure 3.12 The efficiency of computer vision-based methods compared to the simpler thresholding methods. With the grayscale input to the algorithms, the top figure is the result of Otsu's method [122] and simple thresholding, while the bottom result is fibre centre detection by dictionary-based image segmentation, a type of computer-vision-based method [123].

- <u>Threshold-based segmentation</u>

This basic class of segmentation uses the intensity level distribution of the image to decide which part of the image belongs to which class. This is commonly used to determine background and foreground classes in images, using the intensity distribution of the image to decide a threshold value 'T', where all the pixels with intensity values above 'T' will be marked as one class and below this will be labelled as the other.

Similar algorithms like Otsu's thresholding[122] are an extension of the same principle. Otsu's method essentially iterates through all threshold values T and calculates a measure of spread for the pixel levels on either side of the threshold, i.e.

the pixels that either belong to foreground or background. The target is to find the threshold value where the sum of foreground and background spreads is at its minimum, essentially minimizing the sum of intra-class variances.

- Watershed Segmentation

This process uses a pre-processing transformation on the image before it can be segmented. The image to be segmented is changed into a topographical entity where high-intensity pixels are towards the peaks while the low-intensity pixels are towards the basins, these are called catchment basins. The next step is to start flooding these basins with the label pixels until the label pixels from different basins meet, these meeting points are then defined as boundaries, which results in a boundary-separated labelled image, as shown in Figure 3.15. For noisy images, this can result in an error in detecting false basins, leading to over-segmented results. For such cases, an advanced method based on the same principle called marker-based watershed can be used. The user manually annotates the area which is foreground and background, leading to a reduction in false basins and therefore yielding a much better result [124].

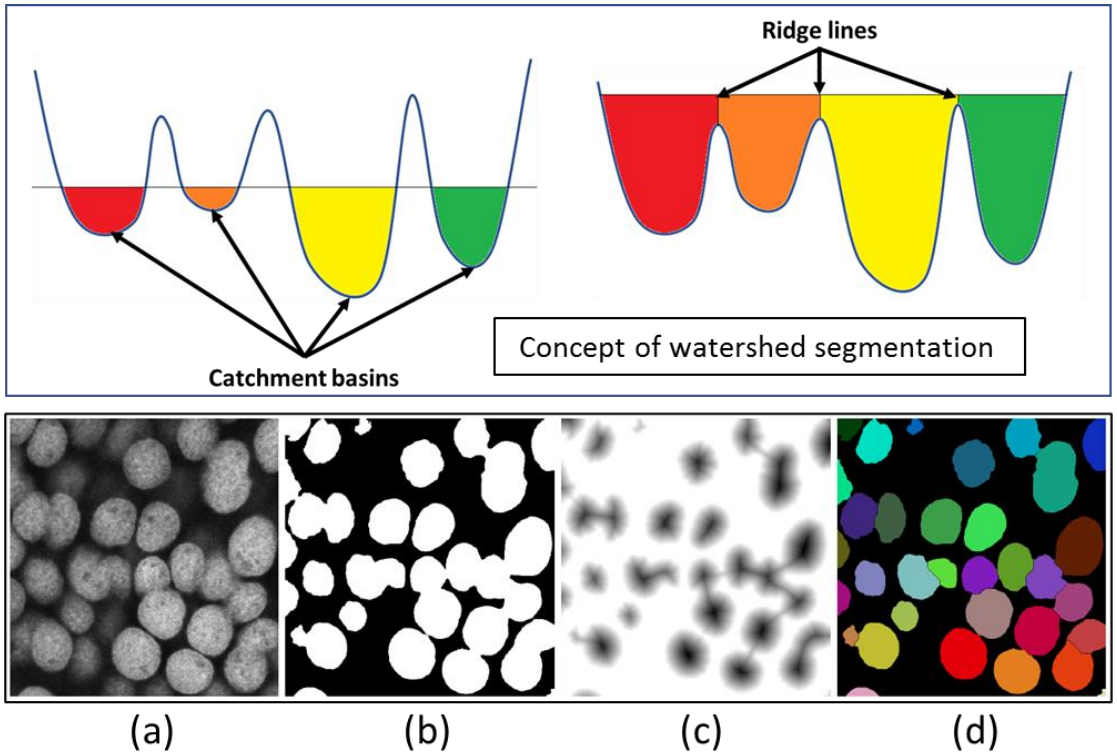

Figure 3.13 Schematic explaining the watershed approach. a) Grayscale image of grains (applicable to fibres as well) is to be segmented into individual grains but b) thresholding leads to poor results. c) Image is converted into a topological entity using distance transform [125], [126], and then each of the basins is flooded with individual label pixels bottom up until the label pixels meet the ridgeline, which is defined as the boundary, thereby rendering d) the image segmented after applying watershed to the inverse distance [127].

- <u>Segmentation based on Hough Transforms</u>

Hough transforms are based on the principle of template matching, by which it tries to extract features that have a definite shape and morphology, including straight lines, curves, circles etc. by matching grayscale features to a predefined geometric template.

Essentially the algorithm goes through points on the image and checks which points have the most likeliness of lying on a specified feature template and then each of the possibilities is voted on the likeliness, as shown in Figure 3.16. The trajectory with the highest number of votes is defined as the feature, and therefore the edge, which leads to the images segmented along this feature border. Feature extraction generally takes

place in a parametric space where suspect features are represented in an (r, Θ) domain [128].

This works better than a regular edge detector algorithm as imperfections or missing points can still be accounted for. For FRPs, we want circular fibre-like blobs extracted out of our images, so this method can be applied, but it would need to be pre-processed to de-noise the images.

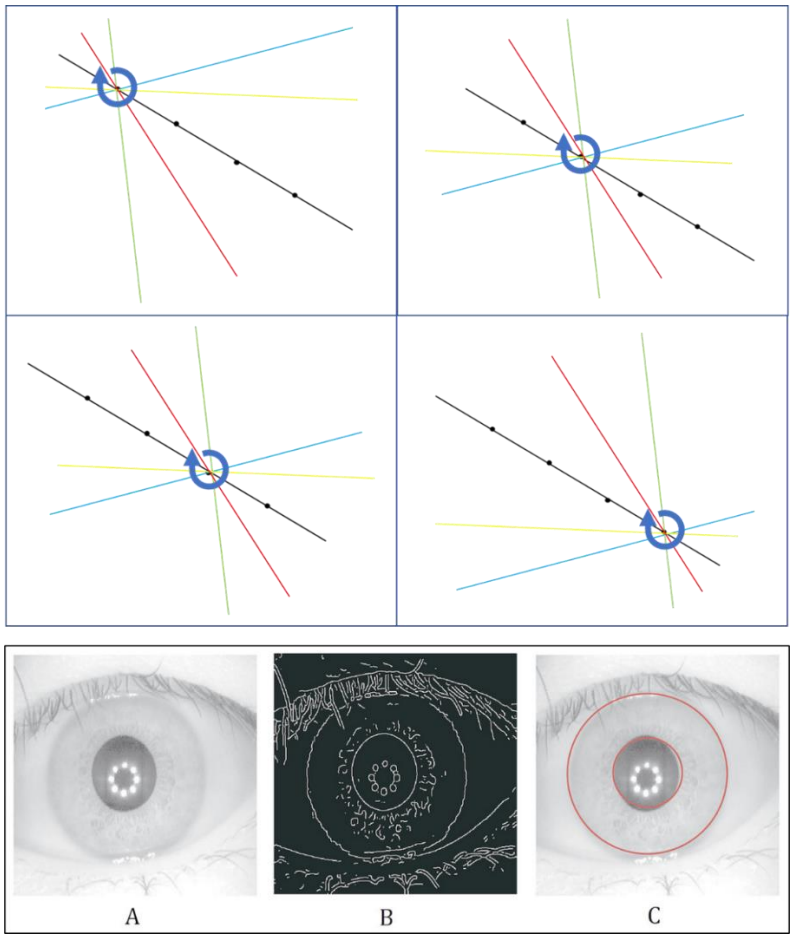

Figure 3.14 Hough transforms explained in a schematic, adapted from [129]. The four black are to be detected as being part of a linear feature in the image, each point is considered, and a line is rotated on its hinge to find if other points end upon it. This is iterated for all four points and the line with the maximum instances of points lying on it is detected as a linear feature. This is extended on a circular feature segmentation of a human eye iris where the A) grayscale image undergoes the b) Hough transform and leads to the c) segmented iris [130].

- <u>Dictionary-based image segmentation</u>

As mentioned in the text above, most advanced segmentation techniques are derived from computer vision, and this dictionary-based approach is one of them. The algorithm is written in MATLAB code and used via a graphical user interface called Insegt, both the algorithm and the code were developed by Emerson et al. [119] and Dahl et al. [131], [132]. The essence of this method is to teach the algorithm what a fibre centre looks like, using a training image. The information it learns is stored in a matrix referred to as a 'dictionary', once the dictionary is learnt, it can go on segmenting fibres and matrix through human annotation.

The algorithm is described in detail below.

The workflow starts with a training image that informs the algorithm via user annotations of what fibre centres and backgrounds look like. The training image is supposed to be very similar to the 3D imaging data that we want to segment, so it's sensible to start with a cross-sectional slice from the same data that needs to be segmented.

The process begins with extracting a lot of overlapping patches from the image. The patch size is supposed to be covering a complete fibre cross-section which can be easily determined. Starting from the top-left pixel we extract a patch with fixed pixel size, $\boldsymbol{M \times M}$ pixels, and move a pixel right and a pixel down, therefore ending up with almost as many patches as the number of pixels in the training image. As we end up with a lot of patches, these patches are clustered into $\boldsymbol{n}$ number of clusters using weighted k-means clustering, where the weight is assigned based on the similarity within the cluster. The mean of each cluster results in a patch, which goes on to form the atoms (rows) in the dictionary, where each cluster is represented by each atom.

For the dictionary the patch size is $\boldsymbol{M \times M}$, so the number of columns of the dictionary is $\boldsymbol{M^2}$. Also, an additional number of blank (initiated) dictionaries are created, the number of them equalling the number of label classes, these are called label dictionaries and have the same dimensions as the intensity dictionaries. In this case, we define two label dictionaries to classify the image into two label classes of fibre centres and background.

Once the dictionaries are randomly initiated, the next step becomes propagating information into those label dictionaries, which is done by digitally annotating the area of a fibre centre and supplying information to the algorithm. The cluster of patches the annotated area belongs to is identified in the intensity dictionary, and the corresponding atom in the label dictionaries is updated with a positive score of '1' or '0' depending on the fibre centre or background. Annotation is done multiple times, for both classes to refine the results until the segmentations deems satisfactory.

This results in an informed probability dictionary, which gives a probability of each pixel belonging to either of the labels. This image of this probability dictionary is then thresholded, often at values near 0.5. This resulting image is a collection of pixels which belong to a fibre centre, of which the centroid pixel is labelled as a fibre centre. This algorithm is run over all the slices and the fibre centres are computed on each of them.

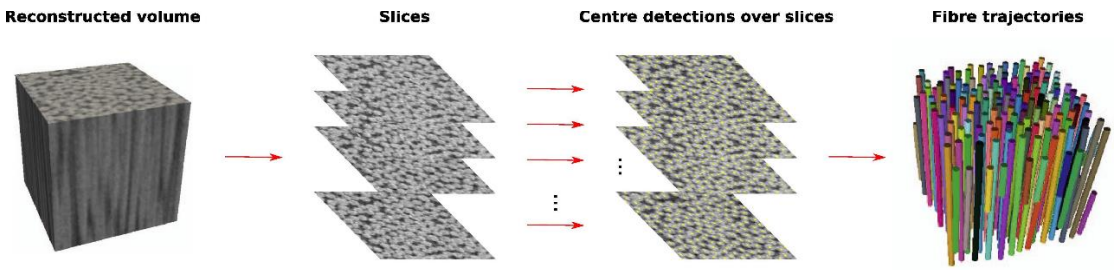

Figure 3.15 Dictionary-based image segmentation used to track individual fibres in a 3D profile. Fibre centres are identified in each cross-sectional slice and then joined across slices to form a 3D trajectory [123], [131].

Each fibre centre pixel is matched with a close corresponding fibre pixel in the previous and the next slice, with a search cone of fixed pixels, thus the 3D trajectory of each fibre is computed, as shown in Figure 3.17.

3.7.4. Errors and artefacts in CT

Throughout the x-ray tomography pipeline, errors can propagate from any of the steps. These errors can amplify as the data is propagated through the pipelines and can yield false results, which renders the results inaccurate. While some of the errors can be from segmentation, most errors can arise from data acquisition and reconstruction, these are called artefacts and can be observed in the reconstructed images. XCT imaging is inherently prone to artefacts as the 3D volume is estimated and computationally reconstructed indirectly from the sinograms of the projection data, unlike direct imaging methods like optical microscopy. Some of the common artefacts are explained below.

- <u>Beam Hardening</u>

This is a common artefact resulting from polychromatic beams from the x-ray sources, especially lab-based x-ray tubes. As explained with Beer Lamberts' Law earlier in the text, when polychromatic beams x-rays through a sample, lower energy x-rays get attenuated much more than the higher energy x-rays, which records a signal on the detector with higher mean energy, falsely implying that the material phase it passed through is weakly attenuating. This can lead to false visual features in the images as streaks and cupping artefacts.

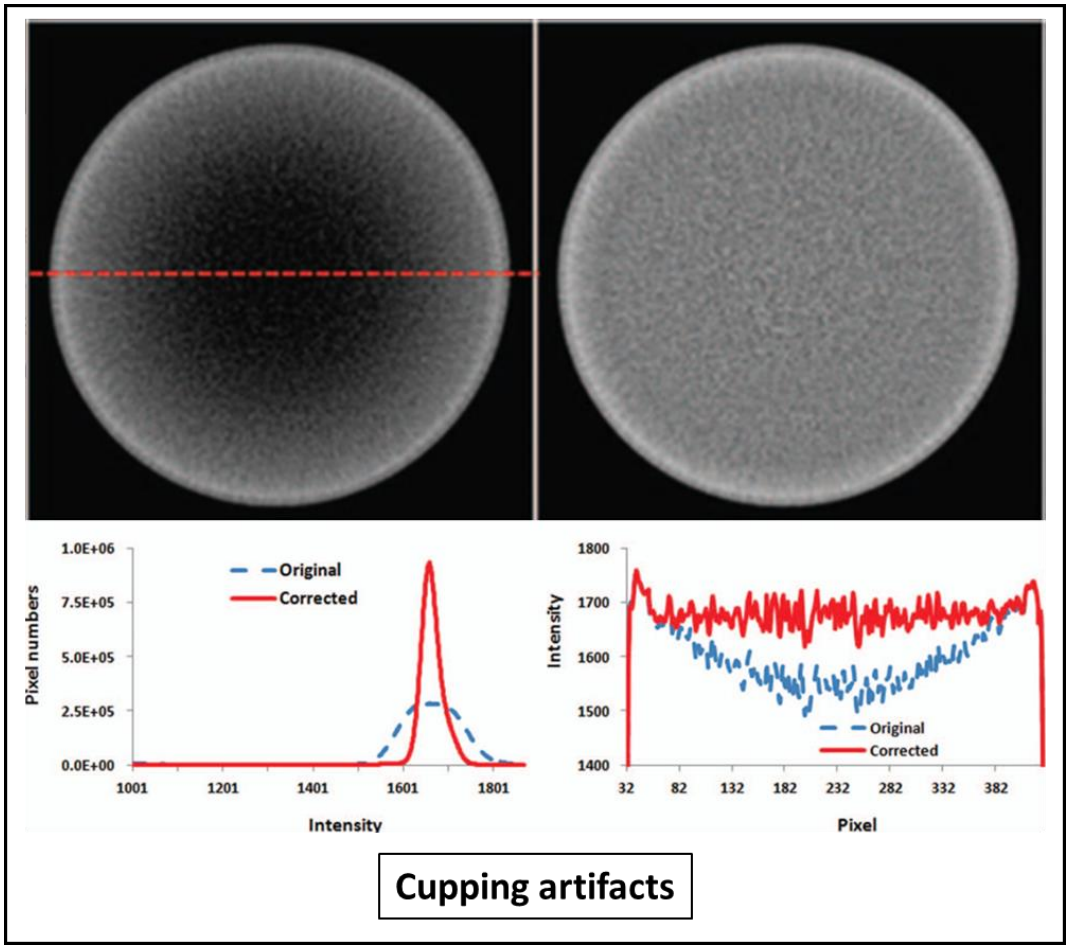

Figure 3.16 Cupping artefacts in a water phantom, with a false denser bulk in the uncorrected image on the left. On the right is the corrected image with a uniform grayscale, as can be seen in the line profiles. Adapted from [133].

Cupping artefacts generally arise from scanning sample geometries which are not uniform across the sampling plane. These could be circular geometries, for which the x-rays passing from the central region will be attenuated much more than the ones grazing the sample on the periphery. This leads to a false belief that the material phase in the centre was weakly attenuating, as seen in Figure 3.18.

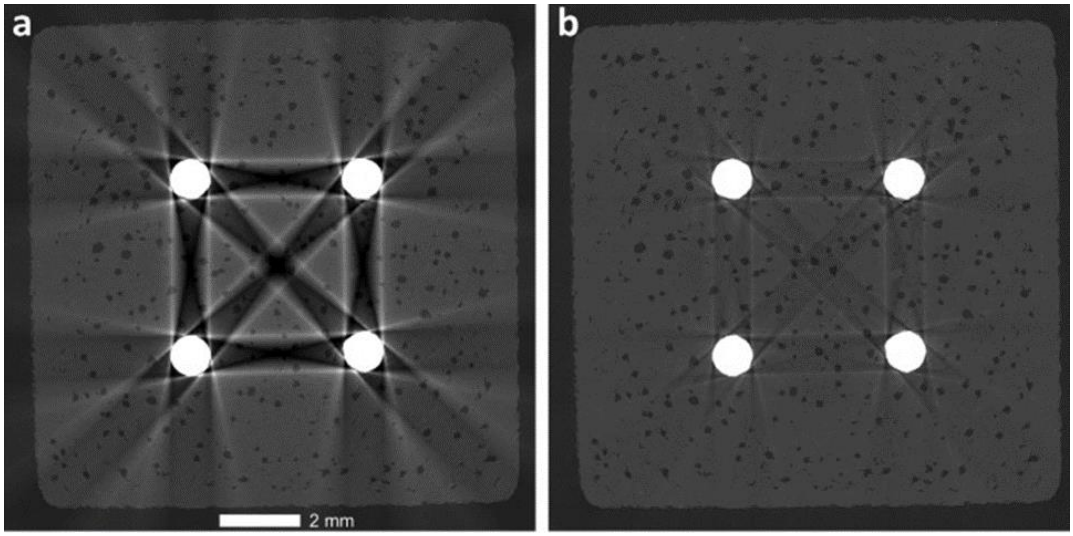

Figure 3.17 Streak artefacts in a nylon polymer (Polyamide 12) including four titanium alloy (Ti-6Al-4V) inserts. a) Streak artefacts that arise from a strongly attenuating metal alloy, b) the partially corrected image using filters [134].

Streak artefacts are more common in materials science where samples scanned are more heterogeneous and multiphase. These arise generally because of multi-angle data capture and highly attenuating phases which lead to high attenuation at certain angles more than others. This leads to non-uniform attenuation across the sample leading to false visual features, as shown in Figure 3.19 [135].

Beam hardening can be corrected through a combination of techniques such as using a filter to filter or 'pre-harden' weak x-rays, so the incident x-rays are relatively monochromatic. Calibration can also be done using an appropriate phantom to assess beforehand how the x-rays behave with multiphase samples, these observations can be used to correct the acquisitions. Correction can also be done using the software, which uses specialized algorithms which are based on modelling and simulating the interactions between the x-rays and the materials [136].

- Ring artefacts

These artefacts are a result of faulty detectors. If the detectors are not calibrated properly, these will result in false features in each angular position which will result in a ring-type of artefacts after the whole reconstruction, as shown in Figure 3.20. This can also arise out of dead pixels in the detector but is usually corrected by bright-field projections. If the disturbance occurs during the scan, this can be corrected using keyframes acquired during regular intervals to compensate [45].

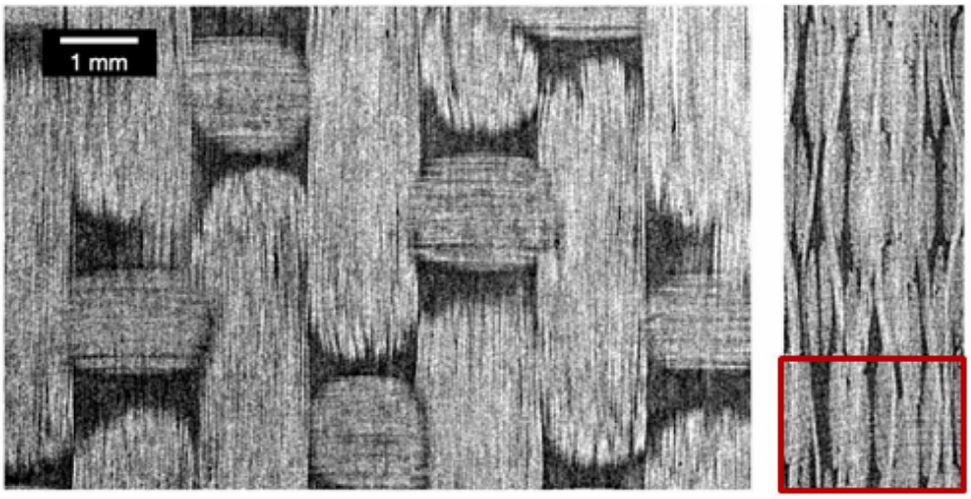

Figure 3.18 Ring artefacts in XCT cross-section of a woven composite of carbon fibres in thermoplastic PEEK. False grayscale values in the corner red box due to ring artefacts make it difficult to segment and quantify the data [137].

- Under-sampling and missing views

These kinds of artefacts usually arise when the angular sampling frequency during the acquisition is lower and there is missing information for reconstruction, as shown in Figure 3.21. These can be avoided by increasing the sampling frequency; however, this poses a problem for in-situ studies as its preferable to acquire the projections in minimum time, which often require taking fewer projections per rotation [138].

Consequently, we must decide a trade-off between the image quality and the duration of temporal events.

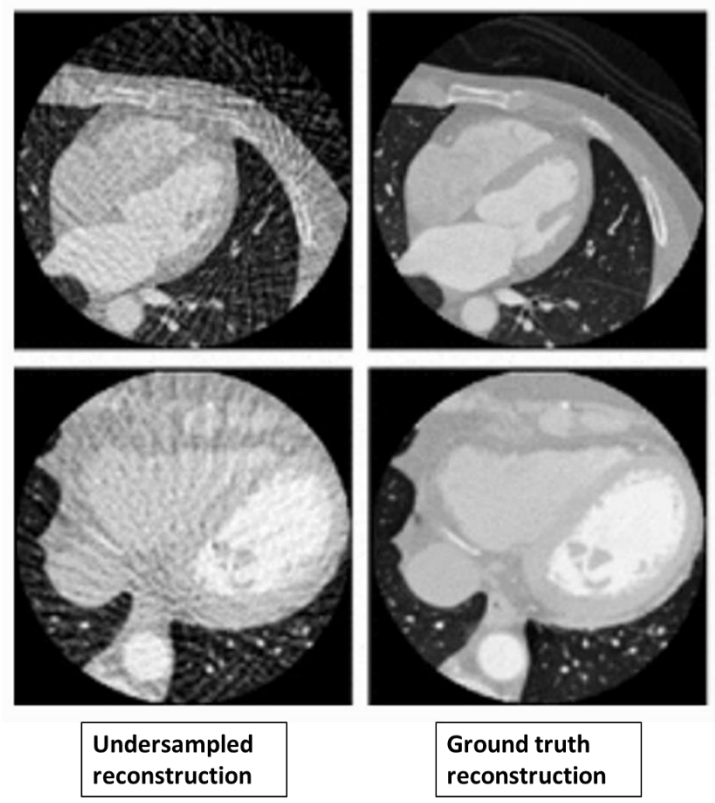

Figure 3.19 Undersampled reconstruction with only 32 angular projections compared to ground truth reconstruction with 512 projections in cardiac CT images [138].

- <u>Wobbling and motion artefacts</u>

Sample movement during scanning can result in blurry projections which can lead to shading and streaking artefacts upon reconstruction, as shown in Figure 3.22. This motion can be caused by incorrect sample placement on the sample holder, lousy mounting or being mounted on flimsy sample stubs like polymer rods. These can also arise by heating vibrations as the target is heated for long scan times which results in instability of the spot size.

These can be mitigated by properly mounting the samples on rigid stubs and holders and cooling the system properly. These can be also corrected during reconstruction by selecting the sharpest image from multiple test reconstructions [136][139].

Figure 3.20 CT motion artefacts in the upper and lower jaw of a human. The image is blurry and difficult to study as it introduces false features [140].

3.7.5. Data quality

To get the most meaningful insights from our data, we need to have the highest quality feasible. Certain parameters which give us an estimate of the data quality can include contrast levels, noise levels (signal-to-noise ratio), and voxel size (spatial resolution). A lot of these parameters have interconnected relationships which force us to have a trade-off rather than the absolute best value. This makes it much more of an optimization problem than a maximization problem.

- <u>Contrast levels</u>

Contrast in XCT refers to the magnitude of difference between grayscale values of various phases. By principle, x-ray imaging generates contrast by different attenuation of each phase in a multiphase material, as seen in Figure 3.23, this is advantageous for visualizing and investigating the materials. From x-ray physics, attenuation is dependent on the energy of incoming x-rays, meaning high-energy x-rays will be weakly attenuated, this leads us to trade-off as low energy maximizes contrast but minimizes signal-to-noise ratio which can hamper detectability of image features such as cracks [141].

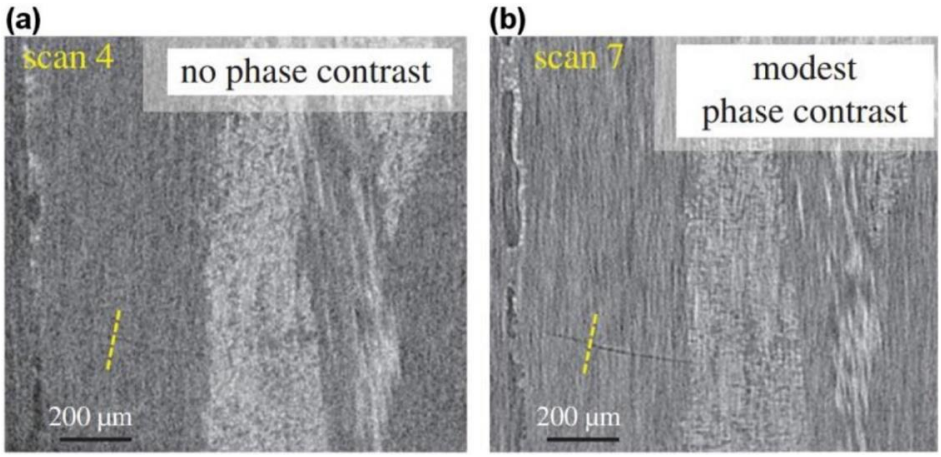

Figure 3.21 XCT image of a woven GFRP showing different contrast levels in two images acquired on Zeiss Versa lab systems. a) the matrix crack is nearly invisible, but the glass fibres are better contrasted to the matrix, b) the matrix crack is visible with glass fibres poorly contrasted to the matrix. This is expected as phase contrast is enhanced at edges and poorer in the bulk [75], [142].

- <u>Spatial Resolution</u>

Spatial resolution is described as the minimum distance between two points which are distinguishable as two separate entities; this is a complex function of the complete acquisition set of parameters, which includes x-ray optics and spot size, mechanical accuracy of the rotating turntable system etc. A voxel is a pixel in 3 dimensions, commonly the thickness equal to the pixel size. As a rule of thumb, the spatial resolution should be at least 2-3 times the voxel size at least, although, for sensible

resolving of features and quantification, it should be much higher, as shown in Figure 3.24 [141].

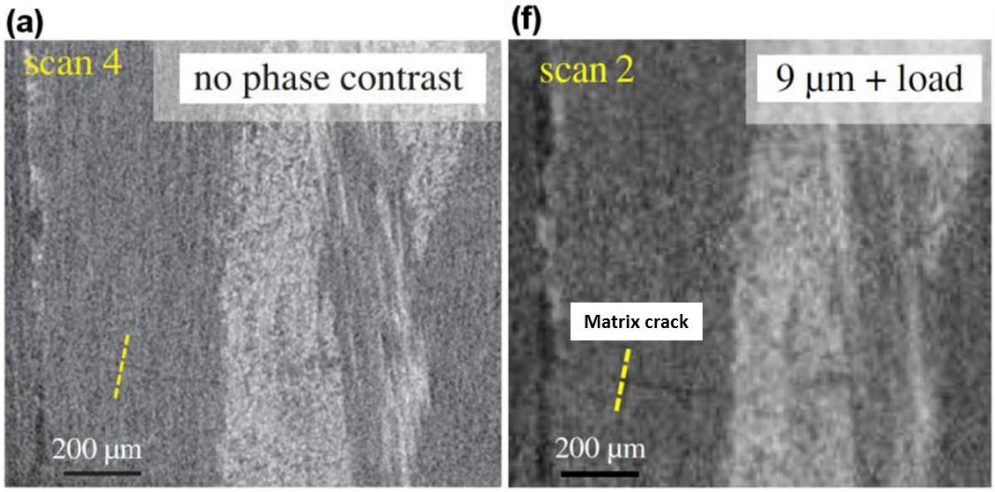

Figure 3.22 Cross-sectional images of the same region in a GFRP with different voxel sizes. a) The left image is at a voxel size of 2 µm, while f) on the right is at 9 µm. The right image looks blurry and misses some of the fine microstructural features [75], [142].

A classic trade-off occurs between voxel size and the field of view as with smaller voxel size the field of view must be reduced to compensate for the fixed number of pixels in the detector. For fibre-reinforced composites, this is especially crucial as the RVE (representative volume element) is large enough to limit the voxel size which in turn limits the detectability and resolution of features.

- <u>Noise levels</u>

Noise levels directly affect the quality of the image dataset, as shown in Figure 3.25. Signal to noise ratio improves as the x-ray signals recorded on the detector increase, following a square root relationship. Signals can be improved by increasing the x-ray energy, or flux (increasing the electron bombardment on the target beyond a threshold can result in target degradation) or increasing the exposure time on the sample. By averaging multiple frames/images for each projection, it is possible to increase the signal-to-noise ratio, improving the image quality [143].

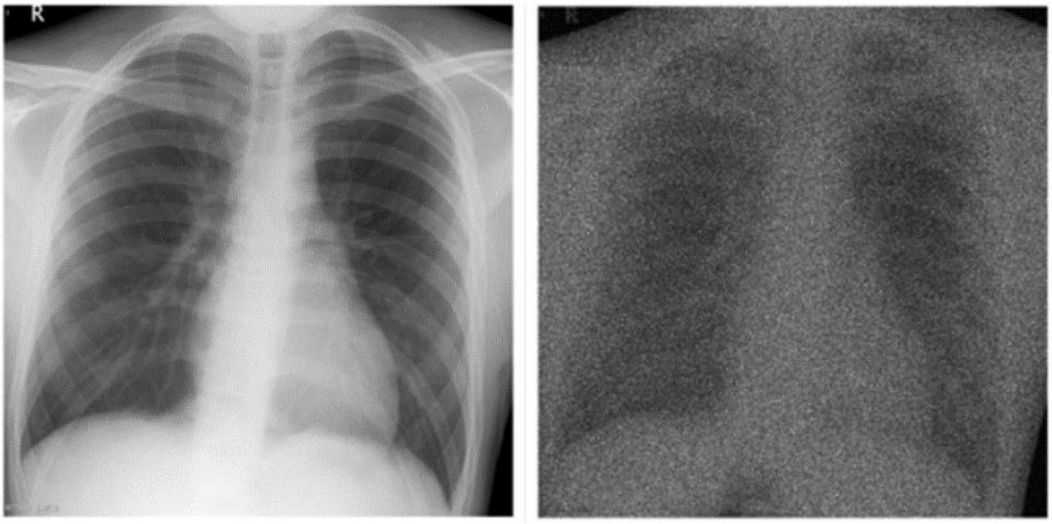

Figure 3.23 Image of a chest x-ray showing less noisy data on the left due to higher exposure time, and synthetically noised data on right. The image on the right lacks useful information that can lead to a diagnosis [144].

Less noise also decreases the need for data pre-processing time taken before the images can be analysed.

Next section details methods that can improve the quality of data, focusing on methods that can be used to improve the detection of damage features.

3.7.6. Measures to improve feature detectability

As this project is focused on assessing the fatigue behaviour of FRPs, we must explore techniques to enhance the detectability of damage features such as cracks, delamination and splitting etc. In this section, we will discuss some of these techniques used in x-ray imaging.

- <u>Subvoxel features</u>

Features which are smaller than the voxel size, or voxels which only partially sampled a feature like small cracks can be detected if the attenuation on that pixel is analysed. As shown in Figure 3.26, the decrease/increase in attenuation for that pixel, depending on whether it contains a lighter or a darker feature can be used to detect sub-voxel features. Considering we know the attenuation values of all the phases in the material,

this can allow us to measure what part of that voxel is occupied by the crack. The limit touched with this type of detection can be as low as 10% size of the voxel [145].

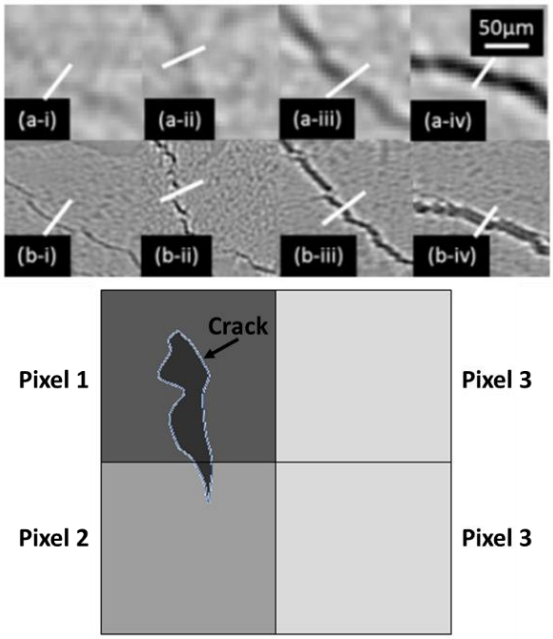

Figure 3.24 Feature presence estimated, where the amount of darker feature present in the voxel changes its grayscale value. This is shown on various levels of crack opening displacements in a material, (approximate) (i–iv) <1.4, 3, 4, and 8 µm respectively, comparisons of image quality between (a) µCT and (b) SRCT [146]–[148].

- Staining by contrast agents

Staining of the composite specimens by contrast agents containing high-attenuating solvents can impart additional contrast for materials where features are small and/or with poor contrast. Having been routinely used in medical XCT, it is now used for improving the detectability of cracks, as shown in Figure 3.27 [60], [149]. Typical dye solutions used can be zinc iodide solutions in aqueous mediums. The samples are usually soaked in dye solutions before scanning. The dye penetrates inside the micro-orifices which get to the cracks after appropriate exposure time. The dye can only penetrate cracks open to the surface, which is a limitation of this technique making it more qualitative than quantitative. Another disadvantage of this method is introducing an alien phase (the contrast agent) into the fractured interfaces, which could alter the

natural response of the material under investigation, making it potentially infeasible to undergo a time-lapse study.

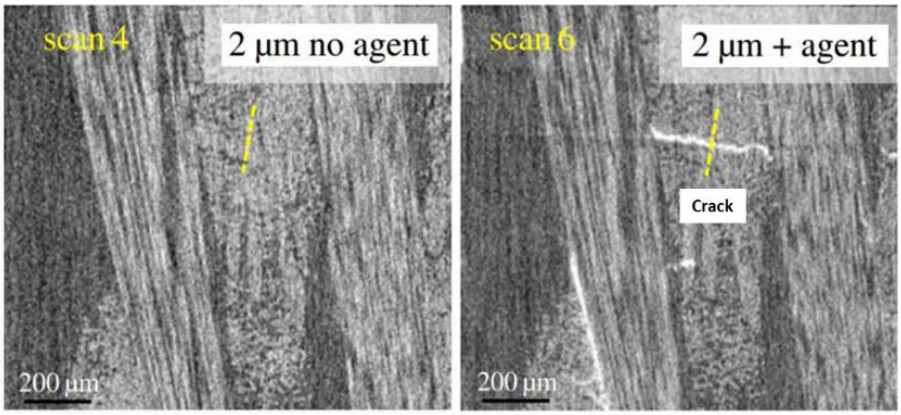

Figure 3.25 Effect of staining using a contrast agent, where on the left the crack was difficult to detect, and on the right, the crack has been highlighted by a highly attenuating contrast agent [142].

- <u>Imaging cracks under tension</u>

Increasing the size of cracks by opening them up during scanning gives a higher chance of being detected. It is common during in-situ mechanical testing to keep the cracks open by imparting static load via the mechanical rigs. Recently, standalone 'tension clamps' have been used in composites [9], where weakly-attenuating carbon rods transfer the load, thereby not interfering with the x-rays when in the field of view, as shown in Figure 3.28. However, the sample must be further away from the source to accommodate the rigs/clamps, for cone-beam XCT this decreases the magnification. It can also block the x-rays if it is made of highly attenuating materials. An improved version of this tension clamp has been used in this PhD project.

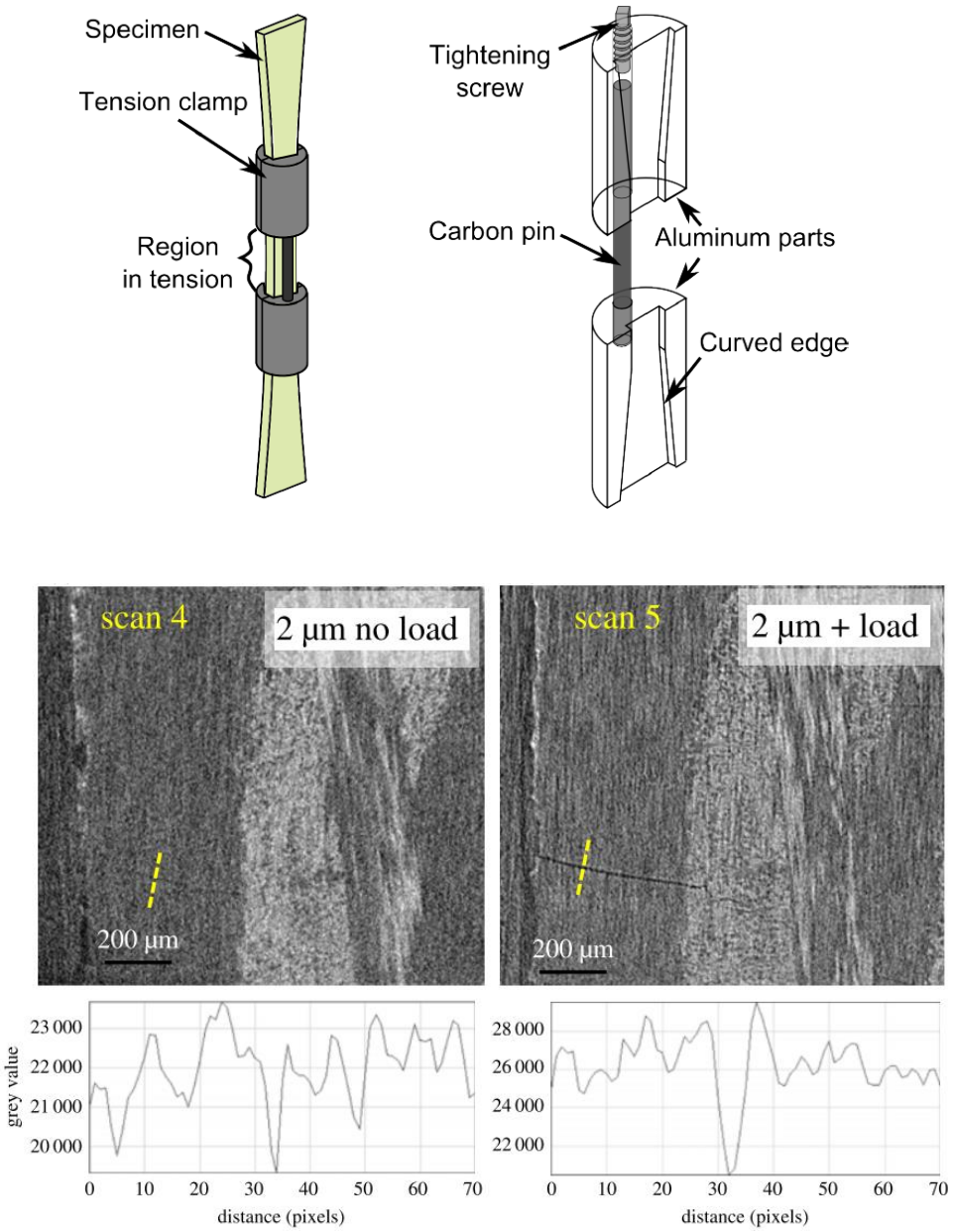

Figure 3.26: On the top is a tension clamp from Jespersen et al. [9] made for imaging cracks under tension, the carbon pins are weakly attenuating and are very stiff as well to keep the cracks open. The carbon pins go in compression when the screws are tightened into the clamp, pushing against the opposite clamp. This compression leads to a reactionary tensile load in the clamp, transferred to the sample via curved edges. On the bottom are results from a different study showing

the effect of using tensile loads to open up cracks and improve their detectability [142].

- Region of interest scanning

Another way to aid feature detection is to scan the whole sample at medium resolution, locate the region of interest (RoI) and then scan the RoI at a higher resolution, multiple RoI can be acquired and stitched in different ways, one of them is shown in Figure 3.29 [150], [151]. This saves time and resources by acquiring high-resolution scans of regions which do not contain damage regions, a strategy for imaging fibre composites where damage originates in specific sites in a heterogeneous fashion. However, this is susceptible to artefacts as for high resolution, the sample will have to go out of the field of view, leading to problems in reconstruction. Specialised reconstruction software including packages from Zeiss and Thermo Fisher Scientific can reconstruct from such cases [152], [153].

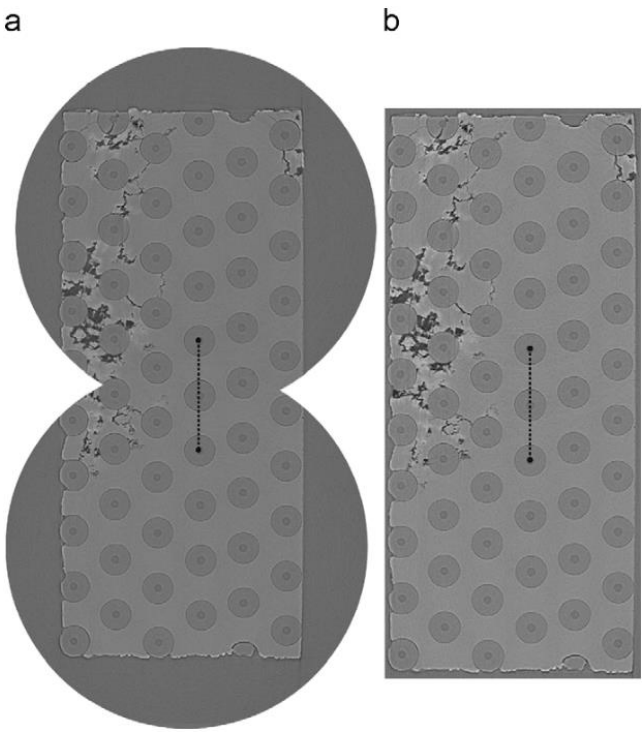

Figure 3.27 Region of interest scanning – a) shows two different images of each half of the sample separately reconstructed, b) shows the reconstruction of stitched 2D projections taken at 2 different lateral positions [150], [151].

- Phase-contrast imaging

As opposed to absorption-contrast imaging, phase contrast imaging uses the wave nature of x-rays, relying on the change in the phase of x-rays rather than the intensity. This is beneficial for multiphase materials with similarly attenuating phases, including CFRPs which have similarly attenuating carbon fibres and polymers, as shown in Figure 3.30. Due to Fresnel effects [113], the phase change is stronger at interfaces and boundaries, therefore edges can be enhanced. The x-rays should be coherent to uniformly register a change in the phase at the detector, making it mostly possible at synchrotron x-ray sources. The sample-to-detector distances can be made larger to amplify the interference of the x-rays with the sample. Superimposition of phase-contrast data on the absorption contrast data can complement each other's advantages. Particular cases of phase-contrast imaging using interferometry with lab sources have been demonstrated for material science [154], [155].

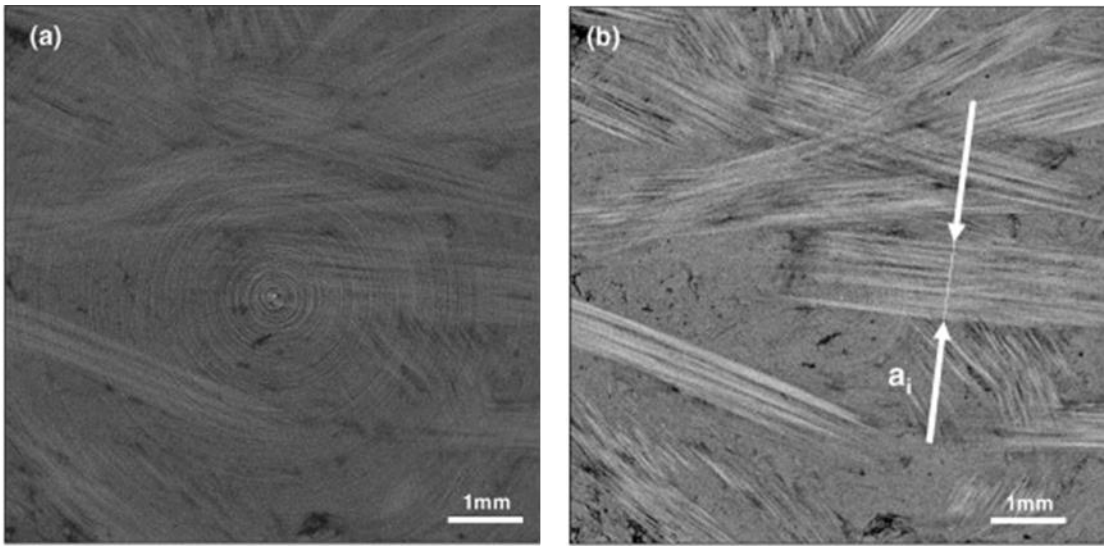

Figure 3.28 Image of a GFRP sheet moulding compound showing a) Poor feature visibility due to absorption contrast and b) Enhanced feature visibility due to phase contrast acquired at a synchrotron [156].

- Stitching volumes and helical scanning

As mentioned in the subsection 'XCT data acquisition', as sample size and resolution are inversely proportional to each because of the limited field of view, sometimes high-resolution scans are taken for individual regions and stitched back together using manual or automated alignment and registration. This problem has been partly mitigated by helical scanning which can scan samples with a high aspect ratio in a single scan procedure, limiting only in width and not height. It also avoids stitching in height which can introduce errors, as shown in Figure 3.31. Apart from being able to scan longer trajectories, helical scanning also offers better image fidelity and accuracy, as each image slice in the volume is a 'centre-slice' [157], [158]. For FBP reconstruction, the centre of the sample is the most accurately reconstructed due to uniform magnification, as we move further away from the centre, the accuracy drops. During helical scanning, each point in the sample passes through the Tam Danielson window [159], so the reconstruction is theoretically exact.

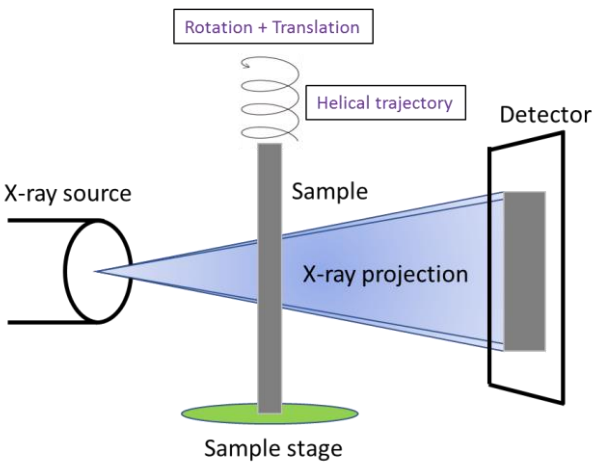

Figure 3.29 Helical scanning with a high cone angle, done as a combination of rotation and translation. Each point on the sample follows a helical trajectory instead of the conventional circular trajectory.

3.7.7. Digital volume correlation

Digital volume correlation (DVC) is a technique used to measure deformation in a material, analogous to digital image correlation (DIC), DVC is a three-dimensional method extended to a volumetric image while DIC is limited to surface observations. DVC is typically used on 3D XCT datasets, but in principle can be used for any non-destructively obtained 3D image datasets including magnetic resonance imaging (MRI) scans, positron emission tomography (PET), and neutron tomography etc. For DVC as well, there needs to be distinctly identified regions for correlation, which can come from the natural contrast of the material or embedding particles[160] as markers, analogous to 'speckling' in DIC. Much like DIC, each part of the volume is divided into smaller sub-regions, which deform by the desired stimuli. These regions are then identified in the subsequent volumetric images via correlation, and the displacement vector is calculated from the old to the new position, as shown in Figure 3.32.

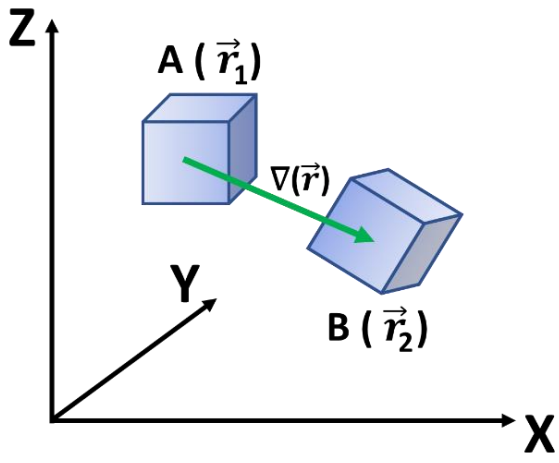

Figure 3.30 The displacement vector is calculated from the original position after the new position has been tracked via correlation.

DVC has been used to study composites for transverse shear strains [161], edge-affected stresses [162], four-point bending in C/C-SiC composites [163], tensile loading in CFRPs [164], and recently, fatigue damage in cross-ply laminates [165]. It is common to use synchrotron tomography for CFRPs for phase contrast, but glass fibres work well with absorption contrast. The strain maps and hotspots can be used in multiple ways, revealing potential sites of damage and/or their initiation-evolution, acquisition steering for region of interest imaging, and validating simulation from models.

Several software packages are available for DVC calculations, including CorrelVol [166], [167], LaVision's Davis and Strainmaster [163], [164], [168], Thermo Fisher Scientific's Avizo [169] (shown in Figure 3.33), BoneDVC [170]–[172] Volume Graphic's VGStudioMax [173], Correlated Solutions' VIC-Volume [174] etc.

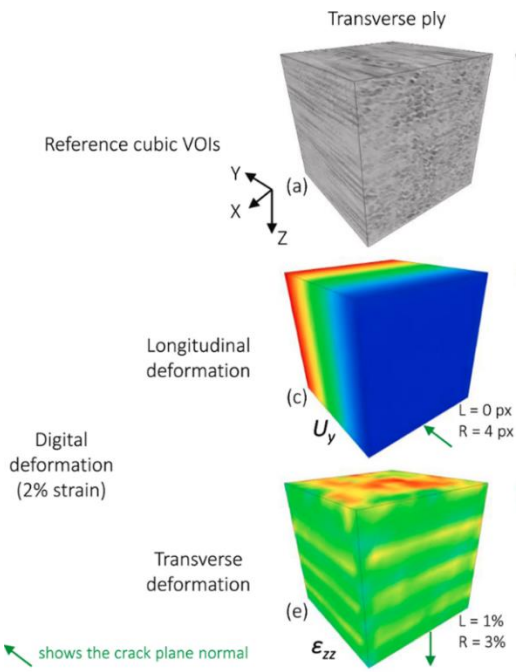

Figure 3.31 FE-based DVC displacement (U) and strain (ε) fields on a cubic volume of interest from a CFRP transverse ply – the presented fields in a, c, and e correspond to 2% longitudinal and transverse digital deformation [169].

3.7.8 X-ray CT for fibre composites

Several studies have employed innovative use of x-ray CT to analyse FRCs. X-ray computed tomography (XCT) is a powerful tool for the non-destructive characterization of fiber reinforced composites. It can identify the internal microstructure, observe cracks and damage, and track processing and damage processes. In situ time-lapse CT data can be used to analyze material damage evolution and generate, distribute, and evolve cracks. XCT is widely used in modeling, microstructure characterization, and crack or damage observations in fiber reinforced composites. It is expected that the use of XCT will aid the development of fiber reinforced composites [175], [176].

One study was carried out to analyze the effect of voids on damage evolution in three-dimensional five-directional (3D5D) braided composites under fatigue loading. The authors used a combination of Micro-CT and novel image algorithms to capture the detailed sequence of events during individual voids' coalescence to cracking. They also used the "two-step" damage classification method to analyze the progressive damage mechanism of 3D5D braided composites under fatigue loading. It was found that the debonding dominates the fatigue damage propagation in the material within 76.9% of fatigue life and accounts for 82.5% of all fatigue damage. The voids located at the interface of yarns were inferred to be the critical voids under fatigue loading. They also quantified the deflection of the crack front of the voids via automated algorithms [177].

Another complementary study a new fusion algorithm for THz and X-ray CT NDT imaging data to detect delamination and inclusion defects in GFRP composites [178]. The algorithm combines saliency region analysis (SRA) and wavelet based multi-scale

transforms (W-MST). It also uses weighted least square optimization (WLSO) to eliminate the effects of unregistered images. The authors compared 36 different combinations of the proposed fusion algorithm using objective evaluation indices such as standard deviation (SD) and spatial frequency (SF). They found that five of these combinations were optimal for five pairs of different source images. The averages of the SD and SF indicators of fused images increased by 126% and 190% compared with the source images, respectively. They found that the new approach can effectively accentuate the complementary advantages of THz and X-ray NDT methods, resulting in quantifiably improved defect inspections.

For innovative segmentation techniques, a method was presented to extract yarn envelopes from tomographic volumes at the mesoscopic scale [179]. The method relies on a classical explicit variational framework, with an adapted vector field kernel for the edge attraction force, using a linear combination of two kernels to achieve a good compromise between smoothing and interstice precision. An elliptic sectional inflation force to make use of the yarn envelope section a priori and inflate the mesh accordingly. The authors' results show nice visual segmentation results that were confirmed quantitatively by comparison with the manually segmented data.

A damage detection maethod is highlighted in this study [180]. An improved domain adaptive Faster R-CNN model for inclusion and void defect detection in spacecraft composite structures (SCS) is proposed. The model combines a feature pyramid network (FPN) with the base network and adapts both the lowest and highest feature maps of FPN in image-level adaptation, which increases the recall rate of small-size defects. In addition, conditional domain adaptation (CDAN) is utilized to make the bounding box features more domain-invariant. The model is trained end-to-end with

stochastic gradient descent (SGD) combined with gradient reversal layer (GRL). The results demonstrate its effectiveness for defect detection in SCS.

Another correlative study combines surface digital image correlation (DIC) with 3D micro-computed tomography (μCT) and corresponding digital volume correlation (DVC) as a non-contact approach to assess the deformation and damage of woven thermoplastic composites [181]. Specimens underwent load-relaxation tensile tests to 90% ultimate extension, inducing micro-scale damage and modest permanent architectural deformation. Results showed that differences in the loading direction and corresponding fiber waviness cause significant differences in surface topography, strain, and internal out-of-plane deformation. The average internal strain that remained after loading was 0.32% (warp) and 1.54% (weft). μCT images of specimen microstructure combined with DIC allowed depth-wise examination of surface features such as transverse cracking. DVC and μCT are effective tools for characterizing woven composite deformation, imperceptible to surface-based methods, and have significant future potential for improving finite element simulations.

To separate individual fibres from binarized data, a method was proposed [182], which identifies solid fibers in various fibrous media with volume fraction up to 45%. The method relies on three main parameters: the threshold value on misorientation, the number of considered neighbors for the computation of the chord lengths, and the dilation operator to be used. The method was evaluated on elementary cases and shown to be effective for separating straight fibers in contact to each other and woven fibers.

3.8. Scanning electron microscopy

Scanning electron microscopy is an established technique for studying material microstructures, using electrons instead of light to see things. The limit of resolution touched by SEM imaging is easily in nanometres because the electron wavelength limit due to the Abbe criterion [183] is relatively small compared to that of visible light. Using a focussed beam of electrons rastered on a sample line by line, it reads information about the microstructure. The beam of electrons is focused on the sample using powerful electromagnets and rastered in x and y directions by a pair of deflection coils across the sample.

The electrons are generated from thermionic emission via 3 common sources; tungsten filament, solid-state crystals including LaB_6 and CeB_6, and field emission guns. Once generated, these electrons are accelerated through an electric field to gain energy, referred to as accelerating voltage. Two major kinds of signals result from the electron material interaction; secondary electrons and backscattered electrons. The secondary electrons have lower energy and thus only the ones ejected from the surface and near the surface regions can be detected, limiting it to topographical surface information. Because of their lower energy, it is preferred to apply a little positive bias to attract the secondary electrons towards the obliquely placed Everhart-Thornley detector, the detector used for secondary signals[183].

Backscattered electrons are higher in energy, therefore can be collected from deeper regions in the samples, which can also provide compositional contrast along with topographical information. The detector is placed on the pole piece centred around the optical axis. The setup is kept under a high vacuum to keep the scattering of the electron at a minimum, as the bigger spot size results in lower resolution and affects the efficiency of the yield collection. Bigger dwell times for the spot results in a higher

signal-to-noise ratio which increases the image quality. For non-conductive samples including GFRPs, an electron charge up in the material can lead to streaking artefacts in the image. This is mitigated by using a conductive coating including gold or palladium, preferably thin to not interfere with the topographical features. Reducing the acceleration voltage helps to use lower energy electrons, which can minimise sample charging.

Common errors in SEM include astigmatism which leads to image distortion and streaky artefacts, caused by uneven focus of the electron beam. These are caused by column misalignment, improper electron gun emission etc. These can be corrected by a properly focused beam and accurate spot size. A stigmator can also be used to further reduce the error.

3.8.1. Sample preparation

Sample preparation routes for SEM are similar to optical microscopy, where the samples can be mounted to be ground and polished to get clean surfaces, using successive grit papers from coarse to fine. The final polishing can be done with oxide or diamond polishing on a rotary board. The composite samples are stubbed on a sample holder with carbon tapes and coated with a gold coat to make it conductive and avoid sample charging. Advanced sample preparation techniques including laser polishing and focused ion beam can be used as well, they are discussed in the next section.

With up to nanometre resolution available in SEMs, multiscale fibre architecture is easily imaged as shown in Figure 3.34 and Figure 3.35. Common damage mechanisms like fibre breakages, matrix cracks, fibre pull-outs and debonding can be easily resolved as well.

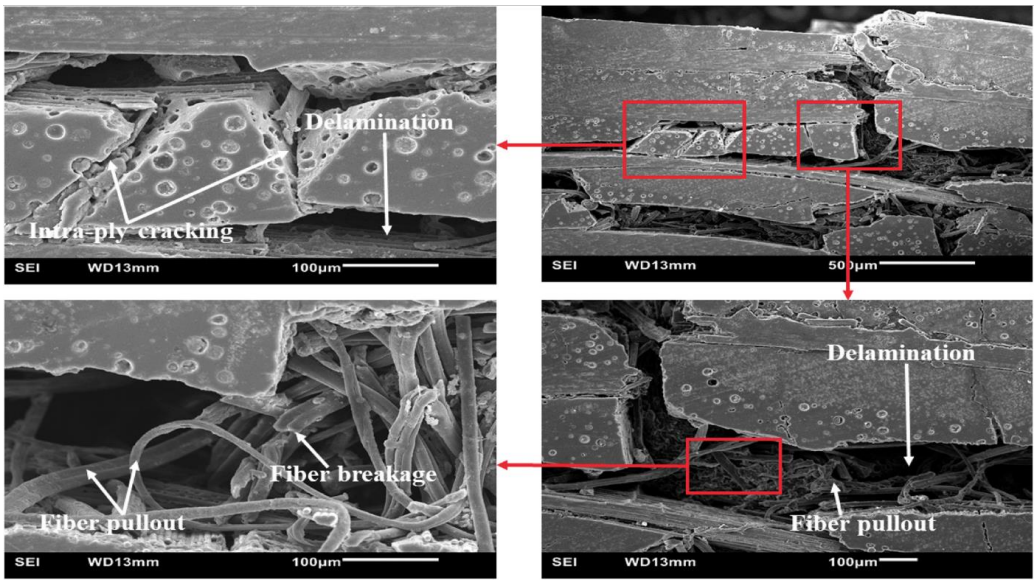

Figure 3.32 Microscale imaging of a CFRP in an SEM, imaging damage mechanisms of delamination, fibre pull-out, fibre breakage, and intra-ply cracking [184].

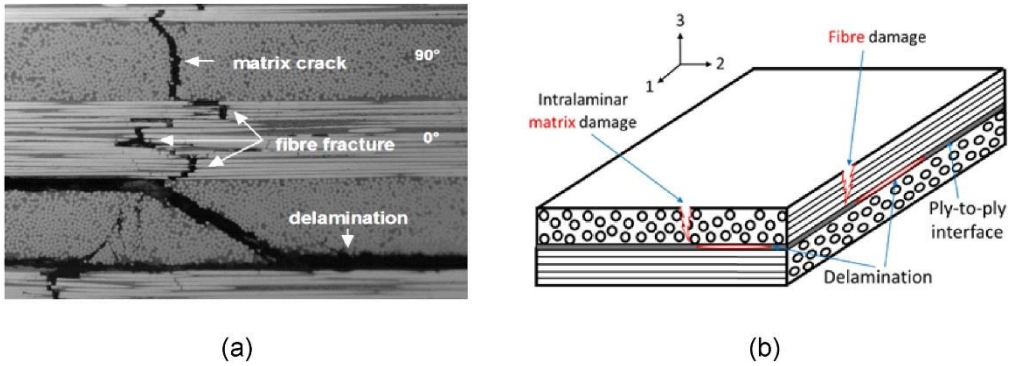

Figure 3.33 Mesoscale imaging of a composite panel made with unidirectional CFRP prepregs, showing damage mechanisms of matrix crack, fibre fracture and delamination [185].

3.9. Serial sectioning with FIB-SEM

Focussed ion beam (FIB) technology uses ion beams typically composed of gallium or Xe plasma targeted on a material. In addition, to prepare clean surfaces to be observed in the SEM, these beams can be used to dig and expose deeply buried regions of interest. to be milled. The fine probe size can remove microns of materials but with

long milling times. The SEM images can be acquired for a series stack of surfaces milled, and these images can be used to reconstruct a 3D volume with a resolution typically higher than the XCT data, although the in-plane resolution is superior to the z out-of-plane resolution. This method is destructive and is typically restricted to post-mortem analysis. A platinum mask is usually applied to avoid unintentional erosion of an area, this also provides sharp edges during the milling operation.

Equipment available today is usually in a dual-beam setup where the same machine has arrangements for SEM imaging and FIB milling and even with a laser miller, Thermo Fisher's Helios PFIB [186] being an excellent example. This allows for consecutive image capture and milling operation so the time to generate 3D volume information is reduced, as shown in Figure 3.36. Milling normally results in faster excision, but induces comparatively higher damage, while grazing incidence is slowest but induces lesser damage. Rocking milling is also a technique used for minimizing damage, which mills in alternate directions for each slice.

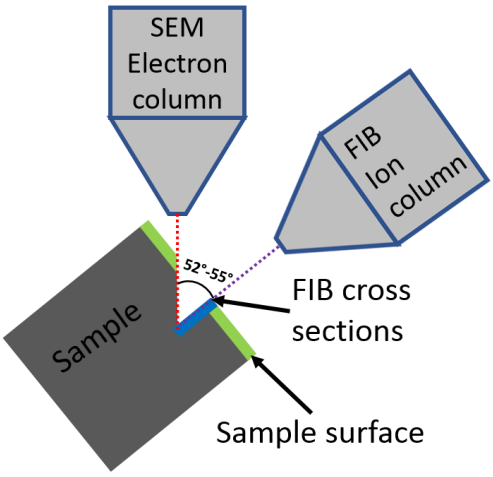

Figure 3.34 Schematic of a dual-beam setup. The ion column is usually at an angle with the SEM, between 52°-55°. The sample stage is motorised in multiple degrees of freedom to manipulate sample orientation.

The milling with a Plasma FIB can be typically 100s of microns in-depth, while each slice can be around nanometres thick at a minimum and can go to 100s of nm. It is possible to mill μm^3 of volumes over hours, as was done by Burnett et al. [186] shown in Figure 3.37. Milling for sample preparation has been done for carbon fibre composites by gallium ion beams [187], [188], shown in Figure 3.38.

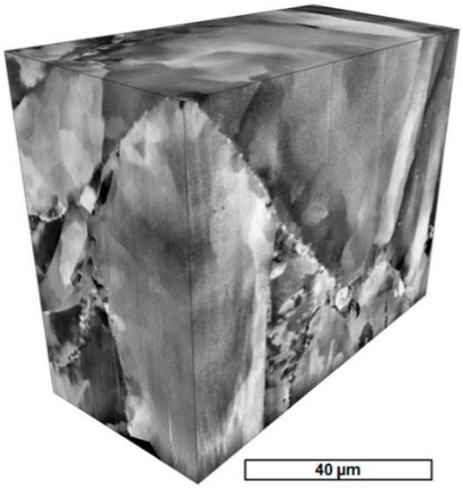

Figure 3.35 Large stainless steel volume milled with a slice of 100nm by a Xe+ Plasma FIB and reconstructed into a volume [186].

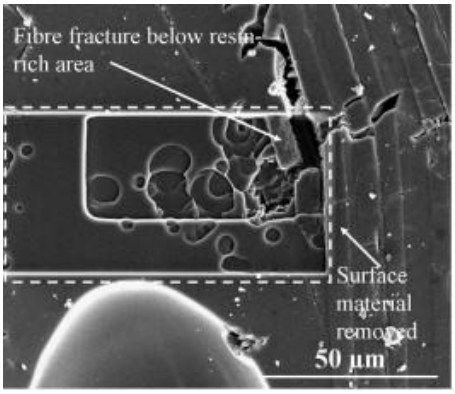

Figure 3.36 Surface milled by a gallium ion beam to expose damage features in the sub-surface regions [188].

Serial section FIB-SEM imaging has been instrumental in establishing correlative workflows for material analysis, registering image volumes of varying resolutions across multiple length scales, particularly XCT data [189].

3.10. Chapter Summary

In this chapter, common destructive and non-destructive techniques used for imaging and characterising composite materials and damage were reviewed, with a focus on x-ray CT. The merits, demerits and trade-offs involved in each technique were discussed. The background and characteristics of x-ray CT were introduced and discussed, with a focus on common segmentation techniques, errors and artefacts, data quality metrics, and methods to aid damage detection. X-ray CT was argued to be a fantastic overarching technique that can detect and study material damage in an in-situ time-lapse manner. Digital image and volume correlation were discussed, as well as how it can generate localised strain information and complement data available from x-ray CT. Scanning electron microscopy along with FIB-SEM was discussed, including how it can complement information from x-ray CT and DIC-DVC in a correlative manner.

Till now, no study has investigated the fatigue behaviour of wind blade UD-NCF GFRPs in a hyper-correlative manner, bringing together complementary techniques of x-ray CT, DIC, DVC and FIB-SEM, to build a *'composite'* knowledge of the damage initiation, progression, and failure. This study attempts to build and exploit this experimental workflow to study the relation of observed stiffness degradation during fatigue and relate it to the strain fields and microstructural features. This knowledge has been used to compare and verify with image-based models and will continue to inform and verify future modelling and simulations.

The next chapter introduces and details the experimental methods undertaken in this PhD study, divided by each of the manuscripts.

4. Experimental methods

This chapter details the experimental work undertaken for this PhD project. Each section of this chapter discussed the methodology used in each of the papers. As mentioned in the text before, this PhD project is a two-pronged approach; the development of a novel experimental time-lapse correlative approach to study fatigue

damage in UD-NCF GFRPs, and to develop novel image analysis methods for fibre composites data to improve its exploitation.

The first and the second section describes the time-lapse workflow including both data acquisition and processing used in Papers 1 and 2. The third section includes the introduction and discussions of one novel and three existing image analysis methods for fibrous composites, benchmarked in Paper 3. The fourth section introduces and discusses another novel image analysis method to automatically detect and track the progression of damage in fibrous composites, which forms Paper 4.

4.1. Time-lapse workflow in Paper 1

This study was a precursor to the capstone study in Paper 1. It involves a time-lapse workflow for observing fatigue damage initiation and progression in UD-NCF GFRPs via x-ray tomography and digital image correlation (DIC). The workflow is outlined in Figure 4.5, where the fatigue test is interrupted at 3 different points in addition to the first reference XCT-DIC acquisition.

In addition to monitoring the surface strain development, strain maps generated via first DIC acquisition allow for strain hotspots identification, which can locate RoIs where damage might occur. This RoI was then imaged in XCT, to track the initiation and progression of damage features. The sample was tested not to complete failure but to a loss of 10% stiffness, which in this study has been considered as a criterion of failure.

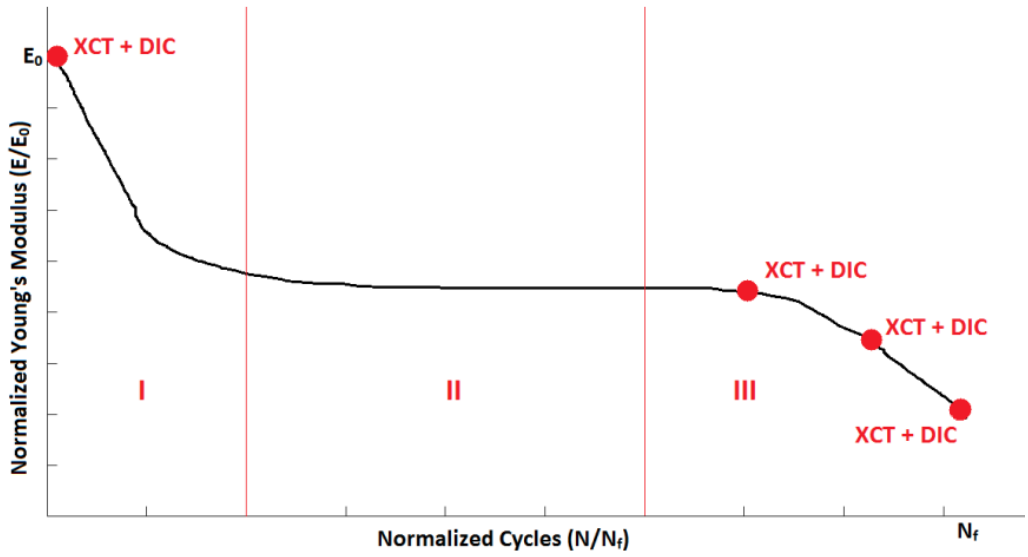

Figure 4.1 Time-lapse workflow used in Paper 2, employing intermittent XCT-DIC observations around three stages of progressive stiffness degradation. Both the Young's Modulus and number of cycles are normalised against initial stiffness E_0 and total number of cycles N_f.

4.1.1. Materials

The materials is the similar to the one used in Paper 1, and has also been supplied by Saertex GmBH, comprising 0° UD Advantex E-CR glass fibre bundles (tex = 600g/km) stitched to 90° backing bundles and impregnated in Olin epoxy using vacuum-assisted resin transfer molding, with a layup of [[0/90]/[90/0]s]. Butterfly geometry fatigue test specimens of length 284mm were cut out using waterjet with a parallel sided gauge length of 44 mm, as shown in Fig. 4.6. The smallest width at the gauge was 10mm wide, with the plate thickness of 3.8 mm. End tabs of length 120mm were stuck on to avoid crushing the ends, tapered over a length of 60mm, to reduce stress concentrations.

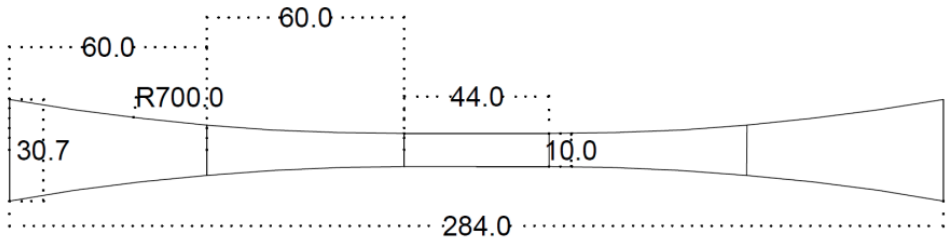

Figure 4.2 Butterfly geometry used to encourage failure in the gauge regions. All dimensions are in mm.

4.1.2. Mechanical testing and digital image correlation

Instron servohydraulics were used for fatigue testing in load-controlled mode. The sinusoidal cycling frequency was 4 Hz with an R-ratio of 0.1 and maximum load corresponding to a strain of 1%. Strain was monitored via clip-on extensometers with (12.5mm/±5mm) gauge length. DIC images over the whole speckled gauge were acquired using a LaVision Strainmaster system at a slow cycle of 0.125 Hz to minimize blurring and imaged at 10Hz frame rate.

The images were correlated to the first 0-strain image, calculated strain maps relative to the reference. Correlation was done on a slightly smaller area excluding the O-rings to avoid mismatches and poor correlation values.

4.1.3. X-ray tomography

XCT scans were carried out on Zeiss Versa 520, where a custom holder was manufactured to hold tall samples and enable repeat accurate positioning for the time-lapse study. The RoI was a hotspot chosen from the DIC strain maps, located close to a backing bundle.

Source to sample distance	Detector to sample distance	Optical magnification	Pixel range	Exposure time	Number of projections/ tomogram	Accelerating voltage	Pixel size
42 mm	150 mm	4x	16-bit	20s	3201	70kV	0.7μm

Table 4.1 XCT scanning on Zeiss Versa 520 kept consistent during the time-lapse study.

The XCT images were registered using the same correlation[190] methods from Thermo Fisher Scientific's Avizo software, allowing for only rigid transformation and rotation. No DVC calculations were carried out.

4.2. Time lapse workflow in Paper 2

This study uses XCT, DIC-DVC and serial section SEM tomography (SST) to generate a three-dimensional, multiscale, and spatially correlated time-lapse dataset to investigate the initiation and evolution of fatigue damage in UD-NCF GFRP, in terms of the types of damage, distribution, and their proximity to microstructural elements. This is then related to the loss in stiffness, a key material property. The XCT and DIC-DVC allow the damage progression and associated strain fields to be monitored, while the 3D SEM generates a clearer, higher resolution image of the final state of one of the sample RoIs to be further correlated and studied.

4.2.1. Fatigue test sample specimens

The composite is a proprietary sample supplied by Saertex GmBH, used in wind turbine blades. It is made of four layers of UD E-CR glass fibre bundles (fibre tex = 600 g/km) stitched via threads to backing bundles, impregnated with Olin epoxy using vacuum-assisted resin transfer moulding (VARTM) and cured at 80° C for 8 hours. The four UD bundles are oriented at 0° (corresponding to the z-direction in the x-ray images) while the backing bundles are oriented perpendicular at 90° across the width in the x-direction, leading to a [90/0/90/0/90/0/90/0/90] layup. This 3.67 mm thick material is tabbed with a tapered cross-ply laminate and waterjet-machined to extract butterfly specimens. This geometry is optimised for fatigue testing as it encourages failure in the gauge regions rather than the grips [191]. Specimens are 226 mm long, with a gauge section 6mm wide and 10mm long, making a cross-sectional area of 22.05 mm^2. To investigate and register the same region in XCT and DIC, gauge boundaries are marked with high-contrast SilverDAG and then the gauge region is speckled over with white and black paint.

Figures 4.1 A and B show the 3D composite architecture in the gauge region obtained by an XCT volume render, where the matrix has been made invisible to aid the visualisation of the fibre bundle arrangement. The UD bundles are much thicker than the backing bundles; while the range of UD fibre diameter is approximately 17-20 μm, backing glass fibres are approximately 9-11 μm. The stitching threads cannot be resolved as they have similar ‘optical density’ compared to epoxy. C and D show the gauge painted with a speckle pattern for DIC acquisition. Throughout this paper, the coordinate system is defined as X (width), Y (thickness), and Z (the UD load-carrying direction).

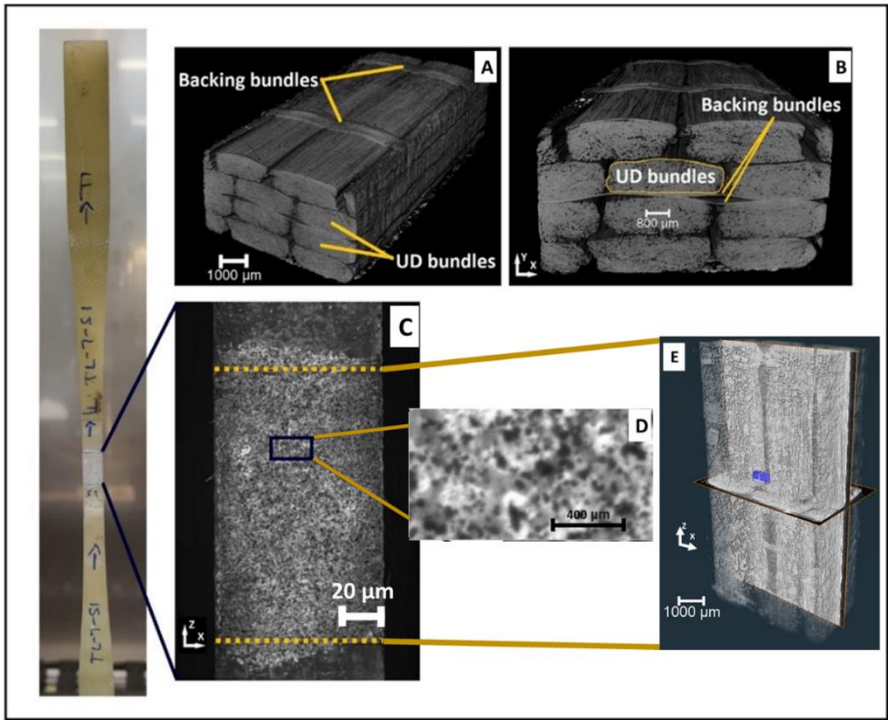

Figure 4.3 Photograph (left) of the butterfly sample geometry. A and B show the gauge region which is made of epoxy reinforced with UD glass fibre bundles and ~10% of backing bundles, where the matrix has been rendered invisible. C & D shows the gauge region speckled with black and white paint to enhance DIC contrast. E shows the gauge region shown in XCT with a translucent volume render (blue box shows typical RoI sizes investigated for damage).

4.2.2. Methods

Figure 4.2 shows the experimental workflow for this paper, where XCT, DIC-DVC and SEM have been combined so as to track the damage and stiffness degradation throughout an HCF fatigue test.

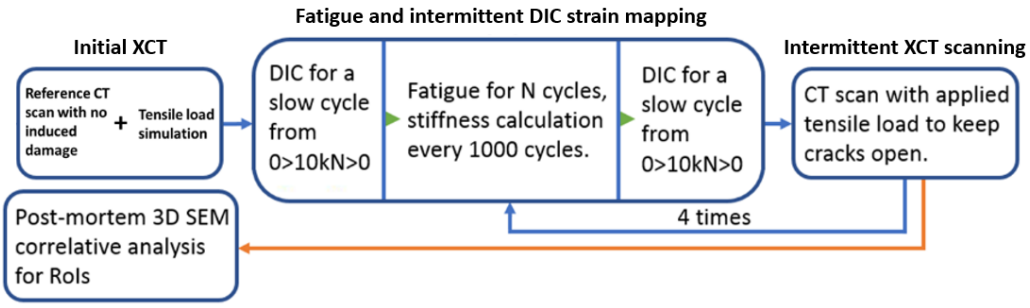

Figure 4.4 Experimental workflow for the time-lapse fatigue investigation by correlative DIC-XCT-SEM in conjunction with tensile load simulation.

This workflow is combined with tensile load simulation using a material model and comparing the simulation results with the experimental results.

Mechanical test procedure

The specimen is fatigued using a sinusoidal loading, where is it fatigued for a total of 120000 cycles and interrupted at 20000, 60000, 80000, 100000, and 120000 cycles. The test is carried on a load-controlled Instron 8802 hydraulic machine at 4 Hz, R= 0.1, for a maximum load of 10 kN applied on the sample, which corresponds to a ε_{max} (maximum applied strain)= 1%.. The axial strain was continuously monitored in the gauge region via a clip-on extensometer (10mm/±1mm). The maximal strain ε_{max}= 1% has been found to encourage progressive damage under HCF [9] and 4 Hz is low enough to avoid self-heating of the epoxy [9]. Stiffness has been measured every 1000 cycles using extensometers by calculating the slope on a stress-strain curve via linear regression.

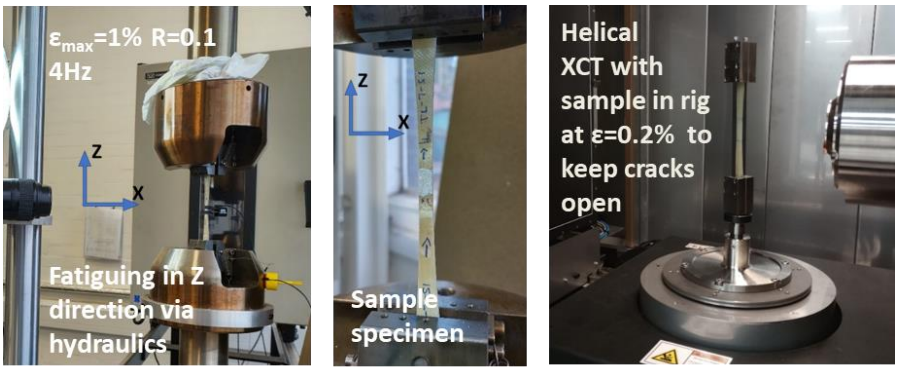

Figure 4.5 Sample specimen fatiguing in the hydraulic rig and being XCT scanned while the cracks are kept open by the tension clamp.

The evolution of the strain field was recorded using an intermittent DIC routine at the beginning and at the end of every fatiguing step. The DIC is acquired on a lower load frequency of 0.02 Hz, cycled from 0 to 10kN and imaged at a 10Hz frame rate, using a single-camera LaVision Strainmaster system, as shown in Figure 4.3. The

subset size used for correlation is 31 pixels where the pixel size is 6.53 μm. The images are correlated to the first image recorded during the slow fatigue cycle (at 0 MPa), so the strain calculated is relative to the 0-load reference image. The images were acquired over the whole FoV of the gauge section, but the correlation and subsequent strain calculation were done on a slightly smaller area to avoid loss of correlation at the edge of the frames.

In order to better delineate the fibre fractures/damage, the sample was XCT scanner under tensile load to keep the cracks open [9], [149], using a tension clamp. The tension clamp uses a pair of carbon rods, one on each side of the sample to impart tension by means of curved clamps, as shown in Figure 4.4. The limitation of the carbon rods getting their ends crushed by the screw points on higher loads has been mitigated in this study by glueing hard stainless steel onto the ends. This prevents screw points from digging into the carbon rods and has been successful in imparting stable loads of up to ~5.7 kN. By attaching the clamp while the sample was loaded it was possible to maintain a load of ~1.8 kN (~81 MPa) , corresponding to a strain of 0.2%.

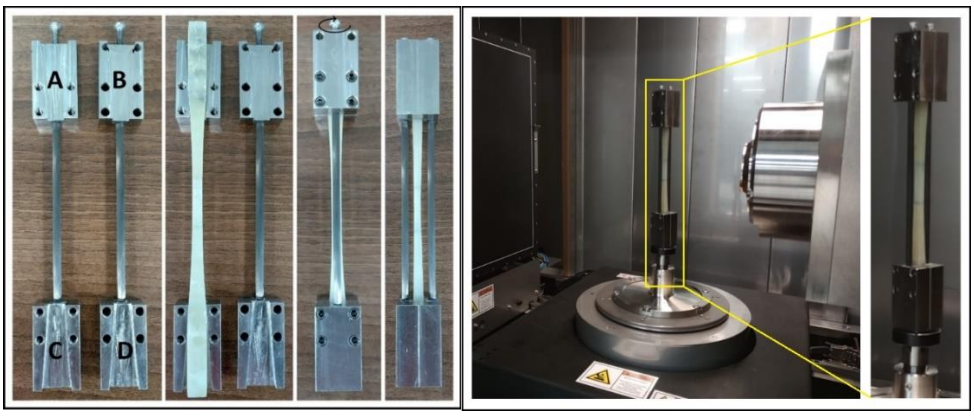

Figure 4.6 The tension clamping procedure, which aids damage detection during XCT scanning. The sample is fixed between pairs (A, B and C, D) of metal jaws and the carbon rod is screw-tightened to impart tension. The helical scanning procedure can scan longer Z-heights than conventional XCT scanners.

X-ray tomography

All the scans were carried out on the Thermo Fisher Heliscan Mk2, which offers high image fidelity with the capability to scan tall samples due to its helical scanning trajectory. The scanning conditions are summarised in the table below.

Source to sample distance	Detector to sample distance	Pixel depth	Exposure time	Number of projections/ revolution	Total number of projections	Accelerating voltage	Tube current	Voxel size
25 mm	810 mm	16-bit	1.45 s	1800	~4000	80kV	95 µA	4.3494 µm

Table 4.2. Scanning parameters used for time-lapse helical scanning on a Thermo Fisher Heliscan Mk2.

This results in a full-field scan of the gauge region (10mm x 3.6mm x 6mm) in a single tomogram. This produces an average file size of 10 GB, for an average acquisition time of 6 hours. The carbon rods from the tension clamp are spatially within the scanning FoV, but due to their low atomic number, they do not attenuate the signal and hamper the image. The sample stub with precise markings allows accurate repeatable placement of samples to maintain consistency across the time-lapse. The XCT scans were undertaken after 20000, 60000, 80000, 100000, and 120000, cycles, including the finish. The sample is not taken to complete failure to enable higher-resolution SEM studies.

DVC analysis was also applied to correlate the CT scans taken at 0 and 120k cycles. The DVC analysis was performed in Avizo's XDigitalVolumeCorrelation module, since the residual strain is expected to be lower, the global mesh-based DVC approach

using a bigger tetrahedral element of 200 □m is used. For such a large volume, it puts constraints on the computational resources to choose a smaller element size.

Finite element modelling for tensile simulation

An image-based finite element model was constructed based on the initial CT scan as described in [192]. First, the fibre bundles were segmented from resin-rich area and then a surface mesh of the segmented fibre bundles is created. Creating a smooth surface mesh is challenging; in our case we used an automated mesh generation as a first step and manually improved the mesh afterwards at an average element length of 150 □m. This process takes approximately 2 hours for the given dataset. Within the created surface mesh, a solid mesh comprising second-order tetrahedral elements comprising ten nodes was created. The remaining volume was then filled with first-order tetrahedral elements representing the resin-rich areas. After the mesh creation, the fibre orientation mapping takes place, following [193]. With the structure tensor method by Jeppesen et al. [194] the fibre orientations are analysed and then mapped to each of the four integration points per element. With the given mechanical material properties, a linear orthotropic material model is assigned and a tensile test with a total strain of 0.25% is simulated.

3D Serial sectioning SEM

Postmortem, a volume of 400 µm x 600 µm x 100 µm was excavated and imaged in the Helios 5 Laser PFIB SEM using 20 kV voltage, 3.2 nA of current, and a 3072 x 2048 ETD image grid. Approximately 1000 slices of 100 nm thickness were milled using Xe+ plasma. Prior to the acquisition, the sample was sputter coated using an Au:Pd 80:20 ratio with a thickness of 10 nm. The acquisition takes approximately 30 hours.

4.3. Image analysis workflows for fibre-reinforced polymers

To make better insights from imaging data of FRPs, quantification over qualitative inspection of images is preferred, where the quantified information is objective and actionable. An array of workflows to quantify FRPs imaging data exist, and some of the popular ones are considered in Paper 3. Apart from three established software workflows – Avizo, Structure Tensor, and Insegt; one novel workflow from Fiji-ImageJ used for image analysis have been introduced – all four of these are discussed and benchmarked against each other. Apart from the introducing a novel workflow and benchmarking, this paper serves as a guided review for members of the composites community interested in image analysis. These methods have been introduced below.

4.3.1. Avizo

Avizo is a proprietary general image analysis platform and graphical user interface (GUI) from Thermo Fisher Scientific hosting a variety of tools for analysing imaging data, from visualisation to processing and quantification. It has a comprehensive suite of tools for analysing FRCs that can segment multiple phases and damage modes such as pores, fibre bundles, matrix, and individual fibres It also has recently introduced AvizoAI as an artificial intelligence tool for advanced automatic image processing which can be used for segmentation. The platform also has a dedicated tool called XFiber which can trace individual fibres, and generate relevant information such as length, radius, tortuosity, distribution, and orientation tensors, among others.

XFiber uses a template matching method via normalised cross-correlation[195] to match the grayscale features – fibres in this case, to a user-defined parametric cylinder

template, which is similar in size to the fibrous feature that needs to be detected. The cross-correlation with a parametric cylinder results in two outputs: a correlation field and an orientation field. The correlation field stores the maximum correlation value, while the orientation field stores the orientation for which the correlation value is maximum, for each voxel. These two fields are then thresholded on minimum correlation values for which fibre centrelines tracing can start and continue. Linking each centre point across all the orthogonal image slices using a search cone generates uniquely identified 3D fibre centre lines which can be used to study 3D morphologies and statistics. This method has been described in Figure 4.7.

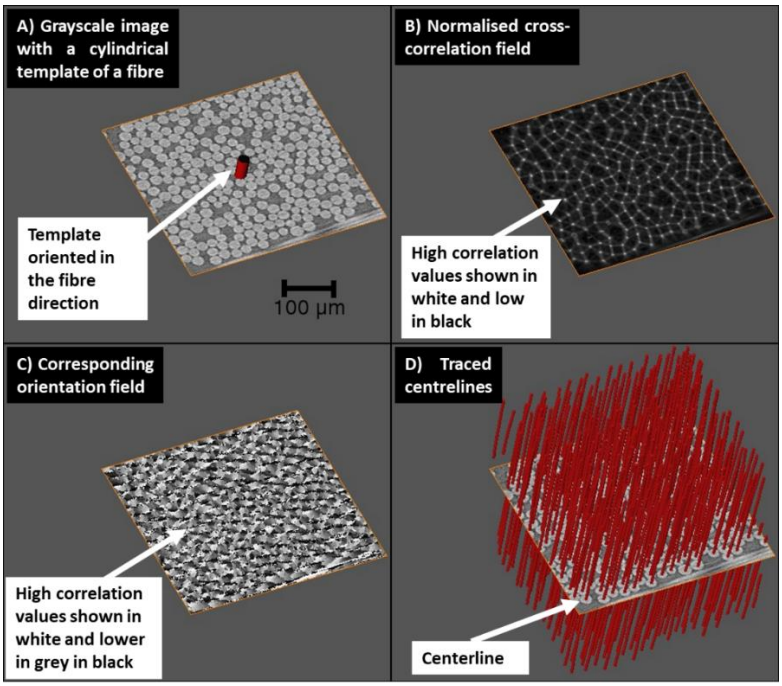

Figure 4.7 A) Greyscale image in Avizo which is cross-correlated with a user-specified cylindrical template, leading to a corresponding B) correlation field and an C) orientation field. D) These fields are then thresholded to generate fibre centre-points which are linked together using a search cone, leading to a unique traced fibre centre-line.

4.3.2. Insegt

This algorithm is based on computer vision and is classed as a supervised segmentation method, manifest as a MATLAB and Python-based graphical user interface (GUI) and code called Insegt–[20], [131]. We use the MATLAB version for this paper. The

algorithm is taught what a fibre centre looks like, using an annotated training image. The information it learns on the training image is stored in a matrix referred to as a ‘dictionary’, once the dictionary is learnt, it can be looked up for segmenting fibre centres and matrix. Therefore, this method falls under the purview of ‘supervised learning’.

The workflow starts with an annotated image marked with fibre centres and matrix, used for training the algorithm on what a fibre centre and fibre background look like. The training image should be similar to the 3D imaging data that needs segmenting – a cross-sectional slice containing fibre blobs.

This training image is fed into ‘dictionaries’; a matrix containing information on the type of pixels that belong to classes of either the fibre centres or the matrix. Looking up these dictionaries for unknown pixels generates a probability map of the likelihood of a pixel belonging to either of the classes. This algorithm is run over all the slices and the fibre centres are computed. Then each fibre centre pixel is linked with a corresponding fibre pixel in the previous and the next slice, with a user-defined search cone of fixed radius, thus the 3D trajectory of each fibre is traced, which can be used to study the orientation and morphology of the fibres.

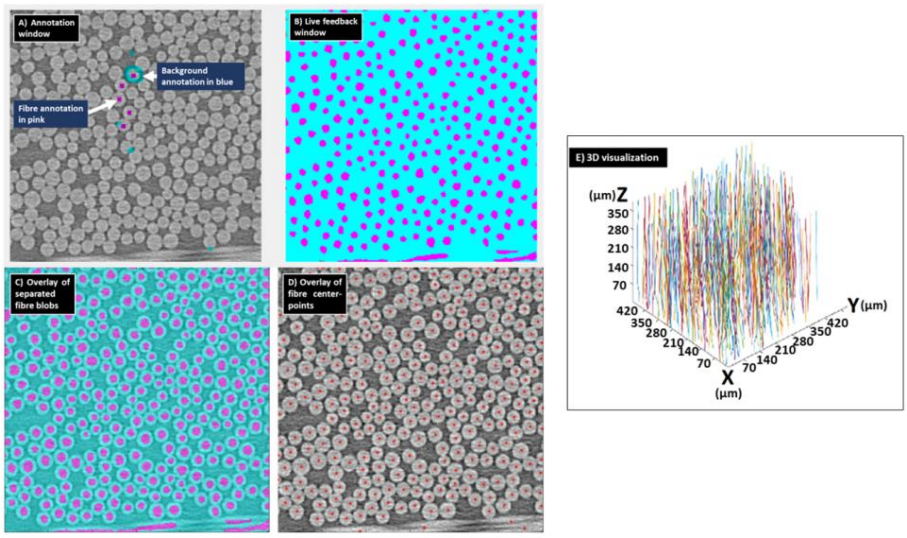

Figure 4.8 A) The fibre 'blobs' can be segmented and separated by annotation; B) feedback can be viewed live in the GUI to improve if required. C) Centroids for these blobs are computed for D) fibre centre-points, and these are linked by a search cone to form E) unique fibre centrelines. The streaks in the bottom of each image are 'backing bundles' which run orthogonal to the 'unidirectional' fibres (detailed in section 3).

The steps to calculate the fibre trajectories are shown in Figure 4.8, where the GUI has an annotation and a live feedback window giving the result of learning from annotations. These blobs are overlayed on the fibres and the centroids of each blob are fibre centres, which are linked to form unique fibre trajectories, also shown in 3D.

4.3.3. Structure Tensor

While the above methods of Avizo and Insegt allow tracing of individual fibres, sometimes only the orientation at each material point is of engineering relevance, as the directional properties in composite materials are exploited. This orientation information is particularly useful in modelling and simulations to study directional mechanical properties. One such method to calculate material point orientations is by computing the structure tensor [196]–[198]. There are several structure tensor methods developed for fibre orientation analysis available [194], [196], [199]. In essence, the orientation of structures is estimated by computing gradients in all directions leading to the direction of the smallest gradient, indicating the strongest orientation in that direction. The changes in the greyscale value are computed around a certain point and can be expressed in a 3x3 matrix [197]. In this study we use the method developed at the Technical University of Denmark, available in Python and MATLAB, of which the Python version was used in this study. Their structure tensor method comes with several advantages. It is publicly available [200], it has proven its robustness in several studies [194], [197], [201], it was successfully used as the basis for finite element modelling of fibre-reinforced composites [192], [202], and only two parameters need

to be set. The noise scale parameter σ should be chosen large enough to filter noise from the greyscale image but small enough to account for local orientation changes. The integration scale parameter ρ is the standard deviation of the Gaussian Kernel which averages orientations around the regarded point. Larger values therefore average larger regions.

The code is written in Python without a graphical user interface. One of the examples is shown in Figure 4.9, which gives a colourmap of all fibres detected to be unidirectional along the z-axis.

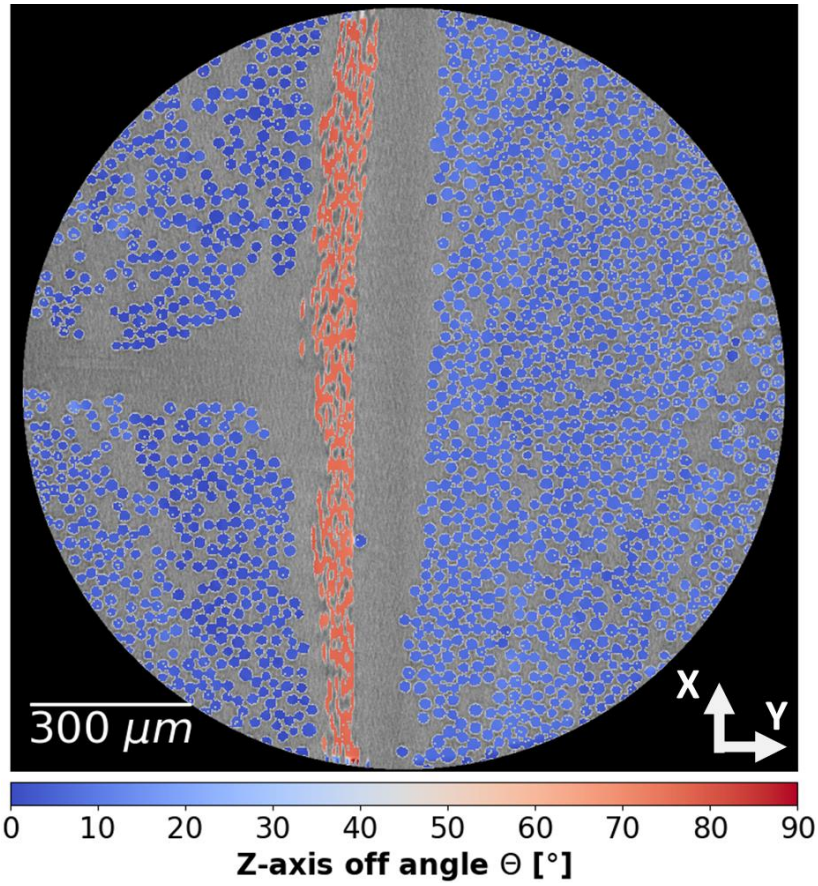

Figure 4.9 Orthogonal unidirectional and backing fibres for a wind turbine section observed via a colourmap of each voxel having ~0° and ~90° directionality towards the z-axis.

4.3.4. Fiji-ImageJ

Fiji is an open-source image processing distribution of ImageJ, conceived as public domain software for processing and analysing scientific images. It was developed by the Unites States National Institute of Health and partners [203] primarily to solve problems in medical imaging and it quickly evolved as a comprehensive tool for broader scientific imaging analysis. Fiji is an extensive distribution of ImageJ which includes numerous native and user-contributed plugins covering an extremely wide variety of image processing routines; denoising, segmentation, registration, stitching, skeletonisation and many more.

Regarding FRCs, the software tools available within Fiji-ImageJ are potent at segmenting different phases including pores, fibre bundles, matrix, and individual fibres – including the damage in them. One of the tools, Trainable Weka Segmentation [204] (TWS) derived from random forest [205] machine learning is adept at segmenting noisy data. It uses annotation on a training image to segment the remaining data automatically, in a way similar to the Insegt software. Using this method as part of a bigger, novel workflow developed for this paper, individual fibre centrelines can be traced and used to study the morphology and relevant information.

The workflow is explained below, illustrated in Figure 4.10.

A) It starts with a 3D image stack containing fibre cross-sections as blobs, imported into Fiji-ImageJ.
B) Trainable Weka Segmentation 2D is used to segment fibre blobs via manually annotating fibres and background, leading to a labelled result of fibre blobs separated from the background of the matrix and other phases. This is then binarized into the black background and white fibres.
C) Detected fibre blobs are separated by watershed.

D) The centroid of each separated blob corresponding to the fibre centre is calculated by finding local maxima.

E) Once the fibre centres are detected, these can be labelled uniquely by running a connected components routine available in Fiji-ImageJ. This returns all the fibres uniquely labelled which lie on a close trajectory.

F) These traced centrelines can be overlayed on the fibres for validation.

G) They can also be visualised in 3D within Fiji-ImageJ as shown below.

In addition, Fiji-ImageJ allows in-house morphological analyses through various toolkit plug-ins hosted within Fiji-ImageJ, particularly BoneJ [206] (developed for skeletal image analysis, but useful for fibrous structures), MorphoLibJ [127] (useful for morphological filtering, reconstruction, segmentation, metrology etc.), DiameterJ [207] (useful for calculating statistics on fibre diameters) and Trackmate [208], [209] (useful for tracking, data visualisation, track analysis etc.), among others.

A small script written for this paper returns a .csv file containing the X, Y, and Z positions of all fibre centre-points belonging to a unique fibre centre-line, for all fibres. This allows for bespoke morphology and other relevant calculations inside or outside of ImageJ, facilitating exportability.

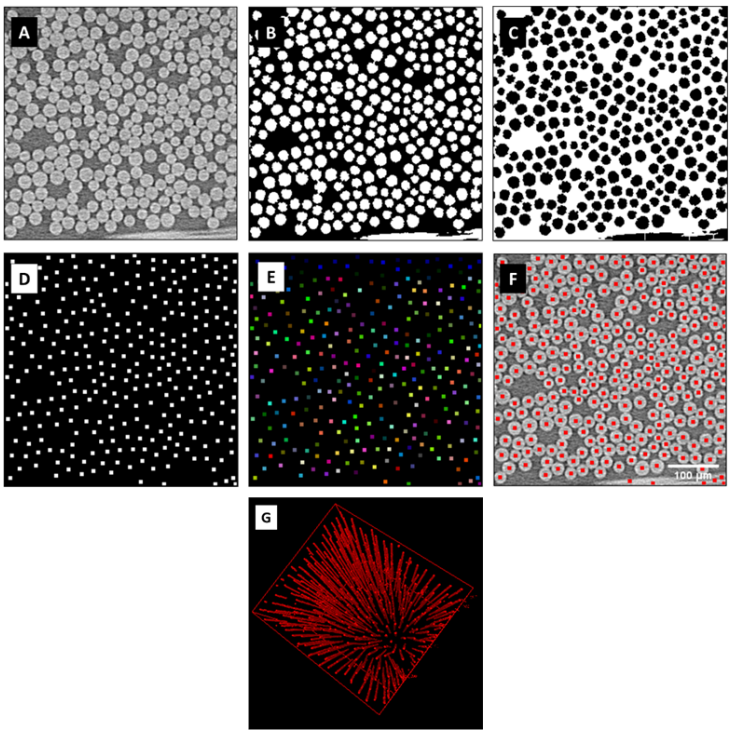

Figure 4.10 The workflow in Fiji-ImageJ is run on a stack of A) grayscale images of fibre cross-sections, which are B) segmented using TWS, these segmented fibre blobs are then C) separated by watershed. For each separated blob, the calculated centroid is a D) fibre centre-point, these are linked by connected components routine to form E) unique fibre centre-lines. The fibre centre-points are F) overlayed over the grayscale fibres for validation, while G) shows the unique fibre trajectories in 3D.

These four software packages have been benchmarked and ranked against each other on an extensive range of performance metrics that are introduced and explained below. To effectively assess the performance of these workflows on a variety of images, bespoke XCT datasets of quasi-unidirectional non-crimp glass fibre-reinforced polymers (UD-NCF GFRPs) and unidirectional quasi-unidirectional carbon-fibre reinforced polymers (UD CFRPs) were acquired at various resolution, contrasts, and noise levels.

4.3.5. Materials

Both the GFRP and the CFRP samples were supplied by Saertex GmBH. The GFRP comprises UD E-glass non-crimp fabric, embedded in epoxy using vacuum-assisted

resin transfer moulding (VARTM). The 0° angle UD bundles are stitched to the 90° angle backing bundles in a layup of [[0/90]/[90/0]$_s$]. The fibres have an average diameter of 20 µm.

The CFRP is manufactured by VARTM, and the backing bundles are made of glass fibres of diameter ~20 µm instead of carbon fibres, while UD carbon fibre has an average diameter of ~ 7 µm.

This material architecture , made of fibres aligned in two different directions of 0° and 45° was chosen as a trade-off between a fully unidirectional and an angle-orientated fibrous structure, helping in assessing the workflows' capability to analyse data omnidirectionally.

. The scans were undertaken on a Zeiss Versa 520 scanner at the Henry Moseley X-ray Imaging Facility. From each scan, cubical volume datasets were extracted in two formats, full-field scans, and sub-volumes. The sub-volumes of G1_Sub.tif, G2_Sub.tif, G3_Sub.tif and G4_Sub.tif correspond to the same material region-of-interest (RoI) and have been cropped accordingly. All of the image stacks were saved in 3D TIFF formats, and slices of the image stacks are shown in Figure 4.11, 4.12, and 4.13.

The scanning conditions are summarized in Table 4.3.

Scans	Exposure time	Voxel size	Sample type	Datasets	Physical size	Memory size	Remarks
G1	16s	1.5µm	Glass	G1 (~1000^3 voxels)	$1.01mm^3$	629.3 MB	**High-fidelity Reference**
				G1_Sub (300^3 voxels)	$0.43mm^3$	51.5 MB	
G2	4s	3µm	Glass	G2_Sub (145^3 voxels)	$0.43mm^3$	5.8 MB	Resolution variant
G3	20s	5.8µm	Glass	G3 (~1000^3 voxels)	$3.9mm^3$	589.2 MB	Resolution variant
				G3_Sub (76^3 voxels)	$0.43mm^3$	0.8 MB	
G4	2s	1.5µm	Glass	G4_Sub (300^3 voxels)	$0.43mm^3$	51.5 MB	Noise variant
C5	20s	1µm	Carbon	C5_Sub (350^3 voxels)	$0.35mm^3$	81.8 MB	Contrast variant

Table 4.3 Scanning conditions and associated metadata for each scan and the extracted datasets used to compare each of the workflows. The optical magnification of 4x, accelerating voltage of 80 kV and pixel depth of 16-bit were the same for all scans. There are three scans with variant resolution levels – G1, G2, and G3; two with variant noise levels – G1 and G4; two with variant contrast levels – G1 and C5. The C5 scan, on account of carbon fibre diameter (~7 µm) being approximately three times smaller than glass fibre (~17-21 µm), becomes a low contrast, and a low-resolution scan.

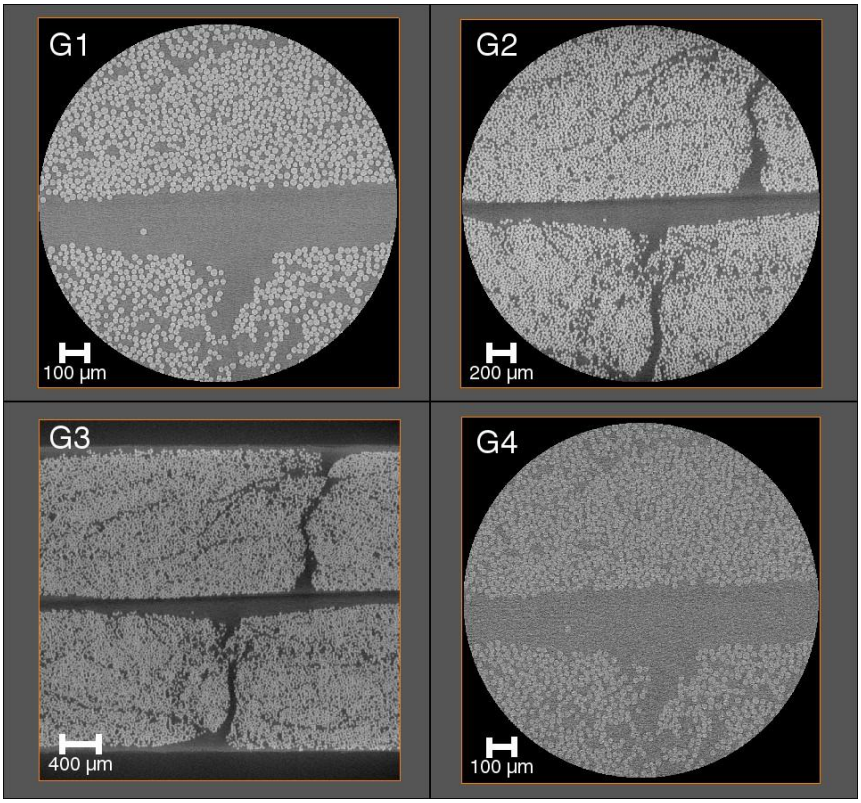

Figure 4.11 All the GFRP datasets acquired at different resolutions levels – G1, G2, G3 and variant noise levels – G1 and G4.

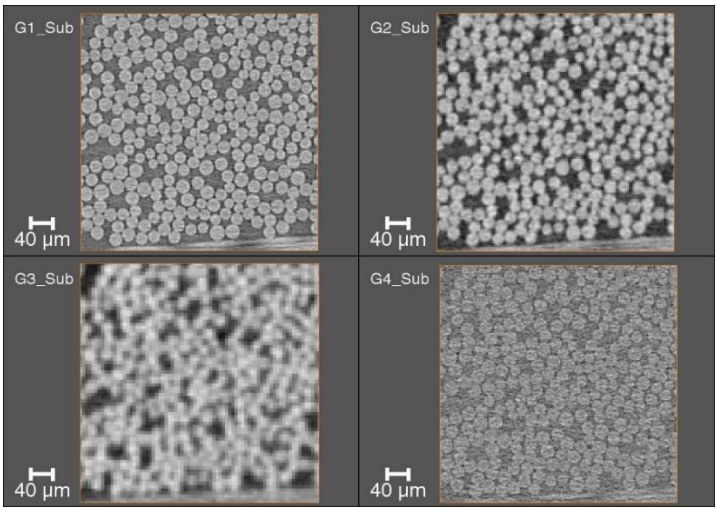

Figure 4.12 Subset datasets from the GFRP of the same region to keep the comparison consistent across variations. It contains mostly UD fibres with some backing fibres.

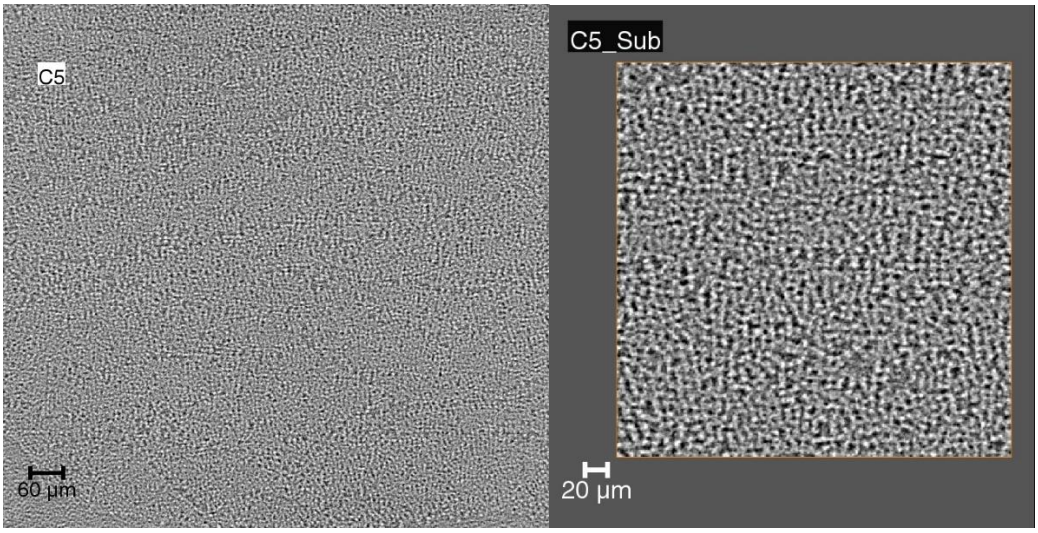

Figure 4.13 Dataset and its subset from a CFRP for a contrast variant comparison. The contrast is quite poor.

The performance on these metrics has been assessed on a system equipped with Windows 8 64-bit, i7 3.30GHz (12 CPUs), 64 GB RAM, and a GPU of NVIDIA GeForce GTX TITAN X with 48 GB MB of memory.

4.3.6. Performance metrics

Using these datasets acquired, the metrics on which the workflows are compared have been defined below.

1) **Information versatility**: This has been assessed for the type of information/data types/data formats that can be output through the workflows, including
   - labelled binary/ternary/multi-phase image data.
   - morphological parameters for individual fibres/matrix: fibre volume fraction, curvature, length, orientation information etc.

   The workflow that can handle and output multiple types of information is ranked higher.

2) **Computational time**: This has been assessed as the time each workflow takes to run on a representative volume of i) ~300 fibres at fibre scale (*G1_sub.tif*) and ii) 2-3 bundles at bundle scale (*G3.tif*).

   Workflows that take less time have been ranked higher.

3) **System requirements**: This is assessed as the minimum PC system requirements of RAM, GPU, and CPU as a performance metric. Methods with lower requirements are ranked higher.

4) **Parameter tuning**: This is assessed by the number of attempts the workflow takes to arrive at an optimum result. The workflows that require more attempts are ranked lower. This will be calculated at both the fibre scale (*G1_Sub.tif***)** and bundle scale (*G3.tif*).

5) **Scalability**: This is assessed by how much the computational time for the workflow goes up from sub-volume (*G1_Sub.tif*) to the full-scale data size (*G1.tif*). Workflows with less time increase are ranked higher.

6) **Performance on different spatial resolution levels**: This is assessed by the workflows' performance for fibre tracing and orientation calculation on three datasets with a pixel size of 1.5 µm (*G1_Sub.tif*), 3 µm (*G2_Sub.tif*), and 5.8 µm (*G3_Sub.tif*). Fibres were manually counted by a three-person panel by scrolling through the high-resolution G1_Sub.tif to confirm continuity and reduce user error, there were 311 fibres with at least more than half the cross-sectional blob in at least two XCT image slices. A higher number of true detections lead to a higher rank, with false detections counting as a penalty and resulting in a lower rank.

7) **Robustness to noise and contrast:** This has been assessed by the workflows' performance for fibre tracing on datasets which have been noised by lower exposure time (*G4_Sub.tif*) and have poorer contrast from CFRP (*C5_Sub.tif*), for fibre-tracing. A higher number of true detections lead to a higher rank, with false detections counting as a penalty and resulting in a lower rank.

8) **Accuracy in fibre-tracing:** The measure of the accuracy is defined here as the absence of any short-range curvature in fibre trajectory, as the UD fibres are straight and only exhibit long-range curvatures, short-range curvature or deviation from a straight line would indicate inaccurate tracing. As shown in Figure 4.14, this can be calculated as the value 'd' by averaging deviation 'c' over the whole fibre trajectory with 'n' centre-points. The fibre centre-points' coordinates have been extracted from each of the workflows for 4 fibres visually confirmed to be comparatively straighter, in the high-resolution dataset G1_Sub.tif. These centre-points were fit on a straight line via linear regression, and the average deviation d on both the XY plane and XZ plane as d_{XY} and d_{XZ} have been reported. Workflows with lower total deviation from a straight line, over the whole fibre trajectory are ranked higher.

$$\boldsymbol{d} = \frac{\sum_{i=1}^{n} c_i}{n} \quad \text{Equation 4.1}$$

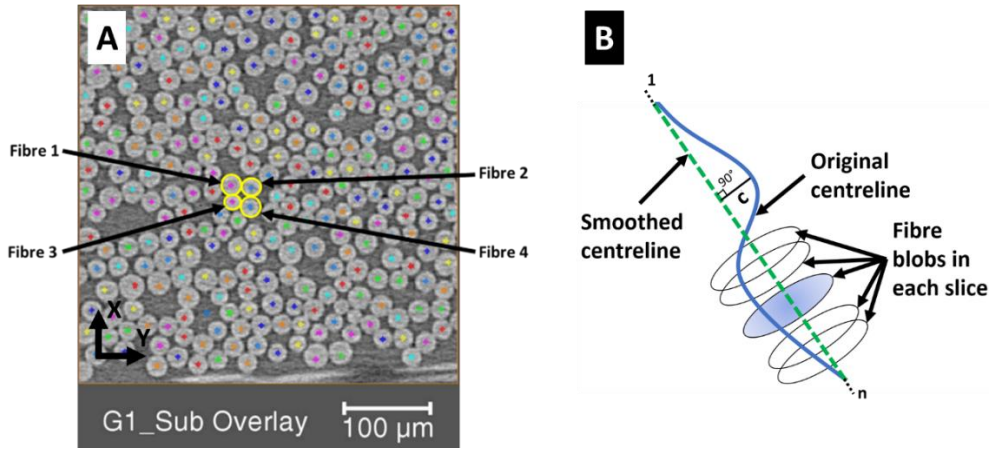

Figure 4.14 A) Four 'straighter' fibres from G1_Sub.tif that are selected for accuracy assessment. B) Short-range curvature of a fibre trajectory is calculated as the deviation from a straight line, and 'c' is the perpendicular distance between an actual fibre centre-point and its corresponding point on the fitted straight line.

9) Feasibility for modelling: This is evaluated on how suitable the segmentation method is as the basis for creating a model on the fibre level. This includes meshing the output labels, exporting the mesh, fibre orientation & bundle waviness and computing fibre volume fraction (local and global).

10) Financial cost: This has been assessed as the financial cost of using these workflows through proprietary software licenses. Workflows available through free software packages have been ranked higher.

4.4. A novel automated workflow involving machine learning to study damage progression of fibre-reinforced composites by time-lapse 3D x-ray tomography

The aim of this paper has been therefore to develop advanced methods of fibre tracing in Avizo [36–38] augmented by machine learning using Trainable Weka Segmentation (TWS) [39] from Fiji-ImageJ [40]. Our workflow out-performs other modern, but traditional machine learning methods, which rely on manual annotation and extremely accurate ground truth data for training the algorithms, by supplying automatically

generated high-fidelity training data, eliminating user-dependent errors. This workflow and its merits are demonstrated on an XCT time-lapse series dataset of a quasi-unidirectional glass-fibre reinforced polymer (GFRP), comprising four 3D image volumes at different stages of tension-tension fatigue damage.

The XCT data analysed in this paper is hosted on Zenodo [210] and has been described elsewhere as part of multiple fatigue studies [9], [58], [69], [211]. The materials and data acquisition process relating to this dataset is explained briefly below. Unfortunately, this method of damage detection fails on the datasets acquired from Chapter 5 and 6, as their spatial resolution is too low. This has been furthered explained later in Chapter 8, Section 8.4.2.

4.4.1. Materials

The material studied is a glass-fibre non-crimp quasi-unidirectional (UD) reinforced polymer composite having a fibre volume fraction, $V_f = 0.57$. The layup of the composite is $[b/biaxial,b/0,b/0]_s$ where "b" refers to the supporting ±45° and 90°off-axis backing layer and "0" to the 0° Z-direction UD fibre bundles, these are stitched to the backing layer using threads.

4.4.2. Fatigue testing

Butterfly-shaped specimens [73], which encourage gauge failure, were used for the fatigue testing being 410 mm in length and 15mm in width. The sample was cycled through a load-controlled tension-tension fatigue test on a universal servo-hydraulic Instron machine, with a stress ratio of R=0.1, load frequency of 5Hz, and a maximum strain of $\varepsilon_{max} = 1\%$. The stiffness degradation is continually monitored using a 25mm gauge extensometer. The test was interrupted for XCT scans at 4 stages, namely after

47300, 57300, 67300, and 77300 cycles. The sample failed soon after the last scan. Regions of interest were identified from hotspots resulting from in-situ infrared thermography.

4.4.3. X-ray tomography

The same region-of-interest (RoI) was CT scanned at each interruption in cycling, using a custom sample holder which allows repeatable sample placement and positioning. The 2000x2000 pixel detector was binned by a factor of 2, resulting in a 1000x1000 pixel image. With an effective pixel size of 3µm this resulted in a ~3mm field of view. The scanning parameters and associated metadata are listed below.

Source to sample distance	Detector to sample distance	Optical magnification	Pixel depth	Exposure time	Number of projections/ tomogram	Accelerating voltage	Effective pixel size
28 mm	35 mm	4x	16-bit	7s	4601	70 keV	3 µm

Table 4.4 XCT scanning parameters used to scan the sample on a Zeiss Versa 520 XCT scanner.

The time-lapse dataset was registered to the first 3D image volume of the sequence using ‘normalised mutual information’ and ‘rigid transformation’ in the ‘Register Images’ module in Avizo, as shown in Figure 4.15. This was for accurate comparison and study of the damage progress, only the common region overlapping across the four images was analysed.

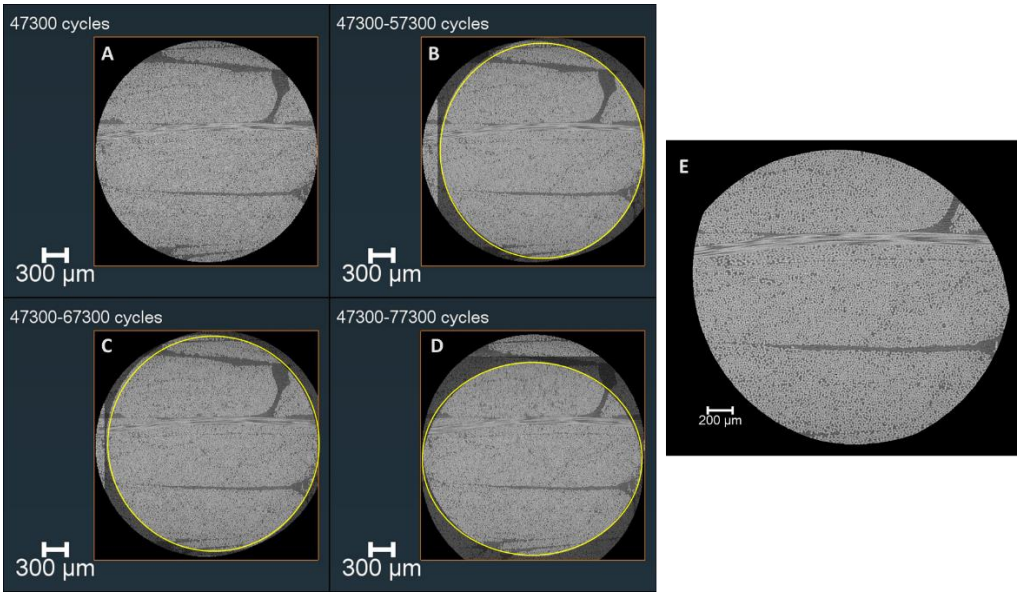

Figure 4.15 A) Slice from CT scan collected after 47,000 cycles and pairs of slices B) 57300 and 47300, C) 67300 and 47300, D) 77300 and 47300, registered in Avizo using the 'Register Images' wizard with the common regions marked in yellow boundary. Only the common overlapping region across all four images, shown in E) is analysed.

4.4.4. Automated fiber-break detection workflow

Our detection workflow is a two-step approach, where the fiber-breaks are initially detected in the 3D image volumes by tracing individual fibres and looking for intensity drops along the traced fibre centerlines. These intensity drops are labelled as fibre breaks and then fed into the machine learning classifier for training. The trained model can then be run on the same, or similar image data (subsequent time-lapse images), and the output given is an improved labelled result with fewer false positive and false negative detections. These final labelled fibre-breaks can then be analysed in multiple ways including statistical analyses of fibre-break density and localized clustering.

This workflow can be run on a series of time-lapse images with the click of a button, and it outputs the identified fibre breaks and related statistics on all the serial images, giving a detailed and an 'at-a-glance' insight into the damage progression, from both a qualitative and quantitative aspect. This scheme is shown in Figure 4.16 and Figure 4.17.

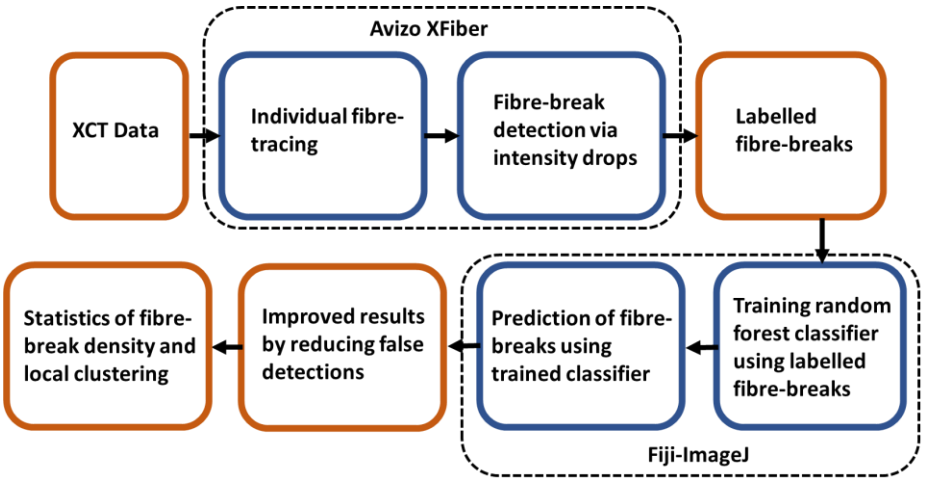

Figure 4.16 The two-step fibre fracture labelling workflow involving two serial steps whereby deep learning improves and updates the first result.

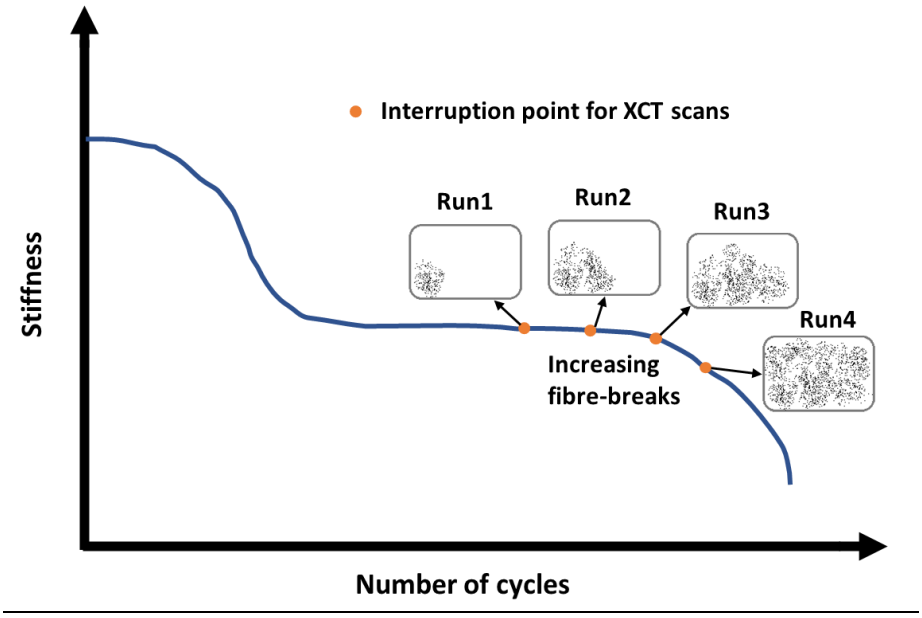

Figure 4.17 The workflow is run multiple times on the whole time-lapse series where statistics of fibre-breaks and 'at-a-glance' statistics are automatically generated. This damage progression can be related to the change in mechanical performance including a drop in stiffness.

Both stages of the workflow are explained in detail below.

Fibre-tracing and initial fibre break detection (FTBD)

A module enabling individual fibre tracing is available in Avizo through its XFiber extension, where a fibre is detected by matching the grayscale features in the 3D image against a user-defined parametric cylindrical template, via normalized cross-correlation [195], [212]. The size of the cylinder template must be similar to the fibres in our case (see figure 4.18 a). The results of the cylinder correlation are two images: a correlation field (figure 4b) and an orientation field (figure 4.18 c). The correlation field stores the maximum correlation value, while the orientation field stores the orientation for which the correlation value is maximum, for each pixel. These two fields are then thresholded on minimum correlation values for which the fibre centreline tracing can start and continue. Once the fibre centre-lines are traced as shown in figure 4.18 d, the grayscale values are sampled along across these centre-lines searching for a drop in grayscale intensity below a user-calculated value 'T'. These drops in intensity values are labelled as fibre breaks, as shown in Figure 4.19. This procedure, called fibre tracing break detection (FTBD), makes the first estimates of the fibre fracture locations. This result is used as the basis for the next Weka classification step of the automated workflow.

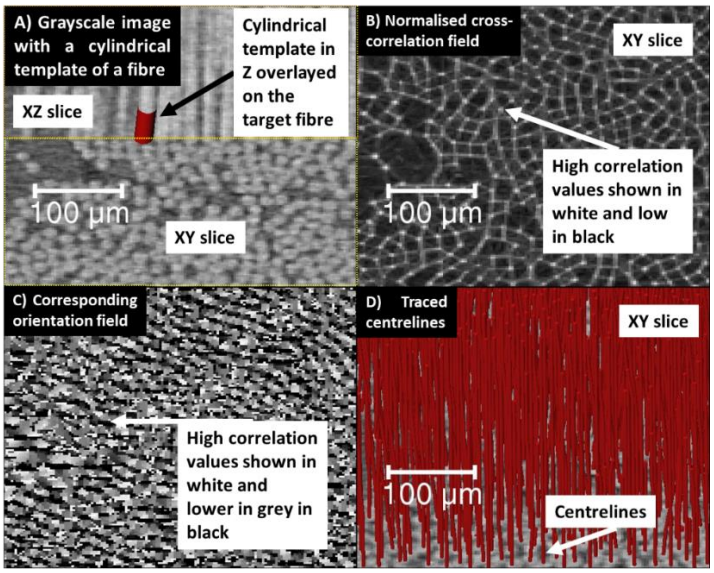

Figure 4.18 XFiber can analyse a greyscale image by cross-correlating it with a cylindrical template specified by the user. This results in a correlation field and an orientation field. By setting a threshold, on these fields, centre-points of fibres can be generated, which are then connected using a search cone to create a single, traced fibre centre-line.

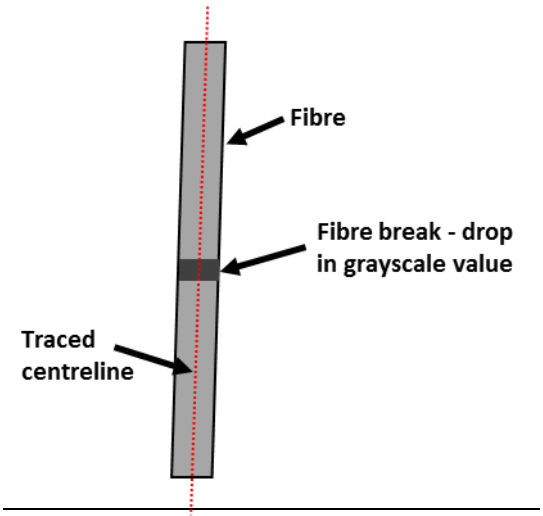

Figure 4.19 The fibre break is detected by sampling the grayscale values along the unique fibre centreline, a value below the user-calculated threshold ‘T’, is detected and labelled as a fibre break. The threshold 'T’ can be easily calculated by finding the grayscale values that correspond to a fibre break, using the probe tools and/or line-profiling a few cracks in Avizo/Fiji.

Weka classification in Fiji using FTBD for training

The FTBD result is used in the 'Trainable Weka Segmentation' (TWS) module available in Fiji-ImageJ to train the classifier. The classifier used in this study is a 'FastRandomForest' type [213]. This is a supervised machine learning algorithm that grows and combines multiple decision trees for classification. This is advantageous over single decision trees as multiple uncorrelated models (individual trees) perform better when grouped [205], [214]. This process which forms the second part of the damage detection workflow uses the following steps:

1) Both the grayscale file and the corresponding FTBD result are read into Fiji-ImageJ.
2) The grayscale file that needs to be analysed is opened in the TWS window which contains separate classes for each type of label, in this case, it is two – fibre breaks, and the background (containing fibres, matrix etc.)
3) The fibre breaks in the FTBD result are transferred as regions of interest (RoI) to an 'ROI Manager' using a native 'Analyse Particles' routine.
4) From the ROI Manager, the RoIs are transferred as 'class 1' (in red) to the TWS automatically using an ImageJ macro script, described in the Appendix. The background can be minimally annotated by manually adding a few annotations to 'class 2' (in green).
5) The segmentation settings, which include the type of training features and the type of classifier (FastRandomForest in this study) can be selected. Ideally, it is sensible to use a smaller but representative sub-volume to optimise the settings in multiple quick training attempts.

6) The classifier is then trained using the selected settings and the segmentation result is generated. If the result of the classification/prediction of fibre breaks looks satisfactory, the classifier can be saved.

Once the classifier has been trained satisfactorily and saved, this classifier model, saved as a .arff file, can be imported and run on a batch of volumes automatically, seamlessly segmenting fibre breaks. This can be done using a Beanshell script [215], described in the Appendix.

4.5. Summary of chapter

All the methods, including the correlative time-lapse workflow, image analysis methods for fibre composites, and the automated damage detection workflow have been explained.

The next chapters are the four manuscripts including one paper that has been published.

5. Observing the evolution of fatigue damage and associated strain fields in a correlative, multiscale 3D time-lapse study of quasi-unidirectional glass fibre composites

Author contribution statement

Anuj Prajapati: Conceptualization, Methodology, Data acquisition, Software, Validation, Writing – Original Draft, Writing – Review and Editing.

Ali Chirazi: Methodology, Software, Validation, Writing – Review and Editing.

Lars P Mikkelsen: Methodology, Validation, Supervision, Writing – Review and Editing.

Timothy Burnett: Methodology, Writing – Review and Editing, Supervision, Funding acquisition.

Philip Withers: Resources, Methodology, Writing – Review and Editing, Supervision, Funding acquisition.

Observing the evolution of fatigue damage and associated strain fields in a correlative, multiscale 3D time-lapse study of quasi-unidirectional glass fibre composites

Anuj Prajapati[1], Ali Chirazi[2], Lars P. Mikkelsen[3], Timothy Burnett[1] and Philip J. Withers[1]

[1] Henry Royce Institute, Department of Materials, The University of Manchester, U.K.

[2] Visualization Sciences Group, Thermo Fisher Scientific, Bordeaux, France.

[3] Composite Mechanics and Structures, DTU Wind Energy, Denmark

p.j.withers@manchester.ac.uk

Abstract. This research is focused on studying the tension-tension fatigue behaviour of a unidirectional (UD) glass-fibre wind turbine composite. The damage features, their progression and the associated strain fields are tracked in a representative volume by employing a novel correlative approach bringing together x-ray computed tomography (XCT) and digital image correlation (DIC). The focus is on studying ex situ the evolution of damage features (fibre breaks and micro cracks) in an interrupted time-lapse manner. The major drops in stiffness are correlated to the number and location of the damage features in the bulk (XCT) and at the surface (DIC). Results from XCT highlight a localized cluster of fibre breaks and matrix cracks near backing bundles along with axial macro-cracks, while DIC shows that the backing bundles cause regions of higher strain. This highlights the relation between the damage features and strain localisation and their effect on the progressive degradation in stiffness during high cycle fatigue (HCF) cycling.

6.1. Introduction

With the global call for increasing investment in, and exploitation of, renewable resources owing to environmental damage manifest as climate change, wind energy remains a strong candidate for the shift of power generation from fossil fuel-based resources to renewable and more environmentally sustainable ones [216]. Over recent years there has been a strong increase in the installation and production capacity of wind farms worldwide [217]. As the wind power generated by a turbine is proportional to the swept area by the rotor blades, there is a clear drive towards longer, larger and thus heavier blades, increasing the strength and fatigue life requirements.

The spar caps, which are the main load-bearing components in the blades, are made of quasi-unidirectional glass and carbon fibre reinforced composites, which experience a high-cycle fatigue (HCF) loading regime, having a service life as high as 30 years encompassing 10^8-10^9 cycles [218]. These materials are selected because of their optimum balance between cost, high stiffness-weight ratio, fatigue resistance and design flexibility. Furthermore considerable performance improvements have been achieved for such composites over the last decade increasing their range of applications [219].

The blades are subjected to repeat edge-wise and flap-wise oscillating loading from the weight plus the centrifugal rotation and wind dynamics respectively, which essentially engage the load bearing glass fiber composites in a fatigue regime.

As a result of the fatigue damage accumulated the blade gradually loses its working stiffness which in extreme cases can even lead to collision with the supporting tower or even catastrophic failure. Consequently, the focus of this study is to understand how loads representative of such cycles affect the mechanical properties over the service life, observing the effect it has on the microstructure and how that builds up over time to affect the macro mechanical response of these materials. This will help us isolate key factors in the microstructure which are critical to this behavior and help us optimize them to improve the mechanical response, both in terms of extending the safe service life and achieving a higher load bearing capacity.

The fatigue behavior of unidirectional composites has been an active area of research since the 70s, inspired initially by the metal fatigue experience, but then slowly moving to accommodate other important aspects of the microstructure, especially the interfacial phenomena between the fibers and the matrix [14], [220]. 'Fatigue life diagrams' [221] can be used to lay out the progressive and non-

progressive governing mechanisms in the fatigue regime, thereby helping to identify which zones of distinct damage features in the diagram are critical to failure. In general, the dominant damage features on the micro scale include, among others, fibre breaks, fibre-matrix debonding, matrix yielding and cracking, and transverse ply cracking. This leads to complex modes of damage progression which are challenging to predict accurately, especially for different layups. Quasi-unidirectional (UD) non-crimp composites offer excellent unidirectional strength and stiffness and are widely used in wind turbine applications. They have the majority of fibres running in the load-bearing axis direction clustered in bundles (tows), while a small number of backing fibres run in off-axis directions. The UD bundles are tied to the backing bundles by means of stitching threads to aid integrity during laying up and manufacturing.

It has been shown [57] that in the early and intermediate stages of fatigue life, the drop in stiffness can be related to the crack densities in the matrix for materials with unidirectional fibre bundles with backing layers at ±45° and 90°. The final stage near failure involving 0° fibre rupture exhibits a rather stochastic behavior, believed to be due to stress concentrations near the tip of the intra ply matrix cracks.

It has been proposed [9], [60] that the damage starts in, and near, the off-axis bundles, especially in regions which are in crossover between the UD and backing bundles, as matrix cracks and fibre breaks, and then progress towards the thickness in a diffuse manner [9], [73]. As the progression is complex and essentially stochastic in the microstructure, it is difficult to predict accurately and reliably.

Recently, combined advanced imaging and characterization methods at the microscale have been put forward which are delivering new insights into the classic initiation, propagation and failure by damage evolution [189].These include not only imaging, but other critical complementary pieces of information regarding stress-

strain fields, morphology and chemistry, among others. On this front, x-ray computed tomography (XCT) has been proven particularly successful for investigating this microscale behavior since this is the scale of the onset of sensible damage, and this technique can provide 3D information non-destructively [75], [149]. It can provide key insights to help resolve the complex morphology and sequencing of the damage by monitoring the damage in UD composites in a time-lapse manner during fatigue [9], [60].

Digital image correlation (DIC) has been developed [222] around the 70's in and has been used to investigate deformation in fibre composites as early as the 90's [223]. DIC involves the tracking of a speckle pattern on the sample specimen surface to infer the displacement and associated strain fields.

In this paper these techniques are used in a complementary workflow to the study the fatigue behavior of UD composites across varying length scales.

6.2. Materials and Experimental Methods

6.2.1. Materials systems

The materials have been supplied by Saertex GmBH, comprising UD E-glass fibre bundles stitched to backing bundles (90º) and impregnated in epoxy using vacuum-assisted resin transfer molding, with a layup of $[[0/90]/[90/0]_s]$ with the backing bundles adjacent to each other and none in the center.

Butterfly geometry fatigue test specimens of length 284mm were cut out using waterjet with a parallel sided gauge length of 44 mm, as shown in Fig. 6.1.

The smallest width at the gauge was 10mm wide, with the plate thickness of 3.8 mm. End tabs of length 120mm were stuck on to avoid crushing the ends, tapered over a length of 60mm, to reduce stress concentrations.

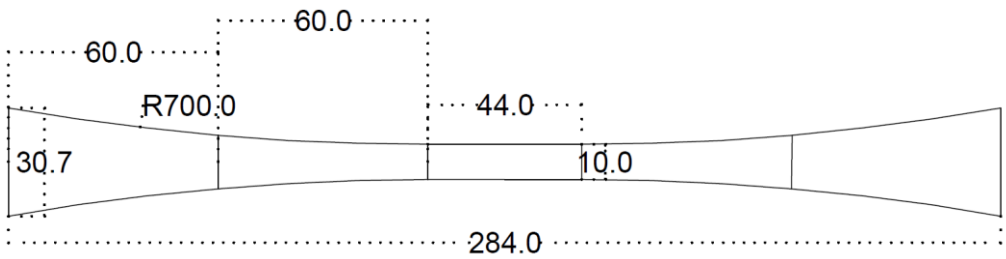

Figure 5.1 Sample specimen cut out in a butterfly geometry. All the dimensions are in mm.

6.2.2. Experimental workflow

A workflow involving time-lapse x-ray CT and digital image correlation was used to identify the progression of damaged regions and their associated strain levels through the fatigue test. Fig. 6.2 shows the characterization workflow aligned with the observed degradation in stiffness degradation. The central focus is to investigate the strain distribution and progression of damage features over the whole gauge as the number of cycles increase. Region I describes the initial drop in stiffness upon fatigue cycling, followed by stable response in region II, followed by a steep decrease in stage III just before failure. The fatigue tests were interrupted for DIC (in-situ) and CT (ex-situ) at 3 intermediate stages in addition to the first stage in the timeline. The region of interest for CT scanning were chosen from the strain hotspots identified from the DIC images. The sample was not tested to failure but rather fatigue cycling was stopped when around 5% stiffness was lost.

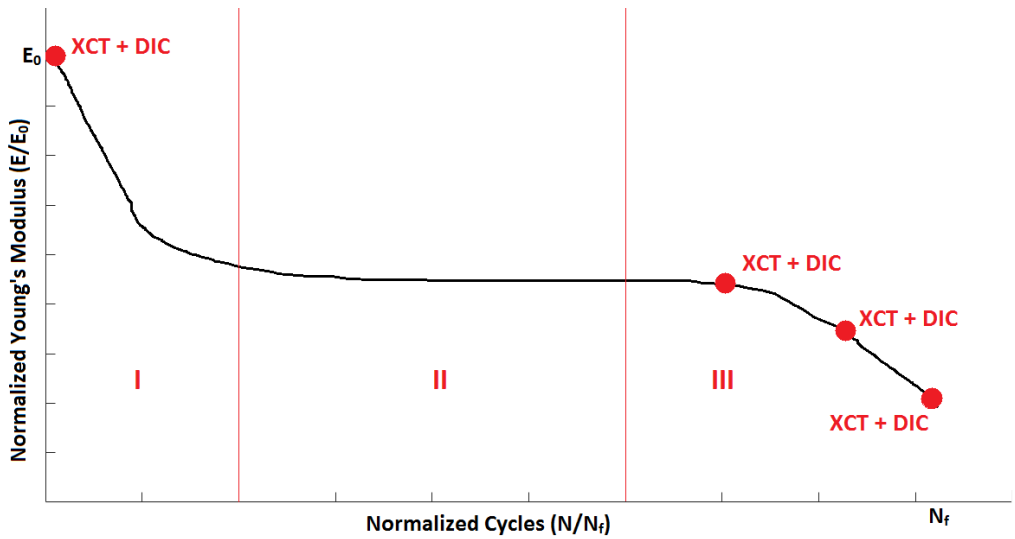

Figure 5.2 Schematic showing the experimental workflow scheduled around the degradation in stiffness, E, and number of cycles, N. The initial stiffness is E_0 and total number of cycles is N_f.

6.2.3. Mechanical testing

The fatigue tests were carried on an Instron Servohydraulic 8802 with a 100kN load cell at maximum strain of 1.0% with a stress ratio of R=0.1, in load control with a sinusoidal waveform and 4 Hz to avoid self- heating.

The strain was monitored with both a clip-on extensometer (5mm extension/12.5 mm gauge). The stiffness was continuously tracked while the DIC images were acquired at a cycle frequency of 0.125 Hz to minimize blurring and the imaging frequency of 10 frames per second, over the whole gauge length of 44mm, for a full single cycle at all the 4 stages. The sample gauge was 'speckled' using a black and white spray paint, to obtain sufficient contrast between the black and white points for correlation. LaVision Strainmaster systems were used both in terms of the software and hardware for the DIC acquisition and processing.

6.2.4. X-ray computed tomography

XCT experiments were carried out on a Zeiss Xradia Versa 520 scanner with the sample mounted on a custom-made holder fixtured to enable it to be mounted as close

in the identical location for each scan in the sequence. As has been demonstrated from [9], [60], the damage starts to occur near the backing bundles, so a RoI (region of interest) containing a backing bundle was scanned. The projections were not binned. The scan settings are summarized in Table 6.1.

Table 5.1 X-ray CT scan conditions used on the Zeiss Versa 520.

Source to sample distance	Detector to sample distance	Optical magnification	Pixel range	Exposure time	Number of projections/ tomogram	Accelerating voltage	Pixel size
42 mm	150 mm	4x	16-bit	20s	3201	70kV	0.7mm

6.3. Results and discussion

The degradation in stiffness over time is shown in Fig. 6.3, with the key points marked. The degradation in stiffness can be divided into 3 regions in accord with [9], [73], [224]. Region I includes the initial stiffness drop, while Region II relates to the period over which the stiffness remains level. Region III leads up to final degradation and the ensuing failure. The curve has been piecewise smoothened with a 4th degree polynomial to filter out the heavy load cell related noise in the stiffness calculations. The co-ordinate system for the sample specimen as: x in width, y in thickness and z in axial length.

As mentioned, the test was interrupted at 3 points (for XCT acquisition) in the loading timeline, at points 1A and 2A and 3A. There is a slight decrease in the modulus after reinstating the test after scans 1 and 2 marked by points 1B and 2B. This behavior has been observed previously [9] and can be attributed to the re-calibration and the sensitivity of the extensometer between the interrupted steps. There is no strong reason

to believe that the low level of x-rays exposure degrades the mechanical properties of the composite, in fact x-ray exposure has been found to increase the matrix stiffness elsewhere [225].

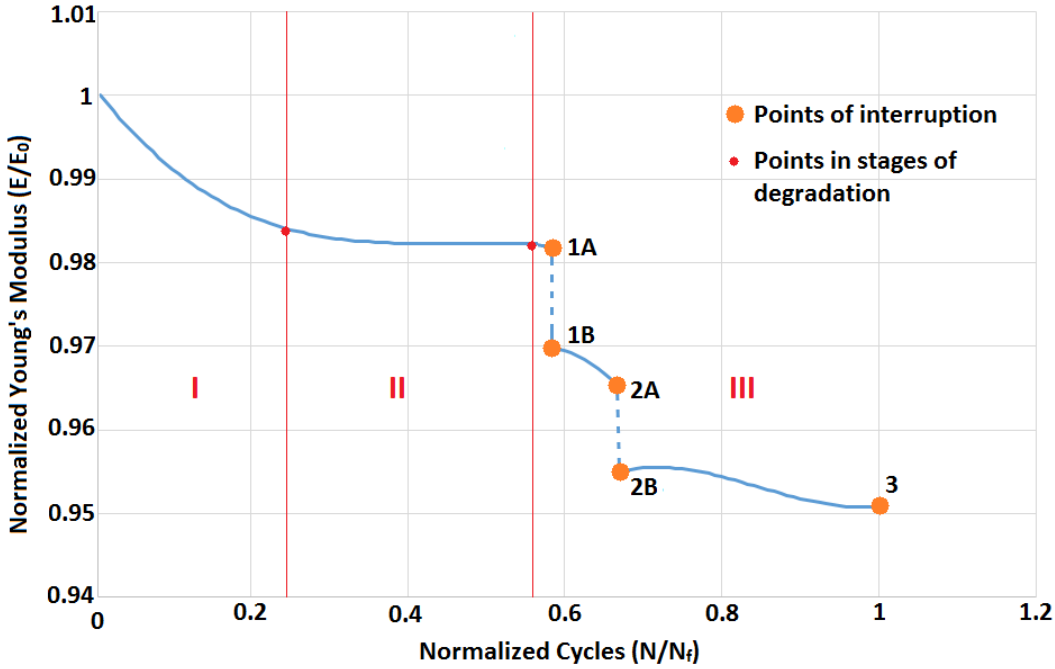

Figure 5.3 Stiffness degradation curve during fatigue cycling with points demarcating interruption for characterization. Region I and III show steady falls in stiffness, while the stiffness is stable during region II. N_f=120,000 cycles

From the DIC maps in Fig. 6.4 we can clearly see hotspot regions that experience higher strain than the maximum gross strain of 1% imparted on the gauge. This is attributed to the presence of the 90° backing bundles running across the material, as can be confirmed in the CT volumes. At hotspots, the strain is as high as 2% which is very close to the tensile failure strain of the plate (2.25%), individual fibres (2.7%) and the matrix (4%). The regions at the periphery, have been masked out for DIC analysis because they go in and out of the field of view invalidating DIC analysis. The linear hotspots in strain (marked by rectangles in Fig. 4) correspond to the location of the backing bundles, while the point hotspots (marked by purple arrows in Fig. 4) are

regions of crossover where the difference in waviness between UD and matrix is higher, which leads to coupled regions of higher and lower compliance.

Not only do the backing bundles perturb the 'homogeneity' of the microstructure, they also cause the UD bundles to be slightly wavy in the regions of the crossover, which leads to bending and a change in local orientation. This may be why some of the glass fibres fracture locally giving rise to other mixed mode damage modes of debonding, matrix cracking and transverse and longitudinal cracks.

As witnessed previously [9], the damage starts predominantly near the region of crossover between the UD bundles and the backing bundles, although in the previous work it was difficult to resolve any matrix cracks due to reasons of scale and resolution. The mixed mode damage propagation is mostly localized in clusters as seen in Fig. 6.5. Individual fibre breaks such as that seen in Fig. 6.6 and the associated debonding changes the local stress state leading to strain concentrations and breaks in neighbouring fibres, as discussed elsewhere [226].

Despite this, lack of evidence for progressive damage accumulation a transverse-longitudinal (YZ) macro-crack (Fig. 6.7) already present in the apparently pristine sample did undergo progressive damage evolution, more so in terms of opening up the crack, combined with more matrix cracking at higher cycles. The width of the macro-crack appears to increase progressively, although there has been no significant progression observed in the length of the crack, which seems to be arrested from the first XCT scan. Although it is probably due to the machining of the specimens and/or manufacturing and/or the first cycle over which the DIC strain map was collected, it is noteworthy that it is arrested at the backing bundle.

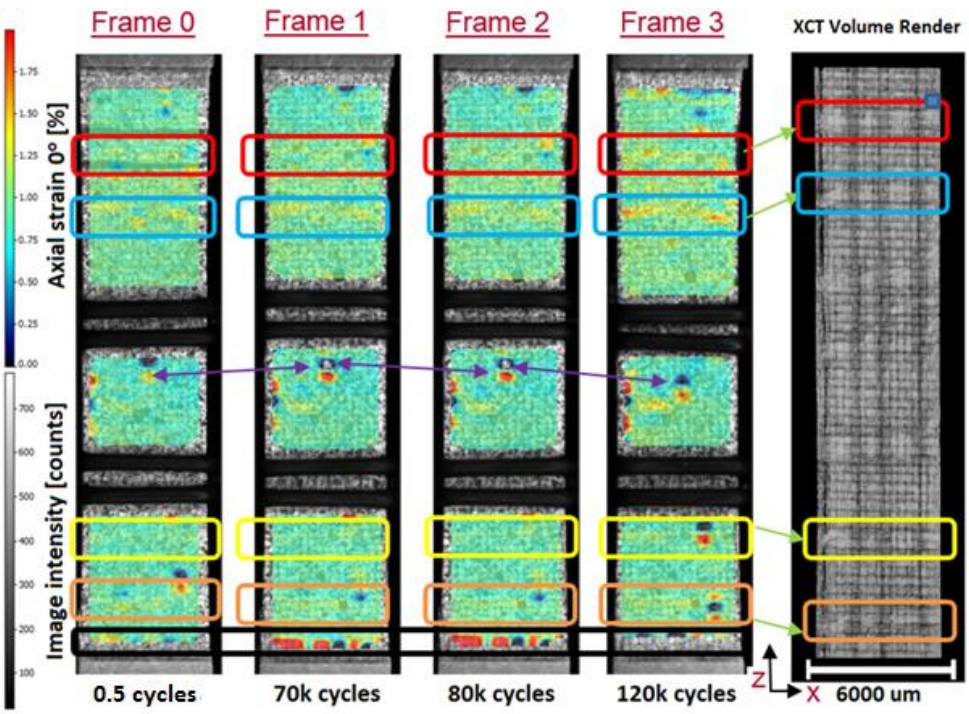

Figure 5.4 DIC maps (between images at 0% strain and peak strain of 1%) showing hotspots in strain broadly correlated with the location of the backing bundles in the XCT volume render. The blue square near the top of the XCT volume shows the region of interest for corresponding XCT scans. The two pair of black bands on each map are O-rings from the extensometer. It should be noted that the alignment of the 90° bundles (red, blue, yellow and orange) are not precisely correlated with the hotspots, because the backing bundles in the bulk (not shown here) are not at the same z position as the ones on the surface shown here. The black box highlights regions which did not correlate correctly due edge effects.

The x-ray CT scans do not appear to show clear evidence of classical progressive damage; instead, damage clusters originated and progressed only after the third scan. This does not definitely rule out the presence of damage in the microstructure prior to the third scan, as the first cracks in the backing bundles have previously been observed after as little as 480 cycles [9]. Indeed it is highly likely that damage has occurred in other regions of the test-piece which were not CT scanned in accordance with the drop in stiffness, as has been found in a number of studies [9], [57], [218].

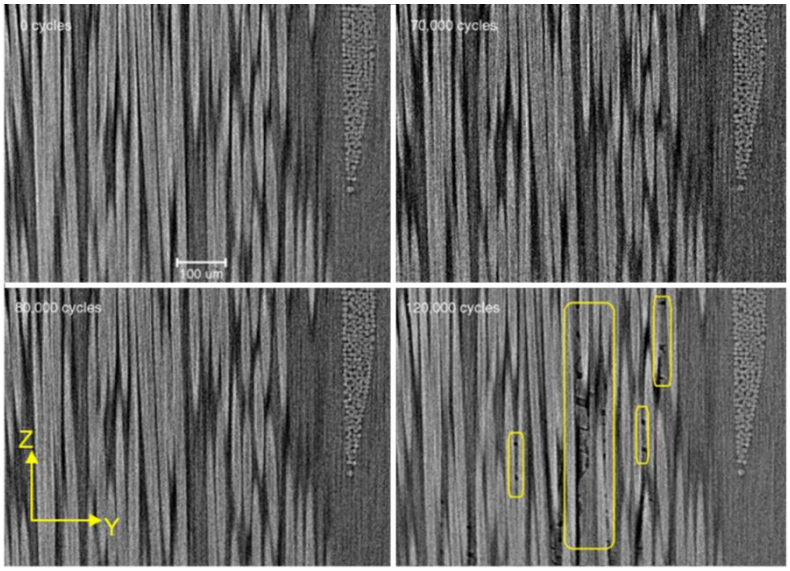

Figure 5.5 A virtual YZ section taken from the region of interest CT at different stages in the fatigue cycling showing a localized damage cluster (boxed) involving matrix cracking and debonding, located in proximity to the backing bundles.

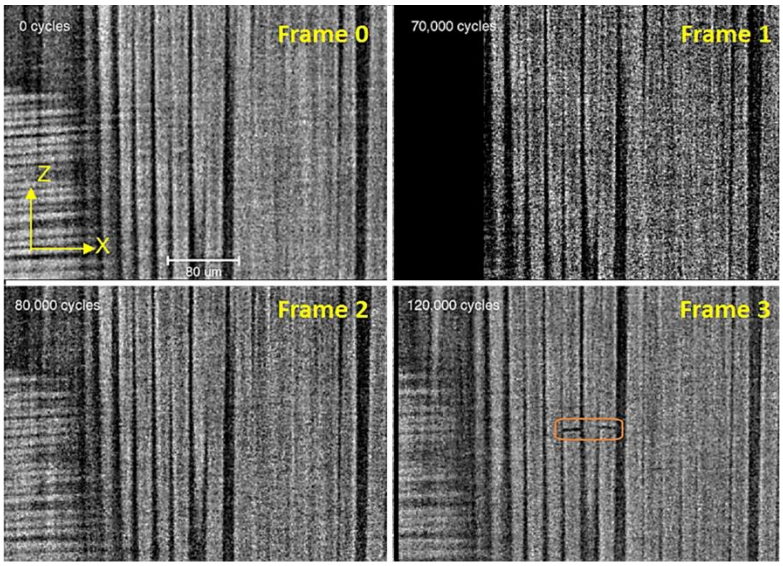

Figure 5.6 Virtual ZX section for the 4 fatigue stages showing neighbouring fibre breaks (boxed) in regions of crossover between the UD bundle and the 90° backing bundles.

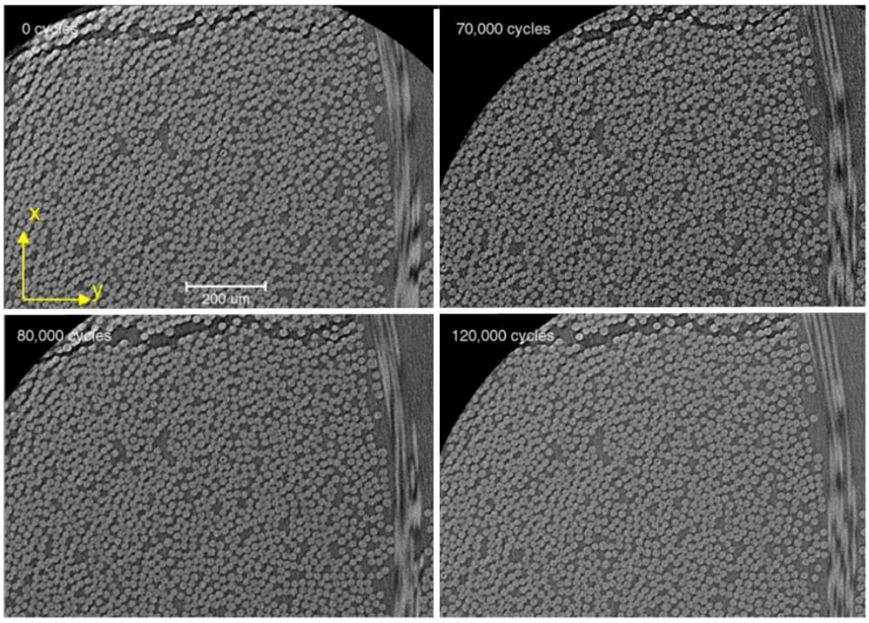

Figure 5.7 Virtual YX cross-section for the 4 fatigue stages showing longitudinal a macro-cracks running through the periphery of the scanned CT volume, progressively extending and opening throughout the fatigue regime but being arrested at the backing bundle.

6.4. Conclusions

This study has shown that the strain field that develops in UD composite during fatigue loading is affected by the presence of the backing bundles. By correlating the strain field maps as a function of the number of fatigue samples with ex situ x-ray CT imaging of the composite it was possible to correlate the resulting stress amplification with localized damage initiation and ultimately to damage propagation and final failure. Advantages of this correlative method include the ability to directly relate hotspots in strain concentration with the underlying microstructure as a function of fatigue life to study the progress of damage accumulation. In this case most of the damage was not observed until just prior to fatigue failure. Next steps of this work will be to focus on designing experimental workflows to follow damage evolution at the microscale and combine it with digital volume correlation (DVC) to study the stress amplification in 3D.

Acknowledgements

This study was funded by EU Horizon 2020 MSCA Innovative Training Network 'MUMMERING' Grant Number 765604. We thank Stuart Morse from The University of Manchester for help in fatigue testing. Support from Saertex for material supply is gladly acknowledged. Access to Thermo Fisher Scientific Avizo™ is acknowledged. Beamtime was kindly provided by the Henry Moseley X-ray Imaging Facility (HMXIF), which was established through EPSRC grants EP/F007906/1, EP/ I02249X/1 and EP/F028431/1. HMXIF is a part of the Henry Royce Institute for Advanced Materials, established through EPSRC grants EP/ R00661X/1, EP/P025498/1 and EP/P025021/1. PJW acknowledges a European Research Council Advanced Grant Correl-CT No. 695638.

5. Time-lapse correlative study of the fatigue damage evolution and strain fields in quasi-unidirectional glass fibre composites using three-dimensional imaging

Author contribution statement

Anuj Prajapati: Conceptualization, Methodology, Data acquisition, Software, Validation, Writing – Original Draft, Writing – Review and Editing.

Robert Auenhammer: Methodology, Software, Validation, Writing – Original Draft, Writing – Review and Editing. **Stuart Morse:** Methodology, Software, Data acquisition Validation.

Daniel Lichau: Methodology, Software, Validation, Writing – Review and Editing.

Ali Chirazi: Methodology, Software, Validation, Writing – Review and Editing.

Lars P Mikkelsen: Methodology, Validation, Supervision, Writing – Review and Editing.

Timothy Burnett: Methodology, Writing – Review and Editing, Supervision, Funding acquisition.

Philip Withers: Resources, Methodology, Writing – Review and Editing, Supervision, Funding acquisition.

Time-lapse correlative study of the fatigue damage evolution and strain fields in quasi-unidirectional glass fibre composites using three-dimensional imaging

Anuj Prajapati[1,3], Robert M. Auenhammer[4,5], Stuart Morse[2], Ali Chirazi[3], Daniel Lichau[3], Lars P. Mikkelsen[4], Timothy Burnett[1] and Philip J. Withers[1]

[1] Henry Royce Institute, Department of Materials, The University of Manchester, M13 9PL, United Kingdom

[2] Department of Materials, The University of Manchester, M13 9PL, United Kingdom

[3] Visualization Sciences Group, Thermo Fisher Scientific, Bât E2, 33800 Bordeaux, France

[4] Composite Materials, DTU Wind Energy, Technical University of Denmark, DK-4000, Roskilde, Denmark

[5] Department of Industrial and Materials Science, Chalmers University of Technology, SE-41296, Göteborg, Sweden

p.j.withers@manchester.ac.uk

Abstract. Fatigue in unidirectional glass-fibre composites (UD GFRP), used as the main load-carrying components in wind-turbine blades, leads to stiffness degradation and poor blade performance. To improve our understanding of the fatigue damage mechanisms, we investigate tensile fatigue of a UD GFRP using a 3D time-lapse, correlative characterisation workflow involving x-ray computed tomography (XCT), digital image and volume correlation (DIC-DVC), image-based modelling and serial-section electron microscopy. A large volume (10mm x 6mm x 3.7mm) is studied by high resolution helical scanning. It is found that damage initiated independently on the surface and in the bulk. Surface voids caused matrix cracking, progressing into off-axis cracks in backing bundles (BB). These off-axis cracks propagate into the UD bundles, leading to high deformation observed as strain localization in DIC-DVC results. The nearby UD fibre failure resulted in localised high compliance, leading to bulk UD and BB fibre failures and a stiffness loss. Micro-notches led to cracking in resin-rich regions, progressing into near-surface longitudinal splits. Some splitting cracks get deflected by the BB and lead to debonding of UD bundles and BB. In the bulk, UD fibre breaks originated close to BB and proceeded more in width than in thickness due to the reduction of BB-induced waviness in width. These clustered UD fibre breaks led to matrix cracks in resin-rich regions, likely initiating neighbouring off-axis cracks and UD fibre breaks, as observed on the surface. UD fibres away from the backing bundle exhibited late-stage failure due to the absence of waviness. DVC results show "banding" of strain concentrations across width in higher compliance resin-rich regions that had backing bundles running in the same length. This is corroborated with the damaged regions and higher stresses observed predominantly in these bands. Agreement between calculated 3D strain maps, predicted stress from the tensile model, and confirmed damage from XCT, corroborates the efficacy of the tensile model and the accuracy of DVC strain maps. At some point, the surface and bulk damage likely joined up with larger splits to progress further and eventually lead to complete failure. Together, all relevant damage mechanisms of fibre breaks, matrix cracks, delamination, associated fibre debonding and their complex interaction are identified which leads to stiffness degradation. This information can be used to improve the material architecture for more fatigue-resistant composites.

5.1. Introduction

Wind power is a key technology in the global shift towards renewable energy resources, driven both by climate change and the recent realisation of the need for greater energy sovereignty. This is evidenced by the rapid rise in completed and proposed wind power installations year-on-year, both offshore and onshore worldwide [2]. To remain competitive, the ratio of power generation to capital and running costs needs to keep increasing. One popular solution is to make the wind blades larger, as the power generated is proportional to the swept area of the blades [5]. This results in the production of larger and heavier blades leading to a demand for stronger, lighter weight, and more fatigue-resistant materials. [19]. These materials are selected because of their optimum balance between cost, high stiffness-weight ratio, fatigue resistance and design flexibility. Furthermore, considerable performance improvements have been achieved for fibre-reinforced composites over the last decade increasing their range of applications [219].

The primary load-bearing components in the blades are spar caps. These are made of quasi-unidirectional glass and carbon fibre-reinforced composites, undergoing a high-cycle fatigue (HCF) loading regime. The service life is as high as 30 years corresponding to 10^8-10^9 load cycles [7]. The edge-wise loads and flap-wise loads present a mixed loading regime of tension and compression, where the latter undergoes tension-tension loading for the wind-facing direction of the blade [7].

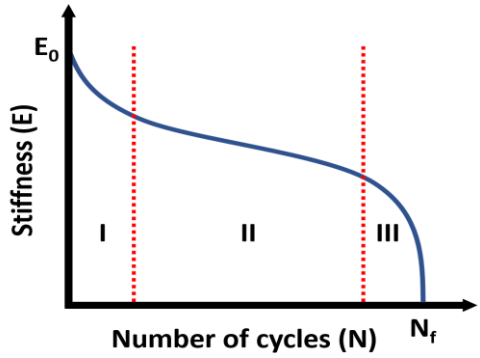

Figure 5.1 Degradation from E_0 (initial stiffness) in three stages during HCF of UD GFRP. It includes I: first steep drop which can be ~1%, II: second stable degradation which can be ~5%, and III third steep drop just before final failure, where the total loss can be >10% before failure (total N_f cycles) [9], [73].

As the fatigue damage progresses, the blade gradually loses its stiffness in three broadly defined stages [9], [73], namely, I: initial drop, II: stable degradation, and the III: final drop before failure, as shown in Figure 5.1. This stiffness degradation in some cases can lead to a blade colliding with the supporting tower or even lead to catastrophic failure[9]. As a result, design against fatigue is a primary factor in developing such materials. This study focuses on understanding the fatigue behaviour of this material, including the evolution of damage and the relation to the key microstructural features and weak links, and how that affects the stiffness degradation. 3D strain and stress fields are computed using DVC and tensile modelling respectively, to assess their relation to the observed damage. Identifying key regions and associated factors in the microstructure responsible for this behaviour can help us improve the overall mechanical response, resulting in the extension of the reliable service life and load-bearing capacity.

5.1.1. Fatigue damage in UD-NCF composites

Fatigue damage in composites has been researched for decades, starting in the 70s, when most of the preliminary knowledge was based on metal fatigue [221]. Cross-ply

and quasi-isotropic carbon fibre composites were investigated for their stiffness degradation in the 1980s, mostly looking at the off-axis cracks and subsequent modes of matrix cracking, fibre/matrix debonding, and such, where UD fibre breaks were not the focus. Several other studies during the 2000s focused on similar initiation and progression of damage [57], [227], [228]. As we know, the tension-tension fatigue damage in UD composites is complex and progressive where different modes of damage including fibre breaks, matrix cracking, longitudinal splitting, and transverse cracking, among others, interact in a complicated and time-dependent manner. Damage progression is reflected in the stiffness degradation [7], [9], [21], [59], [73], [229], [230].

Initiating in regions where backing bundles are close to UD bundles, damage starts as off-axis breaks in the backing bundles, leading to localised breaks in the surrounding UD bundles, contributing to the initial stiffness drop in Stage I [58], [73]. Transverse cracks (also referred to as tunnelling cracks) also propagate within the backing bundles, often through the width, and this can lead to combined and localised progressive failure in UD bundles through the width and thickness, leading to a stable Stage II [231].

Also, as fibres have a strength distribution through the length, this combined with fibre fatigue can lead to random UD fibre breaks, even when they are away from a highly strained region [232], [233]. Eventually, nearby fibres and matrix are not able to bear the load, where damaged planes in proximity join up and lead to complete failure near Stage III [73], [218].

This mixed mode of damage progression has been visually verified through a suite of imaging techniques including SEM [73] and x-ray tomography [58][60]. Existing

knowledge about fatigue behaviour at a microstructural level in composites has been through imaging, and it is important that we expand onto other complementary techniques to improve our understanding. The main techniques used in this paper to investigate and characterise fatigue damage quasi-UD-NCF GFRP are discussed below.

5.1.2. Characterisation of fatigue damage in UD-NCF composites

Advances in material imaging and characterisation have made it possible to investigate complex time-lapse evolving behaviour of a variety of materials. Often these behaviours can be observed in-operando/in-situ/ex-situ, given the complexity of the conditions involved. Among these techniques, x-ray computed tomography (XCT) is a great candidate, particularly for its non-destructive nature and 3D information capability. These have led to a surge in the application of XCT in studying composites undergoing various stimuli of monotonic/fatigue loads [58], [60], [234]–[237], particularly the review of Garcea et al [75] cited >400 times within 4 years. A major interest has been in time-lapse observation of the damage phenomena, often called 4D (time as 4th dimension), where studies can be focused on the classic initiation, propagation, and final failure, identifying weak links in the microstructure which fail early on [58], [60], [123], [234], [235], [238], [239]. This is mostly due to the accurate resolving of complex 3D morphology of microstructural features; often across length scales, evolving through time, which would be speculative if only a 2D image was available.

Fatigue in UD-NCF is ideally investigated using bright, high-flux synchrotron sources owing to their higher frame rates, better quality data using a higher resolution, better signal-to-noise ratio, and phase contrast. However, beamtimes are available for

only a few days, which is unsuitable for high-cycle fatigue, unless the load frequency is increased which risks self-heating and changing the damage mechanisms arising from only load to load-temperature. Increasingly available commercial lab-based x-ray systems are competing with synchrotron-based sources in terms of resolution (Zeiss 810 Ultra, with a voxel size of ~16 nm [152], [240]), high flux (Nikon High Flux Bay at NXCT, Manchester [241]), large field-of-views (Thermo Fisher Heliscan [60]) and phase contrast imaging (EI XPCi, UCL [155], [242], [243]), among others.

As damage features in UD-NCF are micro-scale in size, high-resolution images of around 2-5 μm pixel size are needed, which limits the field-of-view (FoV) to a square of ~10mm x 10mm [244]. Usually, for tension-tension UD-NCF fatigue samples which have multiple fibre bundles across the width with each fibre bundle around 2-3mm in width and sample heights above 150mm [58], [60], [239], this poses a great risk of under-sampling and statistical inadequacy. This is often mitigated by stitching together smaller imaging volumes in a 'tiled' fashion, which introduces other problems including discontinuity artefacts and non-uniform tiles.

ThermoFisher Heliscan Mk2 offers an advanced solution to this problem by allowing a high-resolution high-aspect ratio 3D scan in a single tomogram, where the limitations in field-of-view are lower in height than in width. This is essentially made possible by a helical scanning trajectory which allows one to take projections while rotating and translating vertically instead of just rotating conventionally, while the data is reconstructed via an adapted FBP algorithm [157]. This has been proven to reduce ring and cone-beam artefacts [245] while also allowing for higher image fidelity as each point of the sample is in the most accurate 'centre-slice' as it has to pass through the middle of the Tam-Danielsson window [246].

<u>Digital Image and Volume Correlation (DIC & DVC)</u>

Digital Image Correlation (DIC) is an imaging technique used to generate deformation maps from a series of progressive images of a sample specimen. These images can be from any source, and the sample could be under any stimuli. These images are correlated to each other, often to the first image of the sequence as the reference, using locating individual patches (subsets) and tracking their movement, meaning images should have some unique features and the deformation should not be too large [103]. If the sample does not have features, a speckle pattern can be created with spray paints and such. Most common algorithms include fast Fourier transforms (FFT), normalised cross-correlation and such. The displacement maps can be differentiated to obtain strain maps [247].

DIC has been used to investigate composites for full-field strain measurements at the macro scale for fibre-reinforced polymers (FRPs) in civil engineering [248], three-point bending [249], textile deformation [250]–[252], CFRP laminates [253] etc. Over the past decade, it has also been used to investigate fatigue damage in composites [254]–[258], mostly to investigate strain fields around macro-cracks and to validate models. The popularity has been accredited to versatility and decreasing costs of cameras and computation, for fatigue it is unsuitable to investigate at higher load frequencies >3Hz as very high frame rates are required to capture images without blur. As done in this study, it is commonly mitigated by using a slower fatigue cycle at regular intervals for DIC acquisition, instead of a continuous acquisition. By this, the data size is also reduced as a small 5-second acquisition at a 10Hz frame rate can easily be in gigabytes.

While DIC uses 2D images, the procedure can be extended to volumetric 3D images which is referred to as digital volume correlation (DVC). These 3D images are usually

from synchrotron and lab XCT, taken at different stages of time-dependent response to stimuli. The underlying principle is the same, where a 3D region is correlated in the series of images, and then used for displacements and strain calculation. Understandably, DVC calculations can be quite computationally intensive and are usually done on fewer images than DIC.

DVC has been employed to study monotonic loading damage in discontinuous FRPs [259], laminates [166] and CFRPs [164], [169], [260], even using particles as markers [261]. Most of these studies use synchrotrons to acquire 3D images where phase contrast for materials like CFRPs is used to enhance contrast. Fibres are potential markers for correlation, for CFRPs they can be enhanced using phase contrast, fortunately, glass fibres work well. 3D strain maps obtained via DVC can reveal strained regions, enhancing damage detection and/or revealing 'resilient' regions which do not fail under high strain. These can also be computed between volumes under variant monotonic loads or between the sample at different stages of fatigue life. The latter is undertaken in this study to observe residual irreversible deformation. To date, there have not been studies employing DVC using lab XCT to investigate fatigue damage in wind blade UD-NCF composites.

Correlative analysis with 3D SEM

SEM has been used to investigate composites for at least four decades. They have investigated transverse ply cracks and fibre ruptures in CFRP cross-ply laminates [262], friction and wear in FRPs [263], and fatigue damage in Kevlar [264]. More recently, it has been used to investigate fatigue damage in UD-NCF GFRPs [73]. Its limitations of only 2D images have been seriously mitigated by obtaining serial sections of images across height to form a 3D volumetric image, using alternate

milling-imaging routines. Techniques including focused ion beam (FIB) and laser milling have been successfully used to excise away the definite volume of material, exposing sub-surface and bulk information [265] [266][267].

Due to its destructive nature, it has been limited to post-mortem observations. But with the advent of correlative analysis, 3D SEM has been used to complement data from non-destructive techniques including x-ray tomography, bringing superior resolution information and bridging gaps across length scales [189], [268]–[271]. This enables a successful compromise where lower resolution but non-destructive and therefore time-lapse capable x-ray tomography is greatly complemented with high-resolution 3D SEM data. Often the XCT data is used to locate and guide the SEM scan to regions of interest (RoI) [272], [273]. These datasets are spatially registered in the combined image volume. This can be used to back-trace the progress of a certain microstructural feature. Thereby, the focus is not only on features of interest but also on avoiding extremely large datasets had the volume been sampled at high SEM resolution.

5.1.3. X-ray computed tomography-based numerical modelling

Image-based modelling is a young research field but has seen enormous progress in the last 10 years. As the quality of the numerical model results largely depends on the acquisition, reconstruction, segmentation, and meshing, it must be seen with a holistic perspective. Auenhammer et al. [198] have therefore introduced X-ray computed tomography-aided engineering (XAE) to emphasise the importance of an aligned process from acquisition to modelling. In this study, a model based on the untested sample is created to identify stress concentrations caused by the layup. Several studies have shown stress concentrations in the interface between uni-directional and backing bundles [193], [274]. These stress concentrations in the

original layup, seen in the numerical modelling results, are supposed to cause initial failure in the composite.

Fatigue mechanisms in quasi-UD NCF GFRP are still not fully understood due to a manifold of different failure modes and influence parameters This study brings together the potent techniques of XCT, DIC-DVC, SEM, and image-based numerical modelling to generate a rich 3D multiscale and spatially correlated time-lapse information to investigate the initiation and evolution of fatigue damage in quasi-UD-NCF GFRP, in terms of the types of damage, distribution, and their proximity to microstructural elements. This is eventually related to the loss in stiffness, a key material property. Only the comprehensive combination of all tools will allow us to gain more understanding of fatigue in fibre-reinforced textile composites.

5.2. Materials and Methods

5.2.1. Fatigue test sample specimens

The composite is a proprietary sample supplied by Saertex GmBH, used in wind turbine blades. It is made of four layers of UD E-CR glass fibre bundles stitched via threads to backing bundles, impregnated with Olin epoxy using vacuum-assisted resin transfer moulding (VARTM) and cured at 80° C for 8 hours. The four UD bundles are oriented at 0° (corresponding to the z-direction in the x-ray images) while the backing bundles are oriented perpendicular at 90° across the width in the x-direction, leading to a [90/0/90/0/90/0/90/0/90] layup. This 3.67 mm thick material is tabbed with a tapered cross-ply laminate and waterjet-machined to extract butterfly specimens. This geometry is optimised for fatigue testing as it encourages failure in the gauge regions rather than the grips [191]. Specimens are 226 mm long, with a gauge section 6mm wide and 10mm long, making a cross-sectional area of 22.05 mm^2. To investigate and

register the same region in XCT and DIC, gauge boundaries are marked with high-contrast SilverDAG and then the gauge region is speckled over with white and black paint.

Figures 5.2 A and B show the 3D composite architecture in the gauge region obtained by an XCT volume render, where the matrix has been made invisible to aid the visualisation of the fibre bundle arrangement. The UD bundles are much thicker than the backing bundles; while the range of UD fibre diameter is approximately 17-20 µm, backing glass fibres are approximately 9-11 µm. The stitching threads cannot be resolved as they have similar 'optical density' compared to epoxy. C and D show the gauge painted with a speckle pattern for DIC acquisition. Throughout this paper, the coordinate system is defined as X (width), Y (thickness), and Z (the UD load-carrying direction).

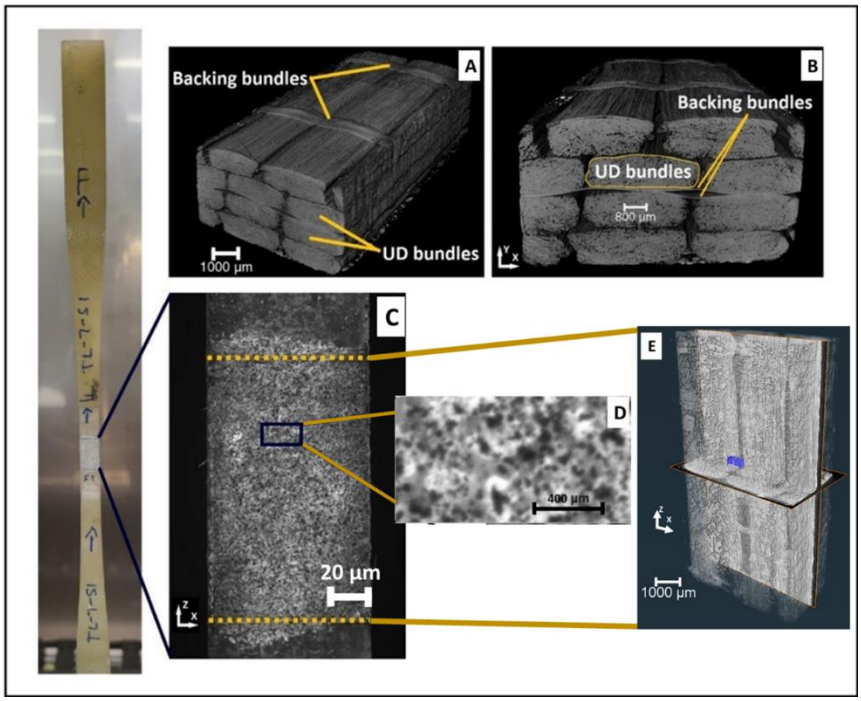

Figure 5.2 Photograph (left) of the butterfly sample geometry. A and B show the gauge region which is made of epoxy reinforced with UD glass fibre bundles and ~10% of backing bundles, where the matrix has been rendered invisible. C & D shows the gauge region speckled with black and white paint to enhance DIC contrast. E shows the gauge region shown in XCT with a translucent volume render (blue box shows typical RoI sizes investigated for damage).

5.2.2. Methods

Figure 5.3 shows the experimental workflow for this paper, where XCT, DIC-DVC and SEM have been combined so as to track the damage and stiffness degradation throughout an HCF fatigue test.

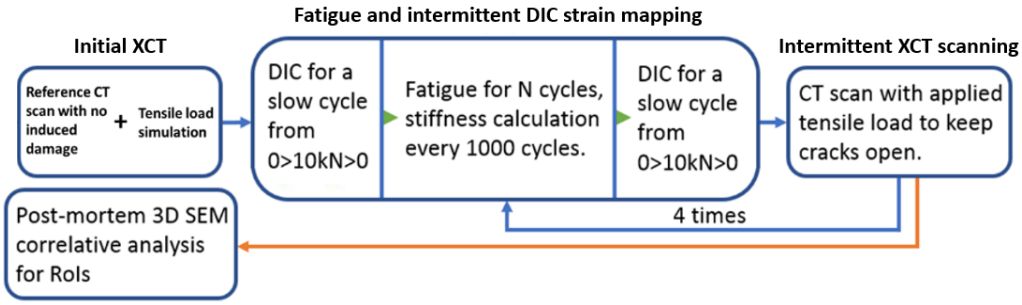

Figure 5.3 Experimental workflow for the time-lapse fatigue investigation by correlative DIC-XCT-SEM in conjunction with tensile load simulation.

This workflow is combined with tensile load simulation using a material model and comparing the simulation results with the experimental results.

<u>Mechanical test procedure</u>

The specimen is fatigued using a sinusoidal loading, where N=20000, 40000, 20000, 20000, and 20000, in load-controlled Instron 8802 hydraulic machine at 4 Hz, R= 0.1, ε_{max}= 1%, $load_{max}$= 10kN. The axial strain was continuously monitored in the gauge region via a clip-on extensometer (10mm/±1mm). The maximal strain ε_{max}= 1% has been found to encourage progressive damage under HCF [9] and 4 Hz is low enough to avoid self-heating of the epoxy [9]. Stiffness has been measured every 1000 cycles using extensometers by calculating the slope on a stress-strain curve via linear regression.

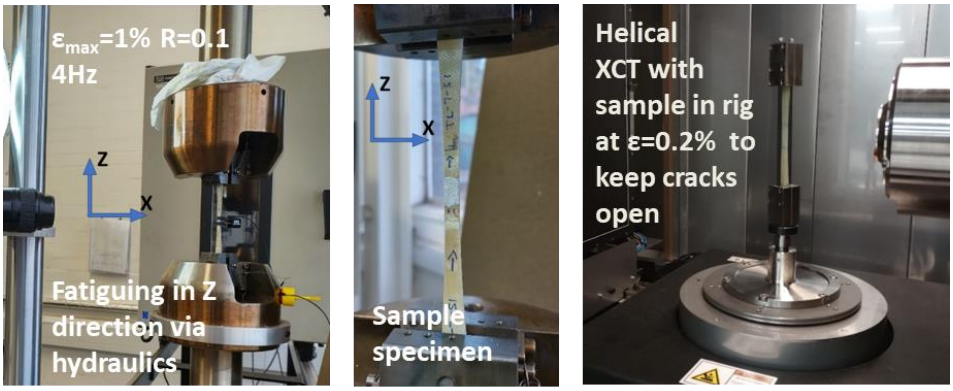

Figure 5.4 Sample specimen fatiguing in the hydraulic rig and being XCT scanned while the cracks are kept open by the tension clamp.

The evolution of the strain field was recorded using an intermittent DIC routine at the beginning and at the end of every fatiguing step. The DIC is acquired on a lower load frequency of 0.02 Hz, cycled from 0 to 10kN and imaged at a 10Hz frame rate, using a single-camera LaVision Strainmaster system, as shown in Figure 5.4. The subset size used for correlation is 31 pixels where the pixel size is 6.53 μm. The images are correlated to the first image recorded during the slow fatigue cycle (at 0 MPa), so the strain calculated is relative to the 0-load reference image. The images were acquired over the whole FoV of the gauge section, but the correlation and subsequent strain calculation were done on a slightly smaller area to avoid loss of correlation at the edge of the frames.

In order to better delineate the fibre fractures/damage, the sample was XCT scanner under tensile load to keep the cracks open [9], [149], using a tension clamp. The tension clamp uses a pair of carbon rods, one on each side of the sample to impart tension by means of curved clamps, as shown in Figure 5.5. The limitation of the carbon rods getting their ends crushed by the screw points on higher loads has been mitigated in this study by glueing hard stainless steel onto the ends. This prevents screw points from digging into the carbon rods and has been successful in imparting stable loads of up to ~5.7 kN. By attaching the clamp while the sample was loaded it

was possible to maintain a load of ~1.8 kN (~81 MPa) , corresponding to a strain of 0.2%.

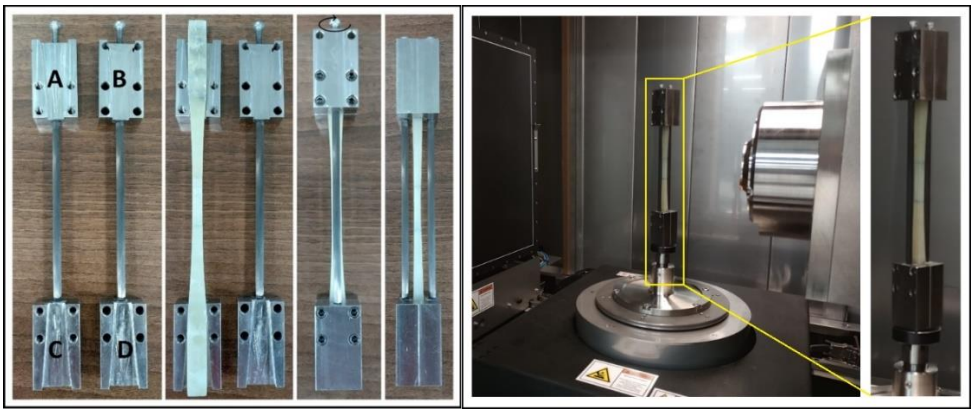

Figure 5.5 The tension clamping procedure, which aids damage detection during XCT scanning. The sample is fixed between pairs (A, B and C, D) of metal jaws and the carbon rod is screw-tightened to impart tension. The helical scanning procedure can scan longer Z-heights than conventional XCT scanners.

X-ray tomography

All the scans were carried out on the Thermo Fisher Heliscan Mk2, which offers high image fidelity with the capability to scan tall samples due to its helical scanning trajectory. The scanning conditions are summarised in the table below.

Source to sample distance	Detector to sample distance	Pixel depth	Exposure time	Number of projections/ revolution	Total number of projections	Accelerating voltage	Tube current	Voxel size
25 mm	810 mm	16-bit	1.45 s	1800	~4000	80kV	95 µA	4.3494 □m

Table 5.1 Scanning parameters used for time-lapse helical scanning on a Thermo Fisher Heliscan Mk2.

This results in a full-field scan of the gauge region (10mm x 3.6mm x 6mm) in a single tomogram. This produces an average file size of 10 GB, for an average acquisition time of 6 hours. The carbon rods from the tension clamp are spatially within the

scanning FoV, but due to their low atomic number, they do not attenuate the signal and hamper the image. The sample stub with precise markings allows accurate repeatable placement of samples to maintain consistency across the time-lapse. The XCT scans were undertaken after 20000, 60000, 80000, 100000, and 120000, cycles, including the finish. The sample is not taken to complete failure to enable higher-resolution SEM studies.

DVC analysis was also applied to correlate the CT scans taken at 0 and 120k cycles. The DVC analysis was performed in Avizo's XDigitalVolumeCorrelation module, since the residual strain is expected to be lower, the global mesh-based DVC approach using a bigger tetrahedral element of 200 μm is used. For such a large volume, it puts constraints on the computational resources to choose a smaller element size.

Finite element modelling for tensile simulation

An image-based finite element model was constructed by Robert Auenhammer from Chalmers, based on the initial CT scan conducted in Manchester, as described in [192]. First, the fibre bundles were segmented from resin-rich area and then a surface mesh of the segmented fibre bundles is created. Creating a smooth surface mesh is challenging; in our case we used an automated mesh generation as a first step and manually improved the mesh afterwards at an average element length of 150 μm. This process takes approximately 2 hours for the given dataset. Within the created surface mesh, a solid mesh comprising second-order tetrahedral elements comprising ten nodes was created. The remaining volume was then filled with first-order tetrahedral elements representing the resin-rich areas. After the mesh creation, the fibre orientation mapping takes place, following [193]. With the structure tensor method by Jeppesen et al. [194] the fibre orientations are analysed and then mapped to each of the four integration points per element. With the given mechanical material properties,

a linear orthotropic material model is assigned and a tensile test with a total strain of 0.25% is simulated.

3D Serial sectioning SEM

Postmortem, a volume of 400 µm x 600 µm x 100 µm was excavated and imaged in the Helios 5 Laser PFIB SEM using 20 kV voltage, 3.2 nA of current, and a 3072 x 2048 ETD image grid. Approximately 1000 slices of 100 nm thickness were milled using Xe+ plasma. Prior to the acquisition, the sample was sputter coated using an Au:Pd 80:20 ratio with a thickness of 10 nm.

5.3. Results and discussion

5.3.1. Stiffness degradation

As shown in Figure 5.6, the stiffness degrades progressively throughout the fatigue timeline as observed in another study [73]. After a fall of ~5% stiffness, the HCF cycling was stopped to enable SEM studies.

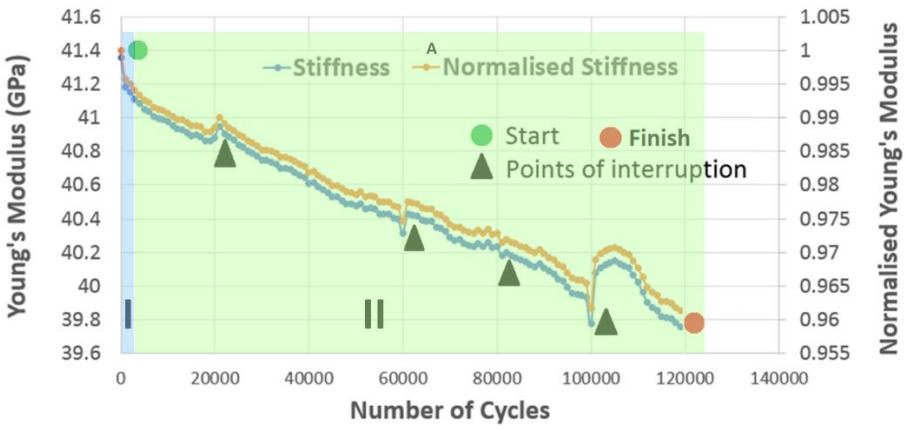

Figure 5.6 Continuous stiffness degradation monitored by an extensometer during HCF test with 4 interruption points till a ~5% loss at which point the fatiguing is stopped. The maximum strain is 1% with an R-ratio of 0.1. The points of interruption are when XCT and DIC acquisitions are taken. The steep drop in I is followed by the stabler degradation in II. The sample is not taken to failure to enable SEM studies.

This pattern of stiffness degradation largely agrees with the published results where stiffness degrades in essentially three stages of an initial steep drop, followed by a stabler degradation and the final steep drop again close to failure [9], [58], [59], [73], [229], [275]. Here, the stiffness drops initially and then degrades progressively. The HCF cycling was stopped prior to stage III. There is a small decrease in stiffness immediately upon restarting the fatigue test after XCT scans, especially after the 100000 cycles interruption. These are mainly because of the slight variability in extensometer placement and the applied static tension during the XCT scans. Additionally, due to imperfect sample alignment in hydraulics, inferior off-axis stiffness can negatively influence the measured axial stiffness. As the sample cycles, it realigns itself to the load axis, where the accurate stiffness is restored, as is evident in this case.

5.3.2. DIC results

The DIC strain maps have been acquired before and after each CT scanning step, as mentioned above. The same gauge region is analysed consistently, and clear high-strain hotspots are visible. Figure 5.7 A shows the distribution of the high-strain hotspots corresponding to damaged regions, throughout the fatigue timeline. As expected, the nature of the damage is progressive and the regions corresponding to extreme strains of $\boldsymbol{\varepsilon_{zz}}>2\%$ and $\boldsymbol{\varepsilon_{zz}}<0$ (corresponding to extreme deformation) keep increasing with the number of cycles, as evidenced in Figure 5.7 B. The hotspots show high strain regions with corresponding low strain regions, above and below the hotspots.

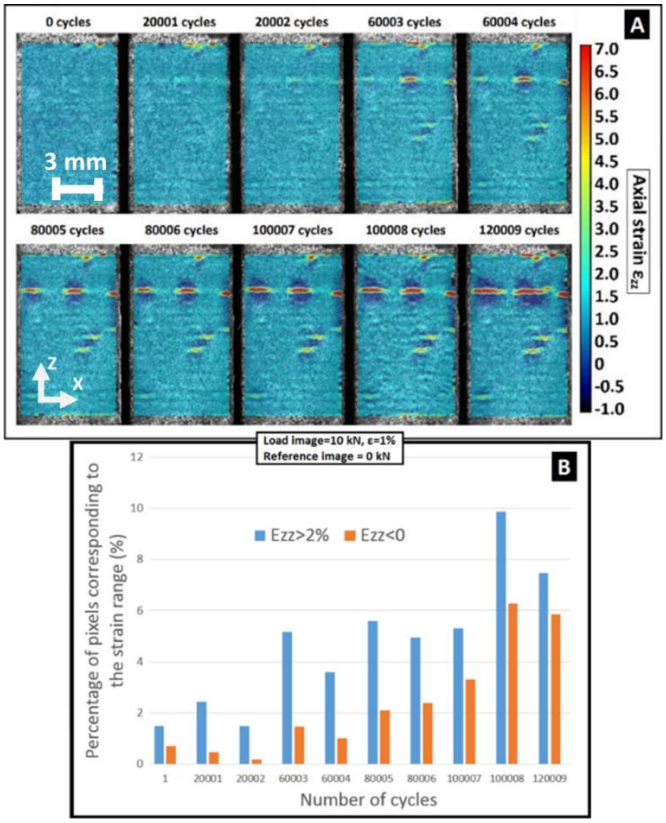

Figure 5.7 DIC results across the time-lapse HCF cycling. The results are calculated between reference 0% strain image and maximum 1% strain image. A) shows the strain maps as a function of number of cycles, the high-strain regions (in red) and associated damage increase as fatigue cycles increase. B) shows the increasing percentage of extreme strain values (positive and negative), corresponding to severe deformation and damage as the number of cycles increase.

5.3.3. Damage progression observed by x-ray CT

This section presents and discusses the damage mechanisms – their progression, distribution, and interaction as observed by XCT. Although quite intuitive, the rich 3D data observed by XCT is difficult to visualise in 2D images. The most intriguing images have been chosen for this section.

Upon closer inspection of these damaged regions in the XCT images, these high strains are attributed to cracks on the surface. Figure 5.8 shows four distinct regions A, B, C, and D – where surface damage is visible. In region A, surface rupture occurs, involving UD bundles and matrix. In region B on the other hand there are three jagged cracks running along the x-direction through UD fibres, backing fibres, and the matrix. As

the strong reinforcing UD fibres have failed, regions A and B are most compliant and damaged as evident in the strain maps, compared to regions C and D, where cracks are only in the matrix. The crack openings in region B can even be seen in the lower-resolution image obtained from the DIC camera. DIC strain maps therefore cannot only detect damage here but can also distinguish if the loss in stiffness is originating from the damage in strong reinforcing fibres or the weaker compliant matrix.

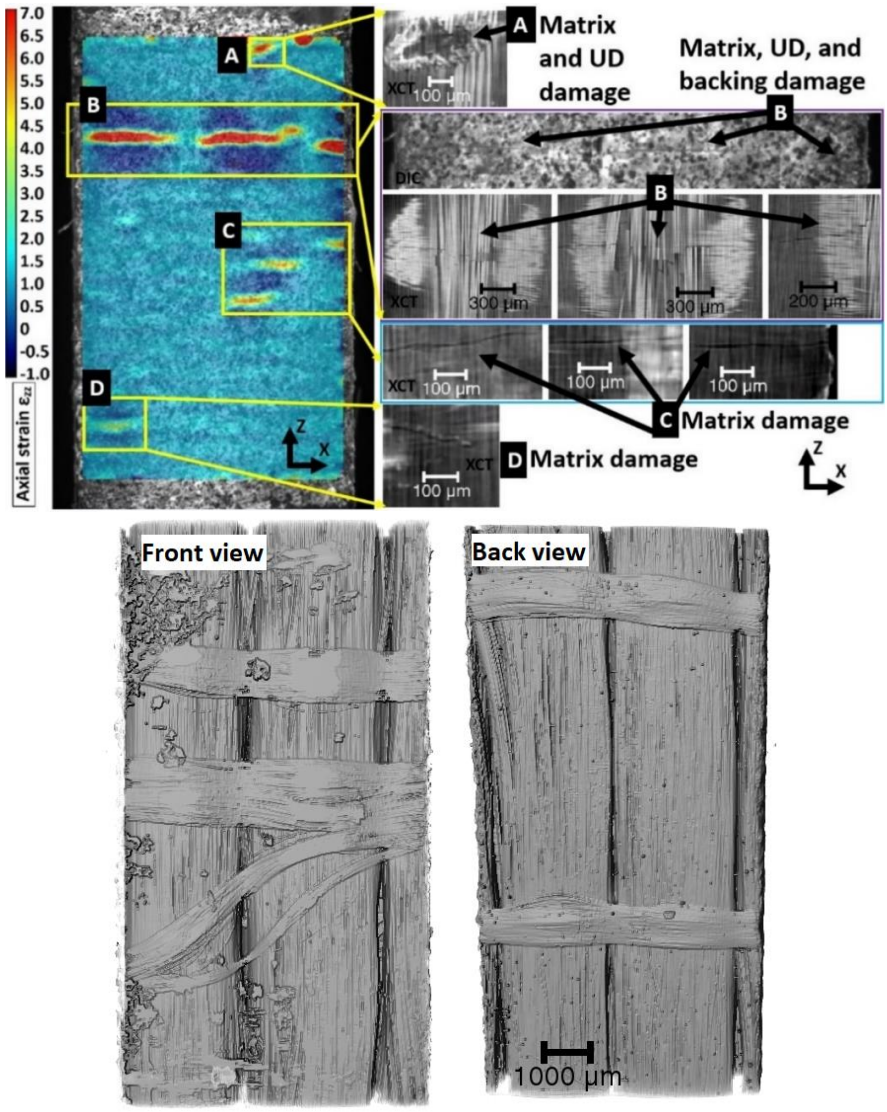

Figure 5.8 Four distinct regions of the front gauge region with visible damage. A and B have damage starting close to backing bundles and lead to UD fibre breaks. These correspond to higher strain values as the stiff reinforcing fibres are broken and cannot resist deformation. C and D have only matrix cracks and therefore lower deformation.

Surface damage from voids

Matrix cracks (also highlighted in the B region of Figure 5.8) are found to initiate from a surface void, as shown in Figure 5.9. The matrix crack proceeded to initiate an off-axis 90° crack in the backing bundle near the surface. This off-axis crack leads to a UD fibre break cluster in the bulk, shown in Figure 5.10. This UD fibre break cluster leads to high deformation and localised loss of stiffness as evidenced in the strain maps from Figure 8. The interaction between matrix cracking and UD fibre breaks is quite complex, and UD fibre debonding is also visible. Within the UD fibres, the matrix cracks seem to be bridging the UD fibre breaks.

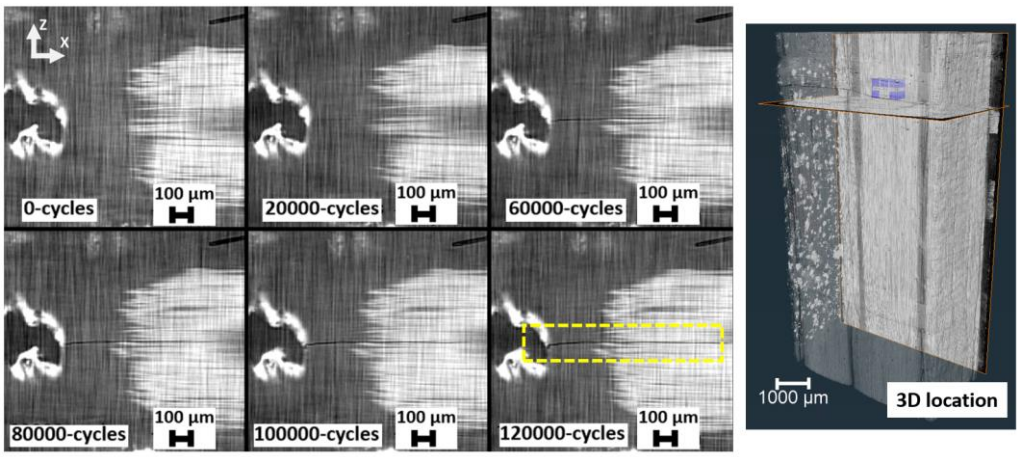

Figure 5.9 Matrix crack (boxed in yellow) originates from a void and progresses into an off-axis crack in the backing bundle. The void is ~100 µm close to the surface of the sample, shown in the 3D location (blue box).

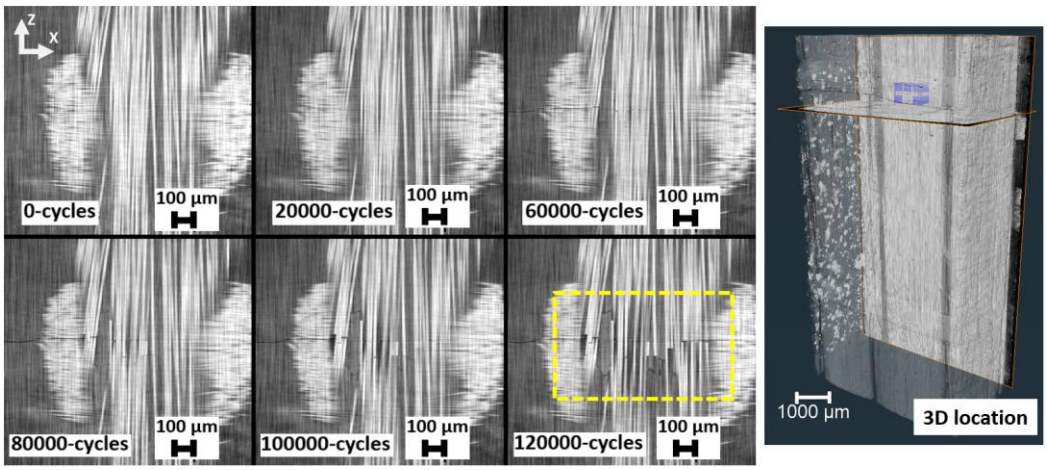

Figure 5.10 The same connected crack (boxed in yellow) from Figure 9 progresses from the backing bundle just beneath into the UD fibres, ~150 µm below the surface, shown in the 3D location (blue box). Note that the interaction between the UD fibre breaks and matrix is quite jagged and complex, with UD fibre debonding also visible.

UD fibre breaks and matrix-cracks

UD fibre breaks are observed to be originating close to backing bundles, as found in other studies [9], [58], [59], [73], [229], [275]. In this study, the expanding cluster of UD fibre breaks, because of higher deformation and compliance, lead the way for a longer matrix crack and eventually link up together, as shown in Figure 5.11.

The UD fibre breaks are seen to progress in the width direction of the gauge, as the neighbouring fibres failing, it puts a higher stress on the remaining fibres. The expansion in width and not as severe in thickness can be possibly attributed to the change in the local fibre volume fraction along the thickness, as shown in Figure 5.12. As known from previous studies [9], [58], [59], [73], [229], [275], one of the reasons damage initiates near backing bundles is because they introduce change in local volume fraction and waviness in the UD bundles and lead to local misalignment with the load

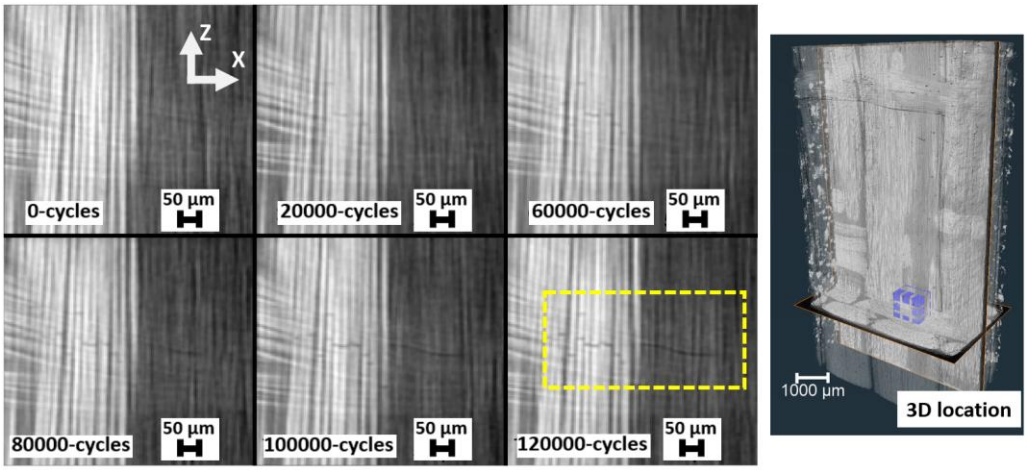

Figure 5.11 UD fibre breaks cluster (boxed in yellow) expanding near the backing bundles and progressing into a matrix crack. The matrix-rich region near the UD fibre breaks goes under severe deformation once the reinforcing fibres break.

We also see UD bundles that are not in proximity to backing bundles exhibit late-stage fibre breaks as they are further away from the matrix and bundle interface, shown in Figure 5.13. These clusters of UD fibre breaks might have led to a matrix crack at later stages as there is a matrix-rich region next to it (as in Figure 5.11) had the test not been stopped.

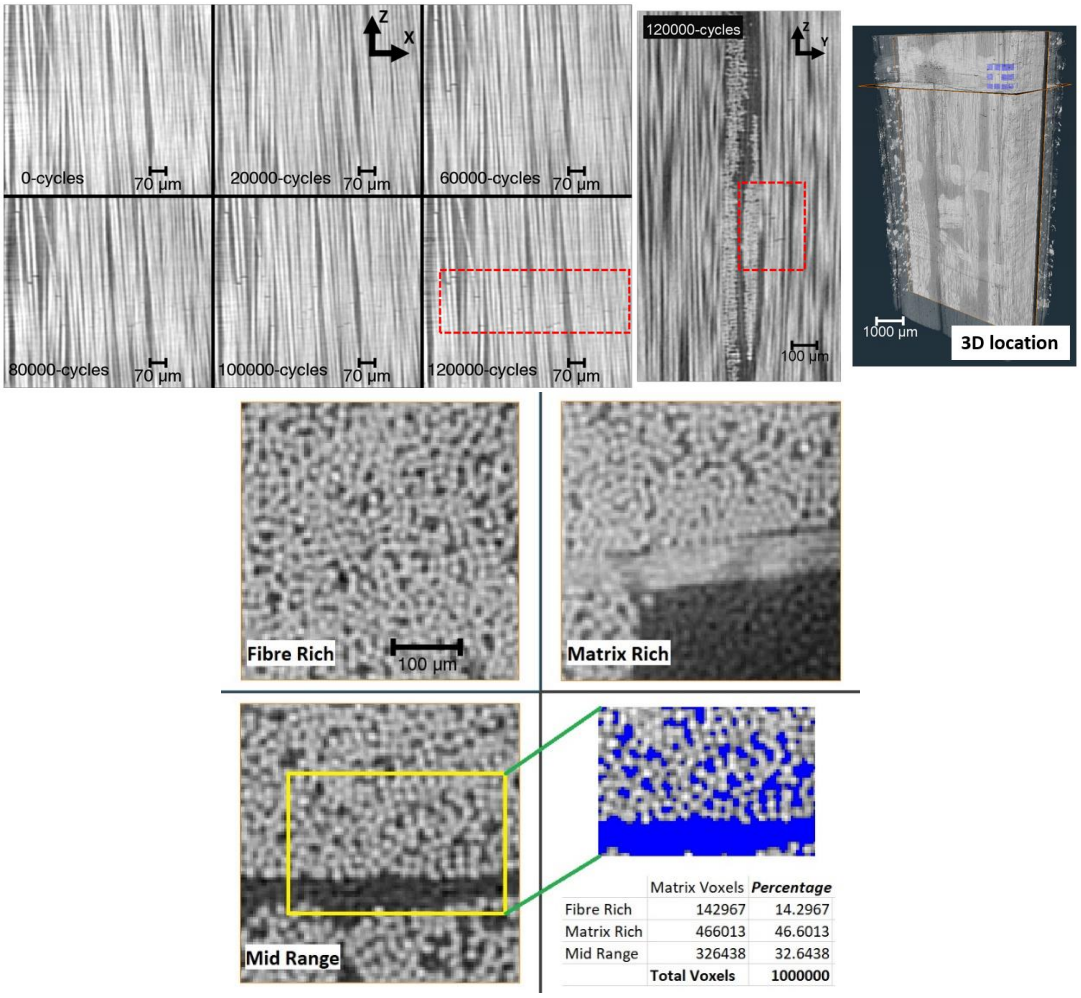

Figure 5.12 A cluster of UD fibre breaks (boxed in red) originating close to and progressing away from the backing bundles, in width. The damage localisation is due to change in local fibre volume fraction, as shown in the picture.

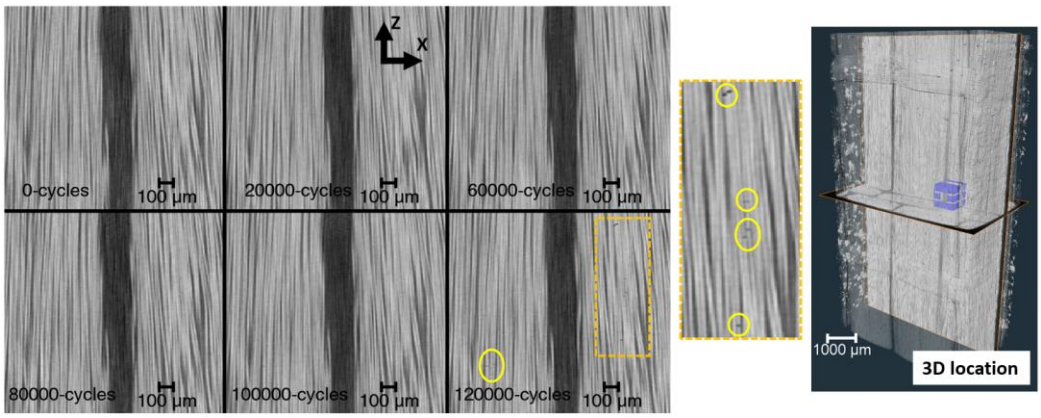

Figure 5.13 UD fibres away from backing bundles developing breaks later than the ones closer to backing bundles, in agreement with the current understanding of damage initiating near backing bundles.

Longitudinal macro-cracks

Four longitudinal splits are found in the material, originating, and progressing minimally throughout the time-lapse, as shown in Figure 5.14. By the time the cracks are imaged, they had progressed to an extent which made it ambiguous to locate the source of the crack. However, these are all near the edges of the sample and possibly originated from the edges, as has been found elsewhere [59], [60].They progress along the length (Z) of the sample, while the crack opening also increases, as shown in Figure 15. To visualise the presence of the macro-cracks with respect to the material architecture, the cracks, UD and backing bundles, matrix and background are segmented automatically using the Trainable Weka Segmentation in Fiji-ImageJ [276], as shown in Figure 5.15. The matrix has been rendered invisible, and one can see the macro cracks running in the UD bundles through the length between and near the backing bundles. Out of these four macro-cracks, C and D exhibit interesting behaviour and are chosen for further analysis.

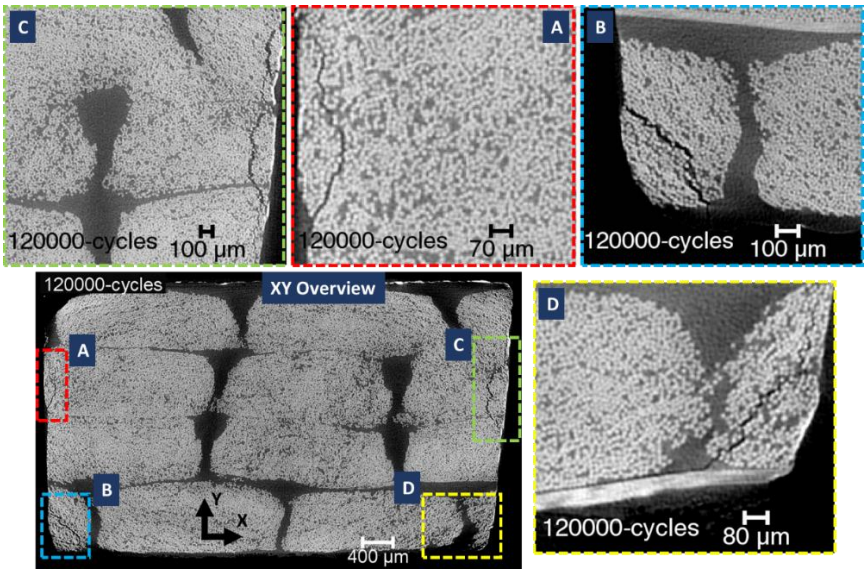

Figure 5.14 Four longitudinal macro-cracks are found in the sample, originating, and progressing through the length during the fatigue test. Macro-crack 'D' is not as visible as it is found in XY slices further in Z. Out of these four, C and D are found to exhibit interesting behaviour and have been further analysed below.

As shown in Figure 5.16, the macro-crack 'D' (identified in Figure 5.14) is a longitudinal split, which originates in an edge UD bundle and proceeds through a resin-rich region leading to delamination between an adjacent UD and surface backing bundle. In [231], it is found that cracks can easily deflect along backing bundle interfaces, especially if the interface is weaker and the crack twisting angle is relatively small. Being at the surface, in this case, the backing bundle is prone to imperfections and can exhibit weaker interfaces.

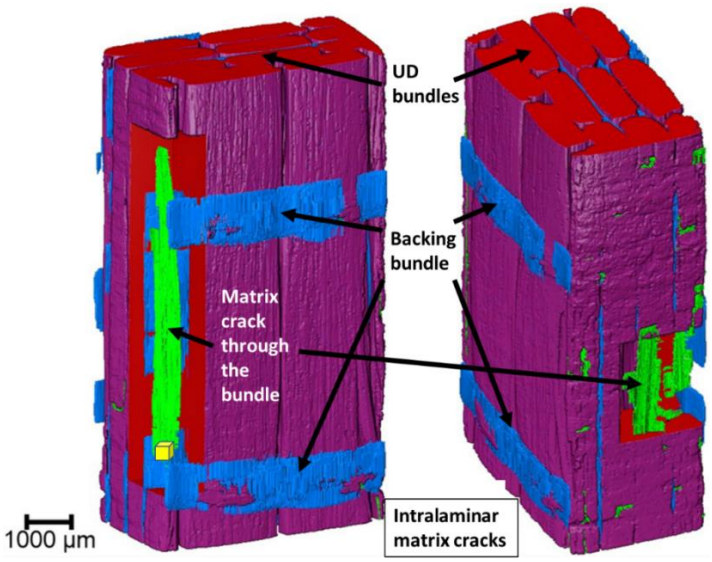

Figure 5.15 Longitudinal macro-cracks (in green) in UD bundles (in red) running across the gauge length close to backing bundles (in blue). The segmentation is an automated prediction of Trainable Weka Segmentation in Fiji-ImageJ. The tiny yellow box (not to scale) shows the volume excavated in PFIB SEM for higher-resolution investigation.

As shown in Figure 5.17, the 'C' split seems to be deflected by the backing bundle, as going around it instead of crossing it. This behaviour was found in [239] as well, where the crack was arrested instead of being deflected around the backing bundle. In [231], it was found that cracks can deflect around the backing bundles, even when the crack approaches nearly perpendicularly to the backing bundle direction.

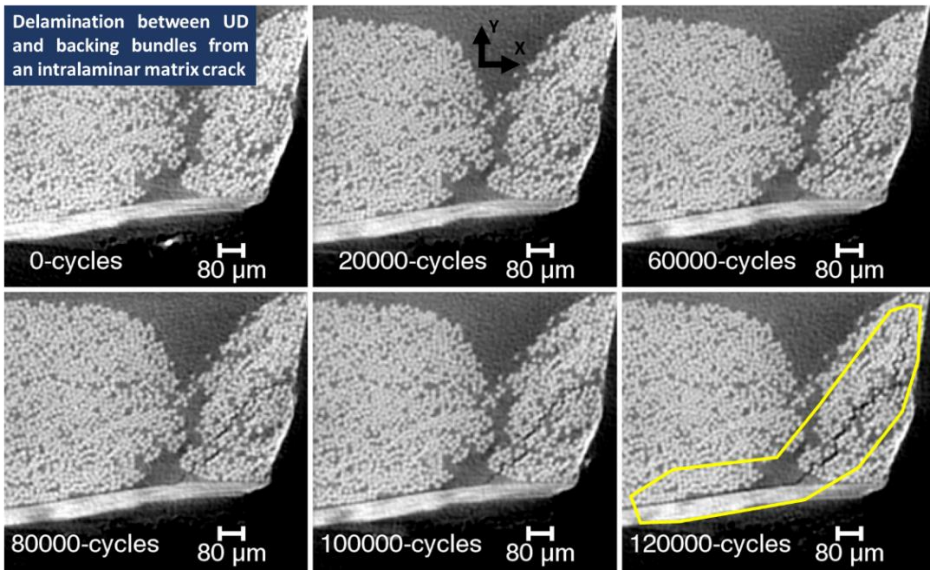

Figure 5.16 Longitudinal matrix crack in UD bundle leading to delamination (boxed in yellow) between an adjacent UD bundle and a surface backing bundle.

Such extreme twisting is due to a sufficiently weak interface, which in this case is possible for the backing fibres as they are so close to the specimen edges with possible imperfections.

It was also observed in [60], where it is argued that the stitching threads which are very close to the backing bundles, actually deflect the cracks. The deflection by stitching thread instead of the backing bundles seems more plausible as the compliant stitching threads would be able to deform more before breaking compared to the brittle backing glass fibres, but more investigation is needed to confirm this. As a result, correlative SEM verification around the sample edges where the macro-cracks are present, is carried out.

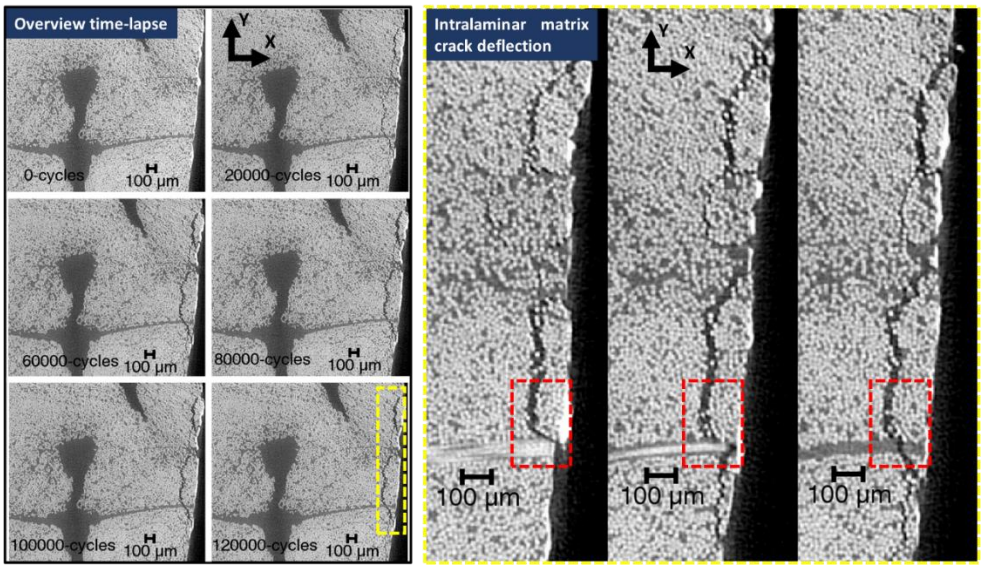

Figure 5.17 Intralaminar matrix crack (boxed in yellow) progressing through the time-lapse, deflected by the backing bundle (boxed in red) and instead progressing around it.

5.3.4. Correlative SEM verification

The serial section electron microscopy enables us to examine some of the damage in greater detail. A region of interest indicated in Figure 15, close to a longitudinal split, is shown in Figure 5.18. UD fibre breaks have been linked together by localised matrix cracking and have been associated with fibre debonding, sometimes long debonding in this case. Especially in Figure 5.18 A, the red box shows the UD fibres which are very close to each other, almost touching. Touching fibres are a known composite defect [33], [34], [277] as they lack the interfacial space for the matrix to bond to them. Figure 5.18 B partly corroborates the crack deflection phenomenon observed in Figure 5.17, where a small thinner crack can be seen in the stitching thread region. Such cracks can be hypothesised to be deflected by a macro-crack running transverse to them. These small cracks along with the stitching threads can be difficult to detect in XCT as their size is half the diameter of a fibre. This supports the argument that it is the stitching threads that deflect the cracks and not the backing fibres.

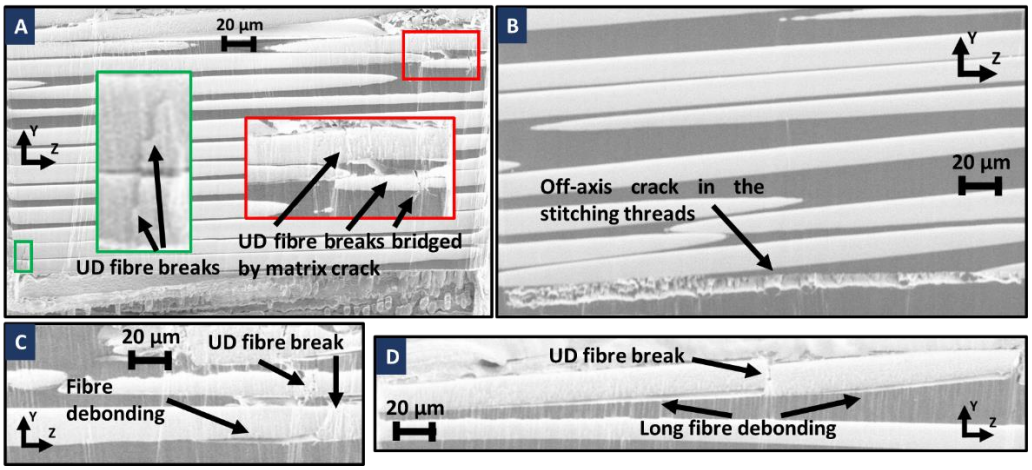

Figure 5.18 Different damage mechanisms observed in detail A) UD fibre breaks bridged by matrix cracking and debonding, close to the stitching threads and backing bundles B) Off-axis crack hypothesised to be deflected in the stitching thread region (stitching thread is not visible here) C) Fibre debonding bridging UD fibre breaks D) Long fibre debonding associated with UD fibre breaks.

5.3.5. DVC results

High strains were found in the regions close to backing bundles in 'bands'. Higher strains are also localised in matrix rich regions and do not differ much across the time-lapse images. Lower fibre volume fraction which results in weaker reinforcement is possibly responsible for the strain localisation. In Figure 5.19, it is observed that the sample after 20k and 80k cycles is under higher strain, possibly due to the loads from tension clamp being irregular.

The observed negative strains are mostly from macro-cracks and splits but could be in part from regions undergoing compression as the load relaxes from the tension clamp. This is evidenced with the increasing number of pixels that correspond to the negative strain across the time-lapse. The black background which is devoid of any contrast suffers from poor correlation values and can also contribute to false values. As the sample is not perfectly cuboidal, it is difficult to crop out the background without losing essential boundary information.

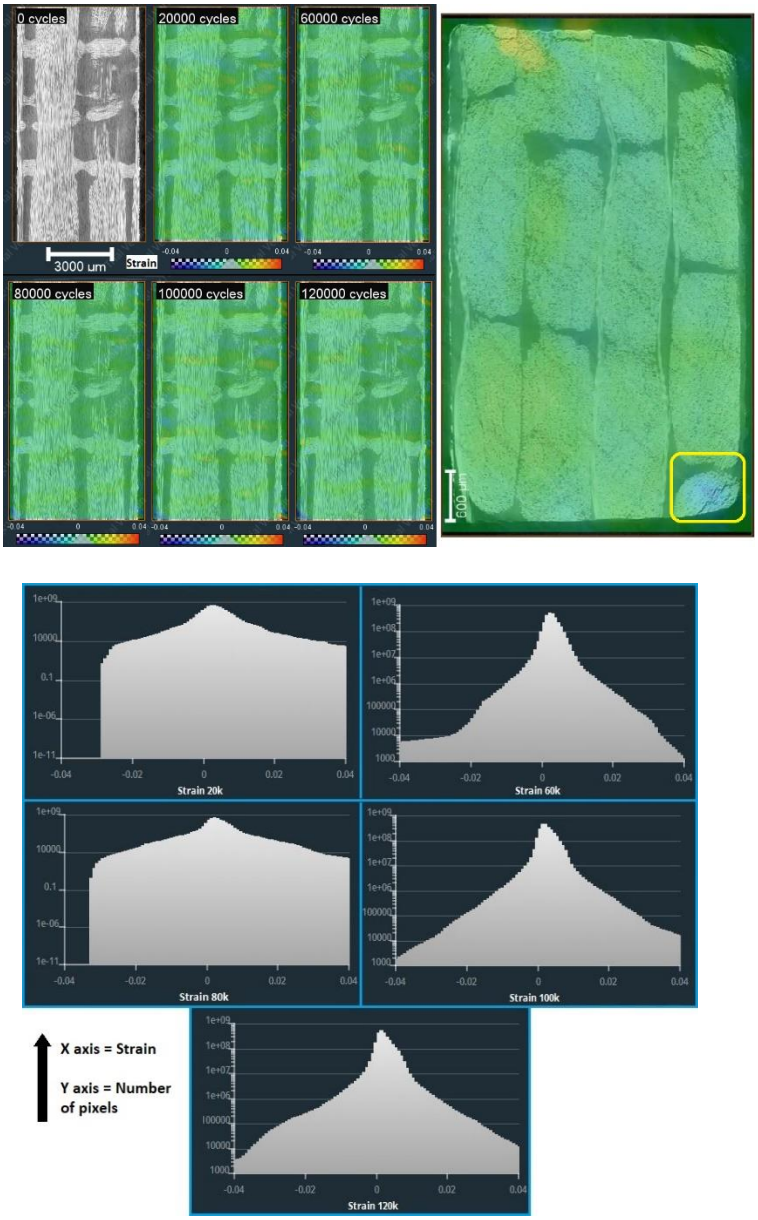

Figure 5.19 Strain maps of the sample obtained by DVC across the time-lapse, including a histogram of pixels corresponding to each strain value. Negative strains correspond to blue colour and can be seen near the longitudinal split (boxed in yellow).

The damage observed by manually browsing through the XCT data slices has been compared with results obtained as stress maps from tensile simulations and strain maps from DVC calculations. The damage, including fibre break clusters, matrix cracks and macro-cracks is marked by a yellow sphere, as shown in Figure 5.19. Towards the bottom, there is a concentration of damage, which upon inspecting the simulation results also is a high-stress region. This region also is seen in the DVC result as strain

bands, where the residual σ_{zz} strain is concentrated in the matrix-rich regions with close proximity to backing bundles, deformation is also high where splits are present. Studies [9], [58], [59], [73], [229], [275] have already shown that the deformation can be higher in the matrix-rich regions, especially the ones where the reinforcing fibres have failed already. A mismatch in the stiffness of fibres and matrix also can lead to stress inhomogeneities, which is also observed in this case.

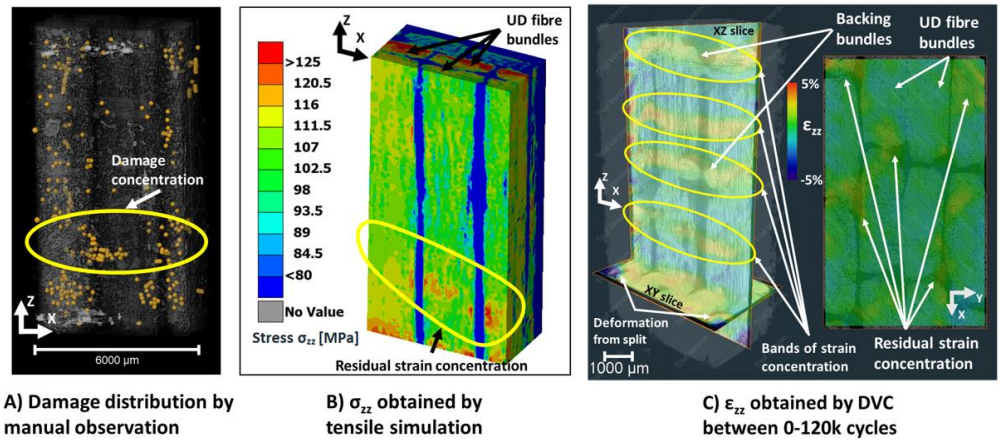

Figure 5.20 Comparison between A) Damage observed (yellow spheres) as fibre breaks, matrix cracks, and splits by manual inspection of XCT slices and overlayed on a translucent volume render, a highly damaged area marked by yellow oval B) Tensile simulation of stress along the Z-UD direction, σ_{zz} is higher in the yellow box C) Strain maps obtained by DVC between the reference 0 cycles image and 120k cycles image, high residual strains 'bands' are observed in matrix-rich regions with proximity to backing bundles. High deformation is also present near splits.

5.4. Conclusion

In this paper, a time-lapse ex-situ correlative workflow, involving x-ray CT, DIC-DVC and SEM was used to investigate complex tension-tension fatigue behaviour of quasi-UD NCF GFRP. These materials are commonly used in load-carrying components of wind blades. The improved tension clamp was able to stably hold the cracks open, which aids damage detection. Helical x-ray CT enabled acquiring a large

image volume of a full 10mm x 3.6mm x 6mm field of view, bypassing small RVE studies. This enabled the full damage distribution to be studied.

The study from DTU [58], [59], [231] found that the damage starts from the cross over regions where backing bundles cross over UD bundles, and the UD fibre breaks originate from off-axis cracks in the backing bundles. The fibre breaks length was found to increase with the increasing number of cycles.

This study found that damage initiated independently on the surface and in the bulk. Surface imperfections, such as voids and micro-scale notches, led to damage. Voids caused matrix cracking, which progressed into off-axis cracks in the thin supporting backing bundles (BB). These off-axis cracks then propagated into the neighbouring load-carrying UD bundles, leading to severe deformation, and observed strain localization in DIC-DVC strain maps. Due to stronger UD fibres failing, the local region became compliant, leading to UD and BB fibre failures in nearby regions and a significant loss in stiffness. DIC strain maps were found to be adept at not only detecting surface damage but also distinguishing if the loss in stiffness originates from the damage in strong reinforcing UD fibres or the weaker compliant matrix. Micro-notches led to micro-cracking in resin-rich regions, which developed into near-surface longitudinal splits. Some of these splitting cracks got deflected or arrested by the BB and could lead to debonding of UD bundles and BB. These splitting cracks, and all the constituent phases including matrix, UD fibre bundles, backing bundles and background were automatically segmented in the XCT images using the competent machine-learning based Weka classifier in Fiji-ImageJ. The longitudinal morphology of the splits including their proximity to the backing bundles and the surface was exposed.

In the bulk, UD fibre breaks originated close to BB and proceeded more in width than in thickness due to the reduction of fibre volume fraction in the width in width, as opposed to the DTU study. This can be party attributed to a different fibre architecture in the two studies. The clustered UD fibre breaks led to matrix cracks in resin-rich regions, which could set off neighbouring off-axis cracks and simultaneous UD fibre breaks, as observed on the surface. This was essentially the mode of damage transfer within the bulk. UD fibres that were away from the backing bundle exhibited late-stage failure due to the higher fibre volume fraction. In this study as well, fibre break length also increased with the increasing number of cycles. From DVC results, "banding" of strain concentrations was observed across width in higher compliance regions that were resin-rich and had backing bundles running in the same height positions. This was also corroborated with the damaged regions observed predominantly in these bands and with a tensile model that showed higher stresses in these bands. The damage was confirmed manually by scrolling through the ortho XZ slices and is a combination of clustered fibre breaks and matrix cracks, both near the surface and in the bulk. One of these damage clusters matched well with stress concentrations predicted from a monotonic tensile model. This tensile model is created from the first image (undamaged) of the time-lapse sequence using mapped material orientations and tetrahedral elements. This damage cluster then also matches well with the high axial strains observed by DVC, focused near backing bundles and matrix-rich regions. This qualitative agreement between calculated 3D strain maps, predicted stress and confirmed damage from XCT, corroborates the efficacy of the tensile model and the accuracy of DVC strain maps. At some point, the surface and bulk damage likely joined up with larger splits to progress further and eventually lead to complete

failure. However, the sample in this study was not taken to complete failure to enable correlative SEM studies.

Together, all relevant damage mechanisms are identified which can lead to stiffness degradation. The correlative multiscale approach helps us understanding the damage better, in terms of interaction and progression and their relation to key microstructural features, including backing bundles. Backing bundles are found to introduce waviness in the microstructure and initiate damage in UD bundles, but they also aid to deflect the cracks. The strain maps obtained from the DIC-DVC highlight weak links in the microstructure, including matrix-rich regions, damaged UD bundles and surface defects.

This study helps us improve our understanding of the fatigue damage mechanisms. This allows us to design better fibre architecture by optimising the weak links including backing bundles, resin-rich regions, surface defects, and densely packed fibres. The improved composite can withstand higher stresses and longer service life. This also enables more accurate modelling of fatigue behaviour, ultimately pushing the design limits and reducing the cost of energy. Furthermore, the correlative workflow and the image analysis methods can be applied to other type of fibre composites to study a variety of time-dependent phenomena.

Declaration of competing interest

The authors declare that they have no known competing financial interests or personal relationships that could have appeared to influence the work reported in this paper.

Acknowledgements

This study was funded by EU H2020 MSCA Innovative Training Network 'MUMMERING' Grant Number 765604. Additional funding was supplied by Fordonsstrategiska Forskning och Innovation, Grant number 2021-05062. Support from Steffen Baitinger from Saertex for material supply is acknowledged. Beamtime and computing resources were provided by the Henry Moseley X-ray Imaging Facility (HMXIF), established through EPSRC grants EP/F007906/1, EP/ I02249X/1 and EP/F028431/1. HMXIF is part of the Henry Royce Institute for Advanced Materials, established through EPSRC grants EP/ R00661X/1, EP/P025498/1 and EP/P025021/1. PJW acknowledges a European Research Council Advanced Grant Correl-CT No. 695638.

7. A comparative study of a novel and existing segmentation and quantification methods for 3D imaging data of fibre composites

Author contribution statement

Anuj Prajapati: Conceptualization, Methodology, Data acquisition, Software, Validation, Writing – Original Draft, Writing – Review and Editing.

Robert Auenhammer: Methodology, Software, Validation, Writing – Original Draft, Writing – Review and Editing.

Lars P Mikkelsen: Methodology, Supervision, Writing – Review and Editing.

Timothy Burnett: Methodology, Writing – Review and Editing, Supervision, Funding acquisition.

Philip Withers: Resources, Methodology, Writing – Review and Editing, Supervision, Funding acquisition.

Introduction of a novel fibre tracing and quantification workflow for 3D imaging data of fibre-reinforced composites and its comparison to existing workflows

Anuj Prajapati[1], Robert M. Auenhammer[2,3], Amin Garbout[1], Lars P. Mikkelsen[3], Timothy L. Burnett[1] and Philip J. Withers[1]

[1] Henry Royce Institute, Department of Materials, The University of Manchester, M13 9PL, U.K.

[2] Material and Computational Mechanics, Department of Industrial and Materials Science, Chalmers University of Technology, SE-41296 Göteborg, Sweden.

[3] Composites Manufacturing and Testing, Department of Wind and Energy Systems, Technical University of Denmark, DK-4000 Roskilde, Denmark.

anuj.prajapati-2@manchester.ac.uk

Abstract. Fibre-reinforced composites (FRCs) can have a very wide range of spatially variant architectures according to their application. X-ray computed tomography (CT), in concert with three-dimensional (3-D) image analysis of their structure is becoming increasingly important given that conventional 2-D imaging is insufficient to resolve the structures with confidence. Post imaging, there is a need to analyse the images to generate quantitative and statistically relevant information, especially in composites with high fibre volume fractions and complex architectures. This paper introduces a novel image analysis workflow and thoroughly compares its performance to existing state-of-the-. The novel workflow is based in Fiji-ImageJ and has been compared and benchmarked to established workflows in Avizo, Insegt, and the Structure tensor method. The comparison has been carried out across a range of performance and suitability metrics on a condition-variant image dataset comprising of different resolution, noise, and contrast levels. All the four workflows were found to be competent and working well in multiple metrics and on different data types. The novel workflow Fiji-ImageJ performed well both on fibre-tracing and image segmentation, including high accuracy and low false detections. In addition, it fares well on lower system requirements, high information versatility, and is free-to-use Avizo performed best in fibre-tracing on noisier and low-resolution datasets, with the option of seamlessly generating meshes for modelling. Insegt performed best in accuracy for fibre-tracing, requiring the least parameter tuning and was the fastest in fibre-tracing. Structure tensor was only able to calculate gross material point orientation without being able to segment data or perform fibre-tracing, but it was categorically faster, accurate, scalable, required least parameter tuning, and is free-to-use.. This paper gives a precise understanding to the composites community of which methods are best for a scientific statement related to fibre-reinforced composites.

7.1. Introduction

Fibre composites have become mainstream in applications requiring high strength-to-weight and/or high stiffness-to-weight ratio [219]. The highest mechanical performance and load-carrying capacity are usually exhibited by unidirectional composites and originate almost solely from the high-stiffness reinforcements glass or carbon reinforcing fibres. However, manufacturing defects, fibre misalignment or waviness can lead degrade the properties significantly [239]. It is even more crucial in compression as the fibres have to be as straight and aligned as possible to avoid premature kinking at loads significantly below those borne in tension [278], [279].

Until now relatively little 3D quantification of fibre architecture has been reported. This is a crucial requirement both from the point of view of optimising microstructure-performance characteristics but also in terms of image-based modelling [192], [280]. However, several workflows are now emerging for quantitative analysis of 3D image data, and this paper aims to introduce a novel workflow and compare it on the performance and suitability against established workflows on varied samples of imaging data to provide an in-depth guide to the composites community.

7.1.1. Three-dimensional imaging and characterisation

Two dimensional microstructural characterisation has been popular since Sorby considered mineral and metallic microstructures in the 1840s [281] and widely applied since at least the 1920s [282], [283]. Morton et al. [284] in the early 50s used real colour-contrasted fibres embedded in the polymer to study the orientation and fibre morphology under an optical microscope, while different variations and modifications on the same technique came up later [285].

Until recently the most common methods of assessing and calculating local orientation in FRCs are based on destructive ellipsometry and serial sectioning, which work

essentially on 2-D microscopic images of polished samples. The local orientation tensors are derived from the dimensions of the ellipse [286], [287].

There are clear limitations to such methods including:

- The material must be destroyed for measurements, precluding subsequent testing or time-lapse studies to evaluate microstructure-performance relationships.
- The results are ambiguous because it is not possible to distinguish a positive or a negative angle on the elliptical cross sections.
- Repeated measurements need to be scaled up for more curved fibres to capture the fast-changing curvature when recording 2D microscopic image slices for generating a 3D orientation.
- Reduced accuracy and precision for fibres that are near-normal or near-parallel to the cross-section of the image plane, as the change in dimensions of the ellipse is less sensitive to the change in angle with the normal of the plane.
- The process of manual polishing is not automated, and therefore leaves room for user bias, while also being time-consuming and labour intensive. Although this has been mitigated by the development of focused ion beam (FIB) systems coupled to scanning electron microscopes (SEM), which can mill away and image microstructures in an automated fashion [265], it is expensive and can analyse only smaller μm^3 volumes.

These limitations demonstrate the need for non-destructive methods of fibre microstructure quantification and analysis through visual data available through 3D imaging techniques, including x-ray computed tomography (XCT) [123], [288] and

confocal laser scanning microscopy [289] The latter has limitations of only penetrating depths up to ~100 microns well as inadequate fluorescence from the materials.

Today, x-ray tomography offers unparalleled advantages for 3D imaging and analysis of complex microstructures, including non-destructive, three-dimensional, multiscale, multi-modal, and time-lapse imaging, all of which add enormous insights into the analysis [75], [113], [245], [290], [291]. For example, resolving glass fibres with ~17 µm diameter, a 4 µm pixel size is feasible which enables 1.2 mm^3 of volumes to be investigated. After the data is acquired and reconstructed, the 3D image can be used to analyse the fibrous structures through a variety of methods which mostly include assigning labels to the phases including fibres, matrix, and/or interfaces. This process is called 'segmentation' and outputs a multi-phase labelled image. Although certain measurements can be taken on the reconstructed grayscale data, it is preferred to segment the data before analysis and parameter extraction.

Yang et al. [292] in the early 2000s extracted individual fibrous information from both real and simulated 3D XCT data with the convolution of the Gaussian filter and a final 'thinning' operation to generate skeletons. Czabaj et al [293]. used a template-matching algorithm to segment fibres and generate 3D meshes for finite element (FE) based simulations. More recently, Sencu et al. [294] have used combined processing of Bayesian filter and erosion to segment and generate FE models of CFRPs. Since 2020, numerous research papers [295]–[300] relating to the characterisation of fibrous microstructure have been published, including image characterization methods based on deep learning and neural networks [301], [302], structure tensors (using intensity gradients in images to compute orientations) [110], extended particle analysis (using particle tracking to compute fibre orientations) [303] among others.

This paper aims to introduce a novel image analysis workflow for 3D data of fibre-reinforced composites and compare-benchmark it against established workflows commonly used for fibrous microstructural characterization. This paper will give an understanding to the composites community of workflows that are best for a scientific statement related to fibre-reinforced composites.

7.2. Experimental methods and materials

The workflows that have been selected for this paper are some of the most used and accessible tools of FRC imaging data analysis today. Some of them are free to use under open-source licenses while some are available through proprietary licenses. The novel and the established workflows are introduced in brief below.

7.2.1. Fiji-ImageJ

Fiji is an open-source image processing distribution of ImageJ, conceived as public domain software for processing and analysing scientific images. It was developed by the Unites States National Institute of Health and partners [203] primarily to solve problems in medical imaging and it quickly evolved as a comprehensive tool for broader scientific imaging analysis. Fiji is an extensive distribution of ImageJ which includes numerous native and user-contributed plugins covering an extremely wide variety of image processing routines; denoising, segmentation, registration, stitching, skeletonisation and many more.

Regarding FRCs, the software tools available within Fiji-ImageJ are potent at segmenting different phases including pores, fibre bundles, matrix, and individual fibres – including the damage in them. One of the tools, Trainable Weka Segmentation [204] (TWS) derived from random forest [205] machine learning is adept at segmenting noisy data. It uses annotation on a training image to segment the remaining data automatically, in a way similar to the Insegt software. Using this method as part

of a bigger, novel workflow developed for this paper, individual fibre centrelines can be traced and used to study the morphology and relevant information.

The workflow is explained below, illustrated in Figure 7.4.

A) It starts with a 3D image stack containing fibre cross-sections as blobs, imported into Fiji-ImageJ.
B) Trainable Weka Segmentation 2D is used to segment fibre blobs via manually annotating fibres and background, leading to a labelled result of fibre blobs separated from the background of the matrix and other phases. This is then binarized into the black background and white fibres.
C) Detected fibre blobs are separated by watershed.
D) The centroid of each separated blob corresponding to the fibre centre is calculated by finding local maxima.
E) Once the fibre centres are detected, these can be labelled uniquely by running a connected components routine available in Fiji-ImageJ. This returns all the fibres uniquely labelled which lie on a close trajectory.
F) These traced centrelines can be overlayed on the fibres for validation.
G) They can also be visualised in 3D within Fiji-ImageJ as shown below.

In addition, Fiji-ImageJ allows in-house morphological analyses through various toolkit plug-ins hosted within Fiji-ImageJ, particularly BoneJ [206] (developed for skeletal image analysis, but useful for fibrous structures), MorphoLibJ [127] (useful for morphological filtering, reconstruction, segmentation, metrology etc.), DiameterJ [207] (useful for calculating statistics on fibre diameters) and Trackmate [208], [209] (useful for tracking, data visualisation, track analysis etc.), among others.

A small script written for this paper returns a .csv file containing the X, Y, and Z positions of all fibre centre-points belonging to a unique fibre centre-line, for all fibres. This allows for bespoke morphology and other relevant calculations inside or outside of ImageJ, facilitating exportability.

These four software packages have been benchmarked and ranked against each other on an extensive range of performance metrics that are introduced and explained below. To effectively assess the performance of these workflows on a variety of images, bespoke XCT datasets of quasi-unidirectional non-crimp glass fibre-reinforced polymers (UD-NCF GFRPs) and unidirectional quasi-unidirectional carbon-fibre reinforced polymers (UD CFRPs) were acquired at various resolution, contrasts, and noise levels.

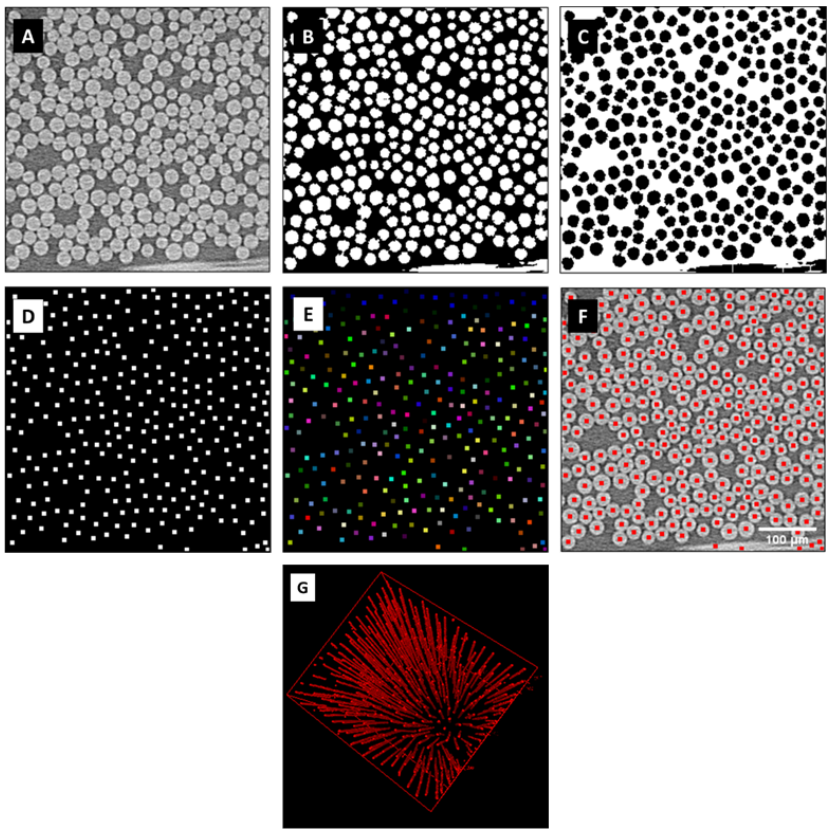

Figure 7.1 The workflow in Fiji-ImageJ is run on a stack of A) grayscale images of fibre cross-sections, which are B) segmented using TWS, these segmented fibre blobs are then C) separated by watershed. For each separated blob, the calculated centroid is a D) fibre centre-point, these are linked by connected components routine to form E) unique fibre centre-lines. The fibre centre-

points are F) overlayed over the grayscale fibres for validation, while G) shows the unique fibre trajectories in 3D.

7.2.2. Avizo

Avizo is a proprietary general image analysis platform and graphical user interface (GUI) from Thermo Fisher Scientific hosting a variety of tools for analysing imaging data, from visualisation to processing and quantification. It has a comprehensive suite of tools for analysing FRCs that can segment multiple phases and damage modes such as pores, fibre bundles, matrix, and individual fibres It also has recently introduced AvizoAI as an artificial intelligence tool for advanced automatic image processing which can be used for segmentation. The platform also has a dedicated tool called XFiber which can trace individual fibres, and generate relevant information such as length, radius, tortuosity, distribution, and orientation tensors, among others.

XFiber uses a template matching method via normalised cross-correlation[195] to match the grayscale features – fibres in this case, to a user-defined parametric cylinder template, which is similar in size to the fibrous feature that needs to be detected. The cross-correlation with a parametric cylinder results in two outputs: a correlation field and an orientation field. The correlation field stores the maximum correlation value, while the orientation field stores the orientation for which the correlation value is maximum, for each voxel. These two fields are then thresholded on minimum correlation values for which fibre centrelines tracing can start and continue. Linking each centre point across all the orthogonal image slices using a search cone generates uniquely identified 3D fibre centre lines which can be used to study 3D morphologies and statistics. This method has been described in Figure 7.1.

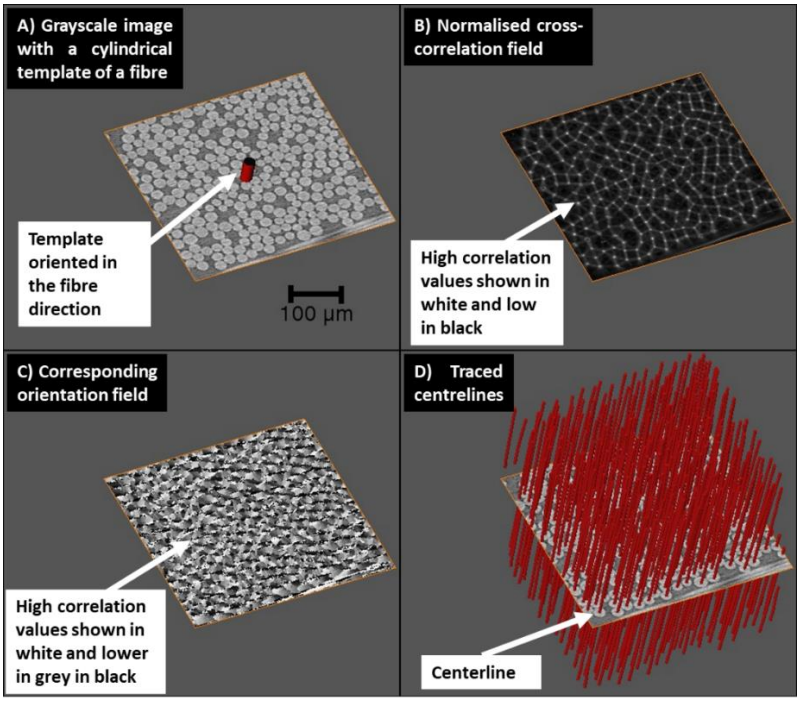

Figure 7.2 A) Greyscale image in Avizo which is cross-correlated with a user-specified cylindrical template, leading to a corresponding B) correlation field and an C) orientation field. D) These fields are then thresholded to generate fibre centre-points which are linked together using a search cone, leading to a unique traced fibre centre-line.

7.2.3. Insegt

This algorithm is based on computer vision and is classed as a supervised segmentation method, manifest as a MATLAB and Python-based graphical user interface (GUI) and code called Insegt [20], [131]. We use the MATLAB version for this paper. The algorithm is taught what a fibre centre looks like, using an annotated training image. The information it learns on the training image is stored in a matrix referred to as a 'dictionary', once the dictionary is learnt, it can be looked up for segmenting fibre centres and matrix. Therefore, this method falls under the purview of 'supervised learning'.

The workflow starts with an annotated image marked with fibre centres and matrix, used for training the algorithm on what a fibre centre and fibre background look like. The training image should be similar to the 3D imaging data that needs segmenting – a cross-sectional slice containing fibre blobs.

This training image is fed into ‘dictionaries’; a matrix containing information on the type of pixels that belong to classes of either the fibre centres or the matrix. Looking up these dictionaries for unknown pixels generates a probability map of the likelihood of a pixel belonging to either of the classes. This algorithm is run over all the slices and the fibre centres are computed. Then each fibre centre pixel is linked with a corresponding fibre pixel in the previous and the next slice, with a user-defined search cone of fixed radius, thus the 3D trajectory of each fibre is traced, which can be used to study the orientation and morphology of the fibres.

The steps to calculate the fibre trajectories are shown in Figure 7.2, where the GUI has an annotation and a live feedback window giving the result of learning from annotations. These blobs are overlayed on the fibres and the centroids of each blob are fibre centres, which are linked to form unique fibre trajectories, also shown in 3D.

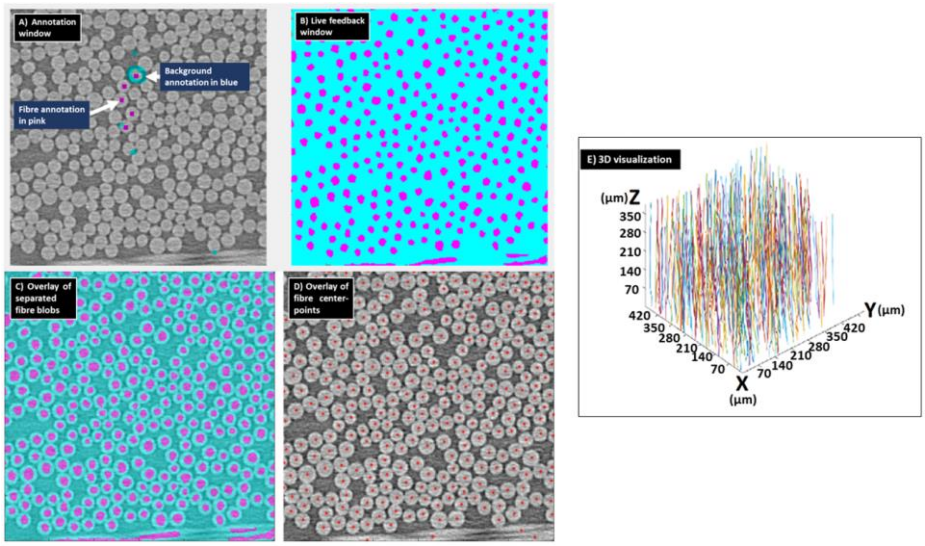

Figure 7.3 A) The fibre ‘blobs’ can be segmented and separated by annotation; B) feedback can be viewed live in the GUI to improve if required. C) Centroids for these blobs are computed for D) fibre centre-points, and these are linked by a search cone to form E) unique fibre centrelines. The streaks in the bottom of each image are ‘backing bundles’ which run orthogonal to the ‘unidirectional’ fibres (detailed in section 7.3).

7.2.4. Structure Tensor

While the above methods of Avizo and Insegt allow tracing of individual fibres, sometimes only the orientation at each material point is of engineering relevance, as the directional properties in composite materials are exploited. This orientation information is particularly useful in modelling and simulations to study directional mechanical properties. One such method to calculate material point orientations is by computing the structure tensor [196]–[198]. There are several structure tensor methods developed for fibre orientation analysis available [194], [196], [199]. In essence, the orientation of structures is estimated by computing gradients in all directions leading to the direction of the smallest gradient, indicating the strongest orientation in that direction. The changes in the greyscale value are computed around a certain point and can be expressed in a 3x3 matrix [197]. In this study we use the method developed at the Technical University of Denmark, available in Python and MATLAB, of which the Python version was used in this study. Their structure tensor method comes with several advantages. It is publicly available [200], it has proven its robustness in several studies [194], [197], [201], it was successfully used as the basis for finite element modelling of fibre-reinforced composites [192], [202], and only two parameters need to be set. The noise scale parameter σ should be chosen large enough to filter noise from the greyscale image but small enough to account for local orientation changes. The integration scale parameter ρ is the standard deviation of the Gaussian Kernel which averages orientations around the regarded point. Larger values therefore average larger regions.

The code is written in Python without a graphical user interface. One of the examples is shown in Figure 7.3, which gives a colourmap of all fibres detected to be unidirectional along the z-axis.

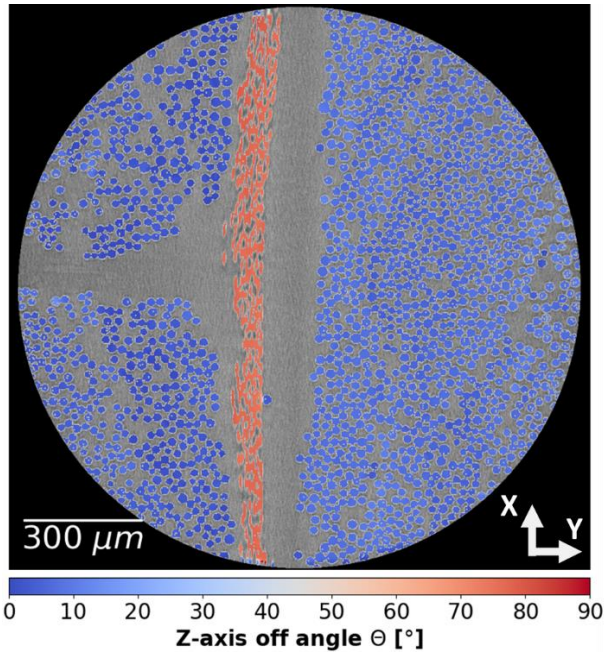

Figure 7.4 Orthogonal unidirectional and backing fibres for a wind turbine section observed via a colourmap of each voxel having ~0° and ~90° directionality towards the z-axis.

7.2.5. Materials

Both the GFRP and the CFRP samples were supplied by Saertex GmBH. The GFRP comprises UD E-glass non-crimp fabric, embedded in epoxy using vacuum-assisted resin transfer moulding (VARTM). The 0° angle UD bundles are stitched to the 90° angle backing bundles in a layup of $[[0/90]/[90/0]_s]$. The fibres have an average diameter of 20 µm. The CFRP is manufactured by VARTM, and the backing bundles are made of glass fibres of diameter ~20 µm instead of carbon fibres, while UD carbon fibre has an average diameter of ~ 7 µm. Although CFRPs have not been studied in this thesis, they have been employed in this paper study as they are a suitable candidate for generating a poor-contrast CT dataset. The contrast between carbon fibres and epoxy is quite poor and serves as a good dataset to check the effectiveness of each of the workflows.

This material architecture , made of fibres aligned in two different directions of 0° and 45° was chosen as a trade-off between a fully unidirectional and an angle-

orientated fibrous structure, helping in assessing the workflows' capability to analyse data omnidirectionally.

Scans	Exposure time	Voxel size	Sample type	Datasets	Physical size	Memory size	Remarks
G1	16s	1.5µm	Glass	G1 (~1000^3 voxels)	$1.01mm^3$	629.3 MB	**High-fidelity Reference**
				G1_Sub (300^3 voxels)	$0.43mm^3$	51.5 MB	
G2	4s	3µm	Glass	G2_Sub (145^3 voxels)	$0.43mm^3$	5.8 MB	Resolution variant
G3	20s	5.8µm	Glass	G3 (~1000^3 voxels)	$3.9mm^3$	589.2 MB	Resolution variant
				G3_Sub (76^3 voxels)	$0.43mm^3$	0.8 MB	
G4	2s	1.5µm	Glass	G4_Sub (300^3 voxels)	$0.43mm^3$	51.5 MB	Noise variant
C5	20s	1µm	Carbon	C5_Sub (350^3 voxels)	$0.35mm^3$	81.8 MB	Contrast variant

Table 7.1 Scanning conditions and associated metadata for each scan and the extracted datasets used to compare each of the workflows. The optical magnification of 4x, accelerating voltage of 80 kV and pixel depth of 16-bit were the same for all scans. There are three scans with variant resolution levels – G1, G2, and G3; two with variant noise levels – G1 and G4; two with variant contrast levels – G1 and C5. The C5 scan, on account of carbon fibre diameter (~7 µm) being approximately three times smaller than glass fibre (~17-21 µm), becomes a low contrast, and a low-resolution scan.

The scans were undertaken on a Zeiss Versa 520 scanner at the Henry Moseley X-ray Imaging Facility. From each scan, cubical volume datasets were extracted in two formats, full-field scans, and sub-volumes. The sub-volumes of G1_Sub.tif, G2_Sub.tif, G3_Sub.tif and G4_Sub.tif correspond to the same material region-of-interest (RoI) and have been cropped accordingly. All of the image stacks were saved in 3D TIFF formats.

The scanning conditions are summarized in Table 7.1.

7.3. Results and discussion

This section introduces and explains the results on performance metrics that the four workflows have been compared and ranked on. The performance on these metrics has been assessed on Windows 8 64-bit, i7 3.30GHz (12 CPUs) processor with 64 GB RAM, and a GPU of NVIDIA GeForce GTX TITAN X with 48 GB of memory.

7.3.1. Performance metrics and results

These methods are ranked from 1 (best) to 4 (worst) according to the following performance parameters.

1) **Output information versatility**: This has been assessed for the type of information/data types/data formats that can be output through the workflows, including;
   - labelled binary/ternary/multi-phase image data.
   - morphological parameters for individual fibres/matrix: fibre volume fraction, curvature, length, orientation information etc.

   The workflow that can handle and output multiple types of information is ranked higher.

- Result: Avizo is ranked 1st, as it is an end-to-end visual programming and imaging environment where the fibre centre-lines can be tracked using the XFiber module and can be used to segment the fibres. These fibre centre-lines and segmentations can be exported in a variety of formats, meshed for finite element modelling, and can be used to compute statistics on the morphology including curvature, number, population, volume fractions etc. The information available for the fibre centrelines tracked are curved and chord

lengths, orientation angles theta and phi, tortuosity, and orientation tensors. The bundles and tertiary features including voids can also be segmented using thresholding tools available in Avizo. Every step can be carried out in the same visual programming environment, which bypasses the need to code every operation. Some higher-end modules are available through user-contributed libraries called Xtras^{TM}. Operations and processing modules not available in the Avizo library can be coded in Tcl and Python using application programming interfaces (APIs), while for C++ a dedicated extension called XPand^{TM} is available.

Fiji-ImageJ is ranked 2nd for its versatility through a comprehensive image analysis environment. It allows analysis without the need to write extensive codes, through its ever-increasing library of plugins which are contributed by users and developers. It allows for advanced computer vision-based segmentation including TWS, which can segment various phases with ease. The novel workflow in Fiji-ImageJ introduced in this paper now allows for tracing individual fibre centrelines and morphological analyses. Several plugins available for advanced analyses within ImageJ, which are mentioned in the workflow introduction make it an attractive workflow to study and analyse FRCs imaging data.

Structure tensor and Insegt are both ranked 4th as ST only generates one orientation tensor per material point (at both fibre level and bundle level), while Insegt only generates individually traced fibre centre-lines. Neither of these has tools to segment/label material phases or generate meshes for modelling from labelled data. From a broader perspective, Python (coding

environment for ST) and MATLAB (coding environment for Insegt) both have image processing capabilities which include material segmentation etc.

A comparison of void and bundle level segmentation from both TWS and texture classification in Avizo is shown in Figure 7.5 and Figure 7.6.

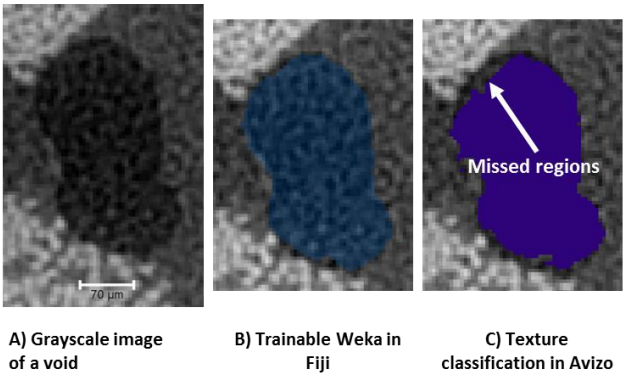

Figure 7.5 Void segmentation from a A) grayscale XCT image (G3) on the left. B) Void segmented using annotation and subsequent prediction in TWS. C) Texture classification used to segment void in Avizo. It is observed that TWS yields more accurate segmentation than texture classification.

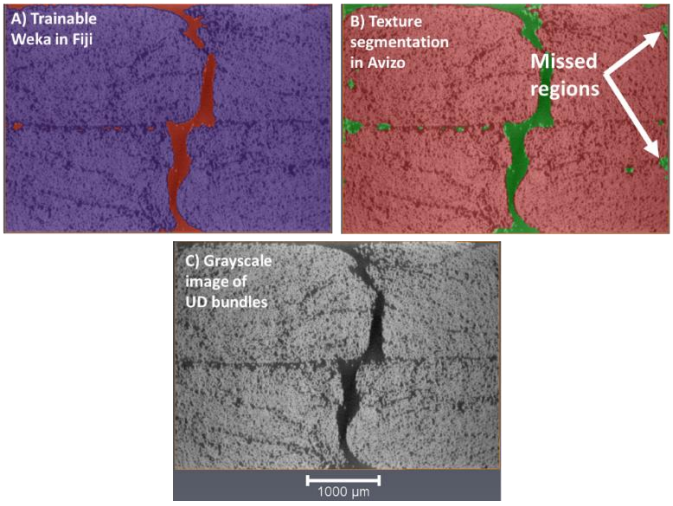

Figure 7.6 Bundle level segmentation via A) TWS and B) Texture classification in Avizo in a C) grayscale XCT (G3) image. Although similar, TWS results are slightly better as texture classification misses some fibrous regions on the periphery.

2) **Computational time**: This has been assessed as the time each workflow takes to run on a representative volume of i) ~300 fibres at fibre scale (*G1_sub.tif*) and ii) 2-3 bundles at bundle scale (*G3.tif*).

- Result: The structure tensor is fastest and is ranked 1st in both cases if only material point orientation is required. As shown in Table 7.2, for individual fibre tracing, Insegt is ranked 2nd, followed by Avizo and then Fiji-ImageJ. For bundle-level segmentation, Avizo does better than Fiji-ImageJ.

Dataset	Time in Avizo	Time in Fiji-ImageJ	Time in Insegt	Time in Structure Tensor
G1_Sub.tif	8 mins (fibre-tracing)	11 mins (fibre-tracing)	7 mins (fibre-tracing)	17 seconds (tensor calculation)
G3.tif	13 mins (texture segmentation)	27 mins (TWS)	N/A	<1s (tensor calculation)

Table 7.2 Time required for all four workflows to run on fibre-level data G1_sub.tif and bundle-level data G3.tif.

3) **System requirements**: This is assessed as the minimum PC system requirements of RAM, GPU, and CPU as a performance metric. Methods with lower requirements are ranked higher.

- Result: Structure Tensor – Minimum requirements set by the Python environment, 4 GB RAM (limited by data size).

  Fiji-ImageJ – Windows (XP, Vista, 7, 8 and 10), Mac OS X 10.8 onwards and Linux (AMD64 and x86), 4 GB RAM (limited by data size), Java 8 installation.

  Avizo – Windows 10 64-bit, with only version 2020.3 working on macOS, Nvidia CUDA architecture required.

  Insegt – Windows 10 64-bit onwards, 4 GB RAM (limited by data size), MATLAB license required.

Fiji-ImageJ and Structure Tensor are ranked 1st as they have the least minimum requirements, followed by Insegt and then Avizo.

4) **Parameter tuning**: This is assessed by the number of attempts the workflow takes to arrive at an optimum result. The workflows that require more attempts are ranked lower. This will be calculated at both the fibre scale (*G1_Sub.tif*) and bundle scale (*G3.tif*).

- Result: Structure tensor and Insegt are both ranked 1st as ST only requires two parameters ρ and σ – the former filters out the noise while maintaining the image texture, and the latter defines the neighbourhood over which the orientation information is averaged. Insegt only requires manual annotation for training the algorithm. The default values work well on a range of fibre-level data. The option of live feedback from annotation mitigates parameter guesswork, as shown in Table 7.3.

  Avizo is ranked 3rd as XFiber requires parameters defining the cylinder template which is calculated on the fibrous feature itself. Parameters for line tracing can be estimated by the results from cylinder correlation. Estimation of parameters based on results of previous steps mitigates guesswork. Texture segmentation requires a few attempts (three in this case) to optimise, but this is done on a single image by default and then the optimised segmentation is run on the whole data.

Fiji-ImageJ is ranked 4th as it requires tuning in TWS step – 2 annotation attempts to get the fibres and matrix segmented. The result of the parameter selection can only be observed after TWS has run over the whole data; this can be alleviated by optimising the parameters on a smaller sub-volume and upscaling it over the whole imaging data.

Dataset	Number of attempts in Avizo	Number of attempts in Fiji-ImageJ	Number of attempts in Insegt	Number of attempts in Structure Tensor
G1_Sub.tif	1 (fibre-tracing)	2 (fibre-tracing)	1 (fibre-tracing)	1 (tensor calculation)
G3.tif	3 (texture segmentation)	2 (TWS)	N/A	1 (tensor calculation)

Table 7.3 Number of attempts required to achieve an optimum result by the four workflows.

5) **Scalability**: This is assessed by how much the computational time for the workflow goes up from sub-volume (*G1_Sub.tif*) to the full-scale data size (*G1.tif*). Workflows with less time increase are ranked higher.

- Result: For material point orientation, Structure Tensor is the fastest with the lowest increase in time when scaled up, for this, it is ranked 1st. Insegt is ranked 2nd for the fastest fibre-tracing and lower increase when scaled up. Accordingly, Avizo is ranked 3rd and Fiji-ImageJ is ranked 4th for slowest fibre-tracing and the highest increase in time while scaling up. This is shown in Table 7.4.

Dataset	Time in Avizo	Time in Fiji-ImageJ	Time in Insegt	Time in Structure Tensor
G1_Sub.tif	8 mins (fibre-tracing)	11 mins (fibre-tracing)	7 mins (fibre-tracing)	17 seconds (tensor calculation)
G1.tif	55 mins (fibre-tracing)	63 mins (fibre-tracing)	44 (fibre-tracing)	4 mins (tensor calculation)
G3_Sub.tif	15 seconds (texture segmentation)	22 seconds (TWS)	N/A	<1 second (tensor calculation)
G3.tif	13 mins (texture segmentation)	27 mins (TWS)	N/A	<1 second (tensor calculation)

Table 7.4 The increase in computational time for a workflow when run on a smaller sub-volume and the full-field volume of fibre-level data (G1_Sub.tif and G1.tif) and bundle-level data (G3_Sub.tif and G3.tif).

6) **Performance on different spatial resolutions**: This is assessed by the workflows' performance for fibre tracing and orientation calculation on three datasets with a pixel size of 1.5 µm (*G1_Sub.tif*), 3 µm (*G2_Sub.tif*), and 5.8 µm (*G3_Sub.tif*). Fibres were manually counted by a three person-panel by scrolling through the high-resolution G1_Sub.tif to confirm continuity and reduce user error, there were 311 fibres with at least more than half the cross-sectional blob in at least two XCT image slices. A higher number of true detections led to a higher rank, with false detections counting as a penalty and resulting in a lower rank.

- Result: The performance and efficacy of these workflows on datasets with different spatial resolutions are shown in Figure 7.7 and statistically in Table 7.5. Avizo's XFibre has lower false detections and is the only workflow that is able to successfully trace fibres on the lowest resolution data, due to this it is

ranked 1st for fibre-tracing at variant resolutions. Fiji-ImageJ is ranked 2nd for lower false detections, while Insegt is ranked 3rd for comparatively higher false detections. Structure tensor's orientation calculation is not included in the fibre-tracing comparison but is exceptional at generating consistent orientation information at all the three resolution levels, as evidenced in Figure 7.8.

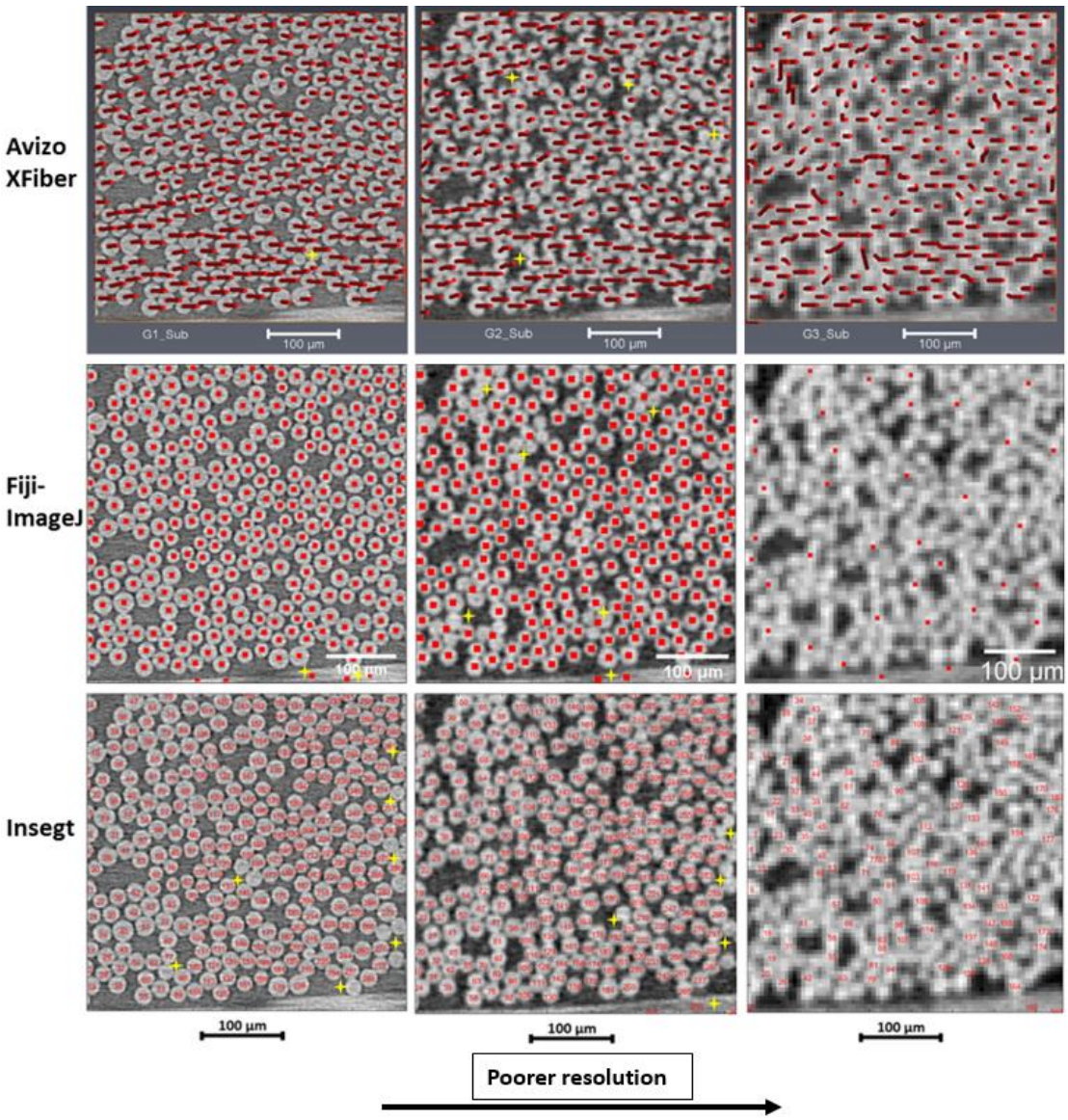

Figure 7.7 Detection of fibre centrelines by the three fibre-tracing workflows on the resolution-variant dataset of G1_Sub.tif, G2_Sub.tif, and G3_Sub.tif. The voxel size increases from left to right, and the results worsen. The yellow marks pinpoint some of the false detections, including both false positives and negatives. Except for Avizo, both the fibre-tracing workflows fail to detect fibres on the low-resolution volume. the left is the actual image on which the algorithm was run, the right image is just denoised for better visualisation to assess the matching of centerlines to the fibres. The streaks in the bottom of the images are backing bundles running orthogonal to the UD fibres.

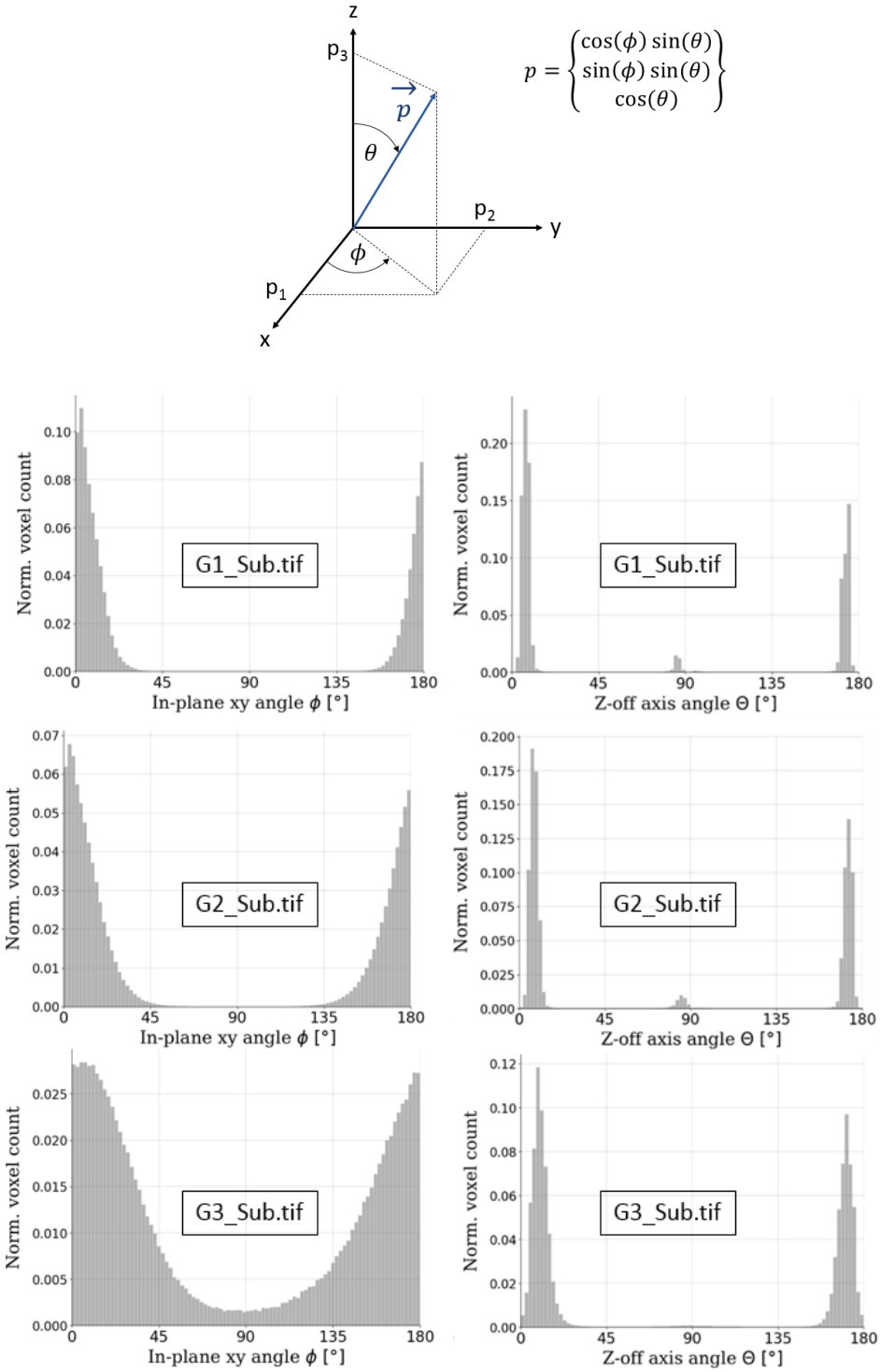

Figure 7.8 Orientation distribution for each resolution-variant dataset calculated by the structure tensor workflow, as in-plane angle Φ and Z-off axis angle Θ, the angles are defined with respect to the axes. The efficacy of this workflow is proven by only a small change in the orientation distribution when calculated on three significantly different voxel sizes.

Dataset | Workflow		Avizo's XFiber	Fiji-ImageJ	Insegt
G1_Sub.tif	No. of traced fibres	311	316	298
	False positives	1	5	0
	False negatives	1	0	13
	% False detection	0.64 %	1.6 %	4.1 %
G2_Sub.tif	No. of traced fibres	267	295	289
	False positives	2	13	21
	False negatives	46	29	43
	% False detection	15.4 %	13.5 %	20.5 %
G3_Sub.tif	No. of traced fibres	265	N/A	N/A
	False positives	7	N/A	N/A
	False negatives	67	N/A	N/A
	% False detection	23.7 %	N/A	N/A

Table 7.5 Number of traced fibres by three workflows for variant resolution datasets including false positive and false negative detections, also reported as a percentage false detection calculated over 311 fibres.

7) **Robustness to noise and contrast:** This has been assessed by the workflows' performance for fibre tracing on datasets which have been noised by lower exposure time (*G4_Sub.tif*) and have poorer contrast from CFRP (*C5_Sub.tif*), for fibre-tracing. A higher number of true detections lead to a higher rank, with false detections counting as a penalty and resulting in a lower rank.

- Result: Avizo's XFiber is ranked 1st due to the lowest number of false detections, with minimal false positives. Fiji-ImageJ is ranked 2nd, with false detections mostly at image boundaries. Insegt is ranked 3rd with a higher number of false detections, both at image boundaries and the bulk. This is shown in Figure 7.9 and Table 7.6. As with the resolution-variant results, Structure tensor's orientation calculation is not included in the fibre-tracing comparison but is exceptional at generating consistent orientation information at both noise levels. This is shown in Figure 7.10.

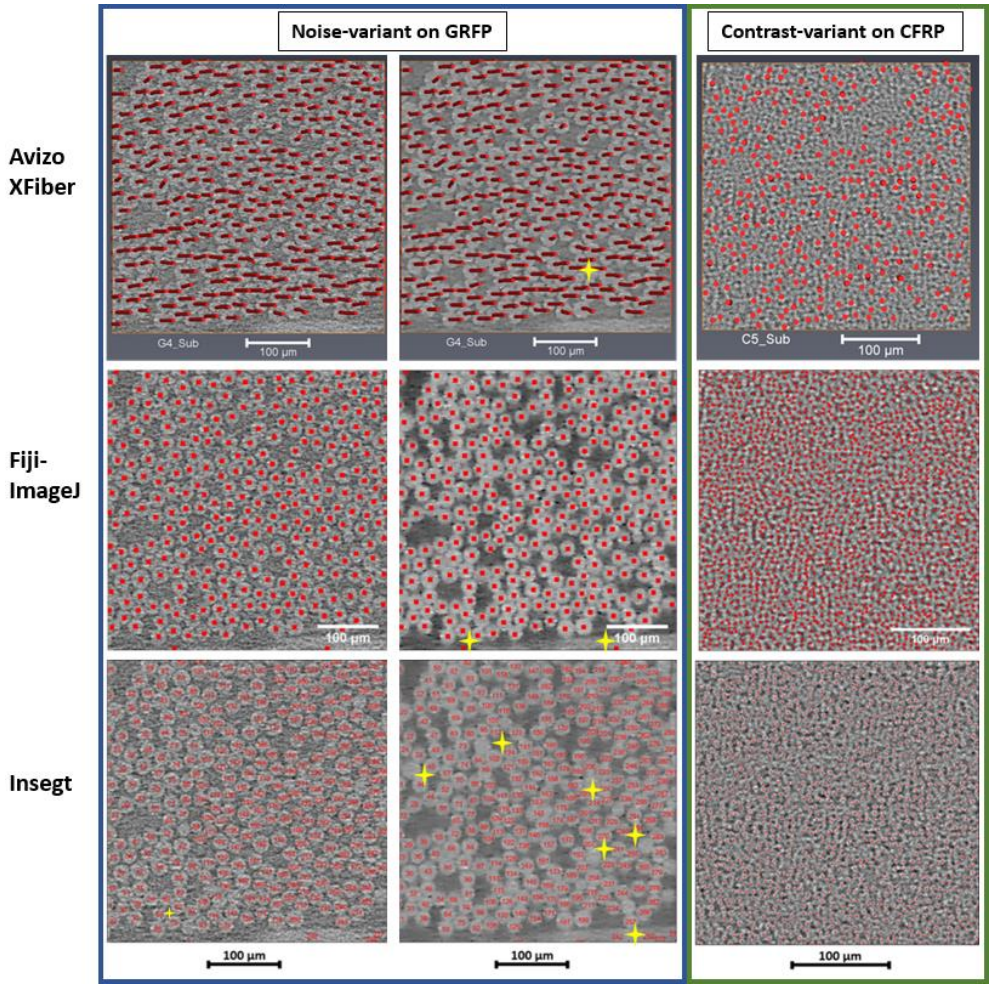

Figure 7.9 Detections of fibre centrelines on G4_Sub.tif. On the left are the actual images on which the workflow was run, the middle images are denoised for better visualisation to assess the matching of centerlines to the fibres. The yellow marks pinpoint some of the false detections, including both false positives and negatives. All the fibre-tracing workflows fail on C5_Sub shown in the images on the right due to poor contrast and low resolution.

Dataset | Workflow		Avizo's XFiber	Fiji-ImageJ	Insegt
G4_Sub.tif	No. of traced fibres	305	307	305
	False positives	1	11	23
	False negatives	7	15	29
	% False detection	2.5 %	8.3 %	16.7 %

Table 7.6 Number of traced fibres on the noisier dataset G4_Sub.tif, including false positive and false negative detections, also reported as a percentage false detection calculated over 311 fibres.

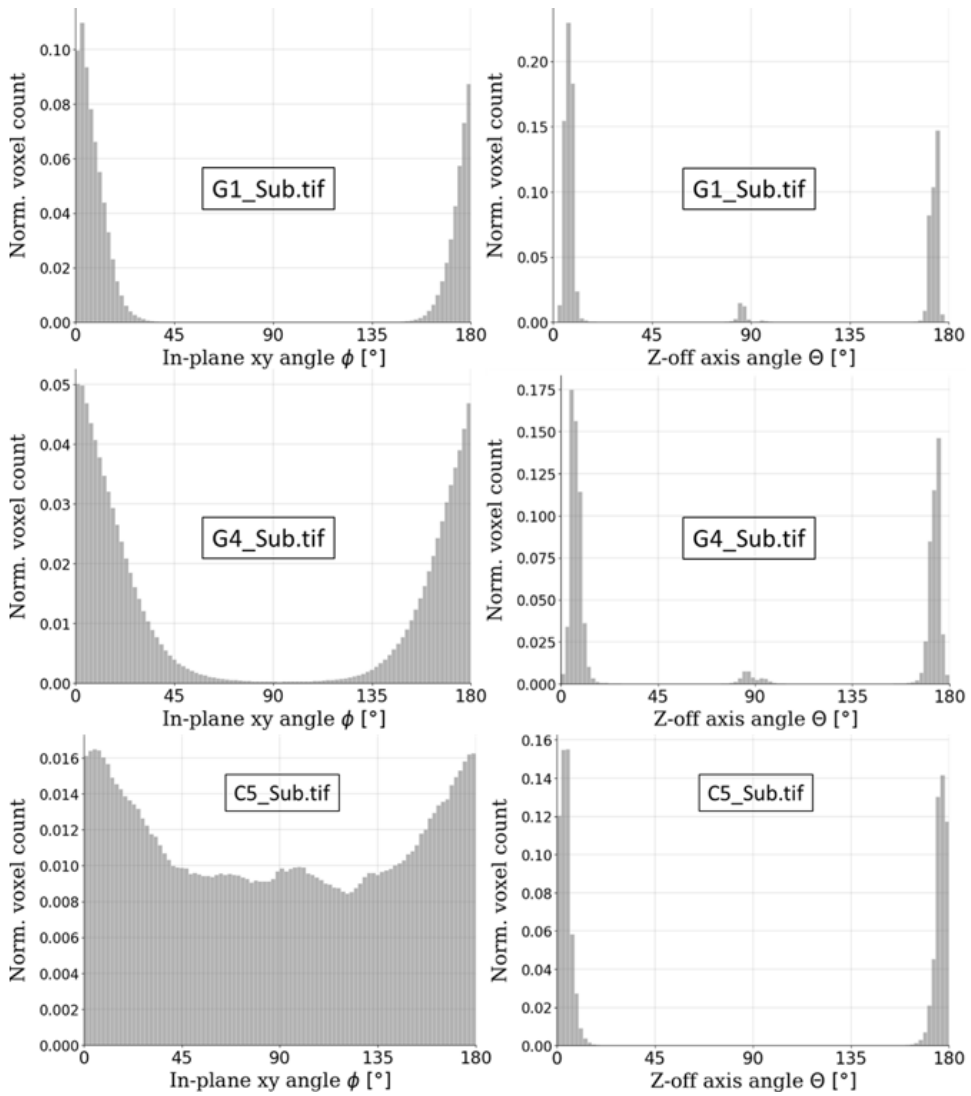

Figure 7.10 Orientation distribution for a noisy dataset (G4_Sub.tif), compared to a less noisy dataset (G1_Sub.tif), calculated by the structure tensor workflow, as in-plane angle Φ and Z-off axis angle Θ. There is only a minor change in the orientation distribution for two distinctly different noise levels. Structure tensor works to an extent on C5_Sub.tif, while the in-plane Φ has a large spread, the Z-off axis angle Θ shows dominant orientation in the Z direction as consistent with the UD fibre direction.

8) **Accuracy in fibre-tracing:** The measure of the accuracy is defined here as the absence of any short-range curvature in fibre trajectory, as the UD fibres are essentially straight and only exhibit long-range curvatures, short-range curvature or deviation from a straight line would indicate inaccurate tracing. As shown in Figure 7.11, this can be calculated as the value ‘d’ by averaging deviation ‘c’ over the whole fibre trajectory with ‘n’ centre-points. The fibre

centre-points' coordinates have been extracted from each of the workflows for 4 fibres visually confirmed to be comparatively straighter, in the high-resolution dataset G1_Sub.tif. These centre-points were fit on a straight line via linear regression, and the average deviation d on both the XY plane and XZ plane as d_{XY} and d_{XZ} have been reported. Workflows with lower total deviation from a straight line, over the whole fibre trajectory are ranked higher.

$$\boldsymbol{d} = \frac{\sum_{i=1}^{n} c_i}{n} \quad \text{Equation 1}$$

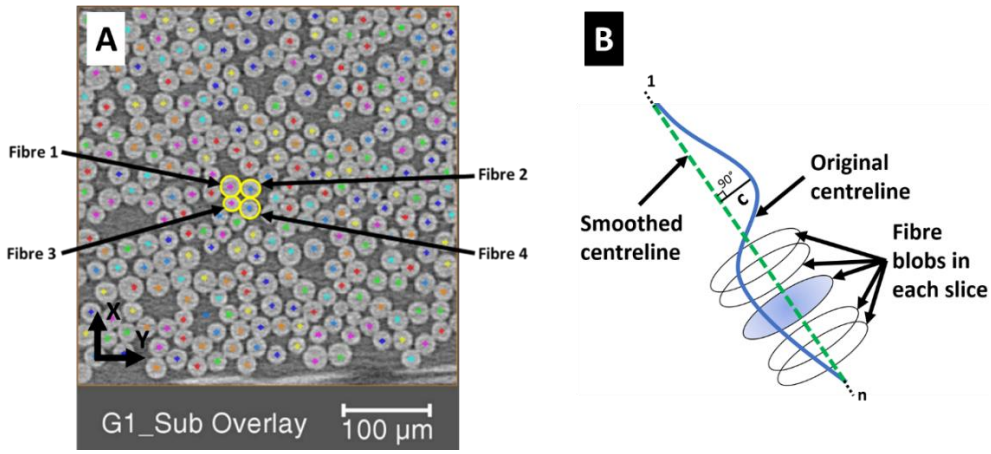

Figure 7.11 A) Four 'straighter' fibres from G1_Sub.tif that are selected for accuracy assessment. B) Short-range curvature of a fibre trajectory is calculated as the deviation from a straight line, and 'c' is the perpendicular distance between an actual fibre centre-point and its corresponding point on the fitted straight line.

- Result: Comparing both the d_{XY} and d_{XZ}, Insegt is the most accurate in tracing fibres, for which it is ranked 1st. It is followed by Fiji-ImageJ due to lower deviation, and then Avizo for higher overall deviation and poorer sampling of only 20 centre-points. This is shown in Figure 7.12 and Figure 7.13.

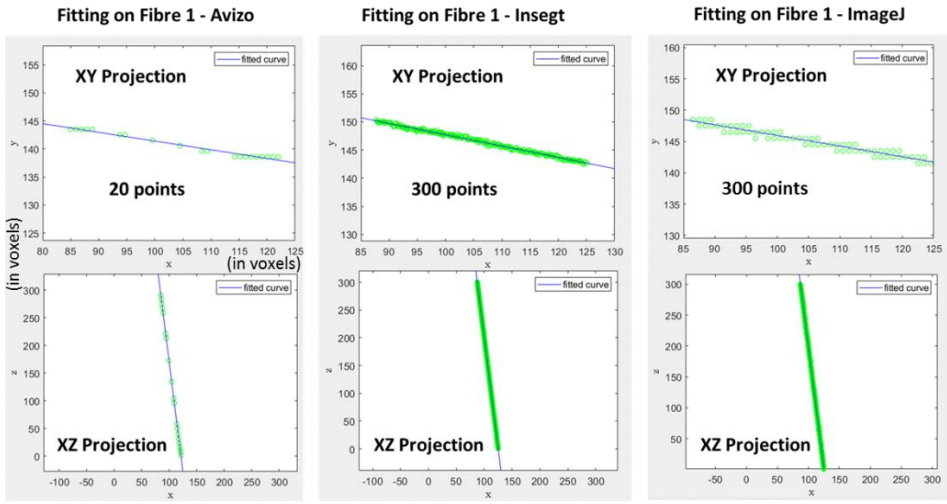

Figure 7.12 Projections of the straight-line fitting through Fibre 1's centre-points for both XY and XZ planes. Notably, Avizo has only 20 centre-points through the entire trajectory while Fiji-ImageJ and Insegt both have 300 unique points for 300 z-slices.

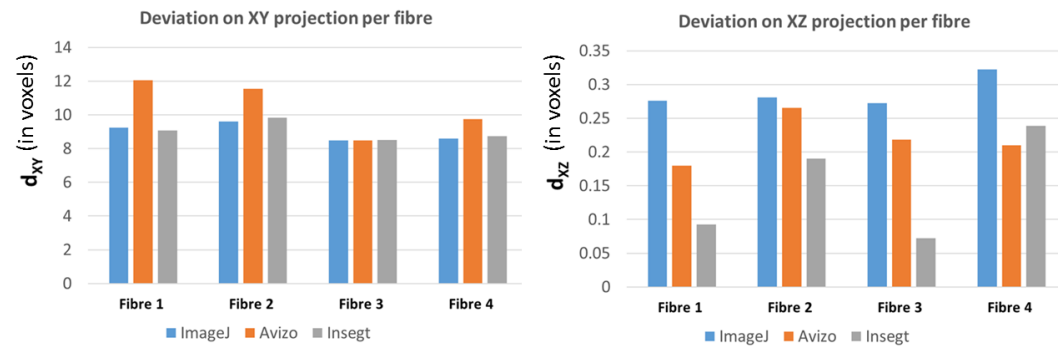

Figure 7.13 Average deviation 'd' projected on both XY and XZ planes in terms of d_{XY} and d_{XZ} calculated on four fibres from G1_Sub.tif. The d_{XY} is nearly identical for Fiji-ImageJ and Insegt, followed by Avizo. While the d_{XZ} is insignificantly smaller and deviation is in the sub-voxel range compared to d_{XY}, it is lowest for Insegt, followed by Avizo and then ImageJ.

9) Feasibility for modelling: This is evaluated on how suitable the segmentation method is as the basis for creating a model on the fibre level. This includes meshing the output labels, exporting the mesh, fibre orientation & bundle waviness and computing fibre volume fraction (local and global).

- Result: Avizo is able to create, improve and output meshes directly. However, the quality of automated mesh generation is limited and cannot be compared with a commercial finite element pre-processor. Further, the mesh manipulations options are rather poor. The possibility to output a mesh and fibre orientations is unique for Avizo though. In combination with a finite element pre-processor and a fibre mapping algorithm accurate tensile modulus prediction of FRC based on 3D image data can be made [32]. Therefore, Avizo is ranked 1st. All other methods can be used for finite element modelling as well, but they require an external mesh source. For ST an open-source code is available that creates a model with fibre orientations given an external mesh based on the image data [38], which gives ST a second place. Fiji-ImageJ and Insegt have been successfully used for modelling as well, but no integrated open-source solution is available.

10) Price: This has been assessed as the financial cost of using these workflows through proprietary software licenses. Workflows available through free software packages have been ranked higher.

- Result: Structure tensor and Fiji-ImageJ are ranked 1st as they both are hosted in free-to-use software packages, while Fiji-ImageJ has its own GUI, ST can be used in any Python integrated development environment (IDE). This is followed by Insegt which requires a MATLAB license and then Avizo, which requires a commercial license.

7.3.2. Rankings at a glance

Technique ---------- Performance metric	Avizo	Fiji-ImageJ	Insegt	Structure Tensor	Comments
Information versatility	1	2	4	4	
Computational time	3	4	2	1	
System requirements	4	1	3	1	
Parameter tuning	3	4	1	1	
Scalability	3	4	2	1	
Performance of fibre-tracing on resolution-variant datasets	1	2	3	N/A	ST ranks best for material point orientation calculations
Performance of fibre-tracing on noise-variant datasets	1	2	3	N/A	ST ranks best for material point orientation calculations
Accuracy in fibre-tracing	3	2	1	N/A	ST cannot perform fibre-tracing
Feasibility in modelling	1	4	4	2	
Financial cost	4	1	3	1	

Table 7.7 All the ranking based on the performance metrics shown at a glance.

7.4. Conclusions

A novel Fiji-ImageJ workflow was introduced in this paper, with powerful capabilities of image segmentation and fibre-tracing. Four workflows used to study and analyse imaging data of FRCs – Avizo, Insegt, Structure Tensor, and the novel Fiji-ImageJ have been assessed, discussed, and ranked on performance and suitability metrics on imaging datasets acquired at various different resolution, noise, and contrasts levels.. All four workflows were found to be competent in multiple metrics. Apart from being a full-fledged image analysis environment, Avizo performed best in fibre-tracing on noisier and low-resolution datasets, with the option of seamlessly generating meshes

for modelling. Insegt performed best in accuracy for fibre-tracing, requiring the least parameter tuning and was the fastest in fibre-tracing. Structure tensor was only able to calculate gross material point orientation without being able to segment data or perform fibre-tracing, but it was categorically faster, accurate, scalable, required least parameter tuning, and is free-to-use. The novel workflow Fiji-ImageJ performed well both on fibre-tracing and image segmentation, including high accuracy and low false detections. In addition, it fares well on lower system requirements, high information versatility, and is free-to-use. There is a possibility to combine multiple workflows to exploit their individual capabilities and improve image analysis, as has been done in [304], where Avizo and Fiji-ImageJ have been used to detect damage in fibre composites automatically using fibre tracing and machine learning.

In addition to the introduction of a novel image analysis workflow, this paper aims to serve as a guided review for wider composites community who intend to employ advanced imaging and its analyses to study fibre-reinforced composites. This paper provides basis for informed decisions on what workflows suit best for a particular data and scientific statement.

Declaration of competing interest

The authors declare that they have no known competing financial interests or personal relationships that could have appeared to influence the work reported in this paper.

Acknowledgements

This study was funded by EU H2020 MSCA Innovative Training Network 'MUMMERING' Grant Number 765604. Additional funding was supplied by Fordonsstrategiska Forskning och Innovation, Grant number 2021-05062. Support from Steffen Baitinger from Saertex for material supply is acknowledged. Discussions with Daniel Lichau and Ali Chirazi from Thermo Fisher; Monica Emerson, Vedrana Andersen Dahl, and Anders Bjorholm Dahl from DTU are acknowledged. Beamtime was facilitated by Julia Behnsen and provided by the Henry Moseley X-ray Imaging Facility (HMXIF), established through EPSRC grants EP/F007906/1, EP/ I02249X/1 and EP/F028431/1. HMXIF is part of the Henry Royce Institute for Advanced Materials, established through EPSRC grants EP/ R00661X/1, EP/P025498/1 and EP/P025021/1. PJW acknowledges a European Research Council Advanced Grant Correl-CT No. 695638.

8. A novel automated workflow involving machine learning to study damage progression of fibre-reinforced composites by time-lapse 3D x-ray tomography

Author contribution statement

Anuj Prajapati: Conceptualization, Methodology, Software, Validation, Writing – Original Draft, Writing – Review and Editing.

Daniel Lichau: Methodology, Software, Validation, Writing – Review and Editing.

Ali Chirazi: Methodology, Software, Validation, Writing – Review and Editing.

Lars P Mikkelsen: Methodology, Validation, Supervision, Writing – Review and Editing.

Timothy Burnett: Methodology, Writing – Review and Editing, Supervision, Funding acquisition.

Philip Withers: Resources, Methodology, Writing – Review and Editing, Supervision, Funding acquisition.

A novel automated workflow involving machine learning to study damage progression of fibre-reinforced composites by time-lapse 3D x-ray tomography

Anuj Prajapati[1,2], Daniel Lichau[2], Ali Chirazi[2], Lars P. Mikkelsen[3], Timothy L. Burnett, and Philip J. Withers[1]

[1] Henry Royce Institute, Department of Materials, The University of Manchester, M13 9PL, U.K.

[2] Visualization Sciences Group, Thermo Fisher Scientific, Bât E2, 33800 Bordeaux, France.

[3] DTU Wind Energy, Technical University of Denmark, 4000 Roskilde, Denmark.

anuj.prajapati-2@postgrad.manchester.ac.uk

Abstract. Understanding damage evolution is not only key to understanding the mechanical behaviour of fibre reinforced composites but is also paramount in informing and verifying material modelling and simulations. We present a damage detection workflow for locating and quantifying fibre breaks in non-destructively acquired 3D x-ray tomography data of unidirectional (UD) glass fibre-reinforced composite (GFRP). It uses a two-step approach; first, the fibre breaks are automatically located by finding intensity drops along traced fibre centrelines in Avizo; these detected fibre breaks are then used to train a competent random forest Weka classifier in Fiji-ImageJ to improve the first result by eliminating false detections. This two-step complementary approach outperforms traditional machine learning methods in that no manual annotation or accurate ground truth training data are required. This completely automated process makes it exceptionally effective at analysing large batches of image volumes including synchrotron time-lapse studies seamlessly. Additional to the location of fibre-breaks, which identifies the weak links in the material architecture and the 3D progression in microstructure, relevant morphological information on fibre-breaks size is also generated. The results clearly show how clusters of fibre fractures propagate from the angled 45°/90° backing bundles into the 0° UD bundles through thickness, joining up in diagonally aligned localised clusters.

8.1. Introduction

Fibre-reinforced composites (FRCs) have seen a tremendous uptake in structural applications which demand high strength-to-weight and a high stiffness-to-weight ratios [305]. The ability to design and manufacture a bespoke fibre architecture to serve a unique set of mechanical requirements means they can be uniquely optimised for fitness to purpose. Their exceptional properties including high durability, strength, stiffness, and corrosion resistance, mean they are becoming the material of choice for a range of relatively low volume applications in sectors including automotive, aerospace, wind energy, marine etc. [305][219]. FRCs can offer exceptional high-cycle fatigue performance making unidirectional FRCs the materials of choice for load-carrying components in wind blades, where the typical service life can be up to 20-30 years for 10^8-10^9 load cycles [7][306]. The superior mechanical performance derived almost completely from the strong fibres, which upon damage can lead to degradation in strength and stiffness [58], [307]. These fibre-breaks are often the first observable damage features that appear in the microstructure and can give rise to other interacting modes of damage including debonding, matrix cracking, interlaminar and intralaminar macro cracking, eventually leading to failure upon progression [9], [67], [191] . This complex interplay between different damage modes with increased cycling, exacerbated by a non-homogenous fibre-architecture makes it difficult to predict FRCs performance and its failure accurately.

To understand the damage states in the FRCs, there exist broadly three modes of investigations: in-service structural health monitoring (SHM), post-mortem investigation, and periodic NDT inspection. SHM includes strain sensors and acoustic sensors to detect and track damage in real time. While in-service SHM has advantage of real-time updates, it is often difficult to discern the nature of damage from the

measured signals. While post-mortem investigations include mostly destructive routes of characterisation – optical microscopy and electron microscopy, periodic non-destructive testing (NDT) techniques – x-ray computed tomography (XCT), digital image correlation (DIC), thermography, ultrasonic testing etc allow for more accurate investigation without destroying the material, to observe the initiation and progression of damage. Some fibre-optics-based techniques [308] and the use of model composites [309] rely on embedding fibre-based sensors into the material which can give strain information; the caveat is the introduction of foreign materials into the microstructure which interferes with the natural response and can lead to inaccurate results. Data generated from ultrasonic testing is often complex and not intuitive, while DIC only allows two-dimensional imaging.

Among these NDT techniques, XCT is exceptional in providing detailed three-dimensional (3D) imaging in a non-destructive setup, allowing for resolving complex 3D morphology of the fibrous microstructure and various damage features, often in a time-lapse workflow [75]. XCT has been widely accepted in the composites community as the tool of choice for multi-scale microstructural studies; resolving features as small as a single carbon fibre [310], to microscale [59], [60], [239], [311], mesoscale [111], [198], to even a full 3.5m wind blade segment [312]. It is however limited in investigating larger structures but allows for studying the underlying damage mechanisms in smaller samples, which ultimately affects structural integrity.

Often XCT investigations on composites damage have been qualitative in nature [9], [73], [111], [239], [311], [313], although some algorithms have been developed for quantifying the fibre orientation and morphology e.g. Insegt software [20], [123], [201], [279] and using commercial software, e.g. Avizo [288], [314]–[317]. In other

cases, damage segmentation has been limited to damage visualisation rather than quantification [58], [234]. Traditional segmentation methods such as greyscale thresholding normally fail on FRCs as the contrast can be low (especially for carbon fibre composites [142], the fibres fine and the images can be noisy. Damage quantification has been partially successful through Hough transform segmentation [318] while Bergan et al. have developed a semi-automated system for quantifying kink band [319]. However, to the knowledge of the authors, no single workflow exists which can segment and statistically quantify fibre-fractures automatically with high precision over large time-lapse image sequences seamlessly.

The aim of this paper has been therefore to develop advanced methods of fibre tracing in Avizo [153], [212], [320] augmented by machine learning using Trainable Weka Segmentation (TWS) [204] from Fiji-ImageJ [321]. Our workflow out-performs other modern, but traditional machine learning methods, which rely on manual annotation and extremely accurate ground truth data for training the algorithms, by supplying automatically generated high-fidelity training data, eliminating user-dependent errors. This workflow and its merits are demonstrated on an XCT time-lapse series dataset of a quasi-unidirectional glass-fibre reinforced polymer (GFRP), comprising four 3D image volumes at different stages of tension-tension fatigue damage.

8.2. Materials and data acquisition

The XCT data analysed in this paper is hosted on Zenodo [210] and has been described elsewhere as part of multiple fatigue studies [9], [58], [69], [211]. The materials and data acquisition process relating to this dataset is explained briefly below.

8.2.1. Materials

The material studied is a glass-fibre non-crimp quasi-unidirectional (UD) reinforced polymer composite having a fibre volume fraction, V_f= 0.57. The layup of the composite is $[b/biaxial,b/0,b/0]_s$ where "b" refers to the supporting ±45° and 90°off-axis backing layer and "0" to the 0° Z-direction UD fibre bundles, these are stitched to the backing layer using threads.

8.2.2. Fatigue testing

Butterfly-shaped specimens [73], which encourage gauge failure, were used for the fatigue testing being 410 mm in length and 15mm in width. The sample was cycled through a load-controlled tension-tension fatigue test on a universal servo-hydraulic Instron machine, with a stress ratio of R=0.1, load frequency of 5Hz, and a maximum strain of ε_{max} = 1%. The stiffness degradation is continually monitored using a 25mm gauge extensometer. The test was interrupted for XCT scans at 4 stages, namely after 47300, 57300, 67300, and 77300 cycles. The sample failed soon after the last scan. Regions of interest were identified from hotspots resulting from in-situ infrared thermography. The samples, fatigue testing, and the x-ray CT scans are not authors' own work but have been done in DTU for other studies [9], [58], [69], [211].

8.2.3. X-ray tomography

The same region-of-interest (RoI) was CT scanned at each interruption in cycling, using a custom sample holder which allows repeatable sample placement and positioning. The 2000x2000 pixel detector was binned by a factor of 2, resulting in a 1000x1000 pixel image. With an effective pixel size of 3μm this resulted in a ~3mm field of view. The scanning parameters and associated metadata are listed below.

Source to sample distance	Detector to sample distance	Optical magnification	Pixel depth	Exposure time	Number of projections/ tomogram	Accelerating voltage	Effective pixel size
28 mm	35 mm	4x	16-bit	7s	4601	70 keV	3 µm

Table 8.1 XCT scanning parameters used to scan the sample on a Zeiss Versa 520 XCT scanner.

The time-lapse dataset was registered to the first 3D image volume of the sequence using 'normalised mutual information' and 'rigid transformation' in the 'Register Images' module in Avizo, as shown in Figure 8.1. This was for accurate comparison and study of the damage progress, only the common region overlapping across the four images was analysed.

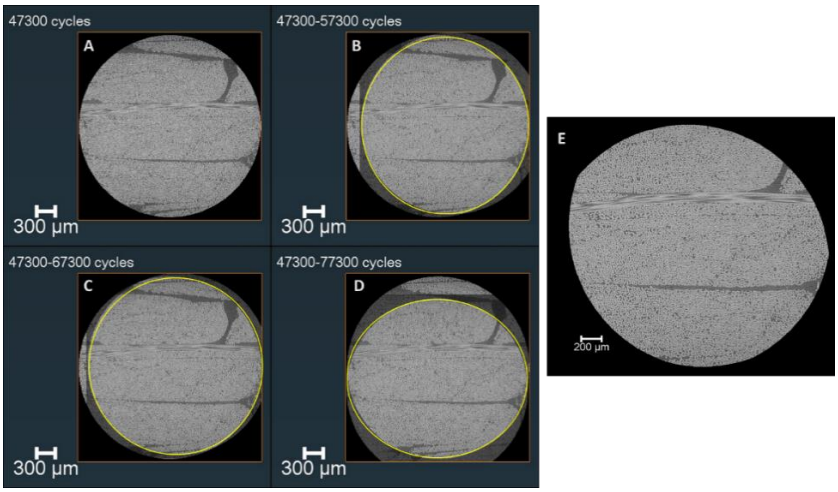

Figure 8.1 A) Slice from CT scan collected after 47,000 cycles and pairs of slices B) 57300 and 47300, C) 67300 and 47300, D) 77300 and 47300, registered in Avizo using the 'Register Images' wizard with the common regions marked in yellow boundary. Only the common overlapping region across all four images, shown in E) is analysed.

8.3. Automated fiber-break detection workflow

Our detection workflow is a two-step approach, where the fiber-breaks are initially detected in the 3D image volumes by tracing individual fibres and looking for intensity drops along the traced fibre centerlines. These intensity drops are labelled as fibre

breaks and then fed into the machine learning classifier for training. The trained model can then be run on the same, or similar image data (subsequent time-lapse images), and the output given is an improved labelled result with fewer false positive and false negative detections. These final labelled fibre-breaks can then be analysed in multiple ways including statistical analyses of fibre-break density and localized clustering. This is shown in Figure 8.2.

This workflow can be run on a series of time-lapse images with the click of a button, and it outputs the identified fibre breaks and related statistics on all the serial images, giving a detailed and an 'at-a-glance' insight into the damage progression, from both a qualitative and quantitative aspect. This scheme is shown in Figure 8.3.

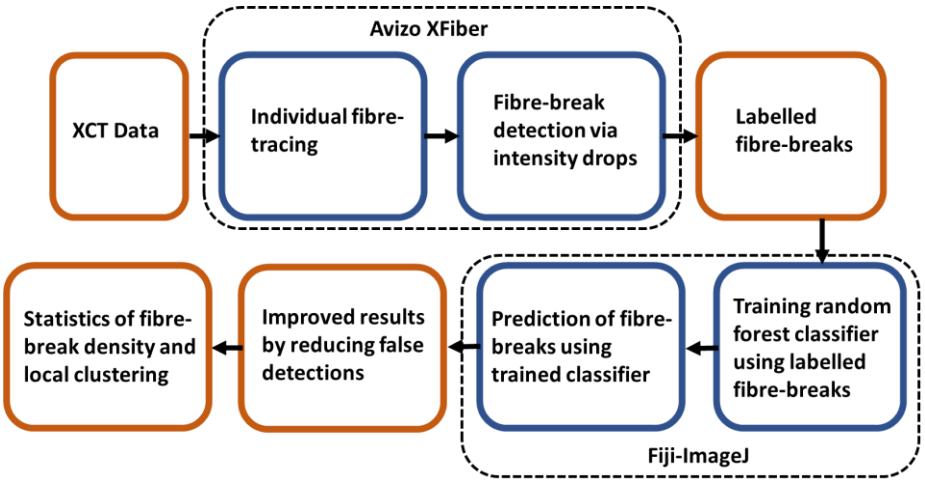

Figure 8.2 The two-step fibre fracture labelling workflow involving two serial steps whereby deep learning improves and updates the first result.

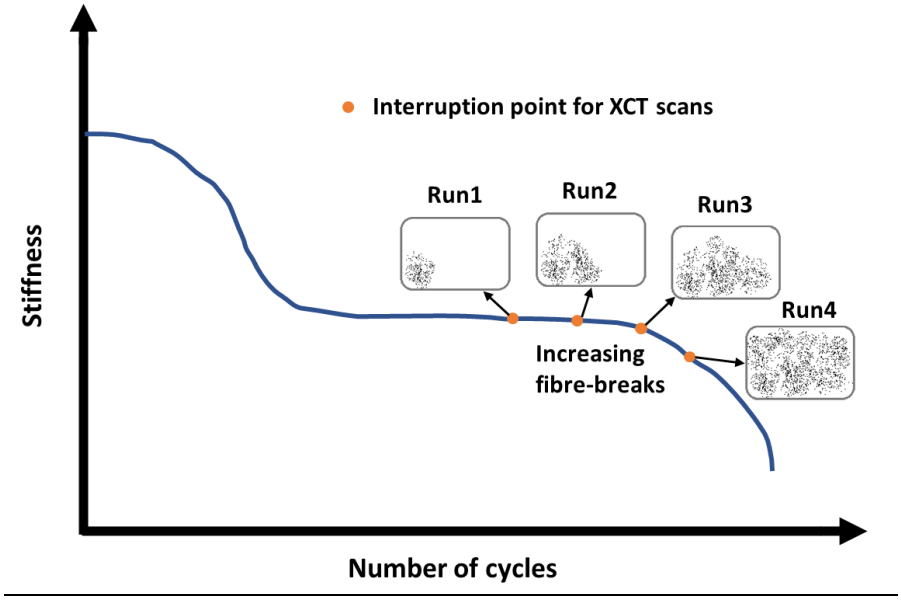

Figure 8.3 The workflow is run multiple times on the whole time-lapse series where statistics of fibre-breaks and are automatically generated. This damage progression can be related to the change in mechanical performance including a drop in stiffness.

Both stages of the workflow are explained in detail below.

8.3.1. Fibre-tracing and initial fibre break detection (FTBD)

A module enabling individual fibre tracing is available in Avizo through its XFiber extension, where a fibre is detected by matching the grayscale features in the 3D image against a user-defined parametric cylindrical template, via normalized cross-correlation [195], [212]. The size of the cylinder template must be similar to the fibres in our case (see figure 8.4a). The results of the cylinder correlation are two images: a correlation field (figure 8.4b) and an orientation field (figure 8.4c). The correlation field stores the maximum correlation value, while the orientation field stores the orientation for which the correlation value is maximum, for each pixel.

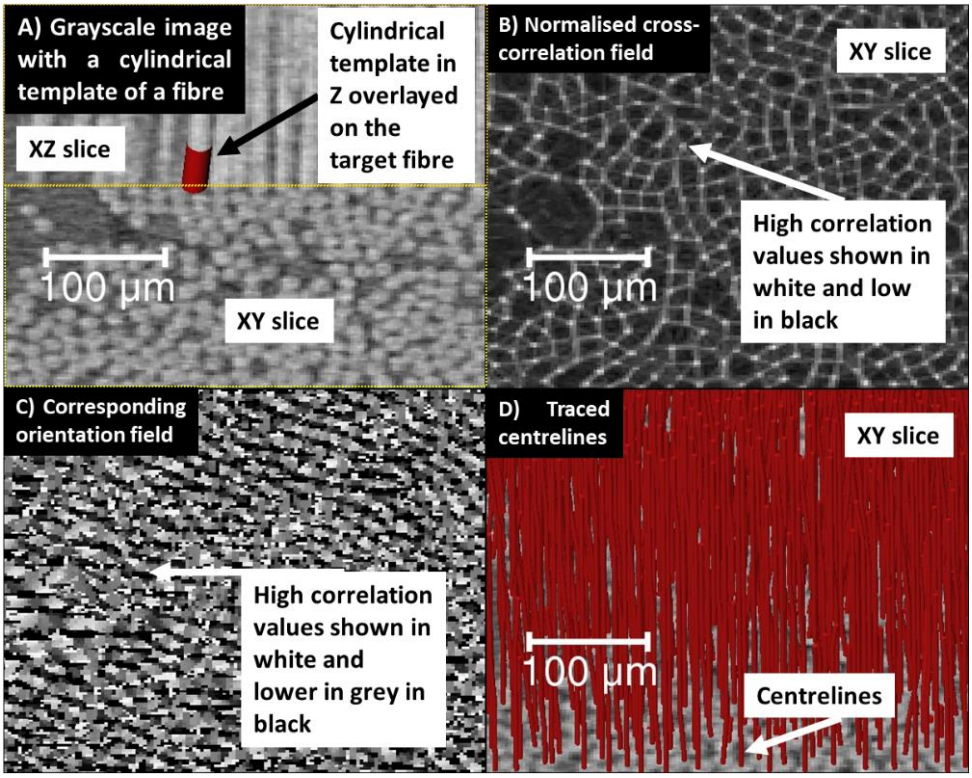

Figure 8.4 XFiber can analyse a greyscale image by cross-correlating it with a cylindrical template specified by the user. This results in a correlation field and an orientation field. By setting a threshold, on these fields, centre-points of fibres can be generated, which are then connected using a search cone to create a single, traced fibre centre-line.

These two fields are then thresholded on minimum correlation values for which the fibre centreline tracing can start and continue. Once the fibre centre-lines are traced as shown in figure 8.4d, the grayscale values are sampled along across these centre-lines searching for a drop in grayscale intensity below a user-calculated value 'T'. These drops in intensity values are labelled as fibre breaks, as shown in Figure 8.5.

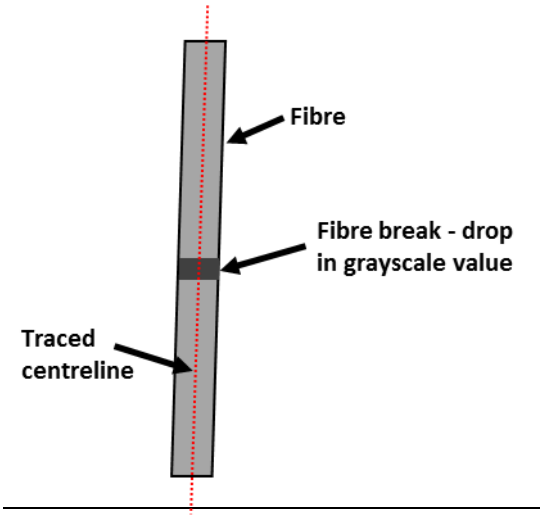

Figure 8.5 The fibre break is detected by sampling the grayscale values along the unique fibre centreline, a value below the user-calculated threshold 'T', is detected and labelled as a fibre break. The threshold 'T' can be easily calculated by finding the grayscale values that correspond to a fibre break, using the probe tools and/or line-profiling a few cracks in Avizo/Fiji.

This procedure, called fibre tracing break detection (FTBD), makes the first estimates of the fibre fracture locations. This result is used as the basis for the next Weka classification step of the automated workflow.

8.3.2. Weka classification in Fiji using FTBD for training

The FTBD result is used in the 'Trainable Weka Segmentation' (TWS) module available in Fiji-ImageJ to train the classifier. The classifier used in this study is a 'FastRandomForest' type [213]. This is a supervised machine learning algorithm that grows and combines multiple decision trees for classification. This is advantageous over single decision trees as multiple uncorrelated models (individual trees) perform better when grouped [205], [214]. This process which forms the second part of the damage detection workflow uses the following steps:

11) Both the grayscale file and the corresponding FTBD result are read into Fiji-ImageJ.

12) The grayscale file that needs to be analysed is opened in the TWS window which contains separate classes for each type of label, in this case, it is two – fibre breaks, and the background (containing fibres, matrix etc.)
13) The fibre breaks in the FTBD result are transferred as regions of interest (RoI) to an 'ROI Manager' using a native 'Analyse Particles' routine.
14) From the ROI Manager, the RoIs are transferred as 'class 1' (in red) to the TWS automatically using an ImageJ macro script, described in the Appendix. The background can be minimally annotated by manually adding a few annotations to 'class 2' (in green).
15) The segmentation settings, which include the type of training features and the type of classifier (FastRandomForest in this study) can be selected. Ideally, it is sensible to use a smaller but representative sub-volume to optimise the settings in multiple quick training attempts.
16) The classifier is then trained using the selected settings and the segmentation result is generated. If the result of the classification/prediction of fibre breaks looks satisfactory, the classifier can be saved.

Once the classifier has been trained satisfactorily and saved, this classifier model, saved as a .arff file, can be imported and run on a batch of volumes automatically, seamlessly segmenting fibre breaks. This can be done using a Beanshell script [215], described in the Appendix.

8.4. Results and discussion

8.4.1. The 2-stage segmentation of fibre fractures

The results of both the FTBD and TWS prediction are shown below in Figure 8.6 and 8.7 respectively. It is evident form Figure 6 that the FTBD results have a significant

number of false negatives and insignificant number of false positives, the former due to relatively inaccurate tracing of the fibres. The fibre tracing depends largely on the resolution and contrast; here the voxel size (3 μm) means that the fibres are 6, or fewer, voxels across and the gaps between fibres even finer. As a result, filtering out the false fibre tracings inadvertently also eliminates a significant amount of true fibre tracings. It is also evident in Figure 4 that some of the smaller fibre breaks that are detected early in the time-lapse sequence but fail to be detected later when they are larger. This is due to the larger fibre break leading to a gap in the tracing continuation because of poor correlation values in the fibre break, which in turn eliminates the fibre trace and restricts sampling of the intensity drop and therefore detection. The FTBD results can be improved by using higher-resolution data where individual fibres can be traced more accurately, but that leads to the trade-off of being able to investigate a smaller field of view. This trade-off can be mitigated by image stitching methods [151] or helical scanning [60], [246], where larger, high aspect ratio samples are scanned in one tomogram. Nevertheless, the FTBD step works well in supplying only true fibre breaks as training data for TWS prediction despite not capturing all the fibre breaks.

In the TWS prediction, there are a non-negligible number of false detections early on, due to smaller size damage features. Along with fewer false negatives, most of the false positives are concentrated very close to the fibres in matrix-rich regions which have grayscale intensities closer to the fibre breaks and damage. It also misses some of fibre debonding which is coupled to fibre breaks as FTBD does not supply training data for fibre debonding and samples and detects fibre breaks only. Improvements in the training data provided by FTBD by methods discussed above can lead to better TWS prediction. Another method to improve detections in non-uniformly illuminated time-lapse images (in changing XCT scanning conditions) would be to concatenate

smaller sub-volumes from multiple 3D images and train the classifier on it. In this study, the 77300 cycles prediction has been used as a mask for earlier predictions to eliminate some of the false detections, especially due in the earlier images having smaller features that are difficult to detect. As a whole, TWS prediction augments and greatly improves the three-dimensional segmentation of the fibre breaks and associated damage from FTBD for non-destructively acquired time-lapse x-ray tomography data.

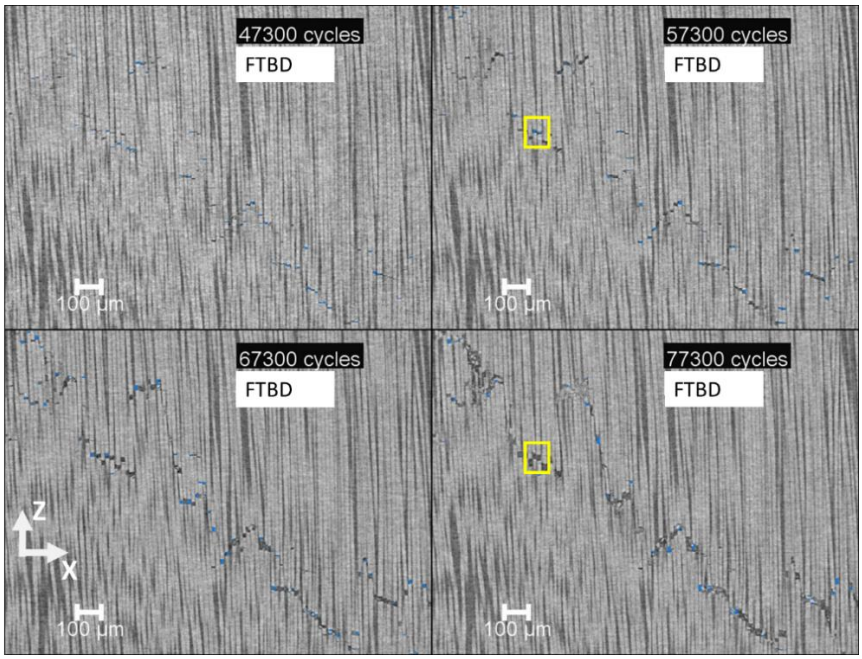

Figure 8.6 FTBD results (labelled in blue) for a CT slice from all four time-lapse images. With increasing number of fatigue cycles the crack openings get larger and are more easily detected. Some of the fibre breaks (boxed in yellow) detected early on are missing in the later images. The results are not accurate, with significant false negatives and virtually non-existent false positives. This unique result, although broadly inaccurate, facilitates accurate annotations where only true fibre breaks are annotated for the next step of TWS prediction.

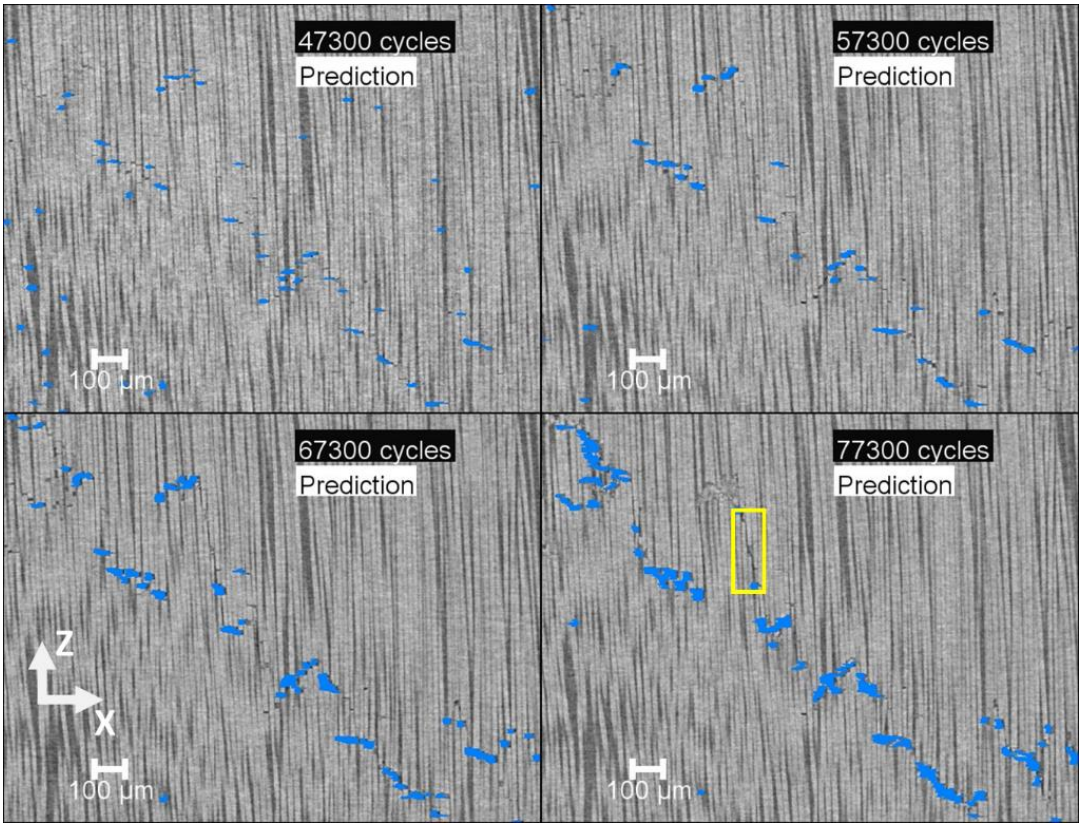

Figure 8.7 The damage prediction superimposed on a single CT slice using the 'FastRandomForest' classifier in TWS, as a function of fatigue over the time-lapse sequence. The prediction has a higher number of false detections in the earlier images, where crack openings are smaller. Some of the debonding (boxed in yellow) are also missed.

All the damage has been projected onto a single XY slice and overlayed on a grayscale XY slice in Figure 8.8. It is evident that damage originates near the backing bundles and progresses away from it in the thickness direction of UD bundles. There appear to be a lot of false detections especially early in the sequence which suggests that damage become less. This is discussed in the next section.

Figure 8.9 shows the 3D distribution of the clustered fibre breaks, where they progress in the thickness direction of the UD bundles in a 45° orientation, nearly aligned with the 45° backing bundles. While the cracks are getting bigger, they are joining together through matrix cracking and localised interfacial debonding.

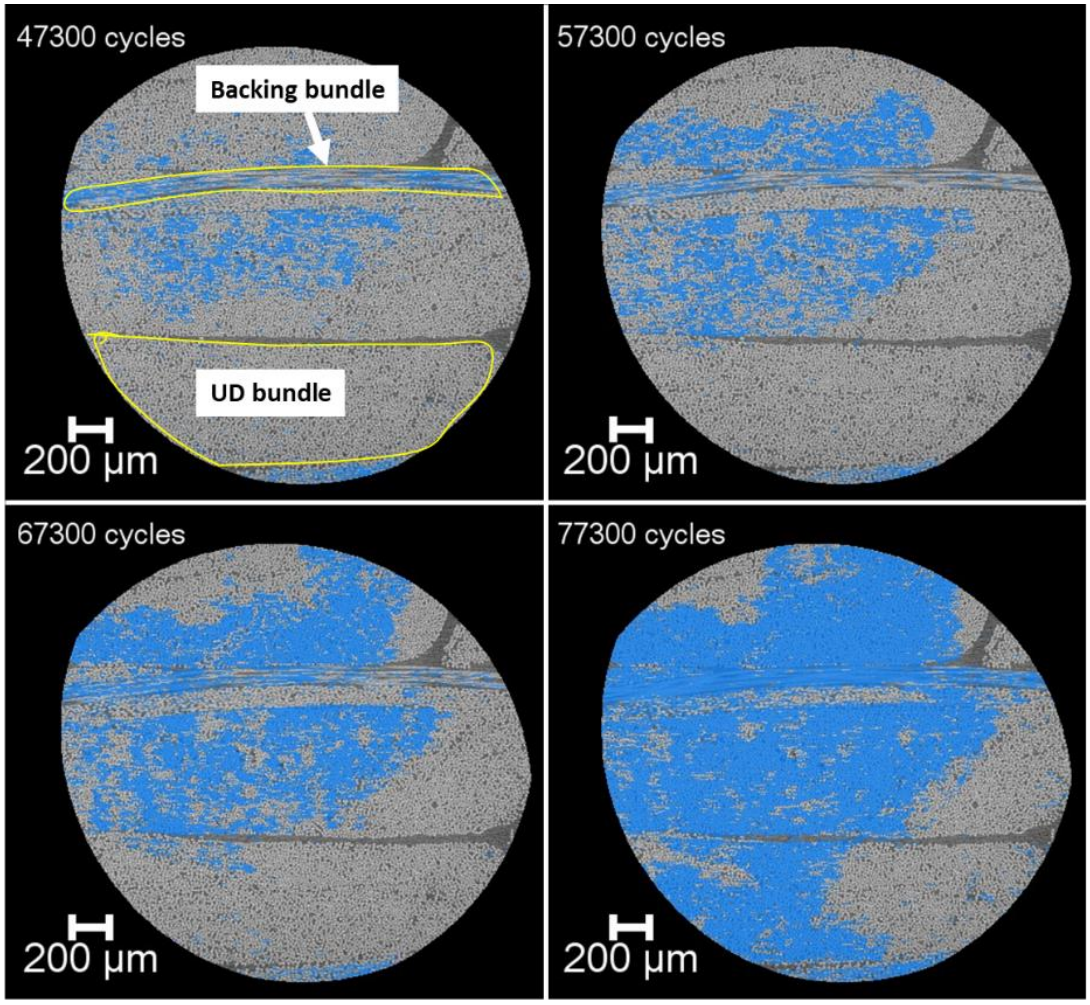

Figure 8.8 Overlay projection onto the X-Y plane showing damage in all the XY slices alongside a (grayscale) CT slice. The damage starts close to backing bundles and then progresses into the UD bundles.

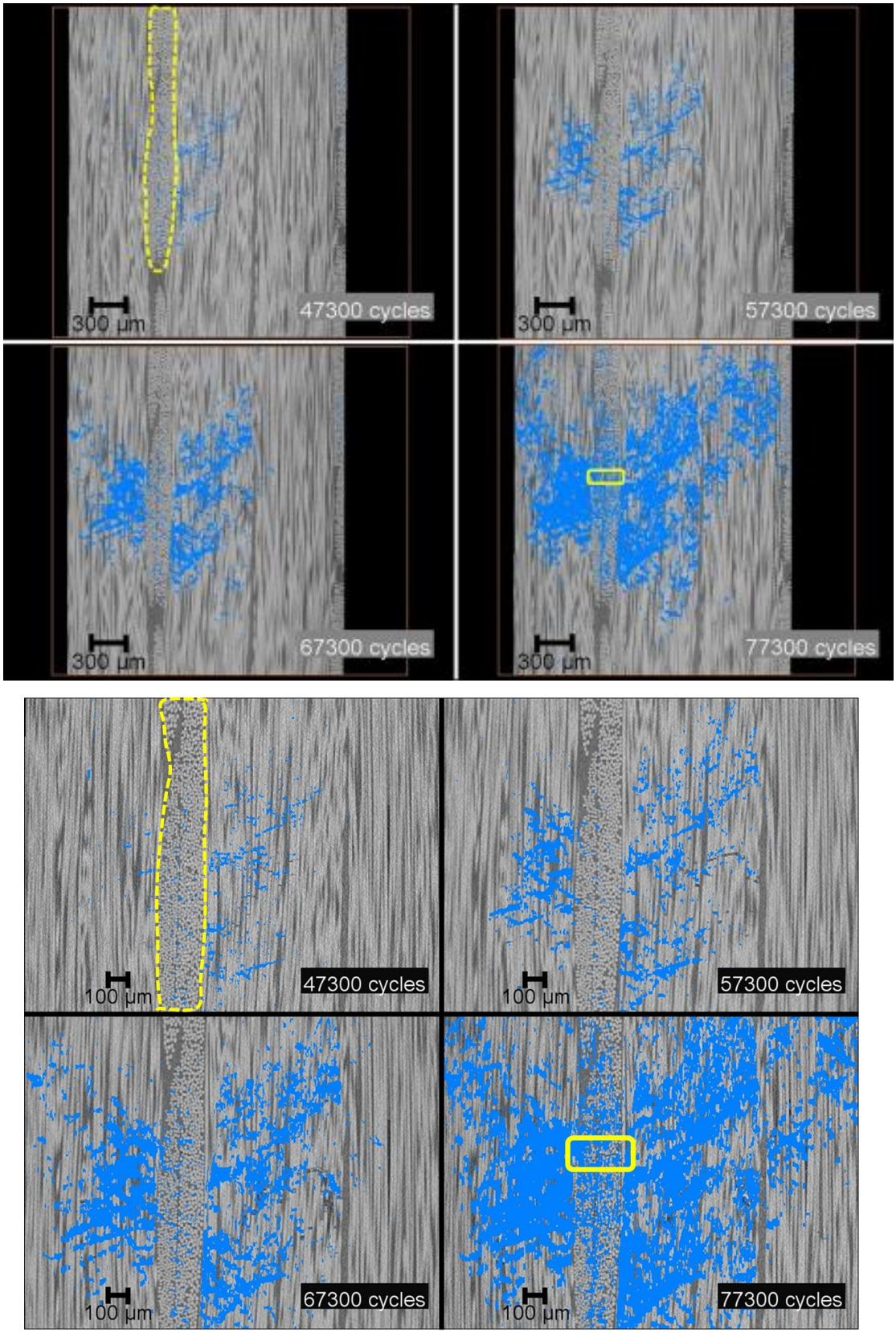

Figure 8.9 Overlay projection onto a Y-Z slice showing damage in all the YZ slices. The damage can be seen starting in and closer to the backing bundles (dashed yellow) and progressing away in thickness to the UD bundles. Some damage progresses in the backing bundles including transverse off-axis cracks (boxed yellow), while some of the detected damage is false and is discussed in 8.4.2.

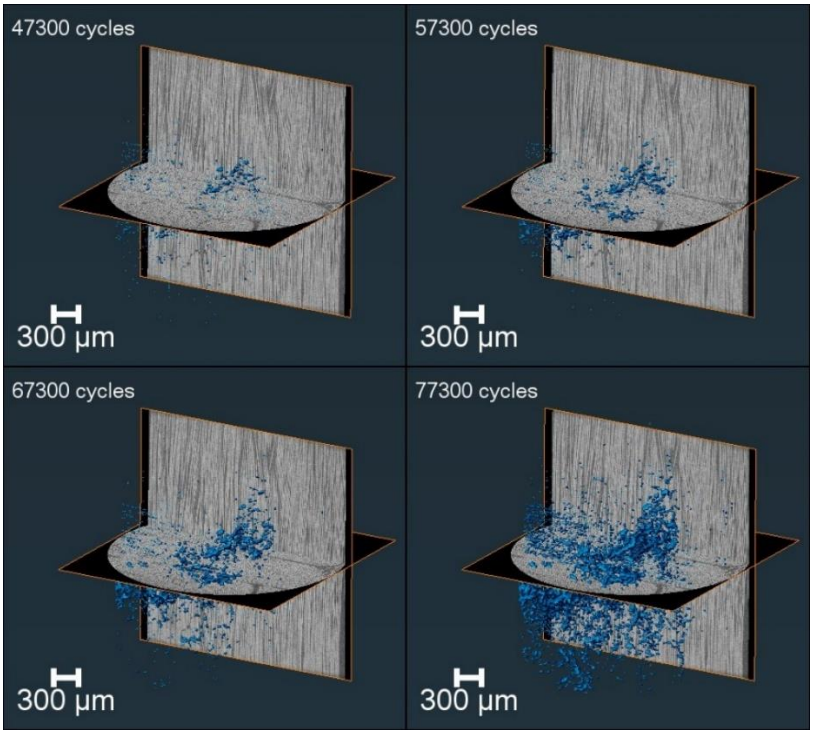

Figure 8.10 The distribution of the clustered fibre breaks progressing diagonally at ~45° with the UD bundles, nearly aligned with the 45° backing bundles.

8.4.2. Study on errors and workflow limitations

Looking carefully at some of the image slices as shown in Figure 8.10, it is evident that the prediction is inaccurate in the off-axis regions, especially in the earlier images. This is because of the damage features are smaller and because there is no available training data from the off-axis regions. The reason for this has been discussed above and is because the FTBD cannot accurately trace the fibres at a lower resolution, especially for backing fibres that are even smaller (~16 µm). Pure matrix regions where no fibres were traced are correctly segmented as background and not as damage. Larger off-axis breaks in the later images are also correctly segmented.

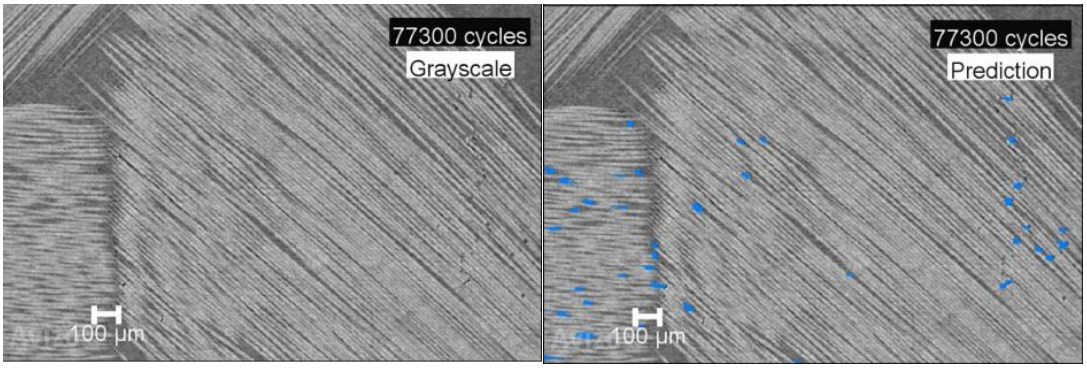

Figure 8.11 Grayscale time-lapse CT slice after 77300 cycles (left) and the corresponding segmented slice (right). Pronounced false detections in the early images of off-axis regions because of smaller damage features and the unavailability of training data in the off-axis regions. The FTBD which supplies training data can only be accurately run in the UD fibres (average diameter ~17 µm) and not the smaller backing fibres (average diameter ~16 µm).

It is clear from Figure 8.11 that the bigger fibre breaks are easier to detect. The average break length in the four images is 3.94 µm, 10.61 µm, 17.71 µm, and 27.9 µm: corresponding to a minimum of 1, 3, 5, and 9 pixels long. This applies to breaks in both the UD and off-axis fibres as evidenced in the previous Figure 4.4. The false detections can be reduced by opening the cracks and increasing their size in situ during XCT scans, either through the mechanical testing rigs or through standalone 'tension-clamp' rigs used in these studies [142], [322]. Other techniques such as staining the cracks with a high atomic number solution have also been used which impart fantastic contrast, although these can interfere with the natural micro-mechanical response of the material [60], [142].

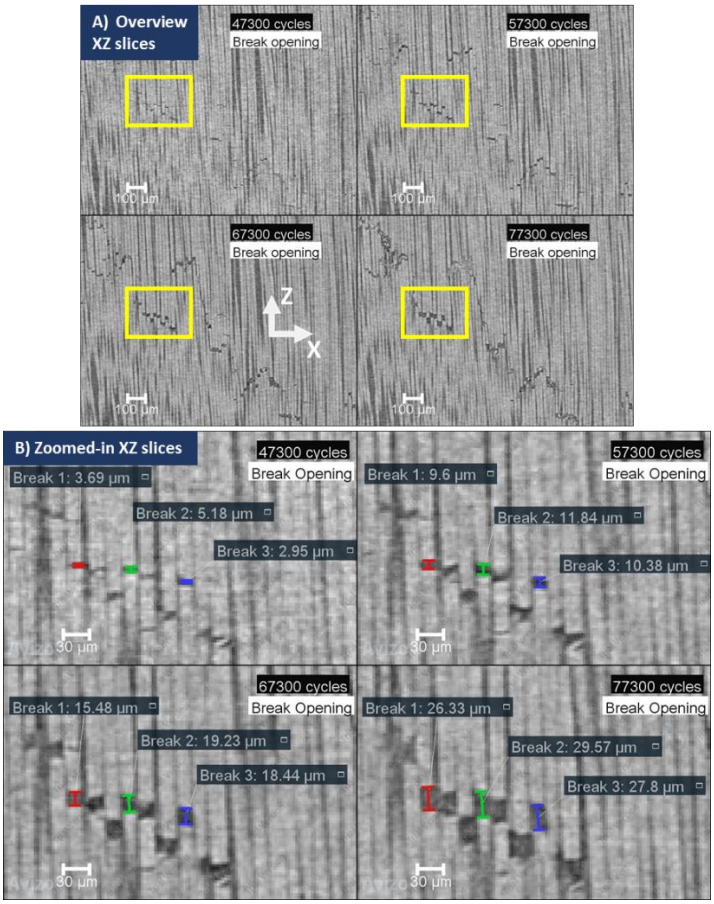

Figure 8.12 Fibre breakage lengths measured for three sample breaks in the same corresponding CT slice for the four different time-lapse scans. A) shows the overview slice and the cluster (boxed in yellow) extracted in B) The break lengths are on an average double of the previous image, corresponding to lower false detections as evidenced in the previous figure.

8.4.3. Study on strengths of the workflow

As discussed above, the fibre breaks and damage in fibre-reinforced composites are incredibly hard to segment and quantify, particularly due to the low contrast and noisy data. The efficacy of this method has been shown in Figure 8.12, where the damage from a small sub-volume has been extracted and sampled for grayscale intensity distribution. The intensities have been sampled between the thresholds of the background 0-value and the value ‘T’ from the FTBD step, this is done to ignore the background and any parts of the matrix/fibre that have been inadvertently sampled.

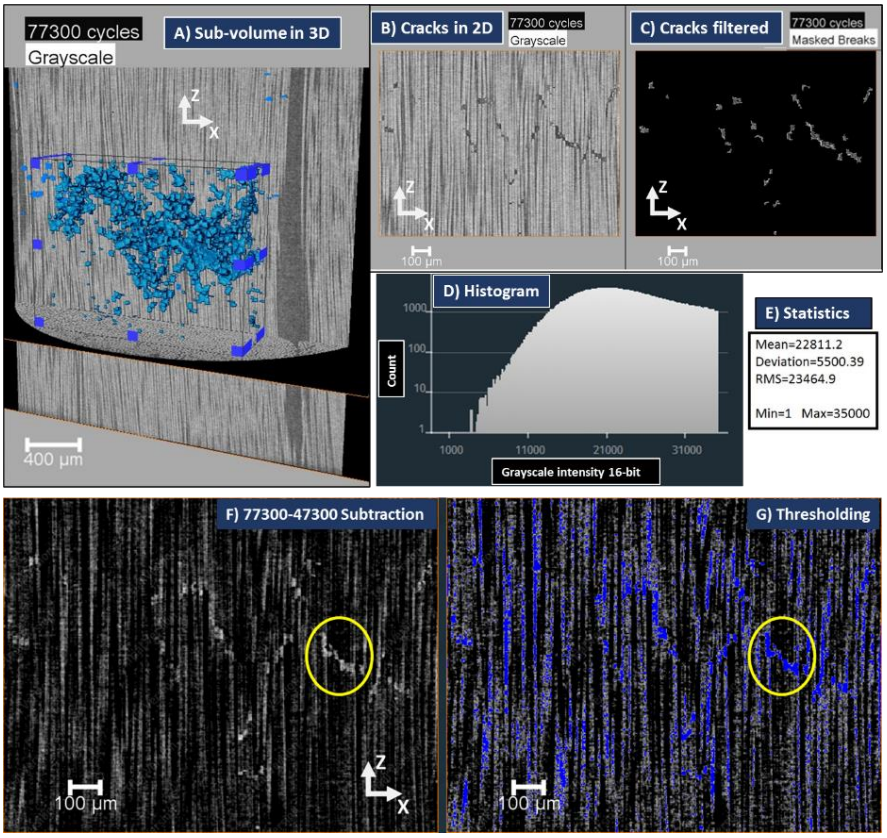

Figure 8.13 The strengths of this workflow in segmenting complex cracks. A) A small sub-volume extracted to sample/profile grayscale intensities in fibre breaks and associated cracks B) An image slice with cracks that are masked C) The masked cracks D) Histogram of grayscale intensities in all the cracks within the sub-volume E) Statistics of the grayscale intensity distribution F) Image subtraction to segment cracks G) Thresholding of the subtracted leading to a poor segmentation.

The grayscale distribution of the damage is broad and nearly covers all the intensities in the 16-bit range, within the thresholds. Such a wide distribution of voxel intensities is difficult to segment, even with more advanced image analysis methods. One of them is shown in Figure 8.12, where the two 47300 and 77300 cycles images are subtracted, which theoretically should expose the 'newer' damage features not present in the previous image. Realistically, the result from thresholding this image is inaccurate and messy, the noise in the datasets and broader grayscale distribution limit it from a useful result. This subtraction method is also prone to errors arising from small 'misregistration' in the 3D image volumes, and non-uniform x-ray illuminations across the time-lapse images. While this subtraction method also needs a series of time-lapse images for a reference in the subtraction, this current workflow can work

on singular image volumes and does not necessarily need a time-lapse series or a reference.

Also, this is the only workflow to the author's knowledge that uses the modern methods of machine learning to automatically segment fibre breaks and associated damage without the need for manually annotated training data. By this, it becomes completely seamless and enables batch processing of large time-lapse XCT datasets for high-throughput damage detection.

8.4.4. Morphology and statistics

Once these fibre breaks are segmented, they can be imported back into Avizo to be studied and measured. A number of individual measures regarding geometries, locations etc. are available in Avizo [153], [323], as shown in Figure 8.13. The largest crack is automatically isolated using size filters, and it is found that smaller individual fibre breaks along the 45° backing bundle join up later to form a large diagonally connected crack, linked by matrix cracking and interfacial debonding.

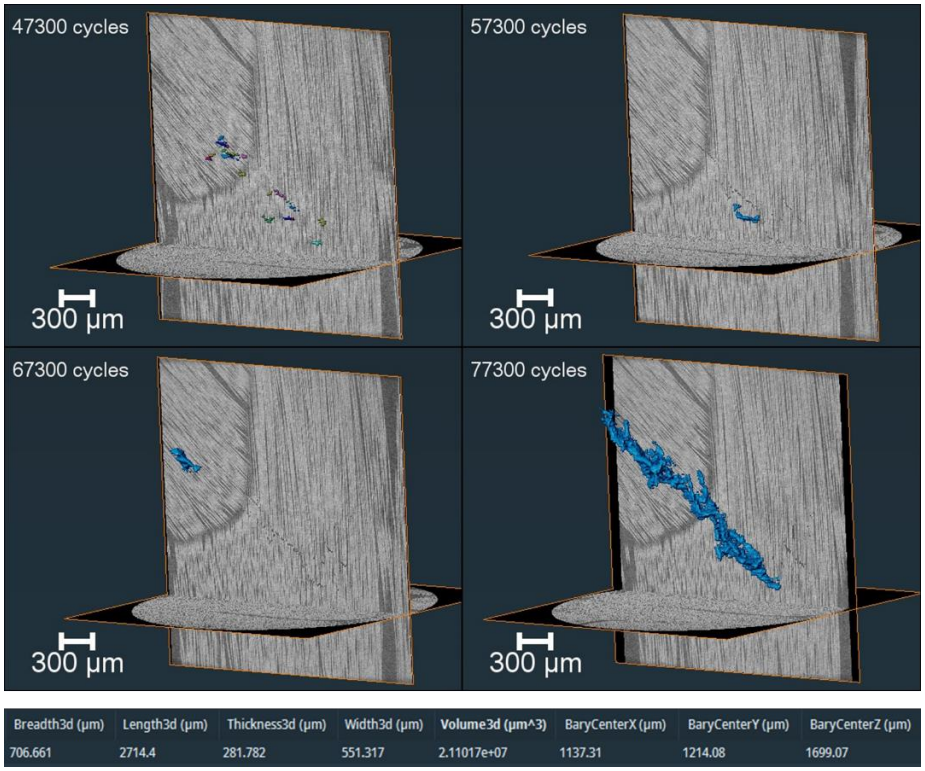

Figure 8.14 Connected components analysis in Avizo to find connected fibre clusters for all the four images. The largest crack was isolated to study its progression. It is found that several smaller fibre breaks link up to form a large, connected crack, joined together by matrix cracking and interfacial debonding, along the 45° backing bundles. Several individual measures for each connected component (clustered fibre breaks in this case) are available in Avizo, and a few of them are included in this Figure. Using these geometric and locational measures, individual fibre break clusters can be identified, followed, and measured throughout the time-lapse.

Using these measures, important information about the progress of damage including the change in size and shape, crack-bridging, and proximity to key microstructural features including off-axis fibres can be generated automatically. This information can be eventually used to verify material models and simulations and assess their efficacy.

8.5. Conclusions

A novel damage detection workflow for the segmentation of fibre breaks and associated damage is proposed. The novelty lies in the way it combines two important steps, firstly the formation of high-fidelity training data obtained by fibre tracing break

detection (FTBD) in Avizo and then using this training data to detect and improve upon missed fibre break detections by a machine learning step. The key strengths and limitations have been identified as;

1) Damage detection for off-axis smaller fibres can be inaccurate – scanning the sample at higher resolutions will improve the detection. The trade-off of a resulting smaller field of view can be mitigated by image stitching and helical scanning.
2) Damage detection of both smaller UD and off-axis fibre breaks can be inaccurate – imaging under load so as to hold the cracks open while scanning can improve the result [142].
3) For erroneous damage detection on earlier time-lapse datasets with smaller damage features, the final time lapse damage detection result can be used as a mask on previous results to filter out inaccurate results. This assumes that the damage can only progress and get bigger or stagnate, it cannot disappear in the later time-lapse images.
4) For time-lapse images with non-uniform grayscale distributions in time (changing x-ray conditions), we found that by training a machine learning model with less capable fibre tracking and fracture FTBD) analysis can improve the result.
5) The workflow is adept at segmenting fibre breaks and associated damage in regions where FTBD was able to sample fibre breaks including UD fibre breaks, in this case, it excludes both off-axis fibres and UD fibres with large fibre breaks.
6) The workflow does not require a reference or a time-lapse series, it is adept at segmenting fibre breaks in both single and time-lapse scans.

7) Using the connected components analysis and the multitude of individual label measures available in Avizo, fibre break clusters can be located, followed, and measured in a variety of ways including the change in size and shape, crack-bridging, proximity to key microstructural features including off-axis fibres, automatically in a batch processing approach.
8) This workflow uses advanced machine learning methods to automatically segment fibre breaks and associated damage without the need for manually annotated training data. This enables batch processing of large time-lapse XCT datasets for faster damage detection.

Declaration of competing interest

The authors declare that they have no known competing financial interests or personal relationships that could have appeared to influence the work reported in this paper.

Acknowledgements

This study was funded by EU H2020 MSCA Innovative Training Network 'MUMMERING' Grant Number 765604. Discussions with Robert Auenhammer from the Chalmers University of Technology and Stuart Morse from The University of Manchester are acknowledged. Computing resources were provided by the Henry Moseley X-ray Imaging Facility (HMXIF), established through EPSRC grants EP/F007906/1, EP/ I02249X/1 and EP/F028431/1. HMXIF is part of the Henry Royce

Institute for Advanced Materials, established through EPSRC grants EP/ R00661X/1, EP/P025498/1 and EP/P025021/1. PJW acknowledges a European Research Council Advanced Grant Correl-CT No. 695638.

Appendix A: Codes

Code to transfer RoIs from ROI Manager to TWS Window (IJ1 Macro)

```
num_rois = roiManager("count");
class=0;
for(i=0;i<num_rois;i++){
roiManager("Select", i);
slice_num = getSliceNumber();
call("trainableSegmentation.Weka_Segmentation.addTrace", class, slice_num);
}
```

Code to run TWS classifier on a batch of image volumes (Beanshell script)

```
#@ File(label="Input directory", description="Select the directory with input images", style="directory") inputDir
#@ File(label="Output directory", description="Select the output directory", style="directory") outputDir
#@ File(label="Weka model", description="Select the Weka model to apply") modelPath
#@ String(label="Result mode",choices={"Labels","Probabilities"}) resultMode

import trainableSegmentation.WekaSegmentation;
import trainableSegmentation.utils.Utils;
import ij.io.FileSaver;
import ij.IJ;
import ij.ImagePlus;
```

```
// starting time
startTime = System.currentTimeMillis();

// caculate probabilities?
getProbs = resultMode.equals( "Probabilities" );

// create segmentator
segmentator = new WekaSegmentation();
// load classifier
segmentator.loadClassifier( modelPath.getCanonicalPath() );

// get list of input images
listOfFiles = inputDir.listFiles();
for ( i = 0; i < listOfFiles.length; i++ )
{
    // process only files (do not go into sub-folders)
    if( listOfFiles[ i ].isFile() )
    {
        // try to read file as image
        image = IJ.openImage( listOfFiles[i].getCanonicalPath() );
        if( image != null )
        {
            // apply classifier and get results (0 indicates number of threads is auto-detected)
            result = segmentator.applyClassifier( image, 0, getProbs );

            if( !getProbs )
                // assign same LUT as in GUI
                result.setLut( Utils.getGoldenAngleLUT() );

            // save result as TIFF in output folder
            outputFileName = listOfFiles[ i ].getName().replaceFirst("[.][^.]+$", "") + ".tif";
```

```
        new FileSaver( result ).saveAsTiff( outputDir.getPath() + File.separator + outputFileName );

        // force garbage collection (important for large images)
        result = null;
        image = null;
        System.gc();
    }
  }
}
// print elapsed time
estimatedTime = System.currentTimeMillis() - startTime;
IJ.log( "** Finished processing folder in " + estimatedTime + " ms **" );
```

9. Conclusions

The goal of the work presented in this thesis was to advance our knowledge of the fatigue behaviour of UD-NCF GFRP that are used in wind blade as load-bearing materials. This aim was realised through a two-pronged approach; a) develop a time-

lapse, correlative fatigue experiment to see the evolution of damage, and b) develop and improve image analysis method for 3D imaging data of fibre-reinforced composites to better understand the observations from the first part, especially from a quantification point of view.

The main focus was on developing novel image analysis methods for 3D data of fibre reinforced composites, and understanding the initiation and progression of damage and how that affects the stiffness degradation of the material. Another key focus was to identify microstructural features which act as weak links in the material architecture and lead to damage.

The findings are concluded below:

9.1. Image analysis methods for fibre-reinforced composites

As the mechanical behaviour of composite materials rely on the morphology and orientation of their constituents, it is important to consider and study this information during investigations. XCT has been instrumental in generating non-destructively acquired 3D images, but often these images are used for qualitative inspections. It is imperative we develop and improve image analysis methods to move from qualification to quantification and improve our understanding of material behaviour. For this, two manuscripts reporting on novel image analysis workflows were written.

The third manuscript involves four workflows used to study and analyse imaging data of FRCs – Avizo, Insegt, Structure Tensor, and Fiji-ImageJ. They have been assessed, discussed, and ranked on performance and suitability metrics on image datasets comprising different resolution, noise, and contrast levels. The novel Fiji-ImageJ workflow was introduced in this paper, with powerful capabilities of image

segmentation and fibre-tracing. All four workflows were found to be competent in multiple metrics. Apart from being a full-fledged image analysis environment, Avizo performed best in fibre-tracing on noisier and low-resolution datasets, with the option of seamlessly generating meshes for modelling. Insegt performed best in accuracy for fibre-tracing, requiring the least parameter tuning and was the fastest in fibre-tracing. Structure tensor was only able to calculate gross material point orientation without being able to segment data or perform fibre-tracing, but it was categorically faster, accurate, scalable, required least parameter tuning, and is free-to-use. The novel workflow Fiji-ImageJ performed well both on fibre-tracing and image segmentation, including high accuracy and low false detections. In addition, it fares well on lower system requirements, high information versatility, and is free-to-use.

In addition to the introduction of a novel image analysis workflow, this paper aims to serve as a guided review for wider composites community who intend to employ advanced imaging and its analyses to study fibre-reinforced composites. This paper provides basis for informed decisions on what workflows suit best for a particular data and scientific statement.

The fourth manuscript involves a novel damage detection workflow for the segmentation of fibre breaks and associated damage. The novelty is in the way it combines two important steps, firstly the formation of high-fidelity training data obtained by fibre tracing break detection (FTBD) in Avizo and then using this training data to detect and improve upon missed fibre break detections by a machine learning step. The key strengths and limitations have been identified as;

1) Damage detection for off-axis smaller fibres can be inaccurate – scanning the sample at higher resolutions will improve the detection. The trade-off of a resulting smaller field of view can be mitigated by image stitching and helical scanning [151], [159].
2) Damage detection of both smaller UD and off-axis fibre breaks can be inaccurate – imaging under load so as to hold the cracks open while scanning can improve the result [324].
3) For erroneous damage detection on earlier time-lapse datasets with smaller damage features, the final time lapse damage detection result can be used as a mask on previous results to filter out inaccurate results. This assumes that the damage can only progress and get bigger or stagnate, it cannot disappear in the later time-lapse images.
4) For time-lapse images with non-uniform grayscale distributions in time (changing x-ray conditions), a concatenated dataset comprising representative sub-volumes from different grayscale distributions used for FTBD training data generation can improve the result.
5) The workflow is adept at segmenting fibre breaks and associated damage in regions where FTBD was able to sample fibre breaks including UD fibre breaks, in this case, it excludes both off-axis fibres and UD fibres with large fibre breaks.
6) The workflow does not require a reference or a time-lapse series, it is adept at segmenting fibre breaks in both single and time-lapse scans.
7) Using the connected components analysis and the multitude of individual label measures available in Avizo, fibre break clusters can be located, followed, and measured in a variety of ways including the change in size and shape, crack-

bridging, proximity to key microstructural features including off-axis fibres, automatically in a batch processing approach.

8) This workflow uses advanced machine learning methods to automatically segment fibre breaks and associated damage without the need for manually annotated training data. This enables batch processing of large time-lapse XCT datasets for faster damage detection.

9.2. Fatigue behaviour of UD-NCF GFRP

A workflow was developed using 3D imaging and characterisation techniques, including x-ray computed tomography (XCT) and serial-sectioning scanning electron microscopy (SEM), localized strain characterization from digital image and volume correlation (DIC-DVC), in tandem with tension-tension fatigue testing. An improved tension clamping procedure was developed to keep the cracks open and aid damage detection. Hard stainless steel was bonded on the ends of the carbon rods to avoid it getting crushed by the screw points. This prevents screw points from digging into the carbon rods and has been successful in imparting stable loads of up to ~5.7 kN.

The observed reduction in stiffness was attributed to damage found from DIC-DVC strain hotspots and damaged regions observed in XCT. These damaged regions were excavated in SEM to enable high-resolution studies.

The study found that damage initiated independently on the surface and in the bulk. Surface imperfections, such as voids and micro-scale notches, led to damage. Voids caused matrix cracking, which progressed into off-axis cracks in the thin supporting backing bundles (BB). These off-axis cracks then propagated into the neighbouring load-carrying UD bundles, leading to severe deformation, and observed strain localization in DIC-DVC strain maps. Due to stronger UD fibres failing, the local

region became compliant, leading to UD and BB fibre failures in nearby regions and a significant loss in stiffness. DIC strain maps were found to be adept at not only detecting surface damage but also distinguishing if the loss in stiffness originates from the damage in strong reinforcing UD fibres or the weaker compliant matrix. Micro-notches led to micro-cracking in resin-rich regions, which developed into near-surface longitudinal splits. Some of these splitting cracks got deflected or arrested by the BB and could lead to debonding of UD bundles and BB. These splitting cracks, and all the constituent phases including matrix, UD fibre bundles, backing bundles and background were automatically segmented in the XCT images using the competent machine-learning based Weka classifier in Fiji-ImageJ. The longitudinal morphology of the splits including their proximity to the backing bundles and the surface was exposed.

In the bulk, UD fibre breaks originated close to BB and proceeded more in width than in thickness due to the reduction of local fibre volume fraction in the width direction. These clustered UD fibre breaks led to matrix cracks in resin-rich regions, which could set off neighbouring off-axis cracks and simultaneous UD fibre breaks, as observed on the surface. This was essentially the mode of damage transfer within the bulk. UD fibres that were away from the backing bundle exhibited late-stage failure due to the absence of waviness and misalignment. From DVC results, "banding" of strain concentrations was observed across width in higher compliance regions that were resin-rich and had backing bundles running in the same height positions. This was also corroborated with the damaged regions observed predominantly in these bands and with a tensile model that showed higher stresses in these bands. The damage was confirmed manually by scrolling through the ortho XZ slices and is a combination of clustered fibre breaks and matrix cracks, both near the surface and in the bulk. One of

these damage clusters matched well with stress concentrations predicted from a monotonic tensile model. This tensile model is created from the first image (undamaged) of the time-lapse sequence using mapped material orientations and tetrahedral elements. This damage cluster then also matches well with the high axial strains observed by DVC, focused near backing bundles and matrix-rich regions. This qualitative agreement between calculated 3D strain maps, predicted stress and confirmed damage from XCT, corroborates the efficacy of the tensile model and the accuracy of DVC strain maps. At some point, the surface and bulk damage likely joined up with larger splits to progress further and eventually lead to complete failure. However, the sample in this study was not taken to complete failure to enable correlative SEM studies.

In conclusion, both the parts of this PhD thesis are crucial in improving our understanding of the fatigue damage, where the first part presents our observations and understanding of fatigue damage, and the second part improves our understanding by adding automation and quantification while also serving the composites community with novel methods and informed choices of image analysis workflows.

The next chapter highlights and discusses avenues for future work and research.

6. Future work

In this project, the efficacy of using a time-lapse, correlative, and a multiscale imaging and characterisation workflow to study the fatigue behaviour of wind blade fibre-reinforced composites has been proven. The workflow involves x-ray tomography, digital image and volume correlation, and electron microscopy in a complementary manner to exploit the advantages of these individual methods. This opens more avenues of advancing this research to further our understanding of the complex fatigue behaviour of fibre-reinforced composites, and several examples are discussed below.

6.1. Extension to carbon-fibre composites

As discussed in Chapter 1 and 2, carbon fibre-reinforced composites are being increasingly adopted in the load-bearing components of wind blades [11], [12], owing to the suite of superior properties of stiffness and lower density[41], [325]. Their higher cost has been a deterrent, but some textile based novel CFRPs have been cheaper to produce and are being trialled in wind blades [43], [46]. This correlative characterisation workflow, although specific, is still adaptable enough for studying the fatigue behaviour of CFRPs and/or hybrid carbon-glass FRPs. For poorer contrast between carbon fibres and epoxies, phase contrast imaging from both lab sources and synchrotron [154], [242], [326] is capable of enhancing contrast, where in-situ DIC and XCT can be combined [327]. Damage detection can be aided by staining and keeping the cracks open by imparting tensile loads [75], [142]. With improvement in manufacturing methods, carbon FRPs could see a greater uptake in the future wind blades, for which this workflow would be advantageous for advanced characterisation.

6.2. Extension to model composites

As discussed in Chapter 5 and 6, this PhD study was undertaken on a commercial wind blade GFRP from Saertex GmBH. While it is beneficial to study the real-world

composite that is actually used in wind blades, this poses certain challenges from a characterisation point of view. The sample was four UD layers thick and therefore translucent, this meant methods such as trans-illuminated white light imaging (TWLI), which have successfully used to detect off-axis cracks [9], could not be used. Also, the width of the sample specimens, which ranged from 6mm – 10mm to have a feasibly representative material architecture, were too wide to image at decent fibre level resolution in XCT. Because of this poorer resolution, the fibres were only partly resolved, and consequently the novel damage detection method from Chapter 8 which requires higher resolution data, failed on specimens from Chapter 5 and 6. To mitigate this, a model composite is proposed for further studies, where ~2000 fibres can be used per bundle compared to the ~5000 fibres per bundle used in this study. This would reduce the sample specimen size and would allow the XCT imaging to be a comfortable fibre-level resolution and enable the automatic damage detection method. It would add more accurate information about damage, their progression, and their location, where the confirmed detected damage could be seamlessly compared to the stress and strain fields obtained by modelling and DIC-DVC.

6.3. Testing on different fatigue parameters

Fatigue damage progression has been known to be dependent on the varying levels of strains, R-ratios and load frequencies [9], [211], [231]. Testing on higher load frequencies can lead to self-heating and therefore change the intended damage mechanisms. This is because the wind blades rotate at typically 30-60 rpm [328] and this can translate to 1-2 Hz of alternating load direction. Wind blades also experience different fatigue regimes including tension-compression and compression-compression, it is important to study the damage progression involving compression, where damage mechanisms are fundamentally different and involve kink bands [20],

[56]. It is also important to assess fatigue behaviour at different strain levels, R-ratios and lower load frequencies to study and accordingly adapt wind blade materials to the relevant energy application, which can vary geographically, differ between offshore and onshore etc.

6.4. Image-based modelling

As evidenced in chapter 5, image-based modelling has greatly augmented finite element modelling, where real-world material architecture including imperfections and features can be used instead of synthetic data [192], [193], [198]. In chapter 5, a monotonic tensile simulation result of stress concentrations was proven to partly corroborate with strain concentrations and confirmed damaged regions arising from material fatigue. The segmented data in Chapter 5, and the possibility of generating orientation information obtained methods discussed in Chapter 7, can be used in build improved models, where repeated loading could be simulated instead of monotonic tensile simulation. The damage progression observed in XCT and the progression of strain fields obtained from DIC-DVC could be used to verify simulations.

References

[1] U. Nations, "Net Zero Coalition | United Nations", Accessed: Oct. 08, 2022. [Online]. Available: https://www.un.org/en/climatechange/net-zero-coalition

[2] "Global Wind Report 2022 - Global Wind Energy Council." https://gwec.net/global-wind-report-2022/ (accessed Jul. 22, 2022).

[3] "Net Zero by 2050 – Analysis - IEA." https://www.iea.org/reports/net-zero-by-2050 (accessed Jan. 26, 2023).

[4] "Projected Costs of Generating Electricity 2020 – Analysis - IEA." https://www.iea.org/reports/projected-costs-of-generating-electricity-2020 (accessed Oct. 08, 2022).

[5] "Physics of Wind Turbines | Energy Fundamentals." https://home.uni-leipzig.de/energy/energy-fundamentals/15.htm (accessed Jan. 26, 2023).

[6] "North Sea Power: New GE Plant Will Make 107-Meter-Long Wind Blades In The U.K. | GE News." https://www.ge.com/news/reports/north-sea-power-new-ge-plant-will-make-107-meter-long-wind-blades-in-the-uk (accessed Oct. 08, 2022).

[7] R. P. L. Nijssen, "Fatigue life prediction and strength degradation of wind turbine rotor blade composites," *PhD Thesis, Delft Univ. Technol. Netherlands, 2006.*, 2006.

[8] I. Herráez, B. Stoevesandt, and J. Peinke, "Insight into Rotational Effects on a Wind Turbine Blade Using Navier–Stokes Computations," *Energies 2014, Vol. 7, Pages 6798-6822*, vol. 7, no. 10, pp. 6798–6822, Oct. 2014, doi: 10.3390/EN7106798.

[9] K. M. Jespersen, "Fatigue Damage Evolution in Fibre Composites for Wind Turbine Blades," DTU Wind Energy, 2017. Accessed: Apr. 10, 2020. [Online]. Available: https://orbit.dtu.dk/en/publications/fatigue-damage-evolution-in-fibre-composites-for-wind-turbine-bla-2

[10] "Carbon fiber for wind turbine blades could bring cost, performance benefits – LabNews." https://www.sandia.gov/labnews/2021/01/29/carbon-fiber-for-wind-turbine-blades-could-bring-cost-performance-benefits/ (accessed Jan. 27, 2023).

[11] "Wind turbine blades: Glass vs. carbon fiber | CompositesWorld." https://www.compositesworld.com/articles/wind-turbine-blades-glass-vs-carbon-fiber (accessed Jan. 27, 2023).

[12] B. L. Ennis *et al.*, "Optimized Carbon Fiber Composites in Wind Turbine Blade Design," Albuquerque, New Mexico, 2019.

[13] "Specific stiffness - Specific strength." http://www-materials.eng.cam.ac.uk/mpsite/interactive_charts/spec-spec/NS6Chart.html (accessed Jan. 26, 2023).

[14] R. Talreja, "Damage and fatigue in composites - A personal account," *Compos.*

Sci. Technol., vol. 68, no. 13, pp. 2585–2591, 2008, doi: 10.1016/j.compscitech.2008.04.042.

[15] X. Chen, "Fracture of wind turbine blades in operation—Part I: A comprehensive forensic investigation," *Wind Energy*, vol. 21, no. 11, pp. 1046–1063, Nov. 2018, doi: 10.1002/WE.2212.

[16] T. Svensson, "Prediction uncertainties at variable amplitude fatigue," *Int. J. Fatigue*, vol. 19, no. 93, pp. 295–302, 1997.

[17] "Reliable rotor blades 1.5 MW - 2 MW wind turbines | LM Wind Power." https://www.lmwindpower.com/en/products/blade-types/1mw-to-2mw (accessed Feb. 01, 2023).

[18] D. P. Rommel, D. Di Maio, and T. Tinga, "Calculating wind turbine component loads for improved life prediction," *Renew. Energy*, vol. 146, pp. 223–241, Feb. 2020, doi: 10.1016/J.RENENE.2019.06.131.

[19] R. P. L. Nijssen, *Fatigue Life Prediction and Strength Degradation of Wind Turbine Rotor Blade Composites*. 2006.

[20] M. J. Emerson, Y. Wang, P. J. Withers, K. Conradsen, A. B. Dahl, and V. A. Dahl, "Quantifying fibre reorientation during axial compression of a composite through time-lapse X-ray imaging and individual fibre tracking," *Compos. Sci. Technol.*, vol. 168, pp. 47–54, 2018, doi: 10.1016/j.compscitech.2018.08.028.

[21] P. Brøndsted, H. Lilholt, and A. Lystrup, "Composite materials for wind power turbine blades," *Annu. Rev. Mater. Res.*, vol. 35, pp. 505–538, 2005.

[22] D. P. C. Aiman, M. F. Yahya, and J. Salleh, "Impact properties of 2D and 3D woven composites : A review," vol. 1774, p. 20002, 2016, doi: 10.1063/1.4965050.

[23] W. Zhou *et al.*, "A comparative study of a quasi 3D woven composite with UD and 2D woven laminates," *Compos. Part A Appl. Sci. Manuf.*, vol. 139, p. 106139, Dec. 2020, doi: 10.1016/J.COMPOSITESA.2020.106139.

[24] A. P. Mouritz, M. K. Bannister, P. J. Falzon, and K. H. Leong, "Review of applications for advanced three-dimensional fibre textile composites," *Compos. Part A Appl. Sci. Manuf.*, vol. 30, no. 12, pp. 1445–1461, Dec. 1999, doi: 10.1016/S1359-835X(99)00034-2.

[25] "Warp and Weft - Meaning & Differences | TREASURIE." https://blog.treasurie.com/warp-and-weft/ (accessed Feb. 01, 2023).

[26] "Textile Composite Materials Classification & Applications, Textile Composite Materials, Laminated Composites, 3-D Woven Fabrics, Multilayer Fabrics, Fibre2fashion - Fibre2Fashion." https://www.fibre2fashion.com/industry-article/4503/classification-and-applications-of-textile-composite-materials-part-1 (accessed Feb. 01, 2023).

[27] "Hybrid Fabric - Cristex Composite Aramid-Woven-Fabric-Carbon-Glass." https://cristex.co.uk/products/woven-fabrics/hybrid/ (accessed Sep. 06, 2023).

[28] P. R. Krishna Mohan, M. Anil Kumar, S. G. Kumar, and P. M. Mohite, "Development of In-house Unidirectional Carbon/epoxy Prepregs and its

Characterization for Aerospace Applications," *Procedia Struct. Integr.*, vol. 14, pp. 176–183, Jan. 2019, doi: 10.1016/J.PROSTR.2019.05.023.

[29] "Prepreg Carbon Fiber | ZOLTEK." https://zoltek.com/products/px35/prepreg/ (accessed Feb. 02, 2023).

[30] "Unidirectional Fabric - Multiaxials - Non-Crimp - Fabric- Cristex Composite." https://cristex.co.uk/products/woven-fabrics/unidirectional-fabric/ (accessed Feb. 02, 2023).

[31] G. Adolphs and C. Skinner, "Non-crimp fabric composites in wind turbines," *Non-Crimp Fabr. Compos.*, pp. 481-495e, Jan. 2011, doi: 10.1533/9780857092533.4.481.

[32] C. H. Zweben, "Composites: Overview," *Encycl. Condens. Matter Phys.*, pp. 192–208, Jan. 2005, doi: 10.1016/B0-12-369401-9/00545-3.

[33] C. M. WARD-CLOSE, J. G. ROBERTSON, and S. P. GODFREY, "Fabrication of Monofilament Reinforced Titanium," *Compr. Compos. Mater.*, pp. 655–678, Jan. 2000, doi: 10.1016/B0-08-042993-9/00025-5.

[34] L. Mishnaevsky Jr and P. Brøndsted, "Statistical modelling of compression and fatigue damage of unidirectional fiber reinforced composites," *Compos. Sci. Technol.*, vol. 69, no. 3–4, pp. 477–484, 2009.

[35] "E-glass & S-Glass Fabrics | JPS Composite Materials." https://jpscm.com/products/e-glass-s-glass/ (accessed Feb. 02, 2023).

[36] "The Differences between Fiberglass and Carbon Fiber." https://www.tencom.com/blog/the-differences-between-fiberglass-and-carbon-fiber (accessed Oct. 20, 2022).

[37] "Comparing the Characteristics of Glass, Kevlar (Aramid) and Carbon Fiber." https://www.christinedemerchant.com/carbon-kevlar-glass-comparison.html (accessed Oct. 20, 2022).

[38] M. J. Shukla, D. S. Kumar, K. K. Mahato, D. K. Rathore, R. K. Prusty, and B. C. Ray, "A comparative study of the mechanical performance of Glass and Glass/Carbon hybrid polymer composites at different temperature environments," *IOP Conf. Ser. Mater. Sci. Eng.*, vol. 75, no. 1, 2015, doi: 10.1088/1757-899X/75/1/012002.

[39] D. B. Miracle *et al.*, *ASM handbook*, vol. 21. ASM international Materials Park, OH, 2001.

[40] D. Jang, M. E. Lee, J. Choi, S. Y. Cho, and S. Lee, "Strategies for the production of PAN-Based carbon fibers with high tensile strength," *Carbon N. Y.*, vol. 186, pp. 644–677, Jan. 2022, doi: 10.1016/J.CARBON.2021.10.061.

[41] D. P. Raghavalu Thirumalai Løgstrup Andersen, T., Markussen, C. M., Madsen, B., & Lilholt, H., "Tensile and compression properties of hybrid composites – A comparative study.," *Proc. 19th Int. Conf. Compos. Mater.*, p. (pp. 1029-1035)., 2013.

[42] "Meet LM 88.4 P - the world's longest wind turbine blade | LM Wind Power." https://www.lmwindpower.com/en/products/blade-types/longest-blade-in-the-

world (accessed Feb. 02, 2023).

[43] "Carbon/glass spar cap enables world's longest wind blade | CompositesWorld." https://www.compositesworld.com/articles/carbonglass-spar-cap-enables-worlds-longest-wind-blade (accessed Feb. 02, 2023).

[44] "Turbines of the year: Rotor blades | Windpower Monthly." https://www.windpowermonthly.com/article/1419306/turbines-year-rotor-blades (accessed Feb. 02, 2023).

[45] S. S. P. Reddy, R. Suresh, M. B. Hanamantraygouda, and B. P. Shivakumar, "Use of composite materials and hybrid composites in wind turbine blades," *Mater. Today Proc.*, vol. 46, pp. 2827–2830, Jan. 2021, doi: 10.1016/J.MATPR.2021.02.745.

[46] C.-H. Ong and S. W. Tsai, "The use of carbon fibers in wind turbine blade design: a SERI-8 blade example," Sandia National Labs., Albuquerque, NM (US); Sandia National Labs …, 2000.

[47] "Innovation is the root of the future | LM Wind Power." https://www.lmwindpower.com/en/products/we-know-blades/innovation-is-the-root-of-the-future (accessed Oct. 20, 2022).

[48] H. F. J. Porter, "Fatigue of metal in wrought iron and steel forgings," *J. Franklin Inst.*, vol. 145, no. 4, pp. 241–261, Apr. 1898, doi: 10.1016/S0016-0032(98)90268-X.

[49] K. Boller, "Fatigue fundamentals for composite materials," in *Composite materials: testing and design*, ASTM International, 1969.

[50] P. Paris and F. Erdogan, ", , , ,, p. .," *Trans. Am. Soc. Mech. Eng.*, vol. 85, no. Series D, p. 528, 1963.

[51] P. C. Paris, "Fatigue—an interdisciplinary approach.," *Proc. Tenth Sagamore Conf.*, vol. Syracuse U, 1964.

[52] M. Ciavarella, M. Paggi, and A. Carpinteri, "One, no one, and one hundred thousand crack propagation laws: A generalized Barenblatt and Botvina dimensional analysis approach to fatigue crack growth", doi: 10.1016/j.jmps.2008.09.002.

[53] O. Konur and F. L. Matthews, "Effect of the properties of the constituents on the fatigue performance of composites: a review," *Composites*, vol. 20, no. 4, pp. 317–328, Jul. 1989, doi: 10.1016/0010-4361(89)90657-5.

[54] "Nondestructive Evaluation Physics : Materials." https://www.nde-ed.org/Physics/Materials/Mechanical/Fatigue.xhtml (accessed Feb. 20, 2023).

[55] M. E. Barkey and S. Zhang, "Fatigue of Spot Welds," *Fatigue Test. Anal.*, pp. 285–311, 2005, doi: 10.1016/B978-075067719-6/50008-7.

[56] L. Mishnaevsky, *Micromechanical modelling of wind turbine blade materials*. Woodhead Publishing Limited, 2013. doi: 10.1533/9780857097286.2.298.

[57] A. Gagel, D. Lange, and K. Schulte, "On the relation between crack densities, stiffness degradation, and surface temperature distribution of tensile fatigue

loaded glass-fibre non-crimp-fabric reinforced epoxy," *Compos. Part A Appl. Sci. Manuf.*, vol. 37, no. 2, pp. 222–228, 2006, doi: 10.1016/j.compositesa.2005.03.028.

[58] K. M. Jespersen and L. P. Mikkelsen, "Three dimensional fatigue damage evolution in non-crimp glass fibre fabric based composites used for wind turbine blades," *Compos. Sci. Technol.*, vol. 153, pp. 261–272, Dec. 2017, doi: 10.1016/j.compscitech.2017.10.004.

[59] K. M. Jespersen, J. A. Glud, J. Zangenberg, A. Hosoi, H. Kawada, and L. P. Mikkelsen, "Uncovering the fatigue damage initiation and progression in uni-directional non-crimp fabric reinforced polyester composite," *Compos. Part A Appl. Sci. Manuf.*, vol. 109, pp. 481–497, Jun. 2018, doi: 10.1016/J.COMPOSITESA.2018.03.002.

[60] Y. Wang, L. P. Mikkelsen, G. Pyka, and P. J. Withers, "Time-lapse helical X-ray computed tomography (CT) study of tensile fatigue damage formation in composites for wind turbine blades," *Materials (Basel).*, vol. 11, no. 11, 2018, doi: 10.3390/ma11112340.

[61] R. Guo, C. Li, Y. Niu, and G. Xian, "The fatigue performances of carbon fiber reinforced polymer composites – A review," *J. Mater. Res. Technol.*, vol. 21, pp. 4773–4789, Nov. 2022, doi: 10.1016/J.JMRT.2022.11.053.

[62] X. Gao *et al.*, "Mode I Fatigue of Fibre Reinforced Polymeric Composites: A Review," *Polym. 2022, Vol. 14, Page 4558*, vol. 14, no. 21, p. 4558, Oct. 2022, doi: 10.3390/POLYM14214558.

[63] W. Ferdous *et al.*, "Testing and modelling the fatigue behaviour of GFRP composites – Effect of stress level, stress concentration and frequency," *Eng. Sci. Technol. an Int. J.*, vol. 23, no. 5, pp. 1223–1232, Oct. 2020, doi: 10.1016/J.JESTCH.2020.01.001.

[64] M. Y. Zaghloul, M. M. Y. Zaghloul, and M. M. Y. Zaghloul, "Influence of Stress Level and Fibre Volume Fraction on Fatigue Performance of Glass Fibre-Reinforced Polyester Composites," *Polym. 2022, Vol. 14, Page 2662*, vol. 14, no. 13, p. 2662, Jun. 2022, doi: 10.3390/POLYM14132662.

[65] U. A. Mortensen, S. Rasmussen, L. P. Mikkelsen, A. Fraisse, and T. L. Andersen, "The impact of the fiber volume fraction on the fatigue performance of glass fiber composites," *Compos. Part A Appl. Sci. Manuf.*, vol. 169, p. 107493, Jun. 2023, doi: 10.1016/J.COMPOSITESA.2023.107493.

[66] B. F. Sørensen and S. Goutianos, "Micromechanical model for prediction of the fatigue limit for unidirectional fibre composites," *Mech. Mater.*, vol. 131, pp. 169–187, Apr. 2019, doi: 10.1016/J.MECHMAT.2019.01.023.

[67] A. Gagel, D. Lange, and K. Schulte, "On the relation between crack densities, stiffness degradation, and surface temperature distribution of tensile fatigue loaded glass-fibre non-crimp-fabric reinforced epoxy," *Compos. Part A Appl. Sci. Manuf.*, vol. 37, no. 2, pp. 222–228, Feb. 2006, doi: 10.1016/j.compositesa.2005.03.028.

[68] H. Pakdel and B. Mohammadi, "Stiffness degradation of composite laminates due to matrix cracking and induced delamination during tension-tension

fatigue," *Eng. Fract. Mech.*, vol. 216, p. 106489, Jul. 2019, doi: 10.1016/J.ENGFRACMECH.2019.106489.

[69] B. F. Sørensen, S. Goutianos, L. P. Mikkelsen, and S. Fæster, "Fatigue damage growth and fatigue life of unidirectional composites," *Compos. Sci. Technol.*, vol. 211, p. 108656, Jul. 2021, doi: 10.1016/J.COMPSCITECH.2021.108656.

[70] B. Mohammadi, M. M. Shokrieh, M. Jamali, A. Mahmoudi, and B. Fazlali, "Damage-entropy model for fatigue life evaluation of off-axis unidirectional composites," *Compos. Struct.*, vol. 270, p. 114100, Aug. 2021, doi: 10.1016/J.COMPSTRUCT.2021.114100.

[71] M. Brod, A. Dean, and R. Rolfes, "Numerical life prediction of unidirectional fiber composites under block loading conditions using a progressive fatigue damage model," *Int. J. Fatigue*, vol. 147, p. 106159, Jun. 2021, doi: 10.1016/J.IJFATIGUE.2021.106159.

[72] T. Jeannin, X. Gabrion, E. Ramasso, and V. Placet, "About the fatigue endurance of unidirectional flax-epoxy composite laminates," *Compos. Part B Eng.*, vol. 165, pp. 690–701, May 2019, doi: 10.1016/J.COMPOSITESB.2019.02.009.

[73] J. Zangenberg, P. Brøndsted, and J. W. Gillespie, "Fatigue damage propagation in unidirectional glass fibre reinforced composites made of a non-crimp fabric," *J. Compos. Mater.*, vol. 48, no. 22, pp. 2711–2727, 2014, doi: 10.1177/0021998313502062.

[74] K. . Reifsnider, "Fatigue of Composite Materials: Volume 4 of Composite Materials Series," vol. V, p. 532, 1991.

[75] S. C. Garcea, Y. Wang, and P. J. Withers, "X-ray computed tomography of polymer composites," *Composites Science and Technology*, vol. 156. Elsevier Ltd, pp. 305–319, Mar. 01, 2018. doi: 10.1016/j.compscitech.2017.10.023.

[76] B. S. Hayes and L. M. Gammon, "Optical microscopy of fiber reinforced composites," p. 271, 2010.

[77] B. S. Hayes, "Optical Microscopy of Composites," *ASM Int.*, p. 284, 2010, Accessed: Feb. 03, 2023. [Online]. Available: https://app.knovel.com/hotlink/toc/id:kpOMFRC00F/optical-microscopy-fiber/optical-microscopy-fiber

[78] P. J. Joyce, D. Kugler, and T. J. Moon, "A Technique for Characterizing Process-Induced Fiber Waviness in Unidirectional Composite Laminates-Using Optical Microscopy," *http://dx.doi.org/10.1177/002199839703101702*, vol. 31, no. 17, pp. 1694–1727, Jul. 2016, doi: 10.1177/002199839703101702.

[79] H. Mahmood, A. Dorigato, and A. Pegoretti, "Temperature Dependent Strain/Damage Monitoring of Glass/Epoxy Composites with Graphene as a Piezoresistive Interphase," *Fibers 2019, Vol. 7, Page 17*, vol. 7, no. 2, p. 17, Feb. 2019, doi: 10.3390/FIB7020017.

[80] C. Meola, S. Boccardi, and G. M. Carlomagno, "Infrared thermography in the evaluation of aerospace composite materials : infrared thermography to composites".

[81] C. Colombo, F. Libonati, F. Pezzani, A. Salerno, and L. Vergani, “Fatigue behaviour of a GFRP laminate by thermographic measurements,” *Procedia Eng.*, vol. 10, pp. 3518–3527, 2011.

[82] J. Montesano, Z. Fawaz, and H. Bougherara, “Use of infrared thermography to investigate the fatigue behavior of a carbon fiber reinforced polymer composite,” *Compos. Struct.*, vol. 97, pp. 76–83, Mar. 2013, doi: 10.1016/J.COMPSTRUCT.2012.09.046.

[83] Y. H. Yu, J. H. Choi, J. H. Kweon, and D. H. Kim, “A study on the failure detection of composite materials using an acoustic emission,” *Compos. Struct.*, vol. 75, no. 1–4, pp. 163–169, Sep. 2006, doi: 10.1016/J.COMPSTRUCT.2006.04.070.

[84] “What Is Acoustic Emission Testing? A Definitive Guide - TWI.” https://www.twi-global.com/technical-knowledge/faqs/acoustic-emission-testing (accessed Feb. 06, 2023).

[85] F. Dahmene, S. Yaacoubi, and M. El Mountassir, “Acoustic Emission of Composites Structures: Story, Success, and Challenges,” *Phys. Procedia*, vol. 70, pp. 599–603, Jan. 2015, doi: 10.1016/J.PHPRO.2015.08.031.

[86] A. Marec, J. H. Thomas, and R. El Guerjouma, “Damage characterization of polymer-based composite materials: Multivariable analysis and wavelet transform for clustering acoustic emission data,” *Mech. Syst. Signal Process.*, vol. 22, no. 6, pp. 1441–1464, Aug. 2008, doi: 10.1016/J.YMSSP.2007.11.029.

[87] “Comparing Acoustic Emission signals of different damage mechanisms in carbon fiber composites - Muravin.” https://www.muravin.com/726-2/ (accessed Feb. 06, 2023).

[88] M. Nikbakht, J. Yousefi, H. Hosseini-Toudeshky, and G. Minak, “Delamination evaluation of composite laminates with different interface fiber orientations using acoustic emission features and micro visualization,” *Compos. Part B Eng.*, vol. 113, pp. 185–196, Mar. 2017, doi: 10.1016/J.COMPOSITESB.2016.11.047.

[89] P. Feres Filho, “ACOUSTIC EMISSION TESTING IN COMPOSITE MATERIALS,” *Non-destructive Test. ’92*, pp. 40–44, Jan. 1992, doi: 10.1016/B978-0-444-89791-6.50014-7.

[90] M. Giordano, A. Calabro, C. Esposito, A. D’Amore, and L. Nicolais, “An acoustic-emission characterization of the failure modes in polymer-composite materials,” *Compos. Sci. Technol.*, vol. 58, no. 12, pp. 1923–1928, Dec. 1998, doi: 10.1016/S0266-3538(98)00013-X.

[91] C. Muir *et al.*, “Damage mechanism identification in composites via machine learning and acoustic emission,” *npj Comput. Mater. 2021 71*, vol. 7, no. 1, pp. 1–15, Jun. 2021, doi: 10.1038/s41524-021-00565-x.

[92] A. C. Okafor, N. Singh, N. Singh, and B. N. Oguejiofor, “Acoustic emission detection and prediction of fatigue crack propagation in composite patch repairs using neural network,” *http://dx.doi.org/10.1177/0892705715573649*, vol. 30, no. 1, pp. 3–29, Mar. 2015, doi: 10.1177/0892705715573649.

[93] Y. Ech-Choudany, M. Assarar, D. Scida, F. Morain-Nicolier, and B. Bellach, "Unsupervised clustering for building a learning database of acoustic emission signals to identify damage mechanisms in unidirectional laminates," *Appl. Acoust.*, vol. 123, pp. 123–132, 2017, doi: 10.1016/j.apacoust.2017.03.008.

[94] "Acoustic emission measurements promise better composite-blade damage analysis." https://www.designworldonline.com/acoustic-emission-measurements-promise-better-composite-blade-damage-analysis-2/ (accessed Feb. 06, 2023).

[95] A. Wronkowicz, K. Dragan, and K. Lis, "Assessment of uncertainty in damage evaluation by ultrasonic testing of composite structures," *Compos. Struct.*, vol. 203, pp. 71–84, Nov. 2018, doi: 10.1016/J.COMPSTRUCT.2018.06.109.

[96] H. Taheri and A. A. Hassen, "Nondestructive Ultrasonic Inspection of Composite Materials: A Comparative Advantage of Phased Array Ultrasonic," *Appl. Sci. 2019, Vol. 9, Page 1628*, vol. 9, no. 8, p. 1628, Apr. 2019, doi: 10.3390/APP9081628.

[97] "Ultrasonic examination in Non-Destructive Examination (NDE) - TWI." https://www.twi-global.com/technical-knowledge/faqs/faq-what-are-the-advantages-and-disadvantages-of-ultrasonic-examination-in-non-destructive-examination-nde (accessed Feb. 06, 2023).

[98] E. Larsson, D. Gürsoy, and S. A. Hall, "Kitchen-based light tomography - a DIY toolkit for advancing tomography - by and for the tomography community," *Tomogr. Mater. Struct.*, vol. 1, p. 100001, Mar. 2023, doi: 10.1016/J.TMATER.2022.100001.

[99] S. Mguil-Touchal, F. Morestin, and M. Brunei, "Various Experimental Applications Of DigitalImage Correlation Method," *WIT Trans. Modelling Simul.*, vol. 17, p. 684, Jan. 1970, doi: 10.2495/CMEM970051.

[100] T. C. Chu, W. F. Ranson, and M. A. Sutton, "Applications of digital-image-correlation techniques to experimental mechanics," *Exp. Mech.*, vol. 25, no. 3, pp. 232–244, 1985, doi: 10.1007/BF02325092/METRICS.

[101] J. Q. Da Fonseca, P. M. Mummery, and P. J. Withers, "Full-field strain mapping by optical correlation of micrographs acquired during deformation," *J. Microsc.*, vol. 218, no. Pt 1, pp. 9–21, Apr. 2005, doi: 10.1111/J.1365-2818.2005.01461.X.

[102] P. L. Reu, W. Sweatt, T. Miller, and D. Fleming, "Camera System Resolution and its Influence on Digital Image Correlation," *Exp. Mech.*, vol. 55, no. 1, pp. 9–25, Jan. 2015, doi: 10.1007/S11340-014-9886-Y/TABLES/1.

[103] B. Pan, H. Xie, Z. Wang, K. Qian, and Z. Wang, "Study on subset size selection in digital image correlation for speckle patterns," *Opt. Express*, vol. 16, no. 10, pp. 7037–7048, 2008.

[104] F. Touchard-Lagattu and M. C. Lafarie-Frenot, "Damage and inelastic deformation mechanisms in notched thermoset and thermoplastic laminates," *Compos. Sci. Technol.*, vol. 56, no. 5, pp. 557–568, 1996.

[105] F. Shadmehri and S. Van Hoa, "Digital Image Correlation Applications in

Composite Automated Manufacturing, Inspection, and Testing," *Appl. Sci. 2019, Vol. 9, Page 2719*, vol. 9, no. 13, p. 2719, Jul. 2019, doi: 10.3390/APP9132719.

[106] J. Górszczyk, K. Malicki, and T. Zych, "Application of Digital Image Correlation (DIC) Method for Road Material Testing," *Materials (Basel).*, vol. 12, no. 15, Aug. 2019, doi: 10.3390/MA12152349.

[107] "X-ray Computed Tomography (CT)." https://serc.carleton.edu/research_education/geochemsheets/techniques/CT.html (accessed Feb. 07, 2023).

[108] A. Hosoi, Y. Arao, H. Karasawa, and H. Kawada, "High-cycle fatigue characteristics of quasi-isotropic CFRP laminates," *Adv. Compos. Mater. Off. J. Japan Soc. Compos. Mater.*, vol. 16, no. 2, pp. 151–166, 2007, doi: 10.1163/156855107780918964.

[109] L. Saucedo-Mora, T. Lowe, S. Zhao, P. D. Lee, P. M. Mummery, and T. J. Marrow, "In situ observation of mechanical damage within a SiC-SiC ceramic matrix composite," *J. Nucl. Mater.*, vol. 481, pp. 13–23, Dec. 2016, doi: 10.1016/j.jnucmat.2016.09.007.

[110] L. Sch, P. Pinter, K. Andr, and P. Elsner, "A novel approach for segmenting and mapping of local fiber orientation of continuous fiber-reinforced composite laminates based on volumetric images," *NDT&E Int.*, vol. 110, pp. 963–8695, 2020, doi: 10.1016/j.ndteint.2019.102194.

[111] Y. Chai *et al.*, "Following the effect of braid architecture on performance and damage of carbon fibre/epoxy composite tubes during torsional straining," *Compos. Sci. Technol.*, vol. 200, p. 108451, Nov. 2020, doi: 10.1016/J.COMPSCITECH.2020.108451.

[112] F. Cosmi and A. Bernasconi, "Micro-CT investigation on fatigue damage evolution in short fibre reinforced polymers," *Compos. Sci. Technol.*, vol. 79, pp. 70–76, 2013, doi: 10.1016/j.compscitech.2013.02.008.

[113] J. Baruchel, J.-Y. Buffiere, and E. Maire, "X-ray tomography in material science," 2000.

[114] F. H. Attix, W. C. Roesch, and E. Tochilin, *Radiation Dosimetry: Instrumentation*, vol. 2. Academic Press, 1966.

[115] P. J. Withers, "X-ray nanotomography," *Mater. Today*, vol. 10, no. 12, pp. 26–34, 2007, doi: 10.1016/S1369-7021(07)70305-X.

[116] T. J. Davis, D. Gao, T. E. Gureyev, A. W. Stevenson, and S. W. Wilkins, "Phase-contrast imaging of weakly absorbing materials using hard X-rays," *Nature*, vol. 373, no. 6515, p. 595, 1995.

[117] S. W. Smith, "The scientist and engineer's guide to digital signal processing," *Calif. Tech. Publ.*, 1997.

[118] L. Borg, J. Frikel, J. S. Jørgensen, and E. T. Quinto, "Analyzing reconstruction artifacts from arbitrary incomplete x-ray CT data," *SIAM J. Imaging Sci.*, vol. 11, no. 4, pp. 2786–2814, 2018.

[119] E. N. Landis and D. T. Keane, "X-ray microtomography," *Mater. Charact.*, vol. 61, no. 12, pp. 1305–1316, 2010.

[120] C. Shashank Kaira *et al.*, "Automated correlative segmentation of large Transmission X-ray Microscopy (TXM) tomograms using deep learning," *Mater. Charact.*, vol. 142, no. January, pp. 203–210, 2018, doi: 10.1016/j.matchar.2018.05.053.

[121] C. Cernazanu-Glavan and S. Holban, "Segmentation of bone structure in X-ray images using convolutional neural network," *Adv. Electr. Comput. Eng.*, vol. 13, no. 1, pp. 87–94, 2013, doi: 10.4316/AECE.2013.01015.

[122] N. Otsu, "A threshold selection method from gray-level histograms," *IEEE Trans. Syst. Man. Cybern.*, vol. 9, no. 1, pp. 62–66, 1979.

[123] M. J. Emerson, K. M. Jespersen, A. B. Dahl, K. Conradsen, and L. P. Mikkelsen, "Individual fibre segmentation from 3D X-ray computed tomography for characterising the fibre orientation in unidirectional composite materials," *Compos. Part A Appl. Sci. Manuf.*, vol. 97, pp. 83–92, 2017, doi: 10.1016/j.compositesa.2016.12.028.

[124] X. Zhang, F. Jia, S. Luo, G. Liu, and Q. Hu, "A marker-based watershed method for X-ray image segmentation," *Comput. Methods Programs Biomed.*, vol. 113, no. 3, pp. 894–903, 2014.

[125] D. Legland, I. Arganda-Carreras, and P. Andrey, "MorphoLibJ: Integrated library and plugins for mathematical morphology with ImageJ," *Bioinformatics*, vol. 32, no. 22, pp. 3532–3534, Nov. 2016, doi: 10.1093/BIOINFORMATICS/BTW413.

[126] "Distance Transform Watershed." https://imagej.net/plugins/distance-transform-watershed (accessed Feb. 08, 2023).

[127] D. Legland, I. Arganda-Carreras, and P. Andrey, "MorphoLibJ: integrated library and plugins for mathematical morphology with ImageJ," *Bioinformatics*, vol. 32, no. 22, pp. 3532–3534, Nov. 2016, doi: 10.1093/BIOINFORMATICS/BTW413.

[128] P. E. Hart, "How the Hough transform was invented [DSP History]," *IEEE Signal Process. Mag.*, vol. 26, no. 6, pp. 18–22, 2009.

[129] Derfopps, "No Title," *[CC BY 4.0 (https//creativecommons.org/licenses/by/4.0)]*, [Online]. Available: https://commons.wikimedia.org/wiki/File:Hough_transform_diagram.svg

[130] H. K. Rana, M. S. Azam, M. R. Akhtar, J. M. W. Quinn, and M. A. Moni, "A fast iris recognition system through optimum feature extraction," *PeerJ Comput. Sci.*, vol. 2019, no. 4, pp. 1–13, Apr. 2019, doi: 10.7717/PEERJ-CS.184/SUPP-1.

[131] V. A. Dahl, C. H. Trinderup, M. J. Emerson, and A. B. Dahl, "Content-based Propagation of User Markings for Interactive Segmentation of Patterned Images," pp. 1–9, 2018, [Online]. Available: http://arxiv.org/abs/1809.02226

[132] A. B. Dahl and V. A. Dahl, "Dictionary based image segmentation," in *Lecture Notes in Computer Science (including subseries Lecture Notes in Artificial*

Intelligence and Lecture Notes in Bioinformatics), 2015, vol. 9127, pp. 26–37. doi: 10.1007/978-3-319-19665-7_3.

[133] X. Yang, S. Wu, I. Sechopoulos, and B. Fei, "Cupping artifact correction and automated classification for high-resolution dedicated breast CT images," *Med. Phys.*, vol. 39, no. 10, pp. 6397–6406, Oct. 2012, doi: 10.1118/1.4754654.

[134] J. Glinz, S. Zabler, J. Kastner, and S. Senck, "Metal Artifacts in Attenuation and Phase Contrast X-Ray Microcomputed Tomography: A Comparative Study," *Exp. Mech.*, vol. 62, no. 5, pp. 837–847, Jun. 2022, doi: 10.1007/S11340-022-00835-9/TABLES/2.

[135] Barett, "Artefacts in CT: Recognition and Avoidance," *RadioGraphics*, vol. 24, pp. 1679–1691, 2004.

[136] R. Schulze *et al.*, "Artefacts in CBCT: a review," *Dentomaxillofacial Radiol.*, vol. 40, no. 5, pp. 265–273, 2011.

[137] G. Fourrier, A. Rassineux, F. H. Leroy, M. Hirsekorn, C. Fagiano, and E. Baranger, "Automated conformal mesh generation chain for woven composites based on CT-scan images with low contrasts," *Compos. Struct.*, vol. 308, p. 116673, Mar. 2023, doi: 10.1016/J.COMPSTRUCT.2023.116673.

[138] A. Kofler, M. Haltmeier, C. Kolbitsch, M. Kachelrieß, and M. Dewey, "A u-nets cascade for sparse view computed tomography," *Lect. Notes Comput. Sci. (including Subser. Lect. Notes Artif. Intell. Lect. Notes Bioinformatics)*, vol. 11074 LNCS, pp. 91–99, 2018, doi: 10.1007/978-3-030-00129-2_11/TABLES/2.

[139] T. Varslot, A. Kingston, G. Myers, and A. Sheppard, "High-resolution helical cone-beam micro-CT with theoretically-exact reconstruction from experimental data," *Med. Phys.*, vol. 38, no. 10, pp. 5459–5476, Sep. 2011, doi: 10.1118/1.3633900.

[140] C. Nardi *et al.*, "Motion artefacts in cone beam CT: An in vitro study about the effects on the images," *Br. J. Radiol.*, vol. 89, no. 1058, Dec. 2016, doi: 10.1259/BJR.20150687/ASSET/IMAGES/LARGE/BJR.20150687.G007.JPEG.

[141] "British Standards. BS ISO 16016-1 Non destructive testing. Radiation method. Computed tomogaphy. Part 3. Operation and interpretation. Technical report.," 2009.

[142] B. Yu, R. S. Bradley, C. Soutis, and P. J. Withers, "A comparison of different approaches for imaging cracks in composites by X-ray microtomography," in *Philosophical Transactions of the Royal Society A: Mathematical, Physical and Engineering Sciences*, Jul. 2016, vol. 374, no. 2071. doi: 10.1098/rsta.2016.0037.

[143] M. L. Bouxsein, S. K. Boyd, B. A. Christiansen, R. E. Guldberg, K. J. Jepsen, and R. Müller, "Guidelines for assessment of bone microstructure in rodents using micro–computed tomography," *J. Bone Miner. Res.*, vol. 25, no. 7, pp. 1468–1486, Jul. 2010, doi: 10.1002/JBMR.141.

[144] S. Lee, M. S. Lee, and M. G. Kang, "Poisson–Gaussian Noise Analysis and

Estimation for Low-Dose X-ray Images in the NSCT Domain," *Sensors 2018, Vol. 18, Page 1019*, vol. 18, no. 4, p. 1019, Mar. 2018, doi: 10.3390/S18041019.

[145] T. M. Breunig, S. R. Stock, A. Guvenilir, J. C. Elliott, P. Anderson, and G. R. Davis, "Damage in aligned-fibre SiC/Al quantified using a laboratory X-ray tomographic microscope," *Composites*, vol. 24, no. 3, pp. 209–213, 1993, doi: 10.1016/0010-4361(93)90165-5.

[146] I. Sinclair, D. J. Bull, T. Baumbach, L. Helfen, and S. M. Spearing, "A comparison of multi-scale 3D X-ray tomographic inspection techniques for assessing carbon fibre composite impact damage," *Compos. Sci. Technol.*, vol. 75, pp. 55–61, 2012, doi: 10.1016/j.compscitech.2012.12.006.

[147] M. Magnusson, R. Lenz, and P. E. Danielsson, "Evaluation of methods for shaded surface display of CT volumes," *Comput. Med. Imaging Graph.*, vol. 15, no. 4, pp. 247–256, Jul. 1991, doi: 10.1016/0895-6111(91)90083-8.

[148] A. Guvenilir, T. M. Breunig, J. H. Kinney, and S. R. Stock, "New direct observations of crack closure processes in AlLi 2090 T8E41," *Philos. Trans. R. Soc. London. Ser. A Math. Phys. Eng. Sci.*, vol. 357, no. 1761, pp. 2755–2775, 1999, doi: 10.1098/RSTA.1999.0464.

[149] B. Yu, R. S. Bradley, C. Soutis, and P. J. Withers, "A comparison of different approaches for imaging cracks in composites by X-ray microtomography," *Philos. Trans. R. Soc. A Math. Phys. Eng. Sci.*, vol. 374, no. 2071, p. 20160037, 2016.

[150] A. Kyrieleis, V. Titarenko, M. Ibison, T. Connolley, and P. J. Withers, "Region-of-interest tomography using filtered backprojection: Assessing the practical limits," *J. Microsc.*, vol. 241, no. 1, pp. 69–82, 2010, doi: 10.1111/j.1365-2818.2010.03408.x.

[151] A. Kyrieleis, M. Ibison, V. Titarenko, and P. J. Withers, "Image stitching strategies for tomographic imaging of large objects at high resolution at synchrotron sources," *Nucl. Instruments Methods Phys. Res. Sect. A Accel. Spectrometers, Detect. Assoc. Equip.*, vol. 607, no. 3, pp. 677–684, Aug. 2009, doi: 10.1016/J.NIMA.2009.06.030.

[152] "Xradia 610 & 620 Versa," 2019, [Online]. Available: https://www.zeiss.com/microscopy/int/products/x-ray-microscopy/zeiss-xradia-610-620-versa.html

[153] "Avizo Software | Materials Characterization Software - UK", Accessed: Feb. 09, 2023. [Online]. Available: https://www.thermofisher.com/uk/en/home/electron-microscopy/products/software-em-3d-vis/avizo-software.html

[154] S. C. Mayo, A. W. Stevenson, and S. W. Wilkins, "In-Line Phase-Contrast X-ray Imaging and Tomography for Materials Science," *Materials (Basel).*, vol. 5, no. 12, pp. 937–965, 2012, doi: 10.3390/ma5050937.

[155] M. Endrizzi, "X-ray phase-contrast imaging," *Nucl. Instruments Methods Phys. Res. Sect. A Accel. Spectrometers, Detect. Assoc. Equip.*, vol. 878, pp. 88–98, 2018, doi: 10.1016/j.nima.2017.07.036.

[156] T. H. Le, P. J. J. Dumont, L. Orgéas, D. Favier, L. Salvo, and E. Boller, "X-ray phase contrast microtomography for the analysis of the fibrous microstructure of SMC composites," *Compos. Part A Appl. Sci. Manuf.*, vol. 39, no. 1, pp. 91–103, Jan. 2008, doi: 10.1016/J.COMPOSITESA.2007.08.027.

[157] T. K. Varslot, A. M. Kingston, S. J. Latham, J. Middleton, M. a Knackstedt, and A. P. Sheppard, "Combining High-Fidelity Helical Micro- Tomography With Region-of-Interest Scanning for Improved Core Characterisation," no. January, pp. 1–12, 2011.

[158] A. Sheppard *et al.*, "Techniques in helical scanning, dynamic imaging and image segmentation for improved quantitative analysis with X-ray micro-CT," *Nucl. instruments methods Phys. Res. Sect. B Beam Interact. with Mater. atoms*, vol. 324, pp. 49–56, 2014.

[159] T. Varslot, A. Kingston, G. Myers, and A. Sheppard, "High-resolution helical cone-beam micro-CT with theoretically-exact reconstruction from experimental data," *Med. Phys.*, vol. 38, no. 10, pp. 5459–5476, 2011, doi: 10.1118/1.3633900.

[160] E. Schöberl *et al.*, "A novel particle-filled carbon-fibre reinforced polymer model composite tailored for the application of digital volume correlation and computed tomography," *J. Compos. Mater.*, vol. 55, no. 14, pp. 1907–1934, Jun. 2021, doi: 10.1177/0021998320966388/ASSET/IMAGES/LARGE/10.1177_0021998320966388-FIG2.JPEG.

[161] R. Brault, A. Germaneau, J. C. Dupré, P. Doumalin, S. Mistou, and M. Fazzini, "In-situ Analysis of Laminated Composite Materials by X-ray Micro-Computed Tomography and Digital Volume Correlation," *Exp. Mech.*, vol. 53, no. 7, pp. 1143–1151, Sep. 2013, doi: 10.1007/s11340-013-9730-9.

[162] P. Lecomte-Grosbras, J. Réthoré, N. Limodin, J. F. Witz, and M. Brieu, "Three-Dimensional Investigation of Free-Edge Effects in Laminate Composites Using X-ray Tomography and Digital Volume Correlation," *Exp. Mech.*, vol. 55, no. 1, pp. 301–311, Jan. 2015, doi: 10.1007/S11340-014-9891-1/FIGURES/12.

[163] F. Wan, R. Liu, Y. Wang, Y. Cao, C. Zhang, and T. J. Marrow, "Damage development during flexural loading of a 5-directional braided C/C-SiC composite, characterized by X-ray tomography and digital volume correlation," *Ceram. Int.*, vol. 45, no. 5, pp. 5601–5612, Apr. 2019, doi: 10.1016/J.CERAMINT.2018.12.020.

[164] E. Schöberl *et al.*, "Fibre-direction strain measurement in a composite ply under quasi-static tensile loading using Digital Volume Correlation and in situ Synchrotron Radiation Computed Tomography," *Compos. Part A Appl. Sci. Manuf.*, vol. 137, p. 105935, Oct. 2020, doi: 10.1016/J.COMPOSITESA.2020.105935.

[165] J. F. R. Sanchez and A. M. Waas, "High resolution experimental data for fatigue predictions of laminated fiber reinforced composites," *AIAA Sci. Technol. Forum Expo. AIAA SciTech Forum 2022*, 2022, doi: 10.2514/6.2022-0669.

[166] R. Brault, A. Germaneau, J. C. Dupré, P. Doumalin, S. Mistou, and M. Fazzini,

"In-situ Analysis of Laminated Composite Materials by X-ray Micro-Computed Tomography and Digital Volume Correlation," *Exp. Mech. 2013 537*, vol. 53, no. 7, pp. 1143–1151, Feb. 2013, doi: 10.1007/S11340-013-9730-9.

[167] A. Germaneau, P. Doumalin, and J. C. Dupré, "3D Strain Field Measurement by Correlation of Volume Images Using Scattered Light: Recording of Images and Choice of Marks," *Strain*, vol. 43, no. 3, pp. 207–218, Aug. 2007, doi: 10.1111/J.1475-1305.2007.00340.X.

[168] "StrainMaster DVC." https://www.lavision.de/en/products/strainmaster/dvc/ (accessed Nov. 30, 2022).

[169] M. Mehdikhani *et al.*, "Digital volume correlation for meso/micro in-situ damage analysis in carbon fiber reinforced composites," *Compos. Sci. Technol.*, vol. 213, p. 108944, Sep. 2021, doi: 10.1016/J.COMPSCITECH.2021.108944.

[170] M. Palanca, G. Tozzi, L. Cristofolini, M. Viceconti, and E. Dall'Ara, "Three-dimensional local measurements of bone strain and displacement: comparison of three digital volume correlation approaches," *J. Biomech. Eng.*, vol. 137, no. 7, Jul. 2015, doi: 10.1115/1.4030174.

[171] M. Palanca *et al.*, "Digital volume correlation can be used to estimate local strains in natural and augmented vertebrae: An organ-level study," *J. Biomech.*, vol. 49, no. 16, pp. 3882–3890, Dec. 2016, doi: 10.1016/J.JBIOMECH.2016.10.018.

[172] E. Dall'Ara, D. Barber, and M. Viceconti, "About the inevitable compromise between spatial resolution and accuracy of strain measurement for bone tissue: a 3D zero-strain study," *J. Biomech.*, vol. 47, no. 12, pp. 2956–2963, Sep. 2014, doi: 10.1016/J.JBIOMECH.2014.07.019.

[173] "Digital Volume Correlation - VGSTUDIO MAX - Products - volumegraphics.com." https://www.volumegraphics.com/en/products/vgsm/digital-volume-correlation.html (accessed Nov. 30, 2022).

[174] "VIC-Volume — Correlated Solutions Digital Image Correlation." https://www.correlatedsolutions.com/volume (accessed Nov. 30, 2022).

[175] S. C. Garcea, Y. Wang, and P. J. Withers, "X-ray computed tomography of polymer composites," *Compos. Sci. Technol.*, vol. 156, pp. 305–319, 2018, doi: 10.1016/j.compscitech.2017.10.023.

[176] Y. Gao, W. Hu, S. Xin, and L. Sun, "A review of applications of CT imaging on fiber reinforced composites," *J. Compos. Mater.*, vol. 56, no. 1, pp. 133–164, Jan. 2022, doi: 10.1177/00219983211050705/ASSET/IMAGES/LARGE/10.1177_00219983211050705-FIG20.JPEG.

[177] X. Liu, X. Wang, D. Zhang, and K. Qian, "Effect of voids on fatigue damage propagation in 3D5D braided composites revealed via automated algorithms using X-ray computed tomography," *Int. J. Fatigue*, vol. 158, p. 106778, May 2022, doi: 10.1016/J.IJFATIGUE.2022.106778.

[178] J. Wang *et al.*, “Nondestructive damage evaluation of composites based on terahertz and X-ray image fusion,” *NDT E Int.*, vol. 127, p. 102616, Apr. 2022, doi: 10.1016/J.NDTEINT.2022.102616.

[179] V. Pidou-Brion and Y. Le Guilloux, “Active yarn meshes for segmentation on X-ray computed tomography of textile composite materials at the mesoscopic scale,” *Compos. Struct.*, vol. 281, p. 115084, Feb. 2022, doi: 10.1016/J.COMPSTRUCT.2021.115084.

[180] Y. Gong, J. Luo, H. Shao, and Z. Li, “A transfer learning object detection model for defects detection in X-ray images of spacecraft composite structures,” *Compos. Struct.*, vol. 284, p. 115136, Mar. 2022, doi: 10.1016/J.COMPSTRUCT.2021.115136.

[181] J. Holmes, S. Sommacal, Z. Stachurski, R. Das, and P. Compston, “Digital image and volume correlation with X-ray micro-computed tomography for deformation and damage characterisation of woven fibre-reinforced composites,” *Compos. Struct.*, vol. 279, p. 114775, Jan. 2022, doi: 10.1016/J.COMPSTRUCT.2021.114775.

[182] D. Depriester, S. Rolland du Roscoat, L. Orgéas, C. Geindreau, B. Levrard, and F. Brémond, “Individual fibre separation in 3D fibrous materials imaged by X-ray tomography,” *J. Microsc.*, vol. 286, no. 3, pp. 220–239, Jun. 2022, doi: 10.1111/JMI.13096.

[183] R. F. Egerton, “Physical Principles of Electron Microscopy”.

[184] I. A. Abdulganiyu, I. N. A. Oguocha, and A. G. Odeshi, “Influence of microfillers addition on the flexural properties of carbon fiber reinforced phenolic composites,” *J. Compos. Mater.*, vol. 55, no. 27, pp. 3973–3988, Nov. 2021, doi: 10.1177/00219983211031633/ASSET/IMAGES/LARGE/10.1177_00219983211031633-FIG2.JPEG.

[185] H. Liu *et al.*, “Modelling damage in fibre-reinforced thermoplastic composite laminates subjected to three-point bend loading,” *Compos. Struct.*, vol. 236, p. 111889, Mar. 2020, doi: 10.1016/J.COMPSTRUCT.2020.111889.

[186] M. Daly *et al.*, “Large volume serial section tomography by Xe Plasma FIB dual beam microscopy,” *Ultramicroscopy*, vol. 161, pp. 119–129, 2015, doi: 10.1016/j.ultramic.2015.11.001.

[187] T. Quick, S. Safriet, D. Mollenhauer, C. Ryther, and R. Wheeler, “Compression Testing of Micro-Scale Unidirectional Polymer Matrix Composites,” in *Fracture, Fatigue, Failure and Damage Evolution, Volume 8: Proceedings of the 2015 Annual Conference on Experimental and Applied Mechanics*, 2015, p. 225.

[188] J. Hapke, F. Gehrig, N. Huber, K. Schulte, and E. T. Lilleodden, “Compressive failure of UD-CFRP containing void defects: in situ SEM microanalysis,” *Compos. Sci. Technol.*, vol. 71, no. 9, pp. 1242–1249, 2011.

[189] T. L. Burnett and P. J. Withers, “Completing the picture through correlative characterization,” *Nat. Mater.*, doi: 10.1038/s41563-019-0402-8.

[190] A. Roche, G. Malandain, X. Pennec, and N. Ayache, “The correlation ratio as a new similarity measure for multimodal image registration,” *Lect. Notes Comput. Sci. (including Subser. Lect. Notes Artif. Intell. Lect. Notes Bioinformatics)*, vol. 1496, pp. 1115–1124, 1998, doi: 10.1007/BFB0056301/COVER.

[191] J. Zangenberg Hansen, “The effects of fibre architecture on fatigue life-time of composite materials,” 2013.

[192] R. M. Auenhammer, N. Jeppesen, L. P. Mikkelsen, V. A. Dahl, B. J. Blinzler, and L. E. Asp, “Robust numerical analysis of fibrous composites from X-ray computed tomography image data enabling low resolutions,” *Compos. Sci. Technol.*, vol. 224, p. 109458, Jun. 2022, doi: 10.1016/J.COMPSCITECH.2022.109458.

[193] R. M. Auenhammer, L. P. Mikkelsen, L. E. Asp, and B. J. Blinzler, “X-ray tomography based numerical analysis of stress concentrations in non-crimp fabric reinforced composites - assessment of segmentation methods,” *IOP Conf. Ser. Mater. Sci. Eng.*, vol. 942, no. 1, p. 012038, Oct. 2020, doi: 10.1088/1757-899X/942/1/012038.

[194] N. Jeppesen, L. P. Mikkelsen, A. B. Dahl, A. N. Christensen, and V. A. Dahl, “Quantifying effects of manufacturing methods on fiber orientation in unidirectional composites using structure tensor analysis,” *Compos. Part A Appl. Sci. Manuf.*, vol. 149, p. 106541, Oct. 2021, doi: 10.1016/J.COMPOSITESA.2021.106541.

[195] A. M. Roseman, “Particle finding in electron micrographs using a fast local correlation algorithm,” *Ultramicroscopy*, vol. 94, no. 3–4, pp. 225–236, Apr. 2003, doi: 10.1016/S0304-3991(02)00333-9.

[196] I. Straumit, S. V. Lomov, and M. Wevers, “Quantification of the internal structure and automatic generation of voxel models of textile composites from X-ray computed tomography data,” *Compos. Part A Appl. Sci. Manuf.*, vol. 69, pp. 150–158, Feb. 2015, doi: 10.1016/J.COMPOSITESA.2014.11.016.

[197] N. Jeppesen, V. A. Dahl, A. N. Christensen, A. B. Dahl, and L. P. Mikkelsen, “Characterization of the fiber orientations in non-crimp glass fiber reinforced composites using structure tensor,” in *IOP Conference Series: Materials Science and Engineering*, Oct. 2020, vol. 942, no. 1, p. 012037. doi: 10.1088/1757-899X/942/1/012037.

[198] R. M. Auenhammer, L. P. Mikkelsen, L. E. Asp, and B. J. Blinzler, “Automated X-ray computer tomography segmentation method for finite element analysis of non-crimp fabric reinforced composites,” *Compos. Struct.*, vol. 256, p. 113136, Jan. 2021, doi: 10.1016/j.compstruct.2020.113136.

[199] Z. Tabor, R. Petryniak, Z. Latała, and T. Konopka, “The potential of multi-slice computed tomography based quantification of the structural anisotropy of vertebral trabecular bone,” *Med. Eng. Phys.*, vol. 35, no. 1, pp. 7–15, Jan. 2013, doi: 10.1016/J.MEDENGPHY.2012.03.003.

[200] “Structure Tensor for Python - PyPI.” https://pypi.org/project/structure-tensor/ (accessed Jan. 24, 2023).

[201] F. B. Salling, N. Jeppesen, M. R. Sonne, J. H. Hattel, and L. P. Mikkelsen, "Individual fibre inclination segmentation from X-ray computed tomography using principal component analysis," *https://doi.org/10.1177/00219983211052741*, vol. 56, no. 1, pp. 83–98, Nov. 2021, doi: 10.1177/00219983211052741.

[202] R. M. Auenhammer, N. Jeppesen, L. P. Mikkelsen, V. A. Dahl, and L. E. Asp, "X-ray computed tomography data structure tensor orientation mapping for finite element models — STXAE," *Softw. Impacts*, vol. 11, p. 100216, Feb. 2022, doi: 10.1016/J.SIMPA.2021.100216.

[203] C. A. Schneider, W. S. Rasband, and K. W. Eliceiri, "NIH Image to ImageJ: 25 years of image analysis," *Nature Methods*, vol. 9, no. 7. NIH Public Access, pp. 671–675, Jul. 2012. doi: 10.1038/nmeth.2089.

[204] I. Arganda-Carreras *et al.*, "Trainable Weka Segmentation: a machine learning tool for microscopy pixel classification", doi: 10.1093/bioinformatics/btx180.

[205] A. Prinzie and D. Van Den Poel, "Random multiclass classification: generalizing random forests to random MNL and random NB," in *Lecture Notes in Computer Science (including subseries Lecture Notes in Artificial Intelligence and Lecture Notes in Bioinformatics)*, 2007, vol. 4653 LNCS, pp. 349–358. doi: 10.1007/978-3-540-74469-6_35.

[206] R. Domander, A. A. Felder, M. Doube, K. Madi, M. Kersh, and D. Schmidt, "BoneJ2 - refactoring established research software," *Wellcome Open Res. 2021 637*, vol. 6, p. 37, Apr. 2021, doi: 10.12688/wellcomeopenres.16619.2.

[207] N. A. Hotaling, K. Bharti, H. Kriel, and C. G. Simon, "DiameterJ: A validated open source nanofiber diameter measurement tool," *Biomaterials*, vol. 61, pp. 327–338, Aug. 2015, doi: 10.1016/j.biomaterials.2015.05.015.

[208] D. Ershov *et al.*, "TrackMate 7: integrating state-of-the-art segmentation algorithms into tracking pipelines," *Nat. Methods 2022 197*, vol. 19, no. 7, pp. 829–832, Jun. 2022, doi: 10.1038/s41592-022-01507-1.

[209] J. Y. Tinevez *et al.*, "TrackMate: An open and extensible platform for single-particle tracking," *Methods*, vol. 115, pp. 80–90, Feb. 2017, doi: 10.1016/j.ymeth.2016.09.016.

[210] K. M. Jespersen and L. P. Mikkelsen, "Ex-situ X-ray computed tomography data for a non-crimp fabric based glass fibre composite under fatigue loading," *Data Br.*, vol. 15, pp. 1003–1005, Dec. 2017, doi: 10.1016/J.DIB.2017.10.074.

[211] B. F. Sørensen and L. P. Mikkelsen, "New advanced materials will enable the bigger wind turbines of the future," *DTU Int. Energy Rep. 2021 Perspect. Wind Energy*, pp. 125–133, 2021, doi: 10.11581/DTU.00000213.

[212] R. Blanc and P. Westenberger, "Comparison of fiber orientation analysis methods in Avizo." Accessed: Dec. 03, 2020. [Online]. Available: http://www.ndt.net/?id=20865

[213] "Fast Random Forest." https://code.google.com/archive/p/fast-random-forest/ (accessed Feb. 28, 2023).

[214] "What is Random Forest? [Beginner's Guide + Examples]."

https://careerfoundry.com/en/blog/data-analytics/what-is-random-forest/ (accessed Feb. 28, 2023).

[215] "Scripting the Trainable Weka Segmentation." https://imagej.net/plugins/tws/scripting#Example:_apply_classifier_to_all_images_in_folder (accessed Feb. 27, 2023).

[216] "Renewable Energy Technologies: Cost Analysis," 2012. Accessed: Apr. 05, 2020. [Online]. Available: https://www.irena.org/documentdownloads/publications/re_technologies_cost_analysis-wind_power.pdf

[217] "Annual Wind Energy Report 2018." [Online]. Available: https://gwec.net/global-wind-report-2018/

[218] A. L. Highsmith and K. L. Reifsnider, "Stiffness-reduction mechanisms in composite laminates," in *Damage in composite materials: basic mechanisms, accumulation, tolerance, and characterization*, ASTM International, 1982. [Online]. Available: https://doi.org/10.1520/STP34323S

[219] B. D. Agarwal, L. J. Broutman, and K. Chandrashekhara, *Analysis and Performance of Fiber Composites.* John Wiley & Sons, Incorporated, 2017.

[220] "Fatigue of Composite Materials," 1973. Accessed: Apr. 06, 2020. [Online]. Available: https://www.astm.org/digital_library/stp/source_pages/stp569.htm

[221] R. Talreja, "Fatigue of Composite Materials: Damage Mechanisms and Fatigue-Life Diagrams.," *Proc. R. Soc. London, Ser. A Math. Phys. Sci.*, vol. 378, no. 1775, pp. 461–475, 1981, doi: 10.1098/rspa.1981.0163.

[222] P. E. Anuta, "Spatial Registration of Multispectral and Multitemporal Digital Imagery Using Fast Fourier Transform Techniques," *IEEE Trans. Geosci. Electron.*, vol. 8, no. 4, pp. 353–368, 1970, doi: 10.1109/TGE.1970.271435.

[223] S. S. Russell, "Image Correlation Nondestructive Evaluation of Impact Damage in a Glass Fibre Composite," 1990. Accessed: Apr. 10, 2020. [Online]. Available: https://ntrs.nasa.gov/search.jsp?R=19910008881

[224] K. L. Reifsnider and R. Jamison, "Fracture of fatigue-loaded composite laminates," *Int. J. Fatigue*, vol. 4, no. 4, pp. 187–197, 1982, doi: 10.1016/0142-1123(82)90001-9.

[225] O. V Startsev, A. S. Krotov, and P. D. Golub, "Effect of climatic and radiation ageing on properties of VPS-7 glass fibre reinforced epoxy composite."

[226] E. K. Gamstedt, "Effects of debonding and fiber strength distribution on fatigue-damage propagation in carbon fiber-reinforced epoxy," *J. Appl. Polym. Sci.*, vol. 76, no. 4, pp. 457–474, 2000, doi: 10.1002/(SICI)1097-4628(20000425)76:4<457::AID-APP3>3.0.CO;2-L.

[227] F. Edgren, D. Mattsson, L. E. Asp, and J. Varna, "Formation of damage and its effects on non-crimp fabric reinforced composites loaded in tension," *Compos. Sci. Technol.*, vol. 64, no. 5, pp. 675–692, 2004, doi: 10.1016/S0266-3538(03)00292-6.

[228] J. Tong, F. J. Guild, S. L. Ogin, and P. A. Smith, "On matrix crack growth in

quasi-isotropic laminates - I. Experimental investigation," *Compos. Sci. Technol.*, vol. 57, no. 11, pp. 1527–1535, 1997, doi: 10.1016/S0266-3538(97)00080-8.

[229] C. E. Demers, "Tension–tension axial fatigue of E-glass fiber-reinforced polymeric composites: tensile fatigue modulus," *Constr. Build. Mater.*, vol. 12, no. 1, pp. 51–58, Apr. 1998, doi: 10.1016/S0950-0618(97)00059-7.

[230] P. W. R. Beaumont, R. A. Dimant, and H. R. Shercliff, "Failure processes in composite materials: Getting physical," *J. Mater. Sci.*, vol. 41, no. 20, pp. 6526–6546, Oct. 2006, doi: 10.1007/S10853-006-0196-3/FIGURES/25.

[231] A. K. Bangaru, B. F. Sørensen, and L. P. Mikkelsen, "Three dimensional microscale characterization of off-axis tunnelling cracks in non-crimp fabric based composites," *Compos. Sci. Technol.*, vol. 226, p. 109502, Jul. 2022, doi: 10.1016/J.COMPSCITECH.2022.109502.

[232] H. B. Kahla, Z. Ayadi, and J. Varna, "Local Delaminations Induced by Interaction Between Intralaminar Cracking and Specimen Edge in Quasi-Isotropic CF/EP NCF Composites in Fatigue Loadings," *Mech. Compos. Mater.*, vol. 56, no. 3, pp. 291–302, Jul. 2020, doi: 10.1007/S11029-020-09881-7/FIGURES/9.

[233] B. Fazlali, S. V. Lomov, and Y. Swolfs, "Fiber break model for tension-tension fatigue of unidirectional composites," *Compos. Part B Eng.*, vol. 220, p. 108970, Sep. 2021, doi: 10.1016/J.COMPOSITESB.2021.108970.

[234] B. Yu, R. Blanc, C. Soutis, and P. J. Withers, "Evolution of damage during the fatigue of 3D woven glass-fibre reinforced composites subjected to tension-tension loading observed by time-lapse X-ray tomography," *Compos. Part A Appl. Sci. Manuf.*, vol. 82, pp. 279–290, 2016, doi: 10.1016/j.compositesa.2015.09.001.

[235] S. C. Garcea, I. Sinclair, S. M. Spearing, and P. J. Withers, "Mapping fibre failure in situ in carbon fibre reinforced polymers by fast synchrotron X-ray computed tomography," *Compos. Sci. Technol.*, vol. 149, no. 2017, pp. 81–89, 2017, doi: 10.1016/j.compscitech.2017.06.006.

[236] P. Wagner, O. Schwarzhaupt, and M. May, "In-situ X-ray computed tomography of composites subjected to fatigue loading," *Mater. Lett.*, vol. 236, pp. 128–130, 2019, doi: 10.1016/j.matlet.2018.10.078.

[237] L. Guo, J. Huang, L. Zhang, and X. Sun, "Damage evolution of 3D woven carbon/epoxy composites under tension-tension fatigue loading based on synchrotron radiation computed tomography (SRCT)," *Int. J. Fatigue*, vol. 142, p. 105913, Jan. 2021, doi: 10.1016/J.IJFATIGUE.2020.105913.

[238] Q. D. Yang *et al.*, "On crack initiation in notched, cross-plied polymer matrix composites," *J. Mech. Phys. Solids*, vol. 78, pp. 314–332, May 2015, doi: 10.1016/J.JMPS.2015.01.010.

[239] A. Prajapati, A. Chirazi, L. P. Mikkelsen, T. Burnett, and P. J. Withers, "Observing the evolution of fatigue damage and associated strain fields in a correlative, multiscale 3D time-lapse study of quasi-unidirectional glass fibre composites", doi: 10.1088/1757-899X/942/1/012039.

[240] "Zeiss VersaXRM520 - Equipment and Facilities - Henry Royce Institute." https://www.royce.ac.uk/equipment-and-facilities/zeiss-xradia-versa-520/ (accessed Mar. 02, 2023).

[241] "Nikon Xtek High Flux Bay - Equipment and Facilities - Henry Royce Institute." https://www.royce.ac.uk/equipment-and-facilities/nikon-xtek-high-flux-bay/ (accessed Mar. 02, 2023).

[242] M. Endrizzi *et al.*, "Edge-illumination X-ray phase contrast imaging: matching the imaging method to the detector technology," *J. Instrum.*, vol. 9, no. 11, p. C11004, Nov. 2014, doi: 10.1088/1748-0221/9/11/C11004.

[243] A. Olivo, "Edge-illumination x-ray phase-contrast imaging," *J. Phys. Condens. Matter*, vol. 33, no. 36, p. 363002, Jul. 2021, doi: 10.1088/1361-648X/AC0E6E.

[244] P. J. Withers *et al.*, "X-ray computed tomography," *Nat. Rev. Methods Prim. 2021 11*, vol. 1, no. 1, pp. 1–21, Feb. 2021, doi: 10.1038/s43586-021-00015-4.

[245] E. Maire and P. J. Withers, "Quantitative X-ray tomography," *Int. Mater. Rev.*, vol. 59, no. 1, pp. 1–43, 2014.

[246] C. Arns *et al.*, "Techniques in helical scanning, dynamic imaging and image segmentation for improved quantitative analysis with X-ray micro-CT," *Nucl. Instruments Methods Phys. Res. Sect. B Beam Interact. with Mater. Atoms*, vol. 324, pp. 49–56, 2014, doi: 10.1016/j.nimb.2013.08.072.

[247] J. Q. Da Fonseca *et al.*, "Full-field strain mapping by optical correlation of micrographs," *J. Microsc.*, vol. 218, no. April, pp. 9–21, 2005.

[248] E. del Rey Castillo, T. Allen, R. Henry, M. Griffith, and J. Ingham, "Digital image correlation (DIC) for measurement of strains and displacements in coarse, low volume-fraction FRP composites used in civil infrastructure," *Compos. Struct.*, vol. 212, pp. 43–57, Mar. 2019, doi: 10.1016/J.COMPSTRUCT.2019.01.024.

[249] M. Mehdikhani, M. Aravand, B. Sabuncuoglu, M. G. Callens, S. V. Lomov, and L. Gorbatikh, "Full-field strain measurements at the micro-scale in fiber-reinforced composites using digital image correlation," *Compos. Struct.*, vol. 140, pp. 192–201, 2016, doi: 10.1016/j.compstruct.2015.12.020.

[250] S. V. Lomov *et al.*, "Full-field strain measurements in textile deformability studies," *Compos. Part A Appl. Sci. Manuf.*, vol. 39, no. 8, pp. 1232–1244, Aug. 2008, doi: 10.1016/J.COMPOSITESA.2007.09.014.

[251] S. V. Lomov *et al.*, "Full-field strain measurements for validation of meso-FE analysis of textile composites," *Compos. Part A Appl. Sci. Manuf.*, vol. 39, no. 8, pp. 1218–1231, Aug. 2008, doi: 10.1016/J.COMPOSITESA.2007.09.011.

[252] C. Oddy, M. Ekh, and M. Fagerström, "Macroscale modelling of 3D-woven composites: Elasto-plasticity and progressive damage," *Int. J. Solids Struct.*, vol. 250, p. 111696, Aug. 2022, doi: 10.1016/J.IJSOLSTR.2022.111696.

[253] C. Goidescu *et al.*, "Damage investigation in CFRP composites using full-field measurement techniques: Combination of digital image stereo-correlation, infrared thermography and X-ray tomography," *Compos. Part B Eng.*, vol. 48,

pp. 95–105, May 2013, doi: 10.1016/J.COMPOSITESB.2012.11.016.

[254] Y. Zhao, M. Noori, W. A. Altabey, R. Ghiasi, and Z. Wu, “A Fatigue Damage Model for FRP Composite Laminate Systems Based on Stiffness Reduction,” *SDHM*, vol. 13, no. 1, pp. 85–103, 2019, doi: 10.32604/sdhm.2019.04695.

[255] F. Ribeiro, J. Sena-Cruz, and A. P. Vassilopoulos, “Tension-tension fatigue behavior of hybrid glass/carbon and carbon/carbon composites,” *Int. J. Fatigue*, vol. 146, p. 106143, May 2021, doi: 10.1016/j.ijfatigue.2021.106143.

[256] M. Lakshmi Aparna, G. Chaitanya, K. Srinivas, and J. A. Rao, “Fatigue Testing of Continuous GFRP Composites Using Digital Image Correlation (DIC) Technique a Review,” *Mater. Today Proc.*, vol. 2, no. 4–5, pp. 3125–3131, Jan. 2015, doi: 10.1016/J.MATPR.2015.07.275.

[257] R. Srilakshmi, M. Ramji, and V. Chinthapenta, “Fatigue crack growth study of CFRP patch repaired Al 2014-T6 panel having an inclined center crack using FEA and DIC,” *Eng. Fract. Mech.*, vol. 134, pp. 182–201, Jan. 2015, doi: 10.1016/J.ENGFRACMECH.2014.12.012.

[258] E. Jo, S. Lee, C. Hong, and W. Ji, “In situ observation of interactive failure modes in a single-edge notched symmetric cross-ply laminate using synchrotron X-ray tomography,” *Compos. Part A Appl. Sci. Manuf.*, vol. 128, p. 105661, Jan. 2020, doi: 10.1016/j.compositesa.2019.105661.

[259] R. F. Agyei, I. Hanhan, and M. D. Sangid, “Detecting damage initiation in short fiber composites via in-situ X-ray tomography and digital volume correlation,” *Compos. Commun.*, vol. 22, p. 100524, Dec. 2020, doi: 10.1016/J.COCO.2020.100524.

[260] J. Marrow, C. Reinhard, Y. Vertyagina, L. Saucedo-Mora, D. Collins, and M. Mostafavi, “3D Studies of Damage by Combined X-ray Tomography and Digital Volume Correlation,” *Procedia Mater. Sci.*, vol. 3, pp. 1554–1559, Jan. 2014, doi: 10.1016/J.MSPRO.2014.06.251.

[261] E. Schöberl *et al.*, “A novel particle-filled carbon-fibre reinforced polymer model composite tailored for the application of digital volume correlation and computed tomography:,” *https://doi.org/10.1177/0021998320966388*, vol. 55, no. 14, pp. 1907–1934, Dec. 2020, doi: 10.1177/0021998320966388.

[262] J. E. Bailey, P. T. Curtis, and A. Parvizi, “On the transverse cracking and longitudinal splitting behaviour of glass and carbon fibre reinforced epoxy cross ply laminates and the effect of Poisson and thermally generated strain,” *Proc. R. Soc. London. A. Math. Phys. Sci.*, vol. 366, no. 1727, pp. 599–623, Jul. 1979, doi: 10.1098/RSPA.1979.0071.

[263] C. Lhymn and J. Bozolla, “Friction and wear of fiber reinforced pps composites,” *Adv. Polym. Technol.*, vol. 7, no. 4, pp. 451–461, Dec. 1987, doi: 10.1002/ADV.1987.060070409.

[264] H. L. Ganczakowski and P. W. R. Beaumont, “The behaviour of Kevlar fibre-epoxy laminates under static and fatigue loadings. Part I—experimental,” *Compos. Sci. Technol.*, vol. 36, no. 4, pp. 299–319, Jan. 1989, doi: 10.1016/0266-3538(89)90044-4.

[265] T. L. Burnett *et al.*, “Large volume serial section tomography by Xe Plasma FIB dual beam microscopy,” *Ultramicroscopy*, vol. 161, pp. 119–129, 2016.

[266] M. A. Groeber, B. K. Haley, M. D. Uchic, D. M. Dimiduk, and S. Ghosh, “3D reconstruction and characterization of polycrystalline microstructures using a FIB-SEM system,” *Mater. Charact.*, vol. 57, no. 4–5, pp. 259–273, 2006, doi: 10.1016/j.matchar.2006.01.019.

[267] A. Sheidaei *et al.*, “3-D microstructure reconstruction of polymer nano-composite using FIB-SEM and statistical correlation function,” *Compos. Sci. Technol.*, vol. 80, pp. 47–54, 2013, doi: 10.1016/j.compscitech.2013.03.001.

[268] T. L. Burnett *et al.*, “Correlative tomography,” *Sci. Rep.*, vol. 4, p. 4711, 2014.

[269] B. Bera, S. K. Mitra, and D. Vick, “Understanding the micro structure of Berea Sandstone by the simultaneous use of micro-computed tomography (micro-CT) and focused ion beam-scanning electron microscopy (FIB-SEM),” *Micron*, vol. 42, no. 5, pp. 412–418, 2011, doi: 10.1016/j.micron.2010.12.002.

[270] R. Zehbe, H. Riesemeier, C. J. Kirkpatrick, and C. Brochhausen, “Imaging of articular cartilage - Data matching using X-ray tomography, SEM, FIB slicing and conventional histology,” *Micron*, vol. 43, no. 10, pp. 1060–1067, 2012, doi: 10.1016/j.micron.2012.05.001.

[271] S. Handschuh, N. Baeumler, T. Schwaha, and B. Ruthensteiner, “A correlative approach for combining microCT, light and transmission electron microscopy in a single 3D scenario,” *Front. Zool.*, vol. 10, no. 1, pp. 1–16, 2013, doi: 10.1186/1742-9994-10-44.

[272] T. Starborg *et al.*, “Experimental steering of electron microscopy studies using prior X-ray computed tomography,” *Ultramicroscopy*, vol. 201, pp. 58–67, Jun. 2019, doi: 10.1016/J.ULTRAMIC.2019.03.002.

[273] B. Yu, R. S. Bradley, C. Soutis, P. J. Hogg, and P. J. Withers, “2D and 3D imaging of fatigue failure mechanisms of 3D woven composites,” *Compos. Part A Appl. Sci. Manuf.*, vol. 77, pp. 37–49, Oct. 2015, doi: 10.1016/J.COMPOSITESA.2015.06.013.

[274] K. Munk *et al.*, “X-ray tomography based finite element modelling of non-crimp fabric based fibre composite,” *ECCM18 - 18th Eur. Conf. Compos. Mater. Athens, Greece.*, pp. 24–28, 2018.

[275] P. Brøndsted, S. I. Andersen, and H. Lilholt, “Fatigue performance of glass/polyester laminates and the monitoring of material degradation,” *Mech. Compos. Mater. 1996 321*, vol. 32, no. 1, pp. 21–29, 1996, doi: 10.1007/BF02254644.

[276] I. Arganda-Carreras *et al.*, “Trainable Weka Segmentation: a machine learning tool for microscopy pixel classification,” vol. 33, no. 15, pp. 2424–2426, 2017.

[277] M. P. Thomas, J. G. Robertson, and M. R. Winstone, “Effect of fabrication parameters on the microstructural quality of fibre-foil titanium metal matrix composites,” *J. Mater. Sci.*, vol. 33, no. 14, pp. 3607–3614, 1998, doi: 10.1023/A:1004655329112/METRICS.

[278] B. Budiansky and N. A. Fleck, “Compressive failure of fibre composites,” *J.*

Mech. Phys. Solids, vol. 41, no. 1, pp. 183–211, Jan. 1993, doi: 10.1016/0022-5096(93)90068-Q.

[279] Y. Wang *et al.*, "Evolution of fibre deflection leading to kink-band formation in unidirectional glass fibre/epoxy composite under axial compression," *Compos. Sci. Technol.*, vol. 213, p. 108929, Sep. 2021, doi: 10.1016/J.COMPSCITECH.2021.108929.

[280] R. M. Sencu, Z. Yang, Y. C. Wang, P. J. Withers, and C. Soutis, "Multiscale image-based modelling of damage and fracture in carbon fibre reinforced polymer composites," *Compos. Sci. Technol.*, vol. 198, p. 108243, Sep. 2020, doi: 10.1016/J.COMPSCITECH.2020.108243.

[281] R. H. Nuttall, "The First Microscope of Henry Clifton Sorby," *Technol. Cult.*, vol. 22, no. 2, p. 275, Apr. 1981, doi: 10.2307/3104901.

[282] H. A. Holz, "Development of the metallurgical microscope and its suggested application to some unsolved problems," *Trans. Faraday Soc.*, vol. 16, no. September, pp. 191–194, Jan. 1920, doi: 10.1039/TF9201600191.

[283] F. W. Constant, "The Microstructure of Some Magnetic Alloys of High Platinum Concentration," *Phys. Rev.*, vol. 35, no. 1, p. 116, Jan. 1930, doi: 10.1103/PhysRev.35.116.

[284] W. E. Morton and K. C. Yen, "THE ARRANGEMENT OF FIBRES IN FIBRO YARNS," 2008, doi: 10.1080/19447025208659646.

[285] A. Khandual, A. Luximon, N. Rout, T. Grover, and I. M. Kandi, "Evaluation of Fibre Migration Angle by Image Processing Using Economic Usb Camera and Matlab: Demonstrated Example," in *Materials Today: Proceedings*, Jan. 2015, vol. 2, no. 4–5, pp. 2463–2471. doi: 10.1016/j.matpr.2015.07.187.

[286] C. Eberhardt, A. Clarke, M. Vincent, T. Giroud, and S. Flouret, "Fibre-orientation measurements in short-glass-fibre compsites - II: A quantitative error estimate of the 2D image analysis technique," *Compos. Sci. Technol.*, vol. 61, no. 13, pp. 1961–1974, Oct. 2001, doi: 10.1016/S0266-3538(01)00106-3.

[287] D. J. Jensen, H. Lilholt, and P. J. Withers, "Determination of fibre orientations in composites with short fibres.," *Mech. Phys. Behav. Met. Ceram. Compos. Risø*, 1988.

[288] R. Karamov, L. M. Martulli, M. Kerschbaum, I. Sergeichev, Y. Swolfs, and S. V. Lomov, "Micro-CT based structure tensor analysis of fibre orientation in random fibre composites versus high-fidelity fibre identification methods," *Compos. Struct.*, vol. 235, p. 111818, Mar. 2020, doi: 10.1016/j.compstruct.2019.111818.

[289] A. R. Clarke, G. Archenhold, and N. C. Davidson, "A NOVEL TECHNIQUE FOR DETERMINING THE 3D SPATIAL DISTRIBUTION OF GLASS FIBRES IN POLYMER COMPOSITES," 1995.

[290] L. Salvo *et al.*, "X-ray micro-tomography an attractive characterisation technique in materials science," *Nucl. instruments methods Phys. Res. Sect. B Beam Interact. with Mater. atoms*, vol. 200, pp. 273–286, 2003.

[291] J. Y. Buffiere, E. Maire, J. Adrien, J. P. Masse, and E. Boller, "In situ

experiments with X ray tomography: An attractive tool for experimental mechanics," *Proc. Soc. Exp. Mech. Inc.*, vol. 67, pp. 289–305, 2010, doi: 10.1007/s11340-010-9333-7.

[292] H. Yang and W. B. Lindquist, "Three-dimensional image analysis of fibrous materials," in *Applications of Digital Image Processing XXIII*, Dec. 2000, vol. 4115, no. 28, pp. 275–282. doi: 10.1117/12.411552.

[293] M. W. Czabaj, M. L. Riccio, and W. W. Whitacre, "Numerical reconstruction of graphite/epoxy composite microstructure based on sub-micron resolution X-ray computed tomography," *Compos. Sci. Technol.*, vol. 105, pp. 174–182, Dec. 2014, doi: 10.1016/j.compscitech.2014.10.017.

[294] R. M. Sencu *et al.*, "Generation of micro-scale finite element models from synchrotron X-ray CT images for multidirectional carbon fibre reinforced composites," *Compos. Part A Appl. Sci. Manuf.*, vol. 91, pp. 85–95, Dec. 2016, doi: 10.1016/j.compositesa.2016.09.010.

[295] C. Zhu, Y. Su, X. Wang, H. Sun, Q. Ouyang, and D. Zhang, "Process optimization, microstructure characterization and thermal properties of mesophase pitch-based carbon fiber reinforced aluminum matrix composites fabricated by vacuum hot pressing," *Compos. Part B Eng.*, vol. 215, p. 108746, Jun. 2021, doi: 10.1016/J.COMPOSITESB.2021.108746.

[296] C. Zhu, Y. Su, D. Zhang, and Q. Ouyang, "Effect of Al2O3 coating thickness on microstructural characterization and mechanical properties of continuous carbon fiber reinforced aluminum matrix composites," *Mater. Sci. Eng. A*, vol. 793, p. 139839, Aug. 2020, doi: 10.1016/J.MSEA.2020.139839.

[297] S. Yu, J. Y. Hwang, and S. H. Hong, "3D microstructural characterization and mechanical properties determination of short basalt fiber-reinforced polyamide 6,6 composites," *Compos. Part B Eng.*, vol. 187, p. 107839, Apr. 2020, doi: 10.1016/J.COMPOSITESB.2020.107839.

[298] S. P. Yap, Y. Goh, W. X. Goh, K. H. Mo, M. Y. J. Liu, and H. A. Ibrahim, "Relationship between microstructure and performance of polypropylene fibre reinforced cement composites subjected to elevated temperature," *https://doi.org/10.1080/19648189.2020.1734489*, vol. 26, no. 5, pp. 1792–1806, 2020, doi: 10.1080/19648189.2020.1734489.

[299] K. Saeed *et al.*, "Characterization of continuous carbon fibre reinforced 3D printed polymer composites with varying fibre volume fractions," *Compos. Struct.*, vol. 282, p. 115033, Feb. 2022, doi: 10.1016/J.COMPSTRUCT.2021.115033.

[300] M. R. Ahmad and B. Chen, "Microstructural characterization of basalt fiber reinforced magnesium phosphate cement supplemented by silica fume," *Constr. Build. Mater.*, vol. 237, p. 117795, Mar. 2020, doi: 10.1016/J.CONBUILDMAT.2019.117795.

[301] M. A. Ali, Q. Guan, R. Umer, W. J. Cantwell, and T. Zhang, "Deep learning based semantic segmentation of μCT images for creating digital material twins of fibrous reinforcements," 2020, doi: 10.1016/j.compositesa.2020.106131.

[302] Y. Sun, I. Hanhan, M. D. Sangid, and G. Lin, "Predicting Mechanical Properties

from Microstructure Images in Fiber-reinforced Polymers using Convolutional Neural Networks."

[303] A. T. Zehnder, V. Patel, and T. J. Rose, "Micro-CT Imaging of Fibers in Composite Laminates under High Strain Bending," *Exp. Tech.*, vol. 44, no. 5, pp. 531–540, Oct. 2020, doi: 10.1007/s40799-020-00374-9.

[304] P. Anuj, L. Daniel, C. Ali, P. M. Lars, L. B. Timothy, and J. W. Philip, "A novel automated workflow involving machine learning to study damage progression of fibre-reinforced composites by time-lapse 3D x-ray tomography".

[305] D. K. Rajak, D. D. Pagar, P. L. Menezes, and E. Linul, "Fiber-Reinforced Polymer Composites: Manufacturing, Properties, and Applications," *Polymers (Basel).*, vol. 11, no. 10, Oct. 2019, doi: 10.3390/POLYM11101667.

[306] W. Stinchcomb and K. Reifsnider, "Fatigue Damage Mechanisms in Composite Materials: A Review," *Fatigue Mech.*, pp. 762-762–26, 2009, doi: 10.1520/stp35914s.

[307] K. M. Jespersen, J. Zangenberg, T. Lowe, P. J. Withers, and L. P. Mikkelsen, "Fatigue damage assessment of uni-directional non-crimp fabric reinforced polyester composite using X-ray computed tomography," *Compos. Sci. Technol.*, vol. 136, pp. 94–103, Nov. 2016, doi: 10.1016/J.COMPSCITECH.2016.10.006.

[308] W. J. Yoo *et al.*, "Damage detection and assessment in fibre-reinforced composite structures withembedded fibre optic sensors-review," *Smart Mater. Struct.*, vol. 11, no. 6, p. 925, Oct. 2002, doi: 10.1088/0964-1726/11/6/314.

[309] R. J. Young, C. Thongpin, J. L. Stanford, and P. A. Lovell, "Fragmentation analysis of glass fibres in model composites through the use of Raman spectroscopy," *Compos. Part A Appl. Sci. Manuf.*, vol. 32, no. 2, pp. 253–269, Feb. 2001, doi: 10.1016/S1359-835X(00)00091-9.

[310] K. Takahashi *et al.*, "X-ray nanoimaging of a transversely embedded carbon fiber in epoxy matrix under static and cyclic loads," *Sci. Reports 2022 121*, vol. 12, no. 1, pp. 1–12, May 2022, doi: 10.1038/s41598-022-12724-1.

[311] B. Yu, "DAMAGE CHARACTERISATION OF 3D WOVEN GLASS-FIBREREINFORCED COMPOSITES UNDER FATIGUE LOADING USING XRAYCOMPUTED TOMOGRAPHY," *Univ. Manchester*, no. Ph.D. Thesis, 2015, [Online]. Available: https://www.research.manchester.ac.uk/portal/en/theses/damage-characterisation-of-3d-woven-glassfibrereinforced-composites-under-fatigue-loading-using-xraycomputed-tomography(e4d6ee91-e3f5-4b33-b9e7-4367cbbfcf0c).html

[312] W. Holub and U. Hassler, "XXL X-ray Computed Tomography for Wind Turbines in the lab and on-site." https://www.ndt.net/search/docs.php3?id=14905 (accessed Dec. 07, 2022).

[313] A. E. Scott, I. Sinclair, S. M. Spearing, M. N. Mavrogordato, and W. Hepples, "Influence of voids on damage mechanisms in carbon/epoxy composites determined via high resolution computed tomography," *Compos. Sci. Technol.*, vol. 90, pp. 147–153, Jan. 2014, doi: 10.1016/J.COMPSCITECH.2013.11.004.

[314] G. W. Melenka and A. Gholami, “Fiber identification of braided composites using micro-computed tomography,” *Compos. Commun.*, vol. 27, p. 100813, Oct. 2021, doi: 10.1016/J.COCO.2021.100813.

[315] D. Yang, H. Zhang, J. Wu, and E. D. McCarthy, “Fibre flow and void formation in 3D printing of short-fibre reinforced thermoplastic composites: An experimental benchmark exercise,” *Addit. Manuf.*, vol. 37, p. 101686, Jan. 2021, doi: 10.1016/J.ADDMA.2020.101686.

[316] M. Miletić *et al.*, “Gradient-based fibre detection method on 3D micro-CT tomographic image for defining fibre orientation bias in ultra-high-performance concrete,” *Cem. Concr. Res.*, vol. 129, p. 105962, Mar. 2020, doi: 10.1016/J.CEMCONRES.2019.105962.

[317] B. Yu, J. Ren, K. Wang, C. Wang, and H. Bian, “Experimental Study on the Characterization of Orientation of Polyester Short Fibers in Rubber Composites by an X-ray Three-Dimensional Microscope,” *Mater. 2022, Vol. 15, Page 3726*, vol. 15, no. 10, p. 3726, May 2022, doi: 10.3390/MA15103726.

[318] F. Sket, A. Enfedaque, C. Alton, C. González, J. M. Molina-Aldareguia, and J. Llorca, “Automatic quantification of matrix cracking and fiber rotation by X-ray computed tomography in shear-deformed carbon fiber-reinforced laminates,” *Compos. Sci. Technol.*, vol. 90, pp. 129–138, Jan. 2014, doi: 10.1016/J.COMPSCITECH.2013.10.022.

[319] Bergan A.C, G. S.C, and W. P.J., “Quantification of damage evolution in cross-ply polymer composites under longitudinal compression by fast computed tomography and semi-automated segmentation”.

[320] R. Karamov, L. M. Martulli, M. Kerschbaum, I. Sergeichev, Y. Swolfs, and S. V. Lomov, “Micro-CT based structure tensor analysis of fibre orientation in random fibre composites versus high-fidelity fibre identification methods,” *Compos. Struct.*, vol. 235, p. 111818, Mar. 2020, doi: 10.1016/J.COMPSTRUCT.2019.111818.

[321] J. Schindelin *et al.*, “Fiji: An open-source platform for biological-image analysis,” *Nature Methods*, vol. 9, no. 7. Nature Publishing Group, pp. 676–682, Jul. 28, 2012. doi: 10.1038/nmeth.2019.

[322] K. M. Jespersen and L. P. Mikkelsen, “Fatigue damage observed non-destructively in fibre composite coupon test specimens by X-ray CT,” *IOP Conf. Ser. Mater. Sci. Eng.*, vol. 139, no. 1, 2016, doi: 10.1088/1757-899X/139/1/012024.

[323] “Thermo Scientific TM Avizo TM Software 9 User’s Guide,” 2018.

[324] B. Yu, R. S. Bradley, C. Soutis, and P. J. Withers, “A comparison of different approaches for imaging cracks in composites by X-ray microtomography,” *Philos. Trans. R. Soc. A Math. Phys. Eng. Sci.*, vol. 374, no. 2071, p. 20160037, Jul. 2016, doi: 10.1098/rsta.2016.0037.

[325] L. Mishnaevsky, K. Branner, H. N. Petersen, J. Beauson, M. McGugan, and B. F. Sørensen, “Materials for wind turbine blades: An overview,” *Materials (Basel).*, vol. 10, no. 11, pp. 1–24, 2017, doi: 10.3390/ma10111285.

[326] S. C. Garcea, I. Sinclair, S. M. Spearing, and P. J. Withers, “Mapping fibre failure in situ in carbon fibre reinforced polymers by fast synchrotron X-ray computed tomography,” *Compos. Sci. Technol.*, vol. 149, pp. 81–89, Sep. 2017, doi: 10.1016/J.COMPSCITECH.2017.06.006.

[327] S. Djaziri *et al.*, “Combined synchrotron X-rays and image correlation analyses of biaxially deformed W/Cu nanocomposite thin films on Kapton,” *J. Appl. Crystallogr.*, vol. 44, pp. 1071–1079, 2011, doi: 10.1107/S0021889811030226ï.

[328] “How Fast Does a Wind Turbine Spin (and Why Does it Matter?) - The Roundup.” https://theroundup.org/how-fast-does-a-wind-turbine-spin/ (accessed Mar. 19, 2023).